Histological insights into growth trajectories, life history, and community age structure in the mammalian stem lineage

Zoe T. Kulik

A dissertation

submitted in partial fulfillment of the

requirements for the degree of

Doctor of Philosophy

University of Washington

2023

Reading Committee:

Christian A. Sidor, Chair

Gregory P. Wilson Mantilla

Tracy E. Popowics

Adam K. Huttenlocker

Program Authorized to Offer Degree:

Biology

University of Washington

Abstract

Histological insights into growth trajectories, life history, and community age structure in the mammalian stem lineage

Zoe T. Kulik

Chair of the Supervisory Committee:
Christian A. Sidor
Department of Biology

Much of our understanding of the terrestrial recovery of the end-Permian mass extinction comes from tetrapod assemblages from the Karoo Basin of South Africa but Triassic tetrapods are found in South America, India, Antarctica, and China, as well as nearby basins in Tanzania and Zambia. These assemblages, and the effects that the end-Permian mass extinction had on tetrapod lineages, are an intensely studied subject as they can provide critical information for species survival during turbulent environmental conditions. However, few studies have examined growth strategies and life history patterns, which can provide crucial information on a taxon's survivorship and success following a mass extinction; and the few that have, are almost exclusively based on South African specimens. Because fossilized bone preserves the original bone mineral fiber orientation and bone tissue composition, relative growth rates and markers of

skeletal maturity can be inferred from histologic thin sections to reconstruct growth patterns of extinct species. In this study, I use bone histology and body size estimates to investigate how different non-mammalian synapsid species adapted their growth trajectories in response to the changed post-extinction environments across Pangea. For the first two chapters, I focus on the dicynodont *Lystrosaurus*, which had a cosmopolitan distribution across Pangea during early Triassic times but whose growth trajectory has only been examined from southern Pangean species. In the last chapter, I document variation in bone tissue composition in Middle Triassic cynodont species to test the hypothesis that a mammal-like growth trajectory (i.e., rapid initial growth that plateaus early in ontogeny) is present in some of the earliest members of the mammalian stem 'recovery fauna' following the end-Permian extinction. This chapter analyzes cynodont life history across an inferred ontogenetic range of co-occurring species from temporally and spatially constrained deposits and offers an unprecedented opportunity to shed light on the growth trajectories of the last major radiation of the synapsid lineage prior to living mammals.

TABLE OF CONTENTS

LIST OF FIGURES

LIST OF TABLES

ACKNOWLEDGEMENTS

In the following chapters, I thank the museum curators, volunteers, field teams, preparators, mentors, funding sources, and undergraduate researchers that made each chapter possible. Here, I'd like to thank the people that supported me throughout my graduate career. Thanks first and foremost to my advisor, Chris Sidor. You have been instrumental in helping me hone my skills as an independent researcher and I thank you for always having my back and supporting me. I'd also like to thank you for teaching me how to think like a scientist and approach projects with a critical eye and with realistic goals. Whether you intend to or not, through your mentoring, you've shown me how *you* think, and that has helped me in ways that I will continue to draw on for the rest of my career.

I'd also like to thank the rest of my supervisory and reading committees, Tracy Popowics, Sharlene Santana, Adam Huttenlocker, and Greg Wilson Mantilla for their support, encouragement, and for the different training opportunities I was able to take advantage of in both the lab and the field. Being a part of the craniodental lab group with Tracy, Sue Herring, and many others, was an amazing way to jumpstart my research in various aspects of bone histology.

I would also like to thank the teaching teams I have been a part of at UW Biology and especially Karen Petersen for providing such a supportive, compassionate, and memorable lab to share the joys of comparative anatomy with countless students. I have loved every moment of teaching with you and am so grateful for your support and encouragement.

I'd also like to thank my past mentors, especially Hans Sues for opening my eyes to the incredibly weird world of Permian reptiles. I am forever grateful for the opportunity to be a part of the Smithsonian prep team and get to know so many giants of the field so early on. I also

would not be where I am today if it weren't for the support and mentoring from Kristi Curry Rogers. Kristi, you inspired me to become a paleontologist from the moment I met you. You introduced me to the field of paleohistology, and to the reality that I could also become a paleohistologist, and I am so thankful for your encouragement and friendship. I would also like to thank the rest of the Rogers family, Ray, Lucy, Hatcher, Jeff and all the geologists and paleontologists in training that brought me so much joy, discovery, and enthusiasm at Macalester and out in the Breaks.

To the UW Paleopod, and the Sidor lab members both past and present, thank you for being the best group of friends and mentors throughout my entire graduate career. Thanks especially to Meg, Luke, Brandon, Savannah, Alex, Steph, Brody, and Dave for answering any and every question I had, for reviewing countless grants and manuscripts, and for helping to navigate the world of academia. I'd also like to thank the rest of the UW Biology community, the grads, postdocs, staff, and faculty for the support system that you all provided, it is truly something that I will miss.

I would also like to thank my family, Lori, David, and Dylan, for helping me to pursue my passion. You raised me to stay curious, to work hard, and to follow a path of lifelong learning and I can never truly express how grateful I am. To my extended family, and especially my in-laws, I thank you for so much joy and laughter that you have brought to my life, especially over these past six years.

Words cannot express how lucky I feel to be part of such a supportive and tight-knit cohort in the Biology Department. Jordan, Jackson, Marina, and Kavya, you have been a constant source of discussion, laughs, and solidarity. A special thanks to my corehort, Jordan and Kavya, for being the brightest parts of some of the hardest years. You have always been there for

me to share a pint, a laugh, or a song, and I cannot imagine what graduate school would have been like without you.

Finally, none of this would have been possible without the support of my partner Guillermo. You have been by my side from day one and reminded me to always trust myself, to never lower my standards, to take advantage of every opportunity, and have been my biggest champion through every one of my successes, both big and small. Thank you for being my super tech support, for pushing me to become the best version of myself, and for always reminding me that there will be a hug and glass of whiskey waiting for me at home after a long day. I love you and I love the life we've built together.

Chapter 1. INTRODUCTION: BACKGROUND ON BONE HISTOLOGY AND ITS UTILITY IN INFERRING GROWTH TRAJECTORIES IN EXTINCT ORGANISMS

Bone histology provides details of an extinct organism's biology and physiology that are otherwise unavailable from morphology or anatomy alone. By studying the microstructural composition of fossilized bones in thin-section, critical insights into vertebrate growth rates, life history patterns, and maturity can be made based on the proportions and degree of organization of different bone tissue types. For example, animals that grow quickly deposit disorganized and highly vascularized bone, whereas slow-growing animals deposit well-organized and less vascularized bone (Amprino, 1947; de Margerie et al., 2002; Montes et al., 2010; Lee et al., 2013). Furthermore, cyclical or annual arrests in growth appear in the bone cortex of long-lived animals as mineralized lines or regionalized bands of slow-growing tissue (analogous to tree rings; Köhler et al., 2012). This relationship between growth rate and bone histology has been corroborated by numerous studies using extant vertebrates and is a widely used tool in paleobiology (de Margerie et al., 2002, de Margerie et al., 2004, Buffrénil et al., 2021).

However, vertebrate diversity has not been systematically sampled; not in a phylogenetic sense, nor using a standardized sampling protocol where one element is iteratively sampled from a size series that spans juveniles to adults. Indeed, early paleohistologists like Enlow and Ricqlès were limited to thin-sectioning fragmentary fossils of dubious taxonomic affinity or unknown element identification (e.g., Enlow and Brown, 1956; Enlow and Brown, 1957; Enlow and Brown, 1958; Ricqlès , 1969). More recently, comprehensive sampling of dinosaur species has revolutionized the once restrictive perspective on consumptive sampling and brought about a

new and highly sought-after avenue of inquiry into the biology of past fauna (Chinsamy, 1994; Horner et al., 1999; Horner et al., 2000).

Renewed and expanding interest in paleohistology has also brought upon an advent of new terminology to characterize and describe bone tissue composition. For this dissertation, I follow the terminology outlined in Francillion-Veilliot (1990) with updates to bone matrix terminology described in Buffrénil et al., (2021). For a detailed review of bone tissue terminology with respect to the specific changes recommended for restricting the use of "fibrolamellar bone" in favor of the broader term "woven-parallel complex" see Chapter 2.3.3: *Bone Tissue Terminology* from Kulik et al., 2021.

1.1.1 ***Factors that impact bone morphogenesis***

The utility of histological analyses is multi-faceted and can be used to answer simple questions like "What microanatomical structures characterize taxon X?" or more complex questions like "Does taxon Y show cyclical growth marks, and if so, how long did it take to reach adult size?". On a more fundamental level, most paleohistology studies focus on one main question: "Are size and age correlated in a size series of the same element?" We assume that size and age are correlated and that larger specimens should be more mature than smaller specimens of the same species, but this assumption does not always hold true. In other words, juveniles and adults may not be represented when all specimens, regardless of size, show immature bone tissue types.

In order to accurately assess changes in bone composition, the various factors that impact bone formation and growth must be considered and controlled for, in as much as they can. A useful framework for thinking about the factors that influence bone formation can be adapted from Seilacher's seminal paper (1970) where he proposed three major influences that shape

morphology (Fig. 1.1) that also shape bone tissue composition. He devised a triangular model where each apex is a factor that acts in varying strengths to impose limitations on morphology, these are: (i) adaptation or biological function, (ii) phylogenetic tradition (i.e., the historical influence of inheritance), and (iii) the architectural factors imposed by the nature of the skeleton. Seilacher's triangle has since been used to generate hypotheses about vertebrate morphology and the various constraints that lineages evolve within (e.g., Bambach, 1993). Decades later, Seilacher and Gishlick introduced a fourth influence that transformed the triangle into a pyramid, and that factor is the effective environment. This addition emphasizes that an individual organism represents one instant on a timeline of morphological change that is forever in flux (Seilacher and Gishlick, 2014).

The same influences outlined in Seilacher's pyramid also operate to impact bone tissue composition. Indeed, bone is a tissue that is first and foremost shaped based on the actions of the soft tissues that surround it (Enlow, 1984; Currey, 2003). The morphology of different elements across the skeleton is inherently shaped by biomechanical forces that also impact the organization of bone tissue in thin-section. For example, weight-bearing bones are under stronger functional demand and therefore have thicker cortices that are shaped by muscle actions. Mechanical demands can be recognized in thin-section by excrescences of disorganized bone that compose sites for muscle attachments (Martin et al., 1998). Therefore, the midshaft of long bones (e.g., femora and tibiae) are targeted for analyses of growth and life history because they generally lack muscle attachment sites that can bias interpretations of skeletal growth (Padian and Lamm, 2013).

Mechanical demands, however, are not the only factor that shapes bone tissue composition. Indeed, ontogeny, phylogeny, and environmental conditions each play a role in the

organization and composition of bone tissue (Padian, 2013). Ontogenetic affects are broadly generalized by the relative rate of bone deposition. It follows that, in general, young, actively growing bones will display the highest rates of bone deposition that are reflected by highly vascularized, disorganized bone, whereas mature bones are composed of poorly vascularized, organized bone tissue. Skeletal maturity is represented by a smoothing of the periosteal layer where no additional appositional growth will occur (Francillon-Vieillot et al., 1990). In contrast, bones that are still increasing in size, tend to have open vascular canals along the subperiosteal surface. Because bones remodel and reorganize throughout ontogeny, the earliest record of growth is removed. Therefore, when reconstructing the growth trajectory, a systematic sample that covers elements at different sizes is vital to accurately informing the earliest rates and patterns of growth throughout ontogeny.

Phylogenetic effects on bone tissue are weaker than others, especially at fine scales (e.g. Cubo et al., 2005; Cubo et al., 2021). However, at broad taxonomic scales, clades show dichotomous bone tissues (e.g., the avascular cortices of temnospondyls compared to the highly vascularized cortices of dinosaurs), but the nuances between closely related species are better explained by growth stage, locomotor mode, or local environmental conditions.

Environmental conditions have profound effects on many aspects of organismal biology, including growth and development. During periods of the year when conditions are optimal, growth proceed at its inherent rate, however, modulations in growth rate are caused by changes temperature, resource availability, and circadian rhythms that operate on seasonal or annual cycles to temporarily slow or arrest growth (e.g., Köhler et al., 2012). During cold, dark, or stressed environmental conditions, seasonal slowdowns in bone deposition occur. Importantly, the stability of environmental conditions (or lack thereof) is hypothesized to be a major driver of

developmental plasticity in vertebrates. In other words, variability in the timing and onset of reproduction within a population is predicted to depend on local conditions called maturation reaction norms, that either select for early onset of reproduction when conditions are good, or delayed reproduction times when conditions are bad (Fig. 1.2). Indeed, the highly variable environmental conditions that have occurred during mass extinctions are predicted to select for earlier maturation and reproduction in synapsid clades that survived ecosystem collapse during the end-Permian mass extinction (e.g., Botha et al., 2016; Huttenlocker and Botha, 2013).

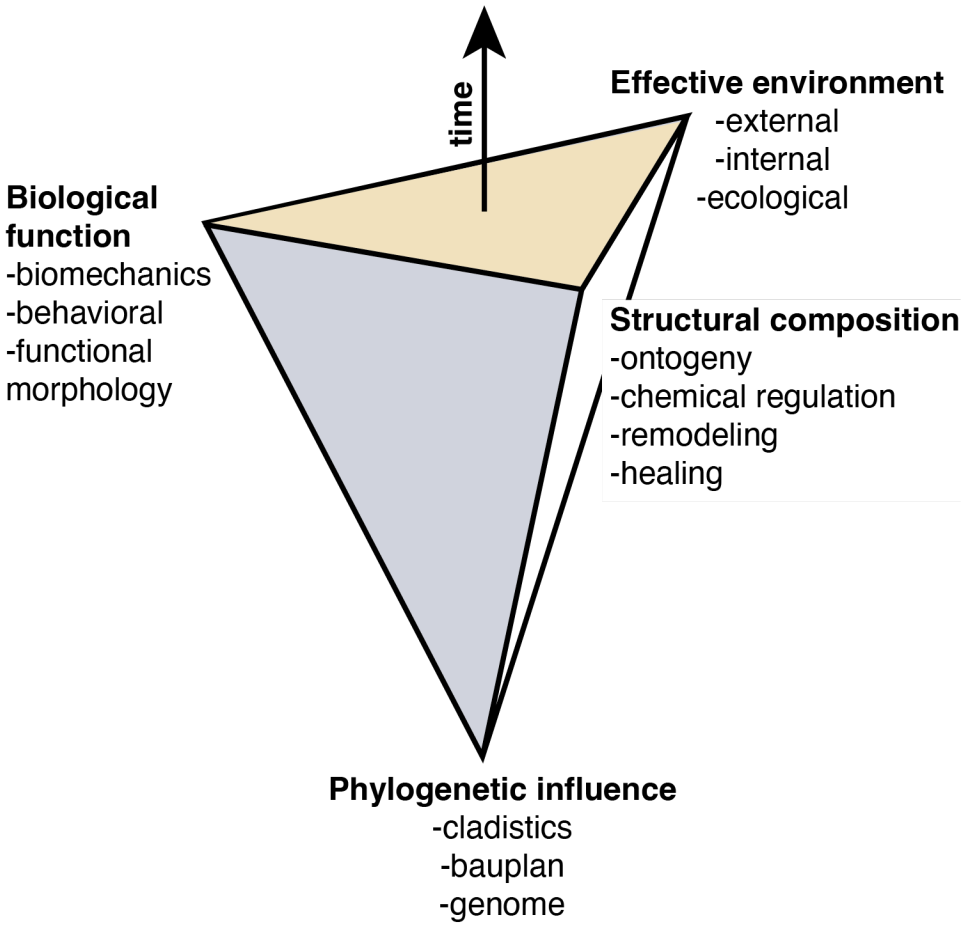

Figure 1.1. Seilacher's pyramid of morphodynamics that explains four major influences on organismal morphology, modified from (Seilacher, 1991) to include effects on bone morphogenesis.

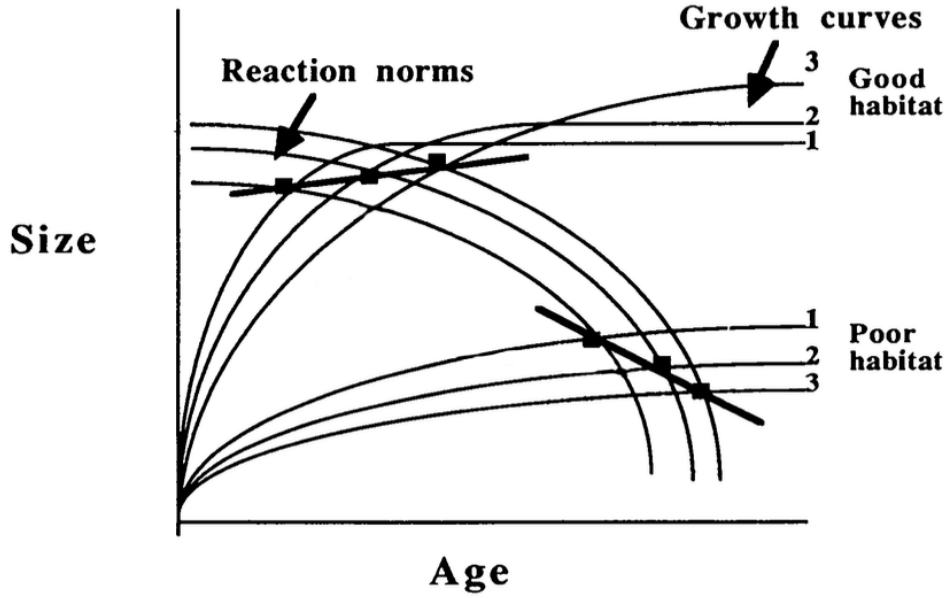

Figure 1.2. Hypothetical maturation reaction norms, modified by Stearns (1989). Reaction norms describe the tendency to mature as a function of an individual's age and size. Changes in growth (for example, caused by changes in population density) produce changes in the observed ages and body sizes at maturation that are due to developmental plasticity. An individual with faster growth under good environmental conditions (line 1) has a tendency to mature at an earlier age and larger body size (black squares) than an individual with a slower growth trajectory (line 3). In poor conditions, the timing of maturation is substantially lengthened, and body size is decreased. Changes in the slope of reaction norms (solid black lines connecting squares) reflect an underlying evolutionary change in the timing of maturation. In this case, the maturation ages and body sizes in the population under poor conditions have shifted as a result of a reduction in growth rates and delayed age of maturity.

Empirical and theoretical studies to evaluate the underlying mechanism to explain growth curves of extant population have resulted in conflicting results. From a theoretical standpoint, extrinsic mortality risk is recovered by multiple models as the drive of early maturation and reproduction (Roff, 2002; Jeschke et al., 2019; Del Giudice, 2015). However, others argue that allocation of resources for current or future offspring plays an equally important role in determining maturation times (Kozlowski, 1996). Others still, argue that selection pressures that shape mortality risk and offspring allocation are so intertwined that teasing apart their individual effects is ineffective and reductionist (Galipaud and Kokko, 2020)

Despite little to no consensus to identify a mechanism that underlies maturation rates, both theoretical and empirical studies operate with the assumption that life history tradeoffs (e.g., current-future investment tradeoffs, offspring quality vs. quantity tradeoffs, and density-dependent mortality risk) form a common fitness landscape for life history strategies to evolve. And that individuals and populations move across this fitness landscape under the same selection (Del Giudice, 2020). Local environmental conditions that these fitness landscape operate in create local variation in the timing of first reproduction (Fig 1.2). Under optimal environmental conditions, organisms are expected to reproduce soon after functional body size are reached. Conversely, under poor conditions, reproduction can either be delayed, in the case where individual plasticity in growth is high enough to allow for rebounds if conditions improve. Alternatively, poor conditions are also hypothesized to select for faster reproduction as a result of highly variable environmental conditions and high mortality risk. However, as discussed above, no functional basis to underly the rate of reproductive timing in life history has been robustly supported or agreed upon (e.g., Del Giudice, 2020).

Patterns of co-varying life history traits have been separated into a fast-slow continuum whereby smaller-bodied species, reproduce early, have large litters, short interbirth intervals, and suffer increased mortality risks (Fig. 1.3; Stearns, 1983; Promislow and Harvey, 1990). Conversely, large animals reproduce late, have large often singleton offspring, have long gestations, and enjoy low mortality risks. Placing species on the fast-slow continuum using body size alone does not adequately account for the variation in life history traits, as demonstrated by Stearns (1983) when body size effects were removed in an intraspecific sample of mammals. More recent authors have added an axis of variation for other factors such as parental investment, or egg size, that explain some of the variation in life history speeds when body size is removed (Fig 1.3).

Fast or slow life history strategies are not unique to mammals and birds, and have also been documented in fish, reptiles, insects, (e.g., Healy et al., 2019; Jeschke and Kokko, 2009; Promislow and Harvey, 1990; Stearns, 1983) and plants (Rüger et al., 2018). Life history patterns are also inferred for extinct tetrapods using bone histology to provide critical insight into to biology of individuals and populations (e.g., Hugi et al., 2020; Klein et al., 2012; Nacarino-Meneses et al, 2016; Orlandi-Oliveras et al., 2018). However, recognizing the onset of reproductive maturity is exceedingly difficult in the fossil record as key aspects of primiparity do not readily preserve. Critically, bone histology provides one of the only lines of evidence to infer developmental patterns in the fossil record and can provide details on how long it took animals to reach functional or maximum size, when reproductive maturity has is assumed to have occurred. Furthermore, the various effects on bone morphogenesis discussed above can be controlled by varying the sampling strategy of which elements, species, or assemblages are thin-sectioned.

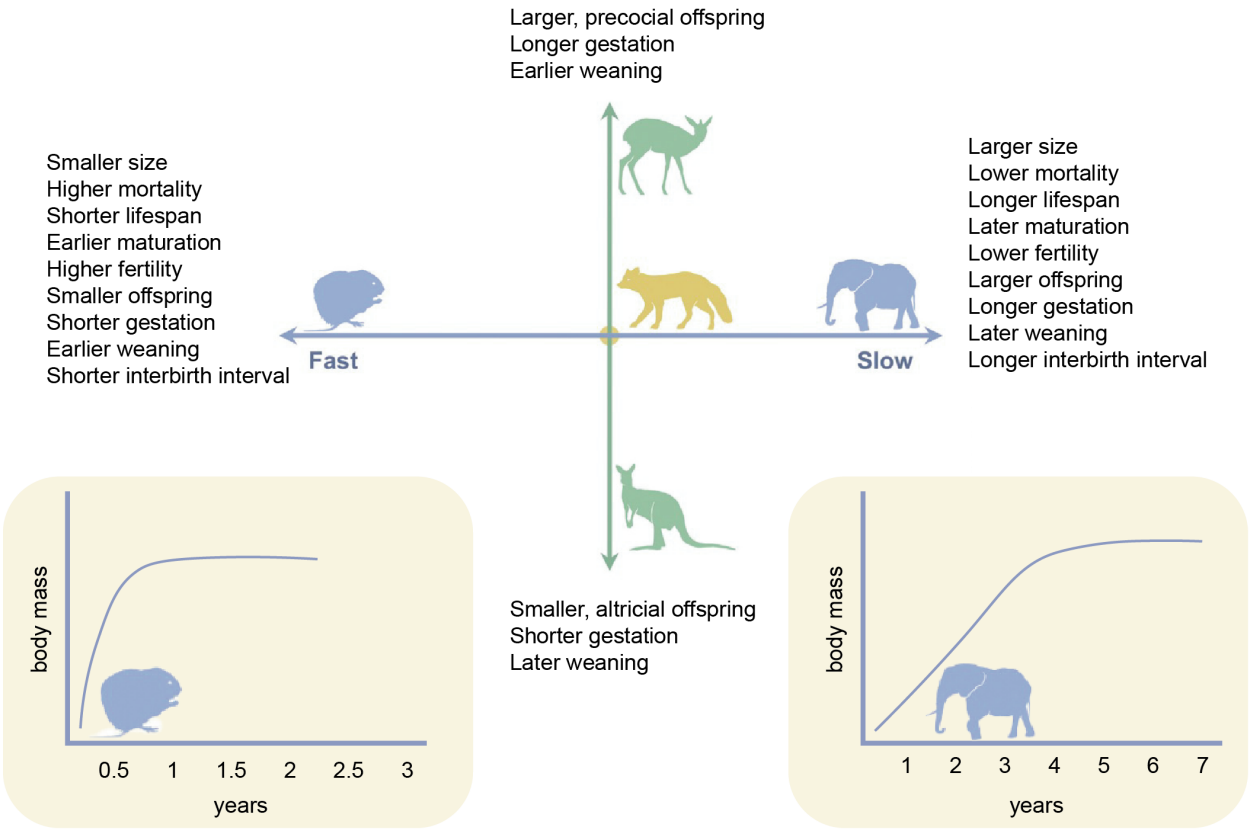

Figure 1.3. A PCA plot representing life history traits across mammalian species modified from Del Giudice (2020) with representative growth curves for fast and slow species highlighted in yellow boxes, respectively. Life history traits are based on Stearns (1983); Promislow and Harvey (1990); Oli (2004); and Del Giudice's reanalysis of data from Bielby et al. (2007) and Jeschke and Kokko (2009).

1.2 REFERENCES

Amprino, R. (1947). La structure du tissu osseux envisagée comme expression de différences dans la vitesse de l'accroissement. *Archives de Biologie*, *58*(4), 317–330.
analysis of life-history variation among mammals. Journal of Zoology, 220, 417–437.

Bambach, R. K. (1993). Seafood through time: changes in biomass, energetics, and productivity in the marine ecosystem. *Paleobiology*, *19*(3), 372-397.

Bielby, J., Mace, G. M., Bininda-Emonds, O. R. P., Cardillo, M., Gittleman, J. L., Jones, K. E., Orme, C. D. L., & Purvis, A. (2007). The Fast-Slow Continuum in Mammalian Life History: An Empirical Reevaluation. *The American Naturalist*, *169*(6), 748–757. https://doi.org/10.1086/516847

Botha-Brink, J., Codron, D., Huttenlocker, A. K., Angielczyk, K. D., & Ruta, M. (2016). Breeding Young as a Survival Strategy during Earth's Greatest Mass Extinction. *Scientific Reports*, *6*(1). https://doi.org/10.1038/srep24053

Buffrénil, V. de, A. de Ricqlès, L. Zylberberg, and K. Padian, eds. 2021. *Vertebrate Skeletal Histology and Paleohistology*. https://www.taylorfrancis.com/books/9781351189590.

Buffrénil, V. de, A. de Ricqlès, L. Zylberberg, and K. Padian, eds. 2021. *Vertebrate Skeletal Histology and Paleohistology*. https://www.taylorfrancis.com/books/9781351189590.

Chinsamy, A. (1994). Dinosaur bone histology: Implications and inferences. *The Paleontological Society Special Publications*, *7*, 213–228.

Cubo, J., Legendre, L., & Laurin, M. (2021). Phylogenetic Signal in Bone Histology. In V. de Buffrénil, A. J. de Ricqlès, K. Padian, & L. Zylberberg (Eds.), *Vertebrate Skeletal Histology and Paleohistology* (1st ed.). CRC Press, Taylor & Francis Group. https://doi.org/10.1201/9781351189590

Cubo, J., Ponton, F., Laurin, M., De Margerie, E., & Castanet, J. (2005). Phylogenetic Signal in Bone Microstructure of Sauropsids. *Systematic Biology*, *54*(4), 562–574. https://doi.org/10.1080/10635150591003461

Currey, J. D. (2003). The many adaptations of bone. *Journal of Biomechanics*, *36*(10), 1487–1495. https://doi.org/10.1016/S0021-9290(03)00124-6

de Margerie, E., Cubo, J., & Castanet, J. (2002). Bone typology and growth rate: Testing and quantifying 'Amprino's rule' in the mallard (*Anas platyrhynchos*). *Comptes Rendus Biologies*, *325*(3), 221–230. https://doi.org/10.1016/S1631-0691(02)01429-4

de Ricqlès, A. (1969). Recherches paleohistologiques sur les os longs des tetrapodes; II, Quelques observations sur la structure des os longs des theriodontes. *Annales de paléontologie. Vertébrés*, *55*(1), 52.

Del Giudice, M. (2020). Rethinking the fast-slow continuum of individual differences. *Evolution and Human Behavior*, *41*(6), 536–549. https://doi.org/10.1016/j.evolhumbehav.2020.05.004

Enlow, D. H. (1984). The "V" principle. *American Journal of Orthodontics*, *85*(1), 96. https://doi.org/10.1016/0002-9416(84)90129-5

Enlow, H., & Brown, S. O. (1956). A Comparative Histological Study of Fossil and Recent Bone Tissues. Part I. *Texas Journal of Science*, *8*(4), 41.

Enlow, H., & Brown, S. O. (1957). A Comparative Histological Study of Fossil and Recent Bone Tissues. Part II. *Texas Journal of Science*, *9*(2), 30.

Enlow, H., & Brown, S. O. (1958). A comparative histological study of fossil and recent bone tissues, Part III. *Texas Journal of Science*, *10*(2), 187–230.

Francillon-Vieillot, H., de Buffrénil, V., Castanet, J., Géraudie, J., Meunier, F. J., Sire, J. Y., Zylberberg, L., & de Ricqlès, A. (1990). Microstructure and Mineralization of Vertebrate Skeletal Tissues. In J. G. Carter (Ed.), *Short Courses in Geology* (pp. 175–234). American Geophysical Union. https://doi.org/10.1029/SC005p0175

Galipaud, M., & Kokko, H. (2020). Adaptation and plasticity in life-history theory: How to derive predictions. *Evolution and Human Behavior*, *41*(6), 493–501. https://doi.org/10.1016/j.evolhumbehav.2020.06.007

Healy, K., Ezard, T. H. G., Jones, O. R., Salguero-Gómez, R., & Buckley, Y. M. (2019). Animal life history is shaped by the pace of life and the distribution of age-specific mortality and reproduction. *Nature Ecology & Evolution*, *3*(8), Article 8. https://doi.org/10.1038/s41559-019-0938-7

Horner, J. R., de Ricqlès , A., & Padian, K. (1999). Variation in dinosaur skeletochronology indicators: Implications for age assessment and physiology. *Paleobiology*, *25*(3), 295–304.

Horner, J. R., de Ricqlès, A., & Padian, K. (2000). Long bone histology of the hadrosaurid dinosaur *Maiasaura peeblesorum*: Growth dynamics and physiology based on an ontogenetic series of skeletal elements. *Journal of Vertebrate Paleontology*, *20*(1), 115–129. https://doi.org/10.1671/0272-4634(2000)020[0115:LBHOTH]2.0.CO;2

Hugi, J., & Sánchez-Villagra, M. R. (2012). Life History and Skeletal Adaptations in the Galapagos Marine Iguana (*Amblyrhynchus cristatus*) as Reconstructed with Bone Histological Data—A Comparative Study of Iguanines. *Journal of Herpetology*, *46*(3), 312–324. https://www.jstor.org/stable/23326900

Huttenlocker, A. K., & Botha-Brink, J. (2013). Body size and growth patterns in the therocephalian *Moschorhinus kitchingi* (Therapsida: Eutheriodontia) before and after the end-Permian extinction in South Africa. *Paleobiology*, *39*(2), 253–277. https://doi.org/10.1666/12020

Jeschke, J. M., & Kokko, H. (2009). Roles of body size and phylogeny in fast and slow life histories. *Evolutionary Ecology*, *23*(6), 867–878. https://doi.org/10.1007/s10682-008-9276-y

Jeschke, J. M., Gabriel, W., & Kokko, H. (2019). r-Strategists/K-Strategists. In *Encyclopedia of Ecology* (Second Edition, pp. 193–201). Elsevier B.V. https://doi.org/10.1016/B978-0-12-409548-9.11121-2

Jones, O. R., Gaillard, J.-M., Tuljapurkar, S., Alho, J. S., Armitage, K. B., Becker, P. H., Bize, P., Brommer, J., Charmantier, A., Charpentier, M., Clutton-Brock, T., Dobson, F. S., Festa-Bianchet, M., Gustafsson, L., Jensen, H., Jones, C. G., Lillandt, B.-G., McCleery, R., Merilä, J., … Coulson, T. (2008). Senescence rates are determined by ranking on the fast–slow life-history continuum. *Ecology Letters*, *11*(7), 664–673. https://doi.org/10.1111/j.1461-0248.2008.01187.x

Klein, N., Sander, P. M., Stein, K., Loeuff, J. L., Carballido, J. L., & Buffetaut, E. (2012). Modified Laminar Bone in *Ampelosaurus atacis* and Other Titanosaurs (Sauropoda): Implications for Life History and Physiology. *PLOS ONE*, *7*(5), e36907. https://doi.org/10.1371/journal.pone.0036907

Köhler, M., N. Marín-Moratalla, X. Jordana, and R. Aanes. 2012. Seasonal bone growth and physiology in endotherms shed light on dinosaur physiology. *Nature* 487 (7407): 358–61. Https://doi.org/10.1038/nature11264.

Kozlowski, J. (1996). Optimal allocation of resources explains interspecific life-history patterns in animals with indeterminate growth. *Proceedings of the Royal Society of London. Series B: Biological Sciences*, *263*(1370), 559–566. https://doi.org/10.1098/rspb.1996.0084

Lee, A., K. Padian, H. N. Woodward, and A. K. Huttenlocker. 2013. "Analysis of growth rates." In *Bone Histology of Fossil Tetrapods*, edited by K. Padian and E Lamm - T., 216–51. University of California Press. Https://doi.org/10.1525/california/9780520273528.003.0008.

Margerie, E. De, J. Cubo, and J. Castanet. 2002. Bone typology and growth rate: testing and quantifying 'Amprino's Rule' in the mallard (Anas Platyrhynchos). *Comptes Rendus Biologies* 325 (3): 221–30. Https://doi.org/10.1016/S1631-0691(02)01429-4.

Margerie, E. De, J.-P. Robin, D. Verrier, J. Cubo, R. Groscolas, and J. Castanet. 2004. "Assessing a relationship between bone microstructure and growth rate: a fluorescent labelling study in the King Penguin chick (*Aptenodytes patagonicus*). *Journal of Experimental Biology* 207 (5): 869– 79. Https://doi.org/10.1242/jeb.00841.

Martin, R. B., Burr, D. B., & Sharkey, N. A. (1998). *Skeletal tissue mechanics*. Springer.

Marty, L., Dieckmann, U., Rochet, M.-J., & Ernande, B. (2011). Impact of Environmental Covariation in Growth and Mortality on Evolving Maturation Reaction Norms. *The American Naturalist*, *177*(4), E98–E118. https://doi.org/10.1086/658988

Montes, L., Castanet, J., & Cubo, J. (2010). Relationship between bone growth rate and bone tissue organization in amniotes: First test of Amprino's rule in a phylogenetic context. *Animal Biology*, *60*(1), 25–41. https://doi.org/10.1163/157075610X12610595764093

Nacarino-Meneses, C., Jordana, X., & Köhler, M. (2016). Histological variability in the limb bones of the Asiatic wild ass and its significance for life history inferences. *PeerJ*, *4*, e2580. https://doi.org/10.7717/peerj.2580

Oli, M. K. (2004). The fast–slow continuum and mammalian life-history patterns: An empirical evaluation. Basic and Applied Ecology, 5, 449–463.

Orlandi-Oliveras, G., Nacarino-Meneses, C., Koufos, G. D., & Köhler, M. (2018). Bone histology provides insights into the life history mechanisms underlying dwarfing in hipparionins. *Scientific Reports*, *8*(1). https://doi.org/10.1038/s41598-018-35347-x

Padian, K. 2013. "Why Study the Bone Microstructure of Fossil Tetrapods?" In *Bone Histology of Fossil Tetrapods*, edited by K. Padian and E Lamm - T., 1–13. University of California Press. Https://doi.org/10.1525/california/9780520273528.003.0008.

Promislow, D. E., & Harvey, P. H. (1990). Living fast and dying young: A comparative analysis of life-history variation among mammals. Journal of Zoology, 220, 417–437.

Rüger, N., Comita, L. S., Condit, R., Purves, D., Rosenbaum, B., Visser, M. D., ... Wirth, C. (2018). Beyond the fast–slow continuum: Demographic dimensions structuring a tropical tree community. Ecology Letters, 21, 1075–1084.

Seilacher, A. (1970). Arbeitskonzept zur konstruktions-morphologie. *Lethaia*, *3*(4), 393-396.

Seilacher, A. (1991). Self-organizing mechanisms in morphogenesis and evolution. Pages. 251–271 in N. Schmidt-Kittler, and K. Vogel (eds.), Constructional morphology and evolution.

Seilacher, A., & Gishlick, A. D. (2014). *Morphodynamics*. CRC Press.

Stearns, S. C. (1983). The Influence of Size and Phylogeny on Patterns of Covariation among Life-History Traits in the Mammals. *Oikos*, *41*(2), 173–187. https://doi.org/10.2307/3544261

Stearns, S. C. (1989). Trade-Offs in Life-History Evolution. *Functional Ecology*, *3*(3), 259–268. https://doi.org/10.2307/2389364

Chapter 2. LIVING FAST IN THE TRIASSIC: NEW DATA ON LIFE HISTORY IN *LYSTROSAURUS* (THERAPSIDA: DICYNODONTIA) FROM NORTHEASTERN PANGEA

Kulik, Z. T., Lungmus, J. K., Angielczyk, K. D., & Sidor, C. A. (2021). Living fast in the Triassic: New data on life history in *Lystrosaurus* (Therapsida: Dicynodontia) from northeastern Pangea. *PLOS ONE*. https://doi.org/e0259369

2.1 ABSTRACT

Lystrosaurus was one of the few tetrapods to survive the Permo-Traissic mass extinction, the most profound biotic crisis in Earth's history. The wide paleolatitudinal range and high abundance of *Lystrosaurus* during the Early Triassic provide a unique opportunity to investigate changes in growth dynamics and longevity following the mass extinction, yet most studies have focused only on species that lived in the southern hemisphere. Here, we present the long bone histology from twenty *Lystrosaurus* skeletal elements spanning a range of sizes that were collected in the Jiucaiyuan Formation of northwestern China. In addition, we compare the average body size of northern and southern Pangean Triassic-aged species and conduct cranial geometric morphometric analyses of southern and northern taxa to begin investigating whether specimens from China are likely to be taxonomically distinct from South African specimens. We demonstrate that *Lystrosaurus* from China have larger average body sizes than their southern Pangean relatives and that cranial morphologies are distinctive. The osteohistological examination revealed sustained, rapid osteogenesis punctuated by growth marks in some, but not all, immature individuals from China. We find that the bone histology of Chinese *Lystrosaurus* shares a similar growth pattern with South African species that show sustained growth until death. However, bone growth arrests

more frequently in the Chinese sample. Nevertheless, none of the long bones sampled here indicate that maximum or asymptotic size was reached, suggesting that the maximum size of *Lystrosaurus* from the Jiucaiyuan Formation remains unknown.

2.2 INTRODUCTION

The Permo-Triassic mass extinction was the most devastating biotic crisis in Earth's history and caused communities to collapse in both the terrestrial and marine realms [1-3]. Fluctuating climates accompanied by an overall increase in global temperatures are hypothesized to have forced 70% of terrestrial vertebrate families to extinction [4-8], although plant extinctions were notably damped [9-11]. Recovery after the Permo-Triassic extinction has been a topic of intense research, but most studies in the terrestrial realm focus on taxonomic diversity and abundance [12-14], or changes in community structure and dynamics following the extinction [6, 3, 15-18]. Few studies have examined how the extremely changed environment of the earliest Triassic impacted growth rate, life history, and longevity of surviving taxa [19-22]. Importantly, most of the studies noted above rely heavily—if not exclusively—on data from the southern hemisphere, in particular the Karoo Basin of South Africa.

Lystrosaurus, a stoutly built dicynodont therapsid that ranged in maximum skull size from approximately 16–39 cm (*L. murrayi* and *L. maccaigi* from South Africa, respectively), is one of the hallmark survivors of the Permo-Triassic extinction due to its remarkable abundance in southern Pangean deposits (23-24, 18]. The success of *Lystrosaurus* has been variously attributed to its generalist diet of tough plant material (e.g., [25, 26]), broad habitat tolerances [27], a burrowing lifestyle [28], unusual thermal tolerances [29], and a developmentally plastic growth strategy that allowed it to weather extreme ecosystem instability [30, 20, 22, 31]. These hypothesized advantages/exaptations for a post-extinction environment have been studied almost

exclusively using specimens from South Africa, but *Lystrosaurus* is known from across Pangea: including Permo-Triassic aged deposits in Antarctica, Mongolia, Russia, China, India, and possibly Mozambique (e.g., [32-39]). The wide paleolatitudinal range of *Lystrosaurus* offers a rare opportunity to investigate differences in lifespan, survivorship, and body size in southern and northern Pangean populations that experienced markedly different environmental conditions in the wake of the Permo-Triassic extinction (e.g., [22, 40]).

2.2.1 *Osteohistological Perspectives on Life History*

Bone histology provides a wealth of information about an extinct animal's growth and life history. Mineralized bone matrix, vascular canal spaces, and cellular spaces persist in fossilized bone, making it possible to determine the relative rate of bone deposition as well as maturity of extinct organisms [41]. Cyclical decreases in skeletal growth rate leave histological markers, termed growth marks, in primary cortical bone. Annuli and lines of arrested growth (LAGs) are two types of cyclical growth marks that are deposited in annual or seasonal cycles [42-44]. Annuli represent periodic decreases in growth rate and are usually identified based on specific, contextual changes in the bone tissue architecture, such as a dramatic decrease of vascular and cellular density, or a temporary shift to parallel-fibered or lamellar bone. LAGs, on the other hand, represent periodic cessations in growth and appear as hypermineralized lines in the primary cortical bone of most vertebrates when bone deposition stops in unfavorable seasons [44-49, 42]. In addition to extrinsically (i.e., environmentally or seasonally) induced growth marks, growth can also arrest during periods of intense stress, such as birth, and during modulations to metabolic activity such as torpor [50, 51]. The periodicity of growth marks (i.e., the extent to which they are regularly spaced throughout the cortex of large, presumably mature individuals) helps to determine whether they represent extrinsic or intrinsic events.

Botha [22] recently conducted a detailed examination of growth and life history patterns in four species of *Lystrosaurus* across the Permian-Triassic boundary using fossils from South Africa. Using a combination of bone histology and body size data, Botha [22] found that Triassic *Lystrosaurus* individuals grew rapidly and had increased mortality at small sizes, as evidenced by the overwhelming abundance of small skulls known from Triassic rocks in the Karoo Basin. This post-extinction change in life expectancy is also inferred from the scarcity of LAGs and annuli in the rapidly deposited cortical bone of Triassic specimens. In comparison, Permian individuals had larger average skull sizes and had numerous growth marks spaced throughout the cortex, suggesting prolonged periods of growth spanning multiple seasons or years [22]. Similar patterns were previously found across a wider taxonomic range of South African therapsid species [20] and lydekkerinid stereospondyls [52, 53]. The predominance of small *Lystrosaurus* (and other tetrapods) with rapidly deposited bone tissue suggests an overall shift in life history strategy across the Permian-Triassic boundary to an early onset of reproductive maturity [20, 52, 53].

Histological data for *Lystrosaurus* outside of the South African Karoo Basin are more limited, but critical to understanding the relationship between latitude (and by extension climate) and life history. Bones of *Lystrosaurus* from the Early Triassic of India lack LAGs and annuli, and have small skulls, consistent with the pattern seen in South Africa [37, 54]. A preliminary report of the bone histology from *Lystrosaurus* from the Turpan-Hami Basin of China suggested that subadult individuals record multiple LAGs [40]. However, in the absence of comparative body size data, it remains unclear if multiple LAGs in the Chinese specimens indicate prolonged periods of growth (i.e., multiple cycles or seasons of growth) or environmental instability (e.g., disruptions to the metabolic rate as a result of resource limitations). Here, we analyze bone

histology from a size range of *Lystrosaurus* postcrania from the Jiucaiyuan Formation of Xinjiang, China (Fig 2.1) as well as body size data across Triassic-aged *Lystrosaurus* assemblages to investigate whether *Lystrosaurus* from northern Pangea had differing life histories than its southern Pangean relatives.

Size Class II
Size Class III
Size Class IV
Unknown
IVPP V27124-6
IVPP V27124-7
IVPP V27126
IVPP V27124-1
IVPP V27124-4
IVPP V27124-3
IVPP V27124-8
IVPP V27124-2
IVPP V27125
IVPP V26548
IVPP V27127
IVPP V27124-5
5 cm
Radius, Ulna, Humerus, Ribs
Femur
Tibia and Fibula

Figure 2.1. Size distribution of *Lystrosaurus* sp. postcrania from the Jiucaiyuan formation included in the histologic analysis. Twenty skeletal elements, with gray bars indicating associations of individuals, span three size classes inferred from femoral length: Size Class II spans 47–63% maximum femoral size, Size Class III includes specimens that are ~ 70% maximum size, and Size Class III includes the largest partial femur. Scale bar = 5 cm.

2.3 MATERIAL AND METHODS

2.3.1 *Geometric Morphometric Analysis of Skull Shape in Lystrosaurus*

An important question to consider when comparing the bone histology of *Lystrosaurus* specimens from China and other regions is whether the same species occur in the different geographic areas. Although the first material of *Lystrosaurus* collected in Xinjiang was referred to the South African species *L. murrayi* [55], a total of seven endemic *Lystrosaurus* species also have been described [56-60]. Colbert [33]; also see [61-63], considered some Chinese specimens to represent *L. murrayi* and *L. curvatus*, and others to represent endemic species. More recent authors have been split over whether *Lystrosaurus* specimens from Xinjiang represent exclusively endemic species or a mixture of endemic and more cosmopolitan species, as well as the number of valid endemic species (e.g., [35, 64-67, 40]).

A comprehensive taxonomic revision of *Lystrosaurus* from Xinjiang is beyond the scope of this paper. However, to gain insight into whether Chinese *Lystrosaurus* specimens are likely to be taxonomically distinct from South African specimens, we conducted a preliminary two-dimensional geometric morphometric analysis of skull shape. The skulls were analyzed in three perspectives – anterior, dorsal, and lateral – following the methodology of [68]; also see [67]. The anterior shape analysis included 45 individual specimens, 15 from China and the remaining 30 from South Africa. The dorsal shape analysis included 107 specimens, 14 from China and 93 from South Africa. Lastly, the lateral analysis included 95 specimens, 9 from China and 86 from South Africa. Landmarks were collected using the tpsDig2ws software [69]. In the case of the anterior and dorsal views, landmarks were digitized on only the left half of the skull. The lateral view digitization included a combination of Type I and Type II landmarks (12 total) with a single curve of six semilandmarks along the outer edge of the snout between landmarks number 1 and 11 (Fig

2.2). The anterior and dorsal views did not contain any semilandmarks, and have 10 and 13 landmarks, respectively. Because taphonomic deformation can complicate the interpretation of shape variation at low taxonomic levels in dicynodonts [70], data collection focused on specimens that appeared to show relatively little evidence of distortion. See the supplementary files for additional details of the morphometric analysis.

The coordinate data were processed and analyzed further with the Geomorph R package [71], where they underwent a generalized Procrustes superimposition. Principal components analyses were used to visualize major patterns of shape variation, and a Procrustes ANOVA was run on each dataset to assess the statistical relationship between shape and country of origin using the method of [72] and the Geomorph package in R. A canonical variates analysis was run using the CVA function of the Morpho package [73] in R to further explore the association between shape and geographic location, as well as the accuracy with which specimens could be classified using skull shape (see *Results*).

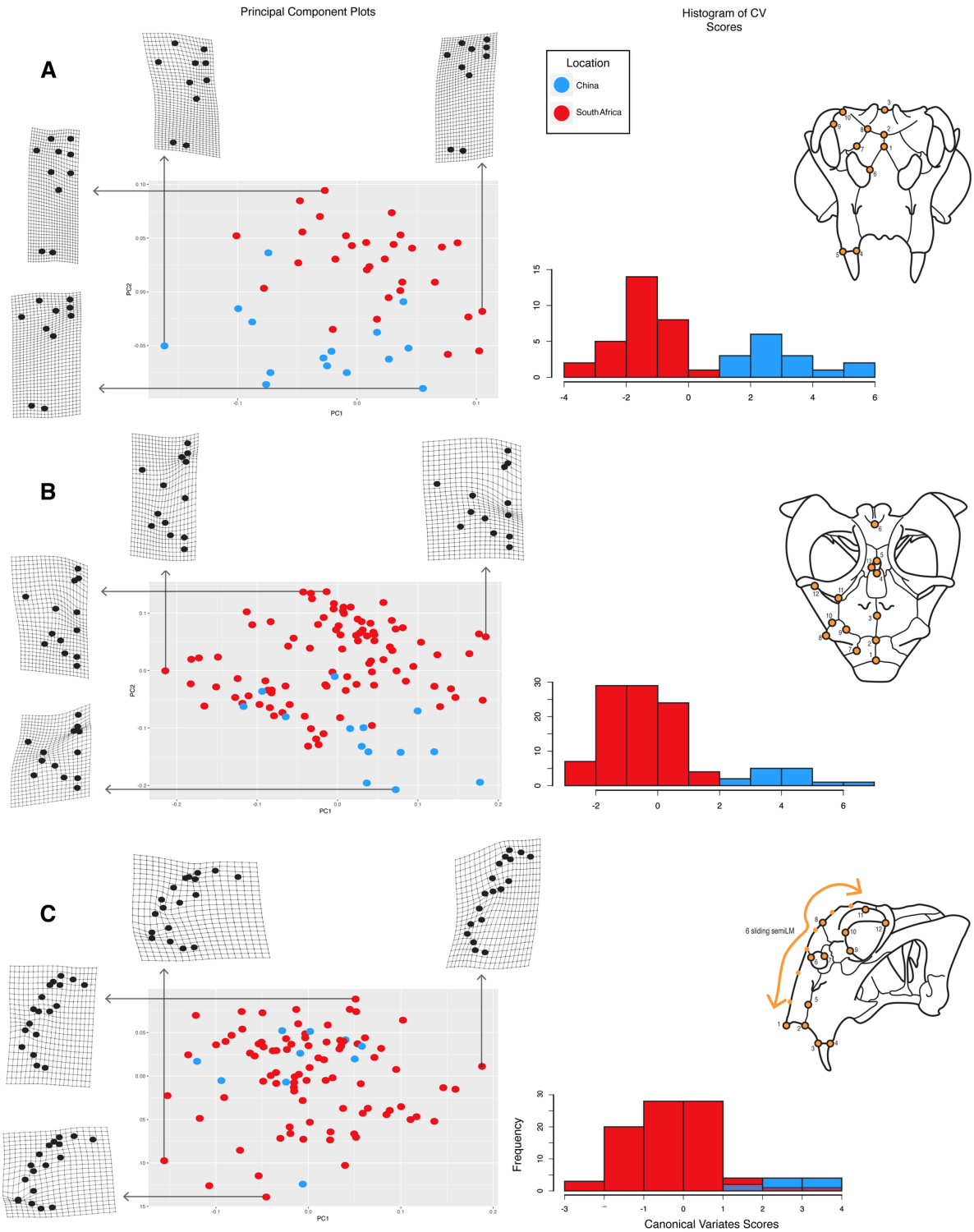
Principal Component Plots
Histogram of CV Scores
A
Location
China
South Africa
PC1
PC2
B
C
6 sliding semiLM
Frequency
Canonical Variates Scores

Figure 2.2. Results of the morphometric analysis comparing specimens of *Lystrosaurus* from China and South Africa. Principal components plots and histogram of canonical variates analysis results for the three perspectives (Anterior – A; Dorsal – B; Lateral – C). Skull drawings on the right correspond to the orientation for each analysis. Orange dots on the specimens show placement of landmarks used in the 2D geometric morphometric analysis (see S1 Supporting Information for more details). Blue dots represent specimens from China and red dots represent specimens from South Africa. Arrows point to the warp grids showing corresponding deformation along each principal component axis. Histograms show frequency of a recovered canonical variate value and show the distinct differences between Chinese and South African specimens, with overlap only occurring in a few specimens in the lateral orientation.

2.3.1 *Histological Sample*

Twenty skeletal elements (humerus, femur, tibia, radius, ulna, fibula, and ribs; Table 1; Fig 2.1) of *Lystrosaurus* sp. Were selected for consumptive analysis from the collections of the Institute of Vertebrate Paleontology and Paleoanthropology (IVPP). The majority of the fossils were recovered from strata approximately 30–50 meters above the base of the Jiucaiyuan Formation in the South Taodonggou area, Turpan-Hami Basin, Xinjiang Uygur Autonomous Region, China. One element (IVPP V 27127) came from a nearby locality in Zhaobishan and was recovered about 312m above the base of the Jiucaiyuan Formation [74]. The Jiucaiyuan Formation overlies the Guodikeng Formation lithologically (=upper Wutonggou low-order cycle) and the Wutonggou low-order cycle, and its lower contact is characterized by a facies change from lacustrine to fluvial deposits [75, 74]. This facies change is interpreted as the boundary between the Permian and Triassic [74] and recent work suggests that the Jiucaiyuan Formation is late Induan-early Olenekian in age [74]. As noted above, the lack of clarity regarding Chinese *Lystrosaurus* taxonomy means that we were unable to assign species-level identifications. However, the majority of our histologic samples come from four individuals. Skeletal elements are differentiated by specimen numbers followed by a letter, in the case of associated individuals (e.g., IVPP V #-a, -b, etc.) The remaining eight specimens are disarticulated elements collected from the same locality and are assigned to one specimen number IVPP V 27124, differentiated by IVPP V 27124-1, -2, etc. In addition to the histologic sample, 50 femora were measured from Early Triassic specimens compiled from the literature [37, 22] and from personal observations to contextualize the range of sizes in this monodominant vertebrate assemblage (S2 Dataset). Additional body size proxies, including basal skull length (S2 Dataset), were measured from *Lystrosaurus* specimens housed in collections at the National

Museum (NMQR), the Evolutionary Studies Institute (ESI), the Iziko South African Museum (SAM), the Field Museum of Natural History (FMNH), the American Museum of Natural history (AMNH), and the Burke Museum of Natural History and Culture (UWBM). Cranial and postcranial measurements were made using Neiko digital calipers.

2.3.2 *Thin Section Preparation*

Thin sections were made following standard osteohistological techniques [76]. Eight of the specimens were sectioned at the University of Washington (UW); the remaining twelve were sectioned at the Institute of Vertebrate Paleontology and Paleoanthropology (IVPP). At the UW, mid-diaphyses were embedded in Epothin Epoxy/Resin 2, sectioned to a thickness of approximately 2 mm on a high-precision diamond-edged saw (Isomet 1000) and glued to glass slides using Devcon 2-Ton epoxy. Slides were ground on a Metaserv 3000 lapidary plate until the specimen was 80 µm thick or until optical clarity was reached. At the IVPP, midshafts were cut and embedded in polyester resin, sectioned into blocks using an Exact 300CP band saw, and glued to glass slides using Technovit 4000 resin. Slides were ground to optical clarity using an automated lapidary plate (Exakt 400CS). High magnification and composite images were taken using a Nikon Eclipse LV100POL microscope under plain and cross-polarized light with a lambda filter. Composite images were processed using Nikon NIS-Elements AR (version 5.20.02) imaging software. High-resolution images are available at Morphobank under project number P4023.

Ontogenetic maturity was assessed through bone tissue microstructure, articular surface texture and morphology, and size compared to other specimens of *Lystrosaurus* from the Jiucaiyuan Formation. The largest femur, estimated at 255 mm, is of comparable length to the

largest known femur (*L. declivis* SAM-PK-K8038) from the Triassic of South Africa, which is 202 mm long. Therefore, we follow the size classes established by Botha [22] for southern Pangean *Lystrosaurus*, but note that our sample lacks Size Class I, or elements less than 40% maximum known size. The remainder of the elements were split into three size categories for analysis (Table 1; Fig 2.1). Size Class II includes the smallest and presumably most immature specimens in the current sample, with femoral lengths that are approximately 120–160 mm long (47–63% of the maximum femur length observed), tibiae and fibulae that are less than 100 mm long, and associated forelimb elements. All but the proximal tibia fragment (IVPP V 27124-3) have poorly formed joint surfaces and show pitting indicative of epiphyseal cartilage attachment in immature individuals [77]. By comparison, the joint surfaces of elements in the larger size classes are more robustly built and more completely ossified. The relative degree of epiphyseal ossification combined with histological features caused us to deviate slightly from Botha's [22] size classes by grouping specimens that are 40-65% maximum known size as Size Class II, rather than her 60% MKS cutoff. Our reasoning for this slight change is that the bone tissue is consistently and characteristically immature (i.e., highly vascularized plexiform to radial tissue without LAGs) in all of the associated elements that are 63% MKS. However, the incomplete tibia (IVPP V 27124-3, estimated length of 94 mm) that is estimated to be within Size Class II has a more developed and ossified joint surface compared to similarly sized tibiae (IVPP V 27124-4, 94 mm in length) so it is likely that with more sampling, the split between Size Class II and III will be refined. Size Class III includes immature specimens that are approximately 70% maximum known size (again, based on femoral lengths from larger, complete, Jiucaiyuan specimens). Finally, Size Class IV includes a single femur with an estimated length of 255 mm (the specimen measures 240 mm and is missing the proximal shaft and head of the femur). To

our knowledge, it is the largest femur of *Lystrosaurus* yet recovered from the Jiucaiyuan Formation, and is ~ 5 cm longer than the largest femur (discussed above) recovered from the Early Triassic of South Africa. Therefore, it presumably represents the most skeletally mature individual in the current sample. However, histological analysis will provide critical context for the relative maturity of this, and all other specimens sampled [78].

2.3.3 *Bone Tissue Terminology*

Bone tissue textures seen in *Lystrosaurus* and other therapsids vary widely from highly vascularized and disorganized woven-fibered bone to organized vascular canals in circumferential layers of parallel-fibered to lamellar bone [79-83, 30, 19]. The overall rate of bone growth affects the degree of organization of the extracellular matrix, with mineral fibers in a lamellar organization under slower growth, and disorganized woven-fibered textures under fast growth. Parallel-fibered bone is an intermediate tissue-type but it frequently occurs in the context of woven-fibered and lamellar bone. When large portions of the cortex consist of parallel-fibered bone, the mineralized extracellular matrix has an alternating anisotropic pattern that looks streaky under cross-polarized light. In many cases, the portion of woven- or parallel-fibered bone that sits between vascular canal spaces is so small that birefringent properties are difficult to discern. When this is the case, it is possible to use the morphology and density of osteocyte lacunae (spaces where bone cells sit in living bone) to approximate the relative organization of mineralized fibers [84, 85]. Woven-fibered bone is statically-derived and includes large, globular, and often densely packed osteocyte lacunae within the mineralized matrix [86, 84]. In contrast, lamellar and parallel-fibered bone are dynamically-derived, and have lenticular or spindle-shaped osteocyte lacunae that are evenly distributed and parallel to the layers of the mineralized matrix [86, 84, 87]. Importantly, in long bone cortices, the fiber network of parallel-

fibered bone can either be aligned to the bone's long-axis (i.e., longitudinal fibers) or perpendicular to it (i.e., circular fibers) which can cause differences in lacunar morphology and fiber birefringence in polarized light depending on the plane of section [44]. When parallel fibers are perpendicular to the sectioned plane, they show mass isotropy or monorefringence, similar to woven-fibered bone [85]. Non-lamellar tissues (parallel- and woven-fibered bone) frequently incorporate large vascular spaces that later become infilled with concentric lamellae of parallel-fibered to lamellar bone as primary osteons. The resulting tissue is a fibrolamellar bone complex (sensu Francillon-Vieillot [45]) wherein a disorganized, nonlamellar matrix incorporates a network of centripetally infilled primary osteons. Ricqlès [88] coined much of the terminology used by paleohistologists and used a restricted definition of the fibrolamellar complex to apply only to bone tissue that strictly had woven-fibered matrix, rather than the combination of woven- and parallel-fibered bone used in other applications of the term. More recently, Stein and Prondvai [85] reinterpreted cortical bone structures using polarized-light microscopy of sauropod thin sections cut from multiple planes. They concluded that the non-osteonal portion of cortical bone was largely parallel-fibered rather than woven and proposed new terminology for what they interpreted as highly organized primary bone (HOPB). They also proposed an additional term, the woven-parallel complex, to combine the organized portions of HOPB with the more traditional terminology used in bone development and growth (for more, see [89]). The term woven-parallel complex describes a broad range of bone tissues with nonlamellar matrices and the term fibrolamellar complex is maintained as a subset of the woven-parallel complex where the cortical bone is densely vascularized with abundant woven-fibered bone forming the scaffold between vascular canals which is then surrounded by parallel-fibered or lamellar bone [89, 44]. This new terminology recognizes the developmental aspects of osteogenesis and the

accumulation of osteoblasts within mineralizing osteoid. However, it may unnecessarily limit the role of woven-fibered bone to a transient tissue type typical of juvenile bone. Woven-fibered bone is known to be present in the typical development, maintenance, and repair of bone tissue throughout ontogeny in vertebrate groups and its abundance in cortical bone may depend on physiological processes rather than development alone [87]. In our histological descriptions below, we follow the recommendation [44, 89] to include lacunar morphology to estimate the proportion of woven- and parallel-fibered bone within the fibrolamellar and woven-parallel complexes and acknowledge the histovariability of parallel- and woven-fibered bone that can occur simultaneously and often in different proportions within the same section forming a spectrum of tissue types that can be difficult to define.

2.4 RESULTS

2.4.1 *Geometric Morphometric Analysis of Skull Shape*

Anterior view: The first five principal components capture 81.41% of the total shape variance in anterior view (PC1 – 30.57%; PC2 – 22.03%; PC3 – 13.82%; PC4 – 8.71%; PC5 – 6.26%) (Fig 2.2A). Shape is a statistically significant predictor of geographic location for the anterior view dataset ($p = 0.001$), and the canonical variates analysis correctly assigned specimen location 100% of the time.

PC1 primarily describes relative proportions of the snout. The subnarial region of the snout and caniniform process are dorsoventrally shorter relative to the height of the nasals and the anterior orbital margin in specimens with low PC1 scores, and there is greater lateral projection of the prefrontals relative to the caniniform process (Fig 2.2A). In contrast, the subnarial region and the caniniform process are proportionally much deeper relative to the

anterior orbital margin and nasals in specimens with high PC1 scores, and the prefrontals and caniniform process are more closely aligned along a vertical axis. PC2 also captures aspects of skull widening and deepening, although in this case the differences are concentrated in the region of the nasals and prefrontals. Specifically, the prefrontal-nasal region is dorsoventrally shorter in specimens with low PC2 scores, and the dorsal and ventral extrema of the prefrontal are displaced laterally relative to the external naris and the lateral end of the nasofrontal suture. Specimens with high PC2 scores have dorsoventrally taller prefrontal-nasal regions, and the dorsal and ventral extrema of the prefrontal are more closely aligned with the external naris and the lateral edge of the nasofrontal suture. The Chinese and South African specimens are most clearly differentiated along PC2, with the Chinese specimens generally having lower PC2 scores.

Dorsal view: The first five principal components capture 79.75% of the shape variance in dorsal view (PC1 – 26.77%; PC2 – 23.57%; PC3 – 17.95%; PC4 – 6.18%; PC5 – 5.26%) (Fig 2.2B). Shape is a statistically significant predictor of geographic location for the dorsal view dataset ($p = 0.001$), and the canonical variates analysis correctly assigned specimen location 100% of the time.

Shape variation along PC1 is dominated by differences in the relative lengths of the interorbital region and the pineal foramen, and by the degree of lateral projection of the orbital rim. Specimens with low PC1 scores are characterized by an anteroposteriorly longer interorbital region and a shorter pineal foramen, and an orbital rim that does not project strongly laterally (Fig 2.2). The pineal foramen is relatively longer anteroposteriorly in specimens with high PC1 scores, and the anterior and posterior corners of the orbital rim (formed by the prefrontal and postorbital bar, respectively) project laterally away from the skull roof. PC2 also captures shape variation associated with relative proportions of the skull roof, as well as orbit shape. Specimens

with low PC2 scores have an anteroposteriorly shorter pineal foramen and longer frontals, and the orbit is anteroposteriorly shorter, with anterior and posterior corners that are relatively aligned. The pineal foramen and orbit are relatively longer in specimens with high PC2 scores, and the posterior corner of the orbit (formed by the postorbital bar) projects farther laterally than the anterior orbital margin (formed by the prefrontal). As with the anterior view dataset, the Chinese and South African specimens are most clearly differentiated along PC2, with the Chinese specimens generally having lower PC2 scores.

Lateral view: The first five principal components capture 77.23% of the shape variance in lateral view (PC1 – 32.64%; PC2 – 18.57%; PC3 – 11.66%; PC4 – 8.58%; PC5 – 5.76%) (Fig 2.2C). Shape is a statistically significant predictor of geographic location ($p = 0.001$), and the canonical variates analysis had an overall classification accuracy of 95.78%, misclassifying two Chinese specimens in the dataset.

PC1 describes differences in the profile of the snout, position of the caniniform process relative to the orbit, and the anteroposterior dimensions of the orbit (Fig 2.2C). Specimens with low PC1 scores have a lower, more anteriorly-convex snout profile with prefrontals that do not project much above the level of the skull roof, and the ventral edge of the caniniform process is located below the anterior orbital margin. The anteroposterior length of the orbit is relatively long. In contrast, specimens with high PC1 scores, have much taller, flatter snout profiles and more dorsally-projecting prefrontals, as well as anteroposteriorly shorter orbits and caniniform processes that are located anterior to the anterior orbital margin. PC2 also captures aspects of snout profile, including the degree of anterior projection of anteroventral corner of the premaxilla and the length of the caniniform process, as well as the dorsoventral height of the orbit. The tip of the premaxilla projects more anteriorly in specimens with low PC2 scores, the caniniform

processes are relatively short, and the orbits are dorsoventrally shorter. Specimens with high PC2 scores have taller orbits, flatter snout profiles, and longer caniniform processes. There is little differentiation of the Chinese and South African specimens on the first three PC axes.

Taken together, our morphometric analyses suggest that there are consistent differences in skull shape between *Lystrosaurus* specimens from China and from South Africa, particularly in anterior and dorsal view. Based on these results, we tentatively suggest that the Chinese and South African populations were distinct at the species level. However, because our analyses do not directly address potential synonymies among the named Chinese species, and the fact that not all of the specimens we sampled histologically are associated with cranial material, we conservatively refer all of our histological samples to *Lystrosaurus* sp.

2.4.2 *Osteohistology Overview*

Lystrosaurus limb elements, regardless of size, have characteristically thick cortices. Cortical thickness (*K*) measures the proportional diameter of the medullary region relative to the total cross-sectional diameter and remained nearly consistent at 0.63 and 0.64 in the smallest and largest femora in our dataset, respectively (see S1 Supporting Information). Medullary cavities are typically infilled with trabecular bone that gradually transitions to a compact cortex. Similar to the bone histology of other dicynodonts and therapsids more broadly, the dominant bone tissue in all sampled size classes of *Lystrosaurus* is well-vascularized cortical bone made up of varying proportions of woven- and parallel-fibered bone with laminar, plexiform, and longitudinally-oriented primary osteons, indicative of rapid osteogenesis [79, 80-83, 30, 19]. Longitudinal canals that frequently anastomose are arranged in circumferential layers in Size Class II whereas laminar vascular canal orientations are common in Size Class III. In Size Class

III and IV, very little of the cortex is remodeled and when secondary osteons are present, they are restricted to the deepest portion of the cortex.

In the small individuals of *Lystrosaurus* studied here, rapidly deposited tissue is interrupted by either LAGs or annuli. These growth marks are found in multiple regions of the cortex, including deep in the cortex and along the sub-periosteal margin. In some individuals, there is variability in the type of growth mark that is deposited among the skeletal elements sampled. For example, the first (i.e., osteologically deeper) growth mark of IVPP V 26548 varies from a LAG in the femur and tibia, to an annulus in the fibula. Interestingly, the largest and presumably most skeletally mature femur that was histologically sampled, shows uninterrupted cortical growth, suggesting that *Lystrosaurus* from the Jiucaiyuan Formation had a high intrinsic rate of growth that could periodically arrest.

Our results are consistent with a recent report of *Lystrosaurus* bone histology from the same formation with respect to the preponderance of highly vascularized, rapidly deposited cortical bone [40]. However, contrary to Han et al. [40], we do not find evidence of peripherally slowed growth rates in individuals that are as large (~60% MKS) and larger than the maximum size sampled in their study. Additionally, we propose an alternative interpretation to the assignment of LAGs in the laminar to plexiform tissue reported in ([40]:fig 2G-H, fig 3C, fig 5, fig 6D, G-H) as bright lines that appear in the context of periosteal bone formation ([90]:fig3C; [91]:fig3). Finally, we report fewer instances of growth marks, particularly in the smallest size class where no evidence of episodic growth marks is seen (contra [40]). When present, we can confidently trace 1 to 3 growth marks (as either LAGs or annuli) around the circumference of individuals that are approximately 70% maximum known size.

2.4.3 *Size Class II*

The smallest association of elements includes cranial and postcranial material (hind limb and forelimb elements) that was collected in situ. A femur, tibia, fibula, ulna, and radius were selected for consumptive sampling (composite images available on Morphobank under project number P4023). The femur measures 122.38 mm in length. When compared to femora from larger, presumably more mature individuals, this femur (IVPP V 27126a) is approximately 50% maximum known size. The bone tissue in each of the five associated limb elements is extremely well-vascularized with longitudinally-oriented primary osteons arranged in circumferential layers with some radial anastomoses (Fig 2.3). Woven fibered bone matrix and large, densely distributed osteocyte lacunae surround the primary vascular canals (Fig 2.3B, E). Vascular canal size and density remain consistently high from the endosteal to the periosteal margin indicating that this individual grew rapidly until death (Fig 2.3D-E). There is no evidence of episodic growth cycles (as either LAGs or annuli) in this individual.

A right proximal fibula (IVPP V 27124-1), right proximal tibia (IVPP V 27124-3), distal tibia (IVPP V 27124-4), distal femur (IVPP V 27124-6) and complete femur (IVPP V 27124-7) were collected individually but are analyzed together here as immature individuals because limb dimensions and histological features are indicative of sustained, active bone growth at death. The complete femur is approximately 50% maximum known size, similar to IVPP V 27126a. In thin section, each of these disassociated elements has a large medullary cavity infilled with a loose trabecular network. Cortical tissue consists of woven-fibered bone with longitudinally oriented primary osteons loosely arranged in circumferential rows. In the proximal tibia, vascular canal size decreases substantially in a regionalized band deep to the sub-periosteal edge but it rebounds to the typical highly vascularized tissue more peripherally, likely representing a temporary shift

in growth rate (Fig 2.3F-G). In the fibula, there are regional differences in vascular canal size and organization that likely represent functional differences in bone apposition rates [92]. For example, longitudinal vascular canals are organized into stacked, circumferential layers on the medial side of the proximal fibula (IVPP V 27124-1) (Fig 2.3B-C) whereas the lateral side is less organized bone (Fig 2.3A). The amount of densely packed osteocyte lacunae in woven-fibered bone is higher in the less organized areas, but many large, globular lacunae are still apparent between primary osteons and in thin sheets in the more organized regions (Fig 2.3B-C). In more organized areas of the highly vascularized tissue, the mineralized matrix surrounding the vascular canals should not be confused with lines of arrested growth (Fig 2.3B-C). At low magnifications, delineated bands of extracellular matrix separate the primary vascular space in periosteally accreted bone [91]. However, at high magnifications, these accretion lines, or bright lines (sensu [91]), do not form continuous rings around the cortex and should not be confused as growth marks or as slower forming tissues like parallel-fibered or lamellar bone [45]. Bright lines lack osteocyte lacunae and represent the saltatory activity of the periosteum when new bone is accreted [45, 91]. In specimens in Size Class II, highly vascularized longitudinal canals in woven- to parallel-fibered matrix continue to the sub-periosteal edge, indicating that individuals died while actively growing.

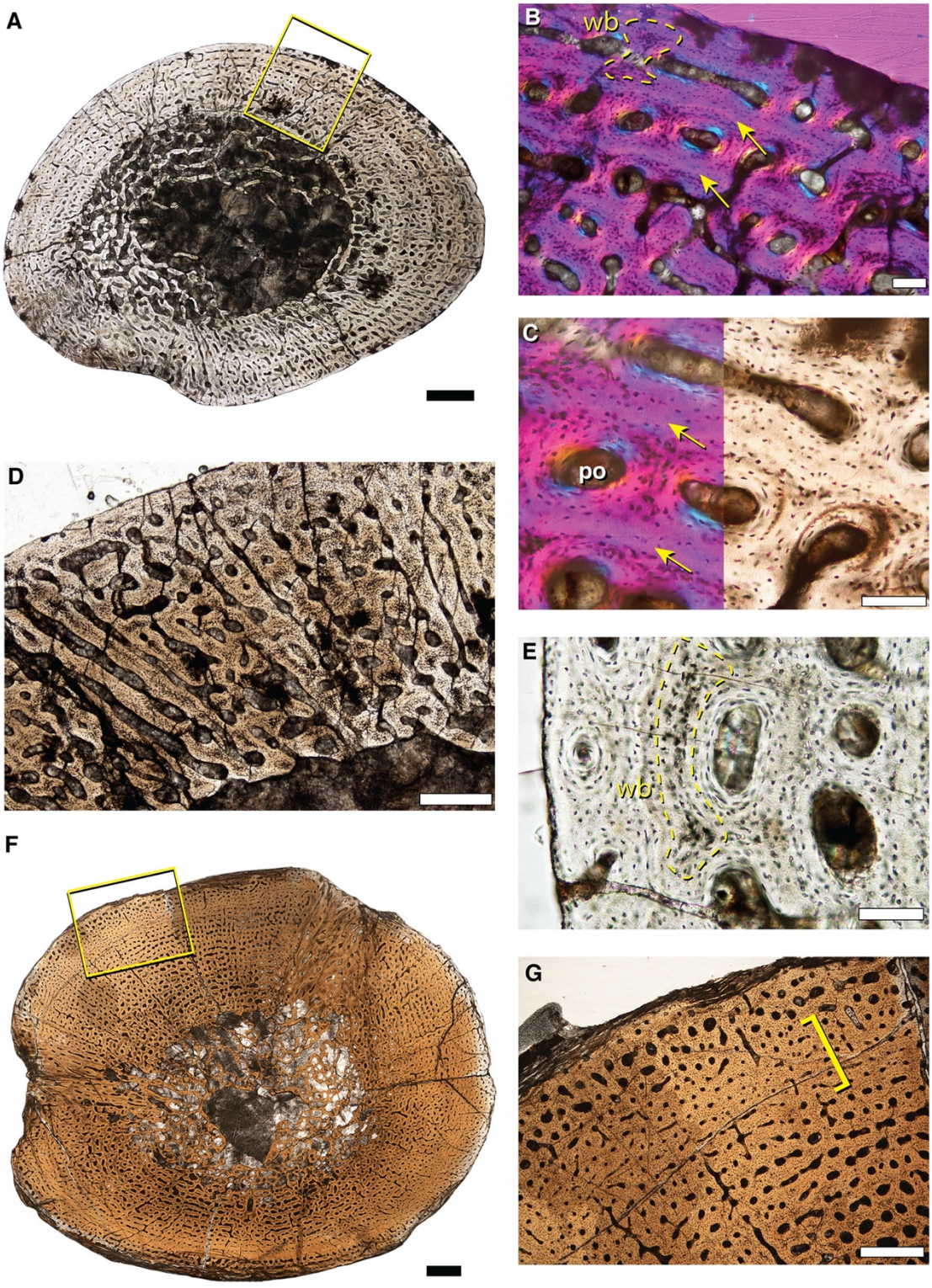
A
B
wb
C
po
D
E
wb
F
G

Figure 2.3. Representative bone histology of Size Class II from the mid-shafts of *Lystrosaurus* sp. hind limb elements. **A**, fibula (IVPP V 27124-1) consisting of well-vascularized tissue with longitudinally-oriented primary osteons in circumferential layers. **B**, 10X magnification of yellow square in **A**, arrows indicate bright lines in the extracellular matrix of periosteally accreted bone and should not be confused as growth marks. **C**, 20X magnification of **B**. **D**, fibula (IVPP V 27126c) cross section consisting of longitudinally and radially oriented primary osteons and dense osteocyte lacunae. **E**, 20X magnification of fibula (IVPP V 27126c) shows woven-fibered bone (yellow arrows) in the peripheral cortex indicating rapid bone deposition at death. **F**, cross section of a proximal tibia (IVPP V 27124-3) with a slight decrease in vascular canal sizes towards the sub-periosteal edge, magnified in **G**. wb= woven-fibered bone; po= primary osteon. Scale bars = 1 mm in **A** & **F**, 500 μm in **D** & **G**, 100 μm in **B**, **C** & **E**.

2.4.4 *Size Class III*

A femur (IVPP V 27125a), tibia (IVPP V 27125b), and fibula (IVPP V 27125c) are associated as one individual that is approximately 70% maximum size based on femoral length. Unlike smaller sampled elements, the cortex is interrupted by two growth marks (Fig 2.4). In all associated elements, a deep cortical LAG is sandwiched between large vascular canals towards the endosteal margin and smaller vascular canals more peripherally (Fig 2.4A-B, lowermost arrows in F, K). In the fibula, the LAG is superficial to a region of immature secondary osteons that sit in the deep cortex (Fig 2.4J). The second of the two growth marks is more variable, in part due to the fragmentary nature of the subperiosteal edge of the femur. In the femur, a poorly vascularized annulus of parallel-fibered to lamellar tissue sits along the sub-periosteal edge and is more apparent in thin areas of the cortex (Fig 2.4D). By contrast, thicker regions of the outer cortex show a mixture of longitudinal and circular primary osteons in circumferential layers that approaches a laminar organization that continues to the incomplete sub-periosteal edge (Fig 2.4C). In the tibia and fibula, the outer cortical growth mark is made up of two LAGs in the tibia, and an annulus of avascular parallel-fibered tissue in the fibula (Fig 2.4E, J-K). Interestingly, the mineral preservation of the tibia and fibula are such that the mineralized bone matrix is clearly visible between each circumferential layer of vascular canals (Fig 2.4F, K, L). These thin, mineralized lines of extracellular matrix should not be confused for growth marks and instead are the mineralizing front of periosteally accreted bone [45, 90]. The vascular orientation shifts in the hind limb elements of this individual from reticular to laminar in the femur (Fig 2.4B), and from disorganized longitudinally oriented primary osteons to circumferentially organized longitudinal primary osteons in the tibia and fibula (Fig 2.4F, I). In addition, primary osteon size decreases towards the outermost periosteal margin but vascular canals remain open to the sub-

periosteal edge (Fig 2.4F-G). The only exception to this pattern is in the thinnest region of the cortices, particularly in the fibula, where the sub-periosteal edge is avascular and consists of well organized, parallel-fibered bone (Fig 2.4D, I, K). However, this organized tissue is discontinuous around the cross section, suggesting that bone growth slowed at differential rates in regions of the outer cortex, but did not fully arrest.

A slightly larger specimen (IVPP V 26548) is an association of hind limb and forelimb elements as well as at least one rib that was previously histologically sampled by Han et al. 2021[40]. The femur (IVPP V 26548a), tibia (IVPP V 26548b), and fibula (IVPP V 26548c) show plexiform tissue interrupted by two growth marks, with some variation in the outer growth mark, especially in the fibula where it splits into two LAGs (Fig 2.5). In the femur and tibia, the deeper growth mark is distinguishable as a dramatic reduction in vascular canal size, immediately followed by a return to the typical, large vascular canals in the middle of the cortex (Fig 2.5A, B, D). Throughout the middle cortex of the femur, the deeper growth mark changes in thickness. In thinner regions of the cortex, the growth mark appears as a cross-cutting LAG separating smaller vascular canals from larger canals more superficially. In the thicker regions of the cortex, the growth mark appears as an annulus, or region of little to no vasculature that is not accompanied by a hyper-mineralized line (Fig 2.5D). In both the femur and tibia, vascular canals reduce in size again towards the sub-periosteal margin, making up the second growth mark of an annulus of avascular parallel-fibered to lamellar tissue (Fig 2.5C). The fibula shows a mid-cortical annulus that is made up of avascular parallel-fibered to lamellar tissue (Fig 2.5G). Similar to the femur and tibia, there is a sub-periosteal reduction in vascular canal size with at least two LAGs that can be traced around the entire cortex of the fibula, indicating variation in the type of growth mark deposited in hind limb elements of the same individual (Fig 2.5E, G, H).

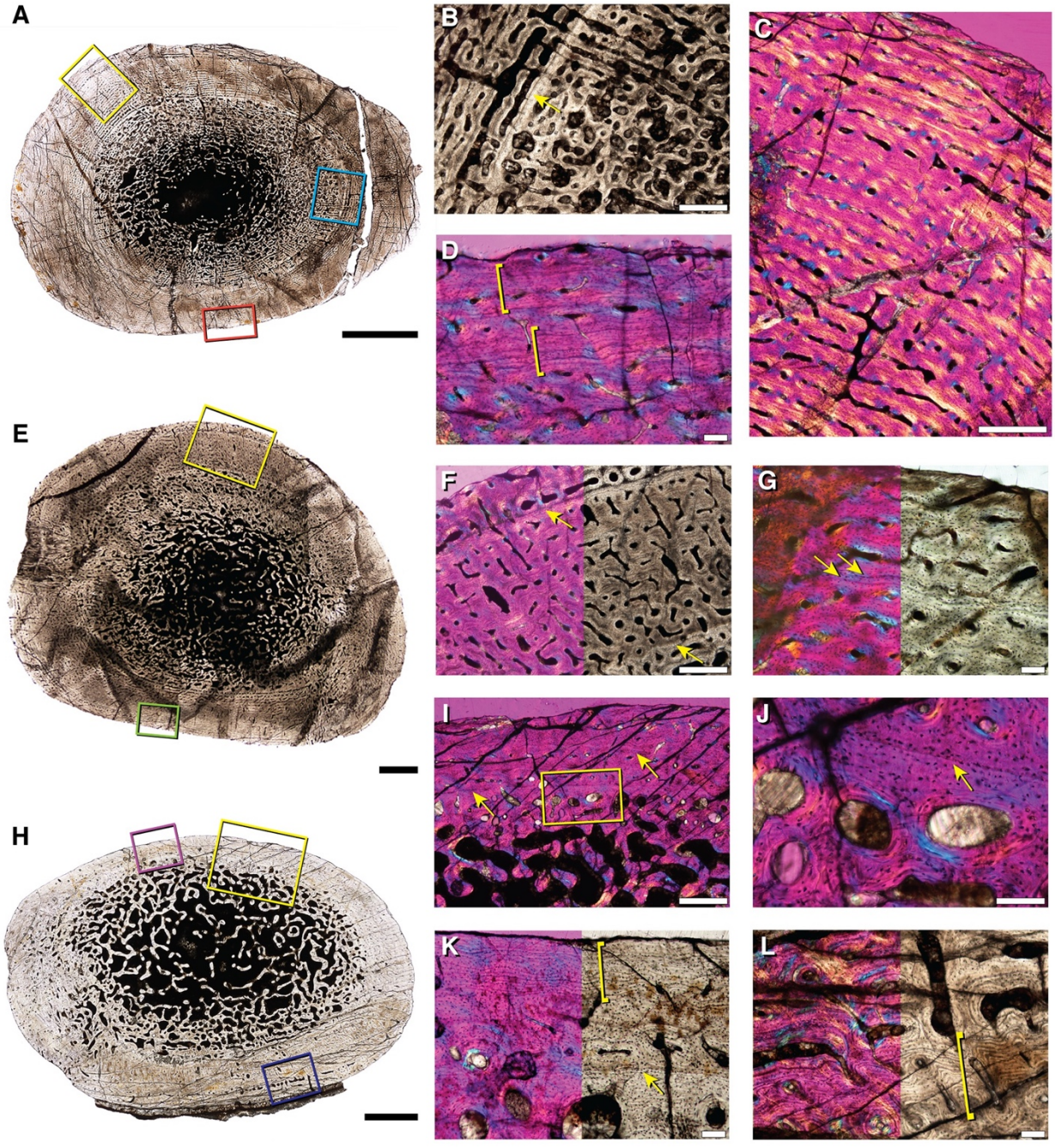
A
B
C
D
E
F
G
H
I
J
K
L

Figure 2.4. Bone histology of associated hind limb elements of *Lystrosaurus* sp. representative of Size Class III. **A**, femur (IVPP V 27125a) with a deep cortical LAG in **B** (blue box in **A**). The outer cortex has regions of high vascularity seen in **C** (yellow box in **A**), and regions marked by a nearly continuous peripheral growth mark of parallel-fibered tissue (denoted by yellow brackets) in **D** (orange box in **A**). **E**, tibia (IVPP V 27125b) has two cortical growth marks seen in **F** (yellow box in **E**; yellow arrows in **F**). The outer growth mark can variably be seen as a double LAG in **G** (green box in **E**; yellow arrows in **G**). **H**, the fibula (IVPP V 27125c) has a thinner cortex interrupted by two LAGs seen in **I** (yellow box in **H**; yellow arrows in **I**). **J**, magnification of yellow box in **I** shows the cross-cutting inner cortical LAG (arrow in **J**). **K**, thinner regions of the cortex appear avascular (purple box in **H**), with stacked mineralized lamellae of parallel-fibered bone (yellow bracket), whereas thicker regions (blue box in **H**) show peripheral pulses of vascularized growth, within the lamellated tissue, seen in **L** (yellow bracket). Scale bars = 5 mm in **A**, 1 mm in **E**, 2 mm in **H**, 500 μm in **B**, **C**, **F** & **I**, and 100 μm in **D**, **G**, **J** – **L**.

Small, simple vascular canals sit within the context of this peripheral lamellar tissue, which is atypical for an external fundamental system (EFS) indicative of somatic maturity, making it more likely that this lamellar tissue represents a temporary cessation in growth, similar to the annulus recorded in the deeper cortex.

A complete humerus (IVPP V 27124-8) of comparable size to IVPP V 26548 [40], has an exceedingly thick cortex with one mid-cortical growth mark (Fig 2.5J). The medullary cavity is nearly infilled by a dense network of trabecular bone. The cortex increases in thickness in the anterodorsal region (up in Fig 2.5J) and consists of highly vascularized laminar bone in woven- and parallel-fibered bone matrix. Vascular canals have a circular orientation and show a marked decrease in size coincident with a mid-cortical LAG (Fig 2.5K). The LAG is traceable around the entire cross-section and is followed by a pulse of highly vascularized tissue with large canal spaces (Fig 2.5K). Vascular canal size reduces slightly towards the sub-periosteal margin which could indicate the beginning of another growth mark, similar to the mid-cortical growth mark.

A distal fragment of an ulna (IVPP V 27124-2; original complete length estimated to be 93 mm) has a thin cortex with a large medullary cavity infilled with a loose network of trabecular bone (Fig 2.5M). The transition from trabeculae to compact cortical bone includes a region of enlarged resorption cavities and immature secondary osteons. The middle and outer cortex is composed of small longitudinal canals that sit in a parallel-fibered matrix where small regions of woven-fibered bone persist (Fig 2.5N, O). Along the sub-periosteal margin, vascular canals are reduced but occasionally open to the bone edge, suggesting that this individual died while still growing (Fig 2.5M). The proportion of parallel-fibered bone in this element is higher than in hind limb elements, however, there is no evidence to suggest somatic maturity or attainment of maximum size.

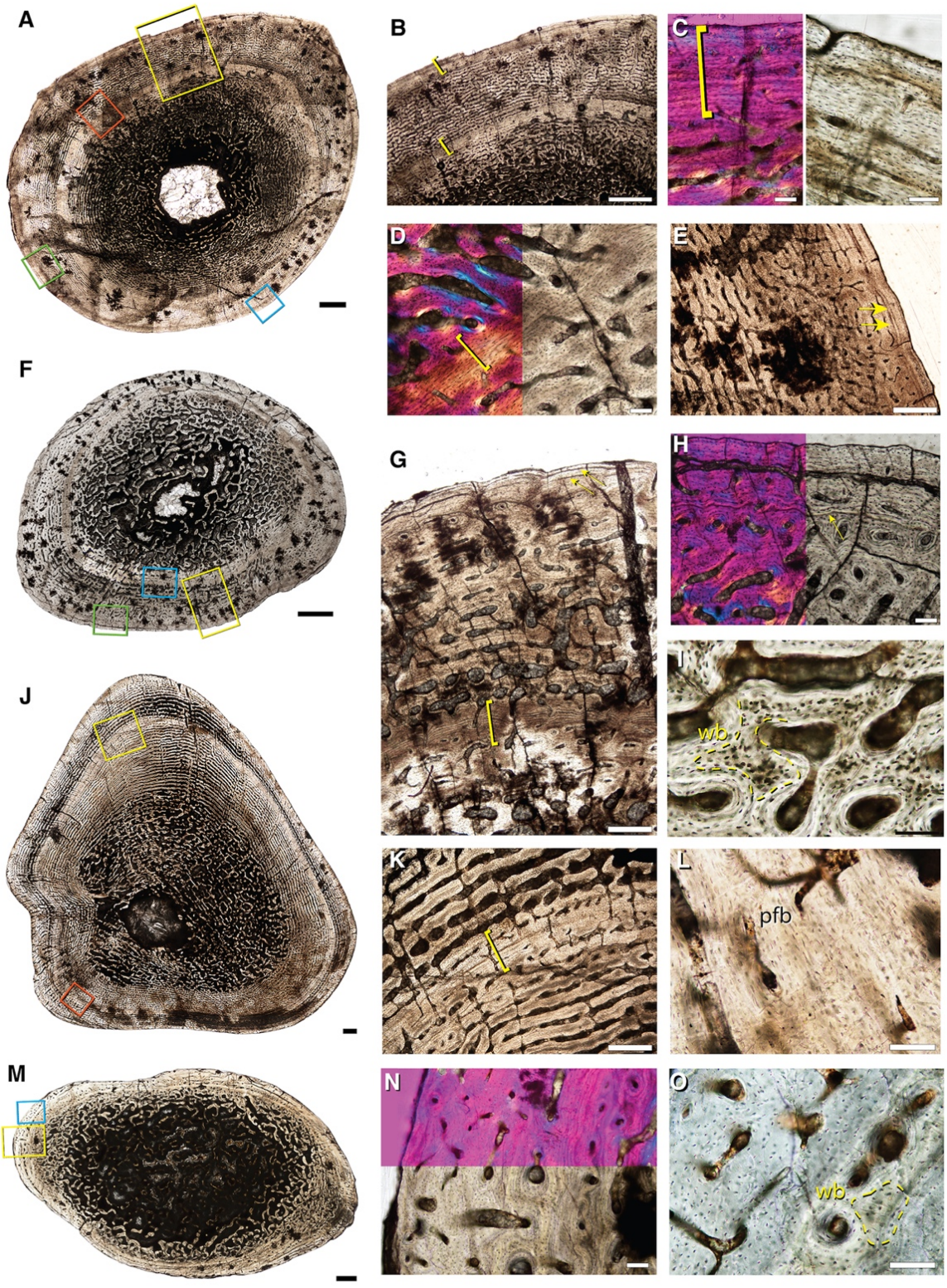
A
B
C
D
E
F
G
H
I
wb
J
K
L
pfb
M
N
O
wb

Figure 2.5. Bone histology of associated elements of *Lystrosaurus* sp. representative of Size Class III. **A**, femur (IVPP V 26548a) has two growth marks. **B**, a deep, mid-cortical annulus (yellow box in **A**; inner yellow bracket in **B**), avascular lamellar tissue makes up the second growth mark (outer yellow bracket in **B**). **C**, magnification of peripheral lamellar tissue, left panel reflects blue box in **A**, right panel reflects green box in **A**. **D**, first (osteologically deeper) annulus (yellow bracket) in plane and cross-polarized light with a lambda filter. **E**, magnification of blue box in **A** of outer cortical growth mark that varies in thickness around the periphery of the thin section, here consisting of two LAGs. **F**, associated fibula (IVPP V 26548c) highlights a similar arrangement of deep and more superficial growth marks consisting of, at times, numerous layers of lamellar tissue in an annulus. **G**, magnification of yellow box in **F** showing two growth marks; annulus (yellow bracket) and peripheral LAGs (yellow arrows). **H**, magnification of green box in **F** showing variation in the outer growth mark such that in some regions it appears as a thicker region of lamellar tissue with one cross-cutting LAG. **I**, high magnification image of the associated tibia (IVPP V 26548b) showing the presence of woven-fibered bone between primary osteons within the middle cortex. **J**, humerus with mid-cortical annulus of reduced vascularity. **K**, magnification of yellow box in **J** of annulus (yellow bracket). **L**, high magnification of parallel-fibered bone making up the annulus in the humerus (orange box in J). **M**, ulna (IVPP V 27124-2) with a thinner overall cortex made up of parallel-fibered and small amounts of woven-fibered bone. **N**, magnification of yellow box in **M** highlighting the thin cortex in plane and cross-polarized light with a lambda filter. **O**, high magnification of outer cortex of the ulna showing small areas of woven-fibered bone (blue box in **M**). wb= woven-fibered bone; pfb= parallel-fibered bone. Scale bars = 1 mm in **A**, **B**, **F**, **J**, & **M**, 500 μm in **E**, **G** & **K**, and 100 μm in **C**, **D**, **H**, **I**, **L**, **N**, & **O**.

2.4.5 *Size Class IV*

Unlike the middle size class, the largest sampled femur (IVPP V 27127) does not have LAGs or annuli (Fig 2.6A). However, much of the cortex is cracked or incompletely preserved, and a large crack runs along the middle cortex, along what might have been a LAG. Despite these cracks, the bone tissue architecture is easily discernible and consists of laminar canals in woven- and parallel-fibered matrix based on the lacunar morphologies at high magnification (Fig 2.6B, C). Woven-fibered bone makes up more of the extracellular matrix in the deep and middle cortex whereas the outer cortex consists of parallel-fibered bone with small areas of woven-fibered bone (Fig 2.6C). There is no indication of transition to slowed bone deposition in the small regions of sub-periosteal bone that remain intact, suggesting a sustained rate of growth at death (Fig 2.6B).

Unknown Size Class

Four partial ribs (IVPP V 27124-5) belonging to an individual of unknown size class are preserved in a block of sediment (Fig 2.6D). In thin section, they have large, infilled medullary cavities that grade into thin, compact cortices. Scarce vascular canals and immature secondary osteons sit in the deeper cortex whereas the outer cortex is avascular and consists of parallel-fibered tissue with well-organized osteocyte lacunae (Fig 2.6E-F). Due to the fragmentary nature of this specimen and the fact that it is not associated with limb bones, it is unclear whether the peripheral parallel-fibered tissue is indicative of an EFS or a temporary cessation in growth. Additionally, ribs grow at different rates than limbs and do not preserve the same record of life history information compared to a midshaft hind limb thin section. Another interesting feature that these ribs reveal is that the cortex differs in thickness between each rib, casting doubt on Ray et al.'s [54] hypothesis that *Lystrosaurus* had exceptionally thick ribs, which they suggested

was indicative of an aquatic lifestyle. From this sample, it is clear that *Lystrosaurus* rib cortical thickness depends on where the thin section was taken.

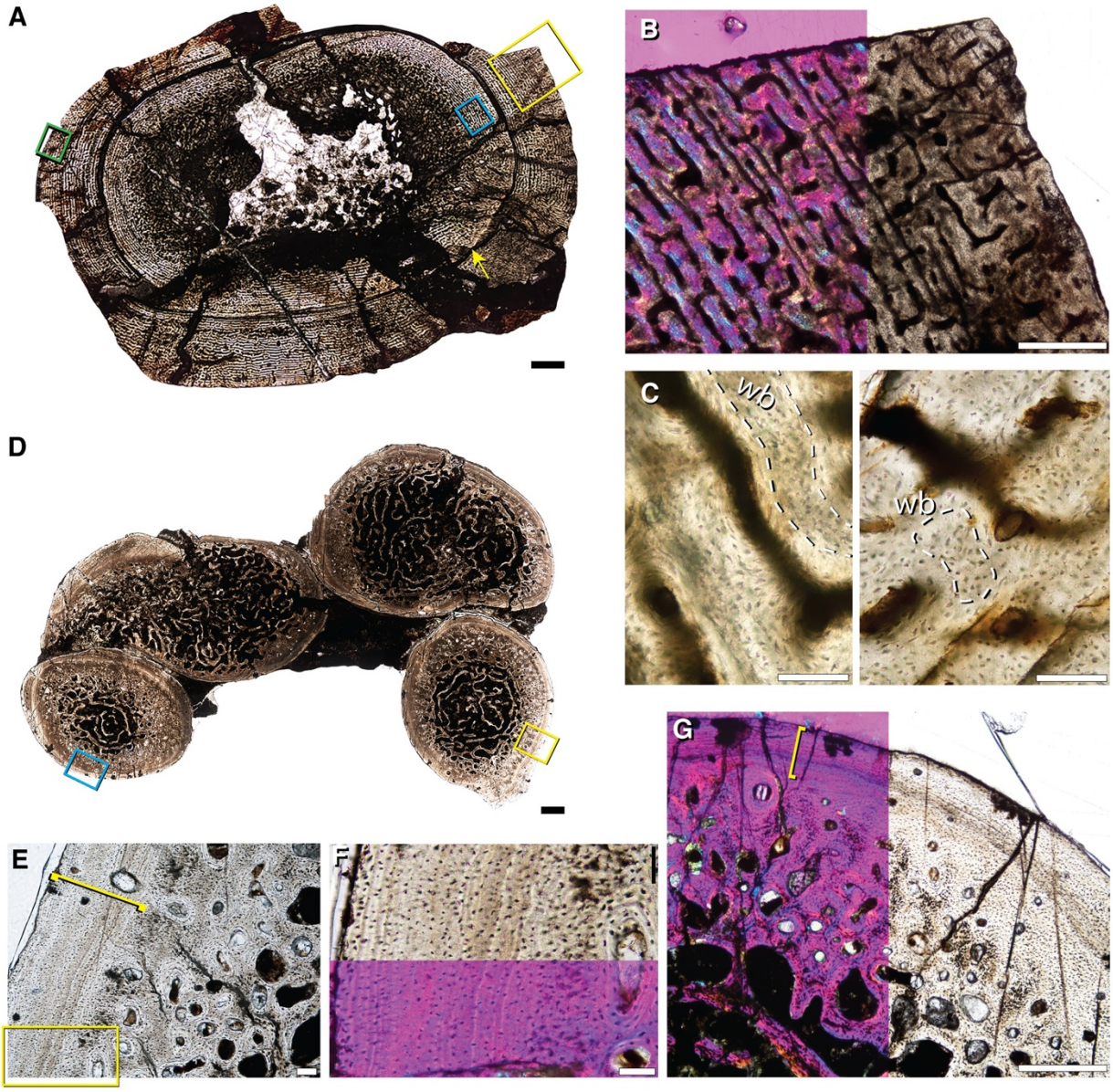

Figure 2.6. Bone histology of the largest femur (IVPP V 27127) of *Lystrosaurus* sp. that represents Size Class IV and rib fragments of unknown size. **A**, the femur is cracked (yellow arrow is a large circular crack) but preserves regions of the entire cortex (yellow box). **B**, the same view of the yellow box in **A** using cross-polarized light with a lambda filter shows well-vascularized, plexiform tissue along the sub-periosteal margin (yellow box in **A**). **C**, left panel shows woven-fibered bone in the deep-middle cortex (blue box in **A**) and outer cortex, right panel (green box in **A**). **D**, rib fragments (IVPP V 27124-5) have infilled medullary cavities, secondary osteons within the deep cortex and a largely avascular compact outer cortex consisting of organized lamellar tissue. **E**, magnification of yellow box in **D** showing the peripheral parallel-fibered tissue in the yellow bracket. **F**, magnification of the yellow box in **E** under plane and cross-polarized light with a lambda filter. **G**, magnification of blue box in **D** similarly shows that peripheral parallel-fibered tissue is present (yellow bracket). wb= woven-fibered bone. Scale bars = 10 mm in **A**, 1 mm in **D**, 500 μm in **B** & **G**, 100 μm in **C**, **E** & **F**.

2.5 DISCUSSION

All *Lystrosaurus* individuals sampled from the Jiucaiyuan Formation show abundant, highly vascularized primary bone tissue throughout the majority of the cortices of the hind limb, humerus, and radius. The ulna and ribs showed fewer vascular canals, overall thinner cortices (contra [54]), and more organized primary bone tissue. Three size classes were identified and histologically described as: II) a highly vascularized cortex of circumferential layers of radial and longitudinal vascular canals in ~50% max known size individuals: III) highly vascularized plexiform tissue interrupted by one to two growth marks that range from one or two closely spaced LAGs or annuli in ~70% maximum known size individuals; and IV) uninterrupted laminar tissue in a 100% maximum known size individual, although the possibility that a crack formed along a LAG cannot be eliminated. These results force us to reconsider what an adult-sized specimen might look like for *Lystrosaurus* sp., as the current sample lacks histologic indicators of somatic maturity (e.g., an external fundamental system) [78]. Botha [22] found similar results for South African species of *Lystrosaurus*, suggesting that species typified by small body size (viz. *L. murrayi*) were very likely capable of reaching much larger sizes, but never lived long enough to do so.

Han et al. [40] suggested that sub-adult *Lystrosaurus* from northern Pangea may have reached some level of somatic maturity inferred from parallel-fibered bone and peripheral LAGs in a dorsal rib. However, histological data from the femur, tibia, and fibula of the same individual indicate episodic cessations in growth instead of an overall pattern of slowed growth. The presence of slower growing bone tissue in the ribs likely reflects differential growth rates seen throughout the skeleton, rather than somatic maturity [93, 49].

2.5.1 *Growth Marks*

Unlike the bone histology reported from South African and Indian *Lystrosaurus*, in which growth marks are rare and often limited to a single LAG or annulus, we find one, and more commonly, two growth marks in immature *Lystrosaurus* from the Jiucaiyuan Formation. The number of growth marks is mostly consistent across associated elements from the same individual as well as across individuals of the same size class (Table 1). Interestingly, the type of growth mark, as either a LAG, a series of closely spaced and occasionally bifurcating LAGs, an annulus consisting of lamellar tissue, or an annulus consisting of parallel-fibered to lamellar tissue, varied throughout the current sample. In most cases, the first (i.e., osteologically deeper) growth mark, or singular growth mark in the case of the humerus, was often recorded as an annulus accompanied by a reduction of vascular canal sizes. The outer cortical growth marks were more variable, and often varied within the same thin section.

We did not find evidence of growth marks in individuals in Size Class II. These individuals had characteristic juvenile bone histology (i.e., large radial to longitudinal vascular canals that frequently anastomose); therefore our analysis disagrees with the assignment of LAGs in juvenile *Lystrosaurus* by Han et al. [40]:fig 3. In some cases, the mineralization front can be mis-identified as a growth mark in the context of periosteally deposited bone. Currey [91] and others (e.g., [90]), describe laminar bone formation where accreted circumferential layers of bone (made up of a woven scaffold that is later infilled with parallel-fibered or lamellar bone in the form of primary osteons) is bordered by the periosteum. As the periosteum jumps peripherally when new bone is accreted, a bright line is left between each circumferential layer and represents the place at which the periosteum was located before new bone was added. This mineralized line differs from a growth mark as it is not continuous around the cortex and is not

hyper-mineralized but appears as a bright line often devoid of osteocyte lacunae [90]. Growth marks, on the other hand, are continuous around the cortex, unless secondary remodeling or cortical remodeling causes discontinuities (i.e., by erosion).

All growth marks observed in our analysis come from Size Class III, which corresponds to individuals that are approximately 70% maximum known size. We can confidently trace up to two growth marks in the current Chinese sample, which is higher than reports from South African and Indian specimens of *Lystrosaurus*, which generally lack growth marks. However, the remainder of the cortical bone tissue in the current Chinese sample reflects the similarly high and consistent rate of bone growth reported from South African and Indian *Lystrosaurus* [22] [54]. A slight increase in the number of growth marks in northern Pangean *Lystrosaurus* could be explained by one or two possible factors that are not mutually exclusive: (i) by an increase in their lifespan or (ii) by environmental stressors.

There is a longstanding hypothesis that the Permo-Triassic extinction caused a Lilliput effect, a persistent reduction in body size, in surviving terrestrial lineages [94-97, 19]. This claim has been investigated histologically in therocephalians, which support an overall reduction in body size following the extinction [97, 19]. A Lilliput effect was also posited for *Lystrosaurus*, based in large part on the overwhelming abundance of small skulls in the Karoo Basin and museum collections in South Africa [98, 99, 20, 21]. However, Botha [22] later rejected a strict Lilliput effect for southern Pangean *Lystrosaurus* (based on fossils from South Africa and India) because of the lack of mature histological tissue in all of the species examined [22]. Instead, she [22] suggested that the large proportion of small skulls in the Triassic was better explained by high mortality in immature individuals, as assessed by their long bone histology.

2.5.2 *Body size*

To better understand how *Lystrosaurus* from the Jiucaiyuan Formation compare to congeners from more southerly parts of Pangea, we gathered body size data (based on basal skull length and femur length) from the literature [54, 22, 40] and personal observations of Early Triassic-aged specimens collected in China, South Africa, and India. From this sample, it is clear that Chinese *Lystrosaurus* have a larger average body size (Fig 2.7, Fig 2.8). However, cranial size distributions suggest that both populations from South Africa and China had the potential to grow to similar maximum recorded sizes (Fig 2.7). The lack of large specimens of *Lystrosaurus* in South Africa aligns with previous interpretations for increased mortality at small sizes there by Botha [22]; also see [20]. Our data provide evidence suggesting that northern Pangean *Lystrosaurus* could have reached larger sizes more readily or easily. However, it is unclear the degree to which differences in sampling practices might affect the body size distributions seen here. A decade of detailed stratigraphic work targeting the Permo-Triassic boundary in South Africa has led to more comprehensive fossil sampling, which should provide a relatively unbiased view of the vertebrate fauna [100, 101]. However, historical collections from the Karoo likely systematically emphasized rare components of the assemblage (e.g., [102]). Likewise, the Permo-Triassic vertebrate record from Xinjiang has not been subject to the same intensive collecting as that of the Karoo Basin, and therefore it currently may not provide an unbiased view of body size distributions or relative abundances of taxa.

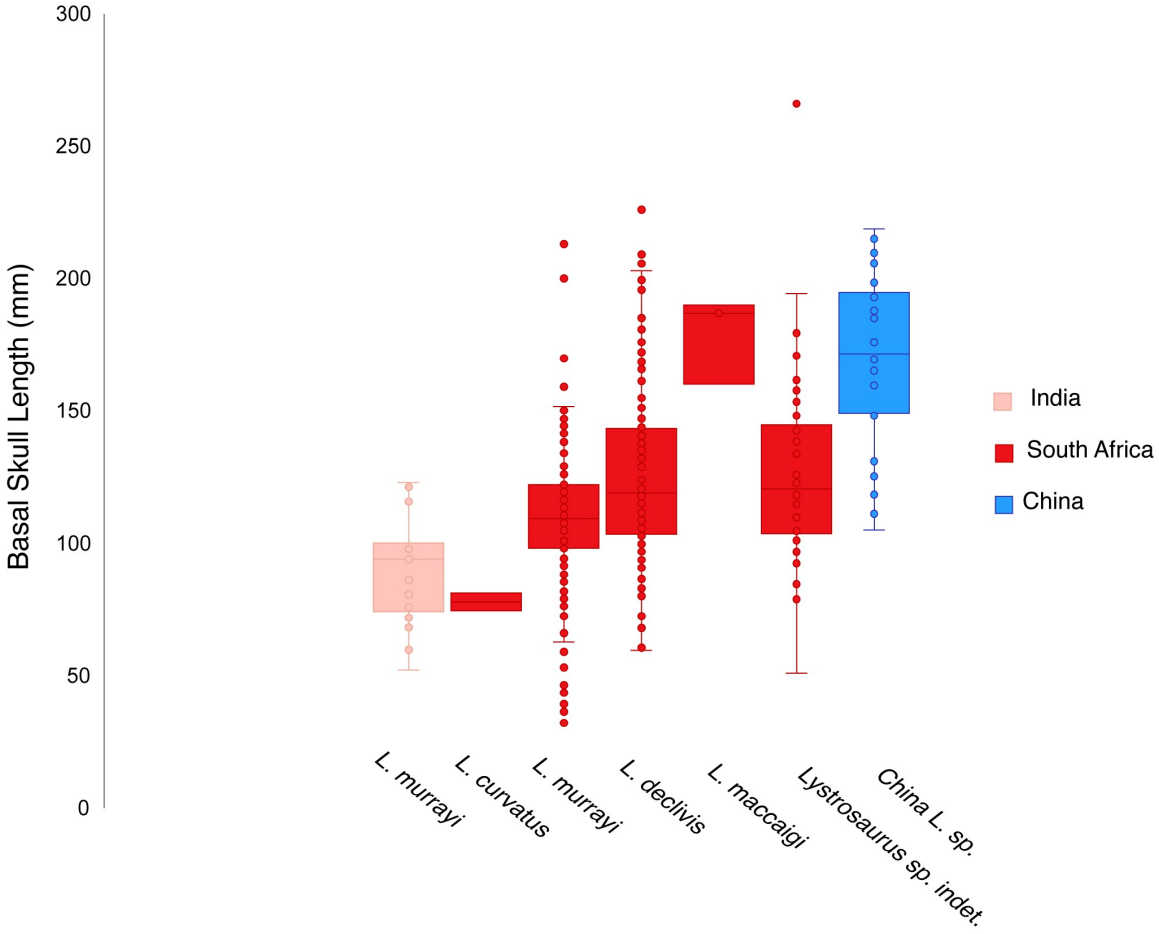

Figure 2.7. Interspecific body size distributions from Early Triassic *Lystrosaurus* show an abundance of large individuals from China. Species from South Africa and China overlap in maximum basal skull length but individuals from China have larger average size. See S2 Dataset for more information.

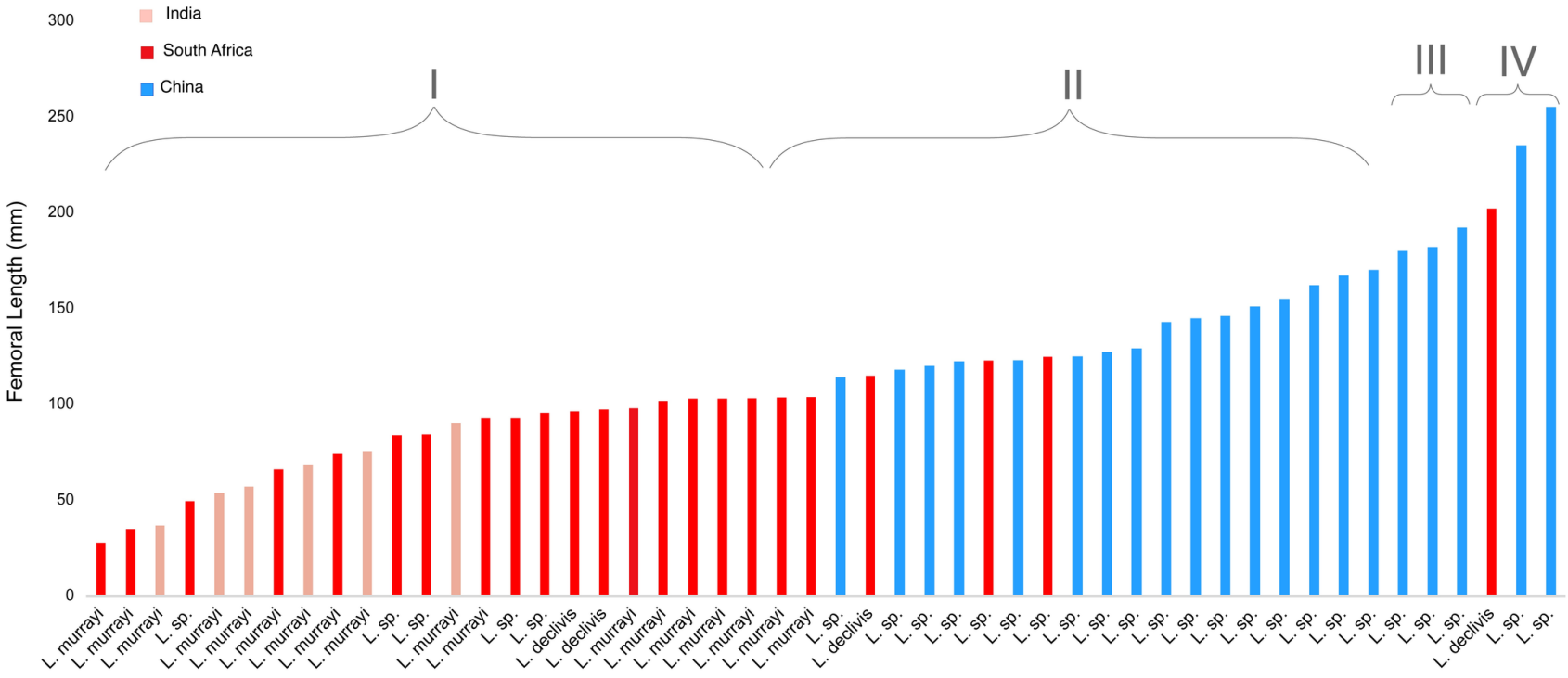
India
South Africa
China
I
II
III
IV
Femoral Length (mm)
300
250
200
150
100
50
0
L. murrayi
L. sp.
L. declivis

Figure 2.8. Interspecific femoral lengths from Early Triassic *Lystrosaurus* show a higher frequency of large sizes from China. Size Classes denote femora that are less than 40% maximum known size (MKS) in I, between 40-65% MKS in II, approximately 70-75% MKS in III, and greater than 79% in IV. See S2 Dataset for more information.

The presence of large individuals with episodic growth marks in all of the subadult-sized elements suggests that *Lystrosaurus* from the Jiucaiyuan Formation were able to reach large sizes through prolonged and sustained rapid growth, unlike Triassic *Lystrosaurus* from South Africa that rarely lived long enough to reach large body sizes despite growing rapidly (Fig 2.7). There are several possible explanations for this pattern. First, physiological differences among the species of *Lystrosaurus* could be responsible. This proposal is difficult to test, as the alpha-taxonomy of Chinese *Lystrosaurus* is in need of revision and phylogenetic studies of the genus have typically only included *L. hedini* as a sole northern hemisphere representative (e.g., [103]). However, to the degree that patterns preserved in hard tissue histology can shed light on physiology, the current data suggests that *L. curvatus*, *L. declivis*, *L. maccaigi*, and *L. murrayi* are effectively indistinguishable [22, 31], which suggests a degree of consistency within the genus.

Climatic differences in the high-southern (60°S) versus mid-northern (45°N) paleolatitudes [104, 105] is another possible explanation for the observed difference in body size and inferred lifespan in *Lystrosaurus*. Paleoclimate reconstructions of the latest Permian to earliest Triassic show extreme increases in temperature and aridity [106-109], mega monsoons [110, 111], chemical weathering, soil erosion, and geochemical and isotopic signatures of mass wasting and greenhouse conditions [112, 8,6/13/23 6:53:00 PM113]. Facies that span the terrestrial Permo-Triassic boundary of the Karoo Basin are interpreted as a change from meandering rivers to low-sinuosity braid-plains, resulting from increased aridity and a die-off of rooted plants that supported river morphologies [114, 115]. However, more recent evidence from isotopic and geochemical data produced differing estimates of the degree to which aridity increased in the Karoo Basin, complicating our understanding of seasonal variation in

precipitation and resource availability [111, 116, 117]. Nevertheless, conditions were disruptive enough to have destabilized terrestrial communities and caused a prolonged interval of faunal turnover in southern Pangea during the extinction interval [118, 15, 18].

The extreme environmental and climatic conditions of southern Pangea are not reflected in the paleoclimate reconstructions of the Jiucaiyuan Formation [74]. Here, relatively stable subhumid to semiarid conditions are interpreted from cyclostratigraphic and paleosol analyses in the South Taodonggou study area [75, 74]. Furthermore, fluvial and lacustrine strata host a diversity of plant, root, and wood fossils that are occasionally preserved in situ and show signatures of wildfires during the Early Triassic [74, 119-121]. In sum, evidence from the paleobotanical record of the Jiucaiyuan Formation suggests a lush and vegetated environment that hosted a diverse terrestrial fauna in earliest Triassic times [64, 40]. Taken together, there is mounting evidence from sedimentologic, isotopic, and cyclostratigraphic data that points to seasonal, semi-arid conditions in the Karoo Basin and stable, sub-humid conditions in the Turpan-Hami Basin.

The extreme environmental and climatic conditions inferred from the Karoo Basin likely truncated *Lystrosaurus* lifespans in the Early Triassic. Similar environmental constraints on maximum size and longevity are also known from Early Triassic therocephalians and terrestrial temnospondyls, which also lack growth marks [19, 52]. By contrast, we propose that the more favorable environmental conditions and vegetated landscape interpreted from the Jiucaiyuan Formation could have hosted longer-lived *Lystrosaurus* during the Early Triassic. Relatively stable environmental conditions could have allowed populations of *Lystrosaurus* to reach larger average body sizes than their southern Pangean relatives. The prevalence of multiple growth marks in some, but not all, immature individuals, further supports developmentally plastic

growth in *Lystrosaurus* first proposed for southern Pangean populations [22]. It also suggests that some individuals experienced periodic arrests of growth, perhaps associated with environmental disruptions, but that these disturbances may not have caused widespread mortality on the scale suggested by the South African record. Similarly, some individuals apparently experienced sufficiently stable conditions for them to grow to comparatively large size without interruption. Alternatively, the uninterrupted growth record of the largest specimen sampled here could also be due to the higher stratigraphic position of this individual; it is possible that upper Jiucaiyuan rocks represent more favorable environmental conditions. Finally, the absence of peripheral parallel-fibered bone or consistent, circumferential lamellar tissue in the current sample indicates that the maximum size of *Lystrosaurus* from the Jiucaiyuan Formation remains unknown.

2.6 CONCLUSIONS

We present bone histology, cranial geometric morphometric analyses, and body size data for *Lystrosaurus* from the Jiucaiyuan Formation of northwestern China and report statistically different cranial morphologies, an extended lifespan, and larger average body size compared to *Lystrosaurus* living in southern Pangea during Early Triassic times. In addition, we report up to two growth marks in immature individuals, which is inconsistent with previous reports of *Lystrosaurus* life histories from the Turpan-Hami Basin [40]. We suggest that it is unlikely that the growth marks reported here represent regular, cyclical patterns and more likely represent instances where bone growth stopped due to unfavorable environmental conditions. Indeed, the absence of growth marks in the largest sampled individual indicates an intrinsically high rate of growth that persisted throughout ontogeny. In addition, the presence of two cessations in growth in individuals from Size Class III indicates that smaller, likely more immature, individuals may

have been more susceptible to fluctuations in environmental conditions. However, appositional bone growth rebounded to a rapid rate following these cessations, indicating a flexible physiology, as previously proposed for higher-latitude populations of *Lystrosaurus* [22, 31]. A better sample of large limb bones (>250 mm) as well as an analysis of tusk dentine deposition, are needed to clarify what impact the Early Triassic environment may have had on *Lystrosaurus* growth and development in northern Pangea.

2.7 ACKNOWLEDGEMENTS

At the IVPP, we thank YI Jian and SHUKANG Zhang for assistance with thin section preparation as well as LIU Jun for access to field data and specimen collections. We also thank Alida Bailleul for helpful discussion and microscope access. Collecting and compiling the entirety of the comparative datasets would not have been possible if it weren't for the following museum curators, collection managers, colleagues, and friends who we deeply thank: Zaituna Skosan, Claire Browning, Christian Kammerer, Roger Smith, Jennifer Botha, Elize Butler, Bernhard Zipfel, Bruce Rubidge, Sifelani Jirah, Viktor Radermacher, Carl Mehling, and Mark Norell. For their helpful discussion on earlier versions of this manuscript, we thank Bryan Gee, Savannah Olroyd, and Elliott Armour Smith. Helpful comments that greatly improved the quality of this work were given by Jennifer Botha and one anonymous reviewer. Finally, we are indebted to Wan Yang for collecting some of the fossils analyzed here, organizing fieldwork in 2019 and leading the multidisciplinary project that instigated this research.

2.8 AUTHOR CONTRIBUTIONS

Conceptualization: Zoe T. Kulik, Kenneth D. Angielczyk, Christian A. Sidor.

Data curation: Zoe T. Kulik.

Formal analysis: Zoe T. Kulik, Jacqueline K. Lungmus.

Funding acquisition: Kenneth D. Angielczyk, Christian A. Sidor.

Investigation: Zoe T. Kulik.

Methodology: Zoe T. Kulik, Jacqueline K. Lungmus, Kenneth D. Angielczyk, Christian A. Sidor.

Project administration: Zoe T. Kulik.

Resources: Kenneth D. Angielczyk, Christian A. Sidor.

Supervision: Christian A. Sidor.

Validation: Zoe T. Kulik, Kenneth D. Angielczyk, Christian A. Sidor.

Visualization: Zoe T. Kulik, Jacqueline K. Lungmus.

Writing – original draft: Zoe T. Kulik.

Writing – review & editing: Zoe T. Kulik, Jacqueline K. Lungmus, Kenneth D. Angielczyk, Christian A. Sidor.

2.9 LITERATURE CITED

1. Raup DM, Sepkoski JJ. Periodicity of extinctions in the geologic past. Proc Natl Acad Sci. 1984 Feb 1;81(3):801–5.
2. Erwin DH. The Permo–Triassic extinction. Nature. 1994 Jan;367(6460):231–6.
3. Chen Z-Q, Benton MJ. The timing and pattern of biotic recovery following the end-Permian mass extinction. Nat Geosci. 2012 Jun;5(6):375–83.
4. Benton M. Diversification and extinction in the history of life. Science. 1995 Apr 7;268(5207):52–8.
5. Benton MJ, Twitchett RJ. How to kill (almost) all life: the end-Permian extinction event. Trends Ecol Evol. 2003 Jul;18(7):358–65.
6. Sahney S, Benton MJ. Recovery from the most profound mass extinction of all time. Proc R Soc B Biol Sci. 2008 Apr 7;275(1636):759–65.
7. Sobolev SV, Sobolev AV, Kuzmin DV, Krivolutskaya NA, Petrunin AG, Arndt NT, et al. Linking mantle plumes, large igneous provinces and environmental catastrophes. Nature. 2011 Sep;477(7364):312–6.
8. Benton MJ, Newell AJ. Impacts of global warming on Permo-Triassic terrestrial ecosystems. Gondwana Res. 2014 May;25(4):1308–37.
9. Retallack GJ, Krull ES. Carbon isotopic evidence for terminal-Permian methane outbursts and their role in extinctions of animals, plants, coral reefs, and peat swamps. In:

Greb SF, DiMichele WA, editors. Wetlands Through Time: Geological Society of America Special Paper. 2006. p. 249–68.
10. Nowak H, Schneebeli-Hermann E, Kustatscher E. No mass extinction for land plants at the Permian–Triassic transition. Nat Commun. 2019 Dec;10(1):384.
11. Mishra S, Jha N, Stebbins A, Brookfield M, Hannigan R. Palaeoenvironments, flora, and organic carbon and nitrogen isotope changes across the non-marine Permian-Triassic boundary at Wybung Head, Australia. Palaeogeogr Palaeoclimatol Palaeoecol. 2019 Nov;534:109292.
12. Botha J, Smith RMH. Rapid vertebrate recuperation in the Karoo Basin of South Africa following the End-Permian extinction. J Afr Earth Sci. 2006 Aug 1;45(4):502–14.
13. Botha J, Abdala F, Smith R. The oldest cynodont: new clues on the origin and early diversification of the Cynodontia. Zool J Linn Soc. 2007;149(3):477–92.
14. Fröbisch J. Vertebrate diversity across the end-Permian mass extinction — Separating biological and geological signals. Palaeogeogr Palaeoclimatol Palaeoecol. 2013 Feb;372:50–61.
15. Roopnarine PD, Angielczyk KD, Weik A, Dineen A. Ecological persistence, incumbency and reorganization in the Karoo Basin during the Permian-Triassic transition. Earth-Sci Rev. 2019 Feb;189:244–63.
16. Bernardi M, Petti FM, Benton MJ. Tetrapod distribution and temperature rise during the Permian–Triassic mass extinction. Proc R Soc B Biol Sci. 2018 Jan 10;285(1870):20172331.
17. Allen BJ, Wignall PB, Hill DJ, Saupe EE, Dunhill AM. The latitudinal diversity gradient of tetrapods across the Permo-Triassic mass extinction and recovery interval. Proc R Soc B Biol Sci. 2020 Jun 24;287(1929):20201125.
18. Viglietti PA, Benson RBJ, Smith RMH, Botha J, Kammerer CF, Skosan Z, et al. Evidence from South Africa for a protracted end-Permian extinction on land. Proc Natl Acad Sci. 2021 Apr 27;118(17):e2017045118.
19. Huttenlocker AK, Botha-Brink J. Bone microstructure and the evolution of growth patterns in Permo-Triassic therocephalians (Amniota, Therapsida) of South Africa. PeerJ. 2014 Apr 8;2:e325.
20. Botha-Brink J, Codron D, Huttenlocker AK, Angielczyk KD, Ruta M. Breeding Young as a Survival Strategy during Earth's Greatest Mass Extinction. Sci Rep [Internet]. 2016 Jul;6(1). Available from: http://www.nature.com/articles/srep24053
21. Codron J, Botha-Brink J, Codron D, Huttenlocker AK, Angielczyk KD. Predator-prey interactions amongst Permo-Triassic terrestrial vertebrates as a deterministic factor influencing faunal collapse and turnover. J Evol Biol. 2017 Jan;30(1):40–54.
22. Botha J. The paleobiology and paleoecology of South African *Lystrosaurus*. PeerJ. 2020 Nov 24;8:e10408.
23. Nicolas M, Rubidge BS. Changes in Permo-Triassic terrestrial tetrapod ecological representation in the Beaufort Group (Karoo Supergroup) of South Africa. Lethaia. 2010 Mar;43(1):45–59.
24. Smith R, Rubidge BS, van der Walt M. Therapsid Biodiversity Patterns and Paleoenvironments of the Karoo Basin, South Africa (pp. 31-63) Roger Smith, Bruce Rubidge and Merrill van der Walt. In: The Forerunners of Mammals. Indiana University Press; 2012.

25. King GM, Cluver MA. The Aquatic *Lystrosaurus*: An Alternative Lifestyle. Hist Biol. 1991;4:323–41.
26. Jasinoski SC, Rayfield EJ, Chinsamy A. Comparative Feeding Biomechanics of *Lystrosaurus* and the Generalized Dicynodont Oudenodon. Anat Rec Adv Integr Anat Evol Biol. 2009 Jun 1;292(6):862–74.
27. Retallack GJ, Smith RMH, Ward PD. Vertebrate extinction across Permian–Triassic boundary in Karoo Basin, South Africa. Geol Soc Am Bull. 2003;115(9):1133.
28. Botha-Brink J. Burrowing in *Lystrosaurus*: preadaptation to a postextinction environment? J Vertebr Paleontol. 2017 Sep 3;37(5):e1365080.
29. Liu J, Angielczyk KD, Abdala F. Permo-Triassic tetrapods and their climate implications. Glob Planet Change. Forthcoming.
30. Botha-Brink J, Angielczyk KD. Do extraordinarily high growth rates in Permo-Triassic dicynodonts (Therapsida, Anomodontia) explain their success before and after the end-Permian extinction? Zool J Linn Soc. 2010 Oct 1;160(2):341–65.
31. Whitney MR, Sidor CA. Evidence of torpor in the tusks of *Lystrosaurus* from the Early Triassic of Antarctica. Commun Biol [Internet]. 2020;3(1). Available from: http://www.nature.com/articles/s42003-020-01207-6
32. Tripathi C, Puri SN. On the remains of *Lystrosaurus* from the Panchets of the Raniganj coalfield. Rec Geol Surv India. 1961;89:407–19.
33. Colbert EH. *Lystrosaurus* from Antarctica. Am Mus Novit. 1974;(2535):44.
34. Gubin Y, Sinitza S. Triassic terrestrial tetrapods of Mongolia and the geological structure of the Sain-Sar-Bulak locality. In: The Nonmarine Triassic. 1993. p. 169–70.
35. Liu J, Li J, Cheng Z. The *Lystrosaurus* fossils from Xinjiang and their bearing on the terrestrial 79ivalvi 79ivalvia boundary. Vertebr Pal Asiat. 2002;40(4):267–75.
36. Sun A. Late Permian and Triassic Terrestrial Tetrapods of North China. Vertebr Palasiat. 1980;XVIII(2):11.
37. Ray S. *Lystrosaurus* (Therapsida, Dicynodontia) from India: Taxonomy, relative growth and Cranial dimorphism. J Syst Palaeontol. 2005 Jan;3(2):203–21.
38. Surkov MV, Kalandadze NN, Benton MJ. *Lystrosaurus georgi* , a dicynodont from the Lower Triassic of Russia. J Vertebr Paleontol. 2005 Jun 27;25(2):402–13.
39. Araújo R, Fernandez V, Polcyn MJ, Fröbisch J, Martins RMS. Aspects of gorgonopsian paleobiology and evolution: insights from the basicranium, occiput, osseous labyrinth, vasculature, and neuroanatomy. PeerJ. 2017 Apr 11;5:e3119.
40. Han F, Zhao Q, Liu J. Preliminary bone histological analysis of *Lystrosaurus* (Therapsida: Dicynodontia) from the Lower Triassic of North China, and its implication for lifestyle and environments after the end-Permian extinction. Fröbisch J, editor. PLOS ONE. 2021 Mar 18;16(3):e0248681.
41. Padian K, Lamm E-T, editors. Bone histology of fossil tetrapods: advancing methods, analysis, and interpretation. Berkeley: University of California Press; 2013. 285 p.
42. Köhler M, Marín-Moratalla N, Jordana X, Aanes R. Seasonal bone growth and physiology in endotherms shed light on dinosaur physiology. Nature. 2012 Jul;487(7407):358–61.
43. Castanet J, Croci S, Aujard F, Perret M, Cubo J, Margerie E de. Lines of arrested growth in bone and age estimation in a small primate: Microcebus murinus. J Zool. 2004 May 1;263(1):31–9.

44. Buffrénil V de, Quilhac A. Bone Tissue Types: A Brief Account of Currently Used Categories. In: Vertebrate Skeletal Histology and Paleohistology. S.l.: CRC PRESS; 2021. p. 147–82.
45. Francillon-Vieillot H, de Buffrénil V, Castanet J, Géraudie J, Meunier FJ, Sire JY, et al. Microstructure and Mineralization of Vertebrate Skeletal Tissues. In: Skeletal Biomineralization: Patterns, Processes and Evolutionary Trends [Internet]. American Geophysical Union; 1990. p. 175–234. Available from: http://dx.doi.org/10.1029/SC005p0175
46. Enlow H, Brown SO. A Comparative Histological Study of Fossil and Recent Bone Tissues. Part II. Tex J Sci. 1957;9(2):30.
47. Enlow H, Brown SO. A comparative histological study of fossil and recent bone tissues, Part III. Tex J Sci. 1958;10(2):187–230.
48. Castanet J, Newman DG, Girons HS. Skeletochronological Data on the Growth, Age, and Population Structure of the Tuatara, Sphenodon punctatus, on Stephens and Lady Alice Islands, New Zealand. 1988;14.
49. Castanet J. Time recording in bone microstructures of endothermic animals; functional relationships. Comptes Rendus Palevol. 2006 Mar;5(3–4):629–36.
50. Nacarino-Meneses C, Köhler M. Limb bone histology records birth in mammals. PLOS ONE. 2018 Jun 20;13(6):e0198511.
51. Sinsch U, Oromi N, Sanuy D. Growth marks in natterjack toad (Bufo calamita) bones: histological correlates of hibernation and aestivation periods. 2007;9.
52. Canoville A, Chinsamy A. Bone Microstructure of the Stereospondyl *Lydekkerina Huxleyi* Reveals Adaptive Strategies to the Harsh Post Permian-Extinction Environment: BONE MICROSTRUCTURE of LYDEKKERINA HUXLEYI. Anat Rec. 2015 Jul;298(7):1237–54.
53. Mchugh JB. Paleohistology of *Micropholis stowi* (Dissorophoidea) and *Lydekkerina huxleyi* (Lydekkerinidae) humeri from the Karoo Basin of South Africa, and implications for bone microstructure evolution in temnospondyl amphibians. J Vertebr Paleontol. 2015 Jan 2;35(1):e902845.
54. Ray S, Chinsamy A, Bandyopadhyay S. *Lystrosaurus murrayi* (Therapsida, Dicynodontia): Bone Histology, Growth and Lifestyle Adaptations. Palaeontology. 2005 Nov 1;48(6):1169–85.
55. Yuan PL, Young CC. On the Occurrence of *Lystrosaurus* in Sinkiang. Bull Geol Soc China. 1934;13(1):575–80.
56. Young CC. On two skeletons of Dicynodontia. Bull Geol Soc China. 1935;(14):483–517.
57. Young CC. Additional Dicynodontia remains from Sinkiang. Bull Geol Soc China. 1939;(19):111–36.
58. Sun A-L. Preliminary report on a new species of *Lystrosaurus* of Sinkiang. Vertebr Pal Asiat. 1964;8:216–7.
59. Sun A-L. Permo-Triassic dicynodonts from Turfan, Sinkiang. Permo-Triassic Vertebr Foss Turfan Basin. 1973;53–68.
60. Cheng Z. Vertebrates. In: Permian and Triassic Strata and Fossil Assemblages in the Dalongkou Area of Jimsar, Xinjiang. 1986. p. 207–18. (People's Republic of China Ministry of Geology and Mineral Resources Geological Memoirs).
61. Cluver MA. The cranial morphology of the dicynodont genus *Lystrosaurus* [Doctoral dissertation]. [Stellenbosch]: Stellenbosch University; 1970.

62. Cosgriff JW, Hammer WR, Ryan WJ. The Pangaean Reptile, *Lystrosaurus maccaigi*, in the Lower Triassic of Antarctica. J Paleontol. 1982;56(2):371–85.
63. King G. Anomodontia. Encycl Paleoherpetology. 1988;1–74.
64. Lucas SG. Chinese Fossil Vertebrates. Columbia University Press; 2001. 390 p.
65. Li J, Sun A. Subclass Synapsida. In: The Chinese Fossil Reptiles and Their Kin. Sci. Press; 2008. p. 379–409.
66. Fröbisch J. Composition and similarity of global anomodont-bearing tetrapod faunas. Earth-Sci Rev. 2009 Aug;95(3–4):119–57.
67. Camp J, Liu J. The taxonomy and cranial morphology of Chinese *Lystrosaurus*. J Vertebr Paleontol. 2011;31(3).
68. Camp J. Morphological variation and disparity in *Lystrosaurus*. University of Iowa; 2010.
69. Rohlf FJ. tpsDig. Stony Brook, NY: Department of Ecology and Evolution, State University of New York at Stony Brook; 2010.
70. Kammerer CF, Deutsch M, Lungmus JK, Angielczyk KD. Effects of taphonomic deformation on geometric morphometric analysis of fossils: a study using the dicynodont *Diictodon feliceps* (Therapsida, Anomodontia). PeerJ. 2020 Oct 7;8:e9925.
71. Adams D, Collyer M, Kaliontzopoulou A, Sherratt E. Geomorph: Software for geometric morphometric analyses. 2016.
72. Adams DC, Collyer ML. Multivariate Phylogenetic Comparative Methods: Evaluations, Comparisons, and Recommendations. Syst Biol. 2018 Jan 1;67(1):14–31.
73. Schlager S. Morpho and Rvcg – Shape Analysis in R: R-Packages for Geometric Morphometrics, Shape Analysis and Surface Manipulations. In: Zheng G, Li S, Székely G, editors. Statistical Shape and Deformation Analysis [Internet]. Academic Press; 2017. p. 217–56. Available from: https://www.sciencedirect.com/science/article/pii/B9780128104934000110
74. Yang W, Wan M, Crowley JL, Wang J, Luo X, Tabor NJ, et al. Paleoenvironmental and paleoclimatic and cyclo- and chrono-stratigraphy of upper Permian–Lower Triassic fluvio-lacustrine deposits in Bogda Mountains, NW China – implications for diachronous plant evolution across Permian-Triassic boundary. Earth-Sci Rev. Forthcoming.
75. Yang W, Feng Q, Liu Y, Tabor N, Miggins D, Crowley JL, et al. Depositional environments and cyclo- and chronostratigraphy of uppermost Carboniferous–Lower Triassic fluvial–lacustrine deposits, southern Bogda Mountains, NW China — A terrestrial paleoclimatic record of mid-latitude NE Pangea. Glob Planet Change. 2010 Aug;73(1–2):15–113.
76. Lamm E-T. 4. Preparation and Sectioning of Specimens. Bone Histology of Fossil Tetrapods. University of California Press; 2013.
77. Holliday CM, Ridgely RC, Sedlmayr JC, Witmer LM. Cartilaginous Epiphyses in Extant Archosaurs and Their Implications for Reconstructing Limb Function in Dinosaurs. Farke AA, editor. PloS ONE. 2010 Sep 30;5(9):e13120.
78. Griffin CT, Stefanic CM, Lessner EJ, Riegler M, Formoso K, Koeller K, et al. Assessing ontogenetic maturity in extinct saurian reptiles. Biol Rev. 2020;56.
79. de Ricqlès A. Recherches paleohistologiques sur les os longs des tetrapodes; II, Quelques observations sur la structure des os longs des theriodontes. Ann Paleontologie. 1969;55(1):1–51.

80. Ray S, Botha J, Chinsamy A. Bone histology and growth patterns of some nonmammalian therapsids. J Vertebr Paleontol. 2004 Sep 10;24(3):634–48.
81. Ray S, Bandyopadhyay S, Bhawal D. Growth patterns as deduced from bone microstructure of some selected neotherapsids with special emphasis on dicynodonts: Phylogenetic implications. Palaeoworld. 2009 Mar;18(1):53–66.
82. Ray S, Botha-Brink J. Dicynodont Growth Dynamics and Lifestyle Adaptations. In: Forerunners of Mammals. Indiana University Press; 2012. p. 29.
83. Olivier C, Houssaye A, Jalil N-E, Cubo J. First palaeohistological inference of resting metabolic rate in an extinct synapsid, *Moghreberia nmachouensis* (Therapsida: Anomodontia). Biol J Linn Soc. 2017 Jun 1;121(2):409–19.
84. Marotti G. Static and dynamic osteogenesis. 2010;4.
85. Stein K, Prondvai E. Rethinking the nature of fibrolamellar bone: an integrative biological revision of sauropod plexiform bone formation. Biol Rev. 2014;89(1):24–47.
86. Ferretti M, Palumbo C, Contri M, Marotti G. Static and dynamic osteogenesis: two different types of bone formation. Anat Embryol (Berl). 2002 Dec 1;206(1–2):21–9.
87. Shapiro F, Wu J. Woven bone overview: structural classification based on its integral role in developmental, repair and pathological bone formation throughout vertebrate groups. Eur Cell Mater. 2019 Oct 1;38:137–67.
88. de Ricqlès A. Evolution of Endothermy; Histological Evidence. Evol Theory. 1974;1(2):51–80.
89. Prondvai E, Stein KHW, de Ricqlès A, Cubo J. Development-based revision of bone tissue classification: the importance of semantics for science. Biol J Linn Soc. 2014 Aug 1;112(4):799–816.
90. Mori R, Kodaka T, Sano T, Yamagishi N, Asari M, Naito Y. Comparative Histology of the Laminar Bone between Young Calves and Foals. Cells Tissues Organs. 2003;175(1):43–50.
91. Currey JD. Differences in the Blood-Supply of Bone of Different Histological Types. J Cell Sci. 1960 Sep 1;s3-101(55):351–70.
92. Currey JD. The many adaptations of bone. J Biomech. 2003 Oct;36(10):1487–95.
93. de Margerie E, Cubo J, Castanet J. Bone typology and growth rate: testing and quantifying 'Amprino's rule' in the mallard (*Anas platyrhynchos*). C R Biol. 2002 Mar 1;325(3):221–30.
94. Urbanek A. Biotic crises in the history of Upper Silurian graptoloids: A Palaeobiological model. Hist Biol. 1993 Jul;7(1):29–50.
95. Harries PJ, Knorr PO. What does the 'Lilliput Effect' mean? Palaeogeogr Palaeoclimatol Palaeoecol. 2009 Dec;284(1–2):4–10.
96. Huttenlocker AK. Body Size Reductions in Nonmammalian Eutheriodont Therapsids (Synapsida) during the End-Permian Mass Extinction. PLOS ONE. 2014 Feb 3;9(2):e87553.
97. Huttenlocker AK, Botha-Brink J. Body size and growth patterns in the therocephalian *Moschorhinus kitchingi* (Therapsida: Eutheriodontia) before and after the end-Permian extinction in South Africa. Paleobiology. 2013;39(2):253–77.
98. Grine FE, Forster CA, Cluver MA, Georgi JA. Cranial Variability, Ontogeny, and Taxonomy of *Lystrosaurus* from the Karoo Basin of South Africa. In: Amniote Paleobiology. University of Chicago Press; 2006. p. 432–506.

99. Botha J, Smith RMH. *Lystrosaurus* species composition across the Permo–Triassic boundary in the Karoo Basin of South Africa. Lethaia. 2007;40(2):125–37.
100. Smith RMH, Botha-Brink J. Anatomy of a mass extinction: Sedimentological and taphonomic evidence for drought-induced die-offs at the Permo-Triassic boundary in the main Karoo Basin, South Africa. Palaeogeogr Palaeoclimatol Palaeoecol. 2014 Feb;396:99–118.
101. Botha J, Huttenlocker AK, Smith RMH, Prevec R, Viglietti P, Modesto SP. New geochemical and palaeontological data from the Permian-Triassic boundary in the South African Karoo Basin test the synchronicity of terrestrial and marine extinctions. Palaeogeogr Palaeoclimatol Palaeoecol. 2020 Feb;540:109467.
102. Kitching JW. The distribution of the Karroo vertebrate fauna: with special reference to certain genera and the bearing of this distribution on the zoning of the Beaufort Beds. University of the Witwatersrand; 1977. 1–131 p.
103. Kammerer CF, Viglietti PA, Hancox PJ, Butler RJ, Choiniere JN. A new kannemeyeriiform dicynodont (*Ufudocyclops mukanelai*, gen. et sp. nov.) from Subzone C of the *Cynognathus* Assemblage Zone, Triassic of South Africa, with implications for biostratigraphic correlation with other African Triassic faunas. J Vertebr Paleontol. 2019;39(2):e1596921.
104. Scotese CR, Wright N. PALEOMAP paleodigital elevation models (PaleoDEMS) for the Phanerozoic [Internet]. 2018. Available from: https://www.earthbyte.org/paleodem-resource- scotese-and-wright-2018/
105. Scotese CR. An Atlas of Phanerozoic Paleogeographic Maps: The Seas Come In and the Seas Go Out. Annu Rev Earth Planet Sci. 2021 May 30;49(1):annurev-earth-081320-064052.
106. Kidder DL, Worsley TR. Causes and consequences of extreme Permo-Triassic warming to globally equable climate and relation to the Permo-Triassic extinction and recovery. Palaeogeogr Palaeoclimatol Palaeoecol. 2004 Feb;203(3–4):207–37.
107. Kiehl JT, Shields CA. Climate simulation of the latest Permian: Implications for mass extinction. Geology. 2005;33(9):757.
108. Winguth AME, Shields CA, Winguth C. Transition into a Hothouse World at the Permian–Triassic boundary—A model study. Palaeogeogr Palaeoclimatol Palaeoecol. 2015 Dec 15;440:316–27.
109. Rey K, Amiot R, Fourel F, Abdala F, Fluteau F, Jalil N-E, et al. Oxygen isotopes suggest elevated thermometabolism within multiple Permo-Triassic therapsid clades. Elife. 2017;6:e28589.
110. Winguth A, Winguth C. Precession-driven monsoon variability at the Permian–Triassic boundary — Implications for anoxia and the mass extinction. Glob Planet Change. 2013 Jun 1;105:160–70.
111. Tabor NJ, Sidor CA, Smith RMH, Nesbitt SJ, Angielczyk KD. Paleosols of the Permian-Triassic: proxies for rainfall, climate change and major changes in terrestrial tetrapod diversity. J Vertebr Paleontol. 2017 Nov 29;37(sup1):240–53.
112. Sun Y, Joachimski MM, Wignall PB, Yan C, Chen Y, Jiang H, et al. Lethally Hot Temperatures During the Early Triassic Greenhouse. Science. 2012 Oct 19;338(6105):366–70.
113. Frank TD, Fielding CR, Winguth AME, Savatic K, Tevyaw A, Winguth C, et al. Pace, magnitude, and nature of terrestrial climate change through the end-Permian extinction in

southeastern Gondwana. Geology [Internet]. 2021 May 19; Available from: https://doi.org/10.1130/G48795.1
114. Smith RMH. Changing fluvial environments across the Permian-Triassic boundary in the Karoo Basin, South Africa and possible causes of tetrapod extinctions. Palaeogeogr Palaeoclimatol Palaeoecol. 1995 Aug;117(1–2):81–104.
115. Ward PD. Altered River Morphology in South Africa Related to the Permian-Triassic Extinction. Science. 2000 Sep 8;289(5485):1740–3.
116. Viglietti PA, Smith RMH, Rubidge BS. Changing palaeoenvironments and tetrapod populations in the *Daptocephalus* Assemblage Zone (Karoo Basin, South Africa) indicate early onset of the Permo-Triassic mass extinction. J Afr Earth Sci. 2018 Feb;138:102–11.
117. Gastaldo RA, Kamo SL, Neveling J, Geissman JW, Looy CV, Martini AM. The base of the *Lystrosaurus* Assemblage Zone, Karoo Basin, predates the end-Permian marine extinction. Nat Commun [Internet]. 2020;11(1). Available from: http://www.nature.com/articles/s41467-020-15243-7
118. Roopnarine PD, Angielczyk KD. Community stability and selective extinction during the Permian-Triassic mass extinction. Science. 2015 Oct 2;350(6256):90–3.
119. Metcalfe I, Foster CB, Afonin SA, Nicoll RS, Mundil R, Xiaofeng W, et al. Stratigraphy, biostratigraphy and C-isotopes of the Permian–Triassic non-marine sequence at Dalongkou and Lucaogou, Xinjiang Province, China. J Asian Earth Sci. 2009 Nov;36(6):503–20.
120. Wan M, Yang W, Wang J. *Amyelon bogdense* sp. nov., a silicified gymnospermous root from the Changhsingian–Induan (?) in southern Bogda Mountains, northwestern China. Rev Palaeobot Palynol. 2019 Apr;263:12–27.
121. Wan M-L, Yang W, Wan S, Wang J. Wildfires in the Early Triassic of northeastern Pangaea: Evidence from fossil charcoal in the Bogda Mountains, northwestern China. Palaeoworld. 2021 Jul;S1871174X21000639.

Table 2.1. Postcranial element length and maximum midshaft diameter for the twenty skeletal elements of *Lystrosaurus* sp. from the Jiucaiyuan Formation that were histologically sampled. Asterisk indicates fragmentary or incomplete specimens with accompanying estimates based on complete specimens in this dataset.

	Spec. No.	Preserved Length (mm)	Estimated Length (mm)	Max Midshaft Diameter (mm)	Growth Marks	Size Class
Femur						
	IVPP V 27124-7	122.38		21.43	0	II
	IVPP V 27124-6	62.74*	129	16.22	0	II
	IVPP V 27126a	62*	162		0	II
	IVPP V 27125a	182		28	2	III
	IVPP V 26548a	192		14.09	2	III
	IVPP V 27127	240*	255	33.5	0	IV
Tibia						
	IVPP V 27126b	92			0	II
	IVPP V 27124-4	56.62*	94	15.86	0	II
	IVPP V 27124-3	53.26*	98	15.71	0	II
	IVPP V 26548b	148		10.47	2	III
	IVPP V 27125b	148*	212	10.36	2	III
Fibula						
	IVPP V 27124-1	46.37*	86	9.76	0	II
	IVPP V 27126c	86		5.89	0	II
	IVPP V 26548c	140		9.02	2	III
	IVPP V 27125c	140		15.84	2-3	III
Humerus						
	IVPP V 27124-8	151.77		23.96	1	III
Radius						

	IVPP V 27126d	62			0	II
Ulna						
	IVPP V 27126e	75			0	II
	IVPP V 27124-2	47.32*	93	17.52	0	III
Ribs						
	IVPP V 27124-5	58.63*	N/A	48.76 – 56.33	EFS?	?

2.10 SUPPORTING INFORMATION

Figures (S1-S6) and corresponding tables (ST1, ST2) for cranial geometric morphometric analysis and bone wall thickness measurements.

Full-size, composite photographs of osteological thin sections are available on MorphoBank: **http://morphobank.org/permalink/?P4023**

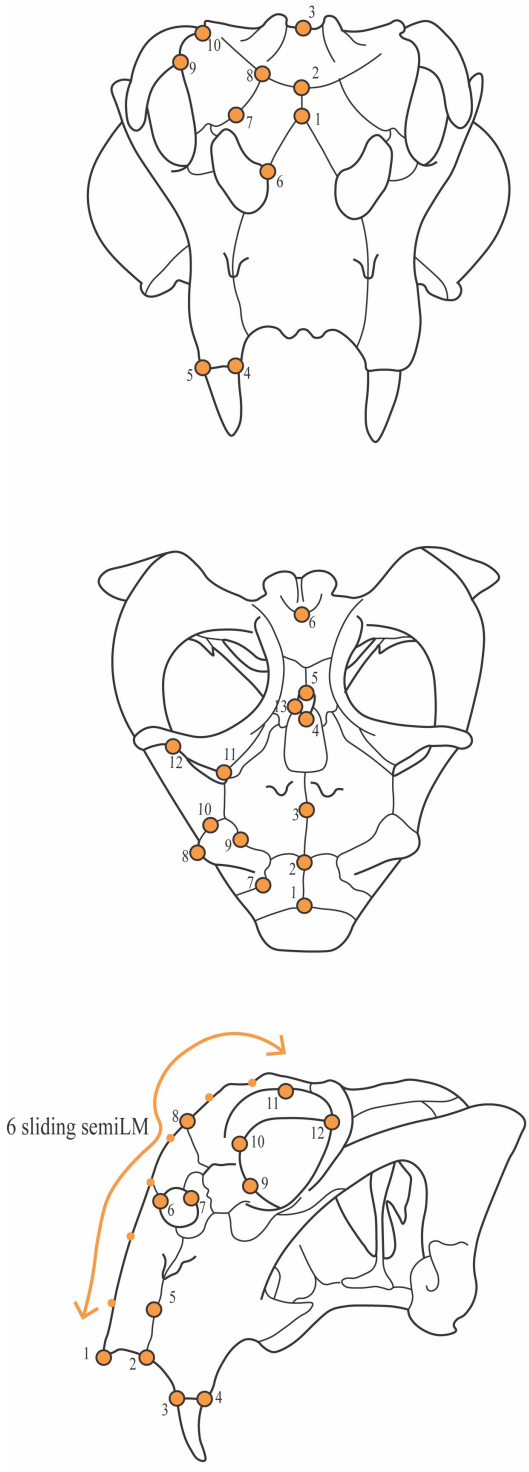

Supplemental Figure 2.1. Landmark selection for geometric morphometric analysis. Orange dots on the *Lystrosaurus* specimens show placement of landmarks used in the 2D geometric morphometric analysis in anterior (top), dorsal (middle), and lateral (bottom) views.

Landmark descriptions:

Anterior:
1– premaxilla-nasal triple junction
2 – nasals-frontals quadruple junction
3 – intersection of frontals with transverse frontal ridge
4 – intersection of premaxilla-maxilla suture with oral margin
5 – ventrolateral corner of maxillary process
6 – anteromedial corner of naris
7 – ventral extreme of prefrontal
8 – junction of the prefrontal, nasal and frontal
9 – lateralmost point of prefrontal
10 – intersection of prefrontal-frontal suture with orbital rim

Dorsal:
1 – nasals-premaxilla triple junction
2 – nasals-frontals quadruple junction
3 – middle of sagittal frontal suture
4 – anterior extreme of the pineal foramen
5 – posterior extreme of the pineal foramen
6 – parietals-supraoccipital triple junction
7 – nasal-prefrontal-frontal triple junction
8 – lateral angle of prefrontal
9 – middle of prefrontal-frontal suture
10 – intersection of prefrontal-frontal suture with orbital rim
11 – of frontal-postfrontal suture with orbital rim
12 – lateralmost extent of the postorbital bar

Lateral:
1 – anterior tip of premaxilla
2 – premaxilla-maxilla sutural contact with oral margin
3 – anteroventral-most point of maxillary process
4 – lateroventral-most point of maxillary process
5 – dorsoventral midpoint of premaxilla-maxilla suture
6 – anteriormost point of naris
7 – posterodorsal corner of naris
8 – anteriormost point of the prefrontal
9 – anteroventral corner of orbit
10 – anteriormost point of orbit
11 – dorsalmost point of interior margin of orbit
12 – posteriormost point of orbit

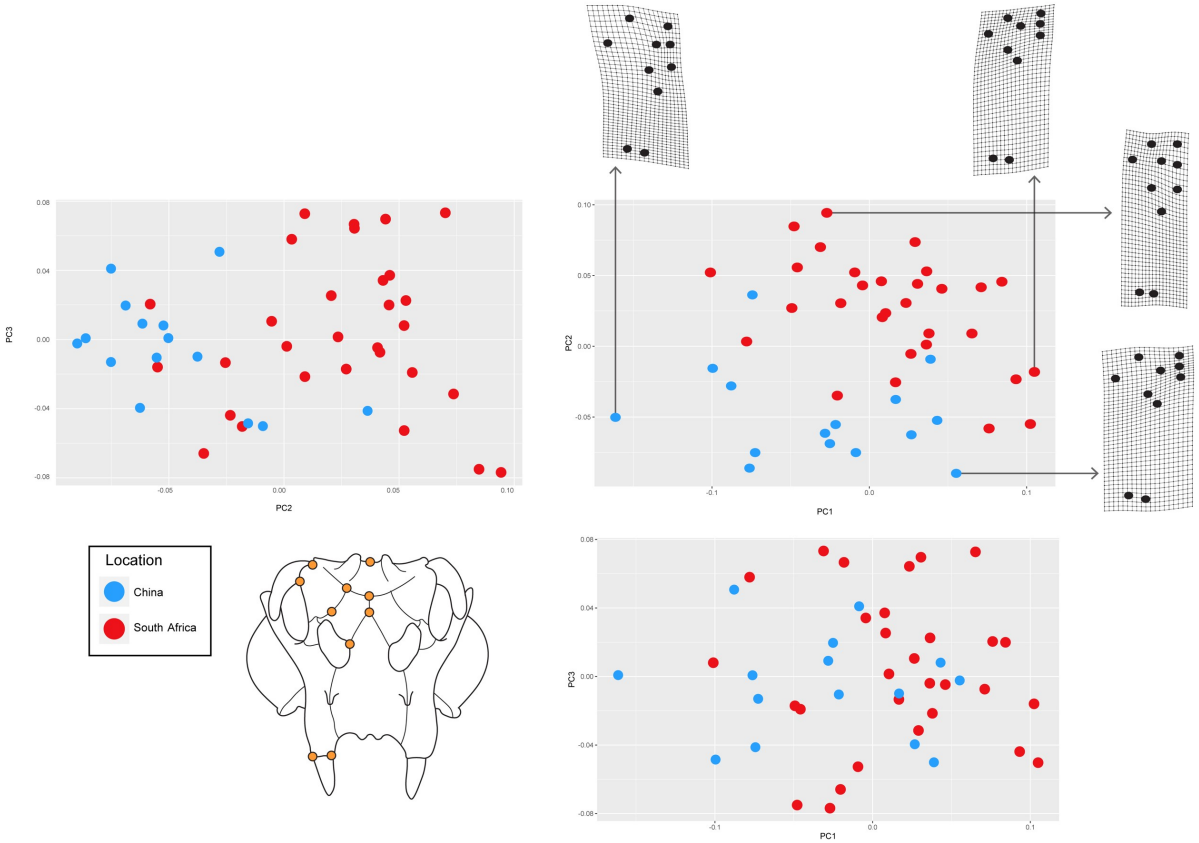

Supplemental Figure 2.2. Principal components plots (PC1-PC3) for the anterior perspective. Skull drawing of *Lystrosaurus* on the lower left correspond to the orientation for this analysis. Orange dots on the specimen show placement of landmarks used in the 2D geometric morphometric analysis. Blue dots represent specimens from China and red dots represent specimens from South Africa. Arrows point to the warp grids showing corresponding deformation along each principal component axis.

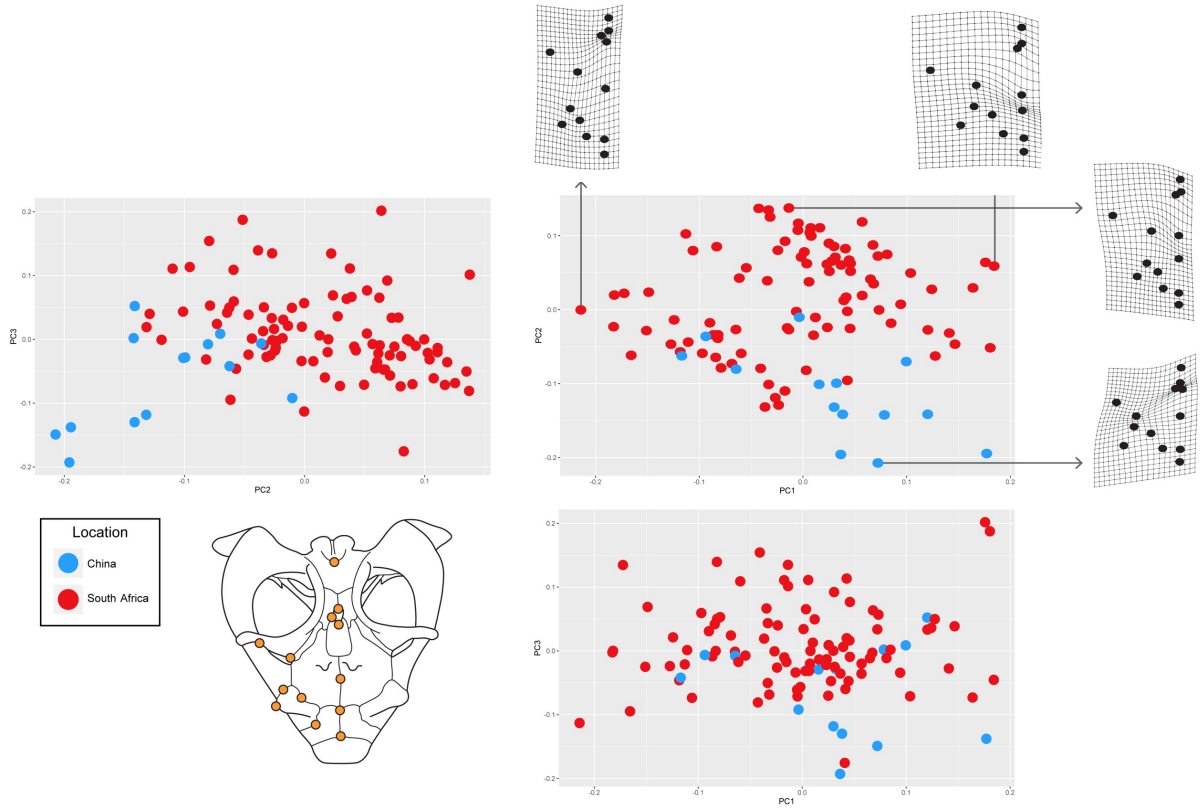

Supplemental Figure 2.3. Principal components plots (PC1-PC3) for the dorsal perspective. Skull drawing of *Lystrosaurus* on the lower left correspond to the orientation for this analysis. Orange dots on the specimen show placement of landmarks used in the 2D geometric morphometric analysis. Blue dots represent specimens from China and red dots represent specimens from South Africa. Arrows point to the warp grids showing corresponding deformation along each principal component axis.

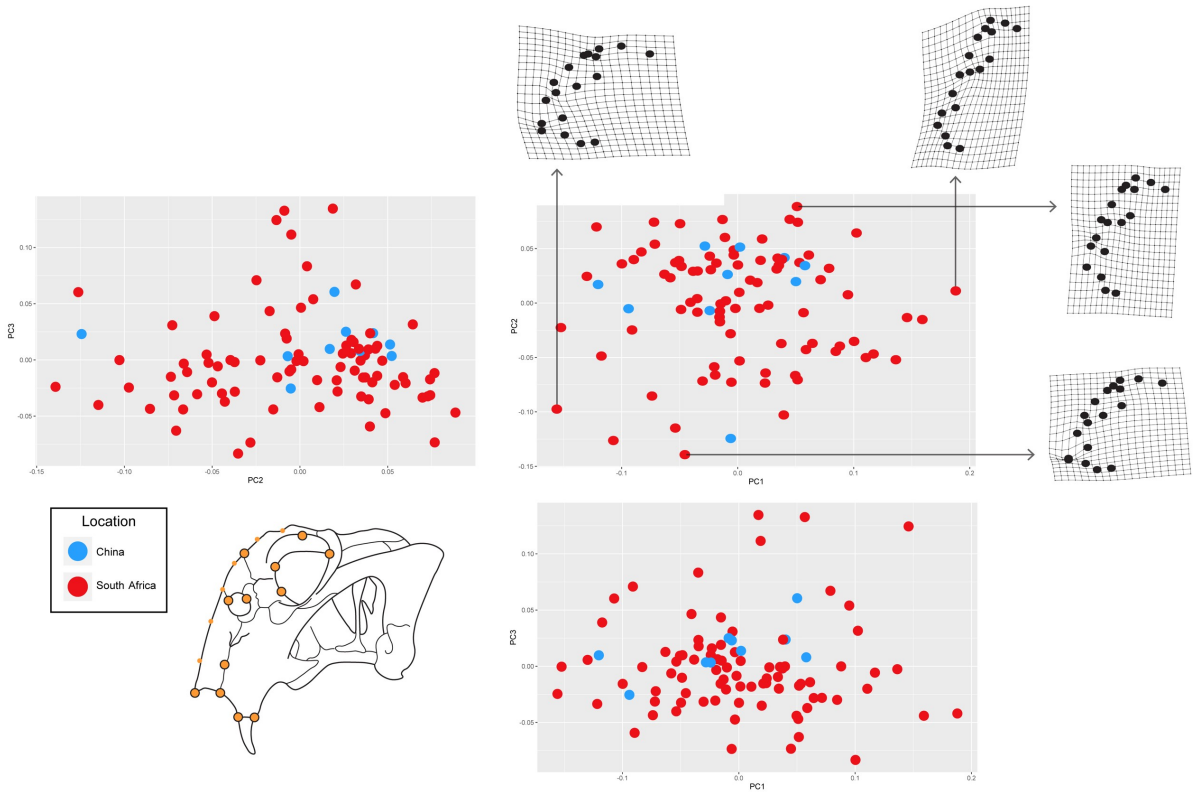

Supplemental Figure 2.4. Principal components plots (PC1-PC3) for the lateral perspective. Skull drawing of *Lystrosaurus* on the lower left correspond to the orientation for this analysis. Orange dots on the specimen show placement of landmarks used in the 2D geometric morphometric analysis. Blue dots represent specimens from China and red dots represent specimens from South Africa. Arrows point to the warp grids showing corresponding deformation along each principal component axis.

Supplemental Table 2.1. Cross-sectional area and diameter measurements of femoral thin sections that were used to calculate cortical thickness (*K*), the proportional area of the medullary region relative to the total area of the bone cross-section. We report proportional cortical thickness based on area (K_A) and diameter (K_D). Measurements are shown below and were taken on the smallest femur, IVPP V 27124-7 (Fig S5) and largest femur, IVPP V 27127 (Fig S6) in FIJI.

Specimen Number	Cross-sectional area (mm^2)	Cross-sectional Major axis (mm)	Cross-sectional Minor axis (mm)	Medullary cavity area (mm^2)	Medullary Major axis (mm)	Medullary Minor axis (mm)	K_A	K_D
IVPP V 27124-7	266.75	21.91	15.5	105.64	13.78	9.76	0.40	0.63
IVPP V 27127	654.62	34.52	24.15	233.46	22.12	13.44	0.36	0.64

Supplemental Figure 2.5. Cortical thickness measurements of specimen IVPP V 27124-7. Outer and inner yellow polygons trace the region of compact cortical bone. Measurements were taken using FIJI. Scale bar = 5000 µm.

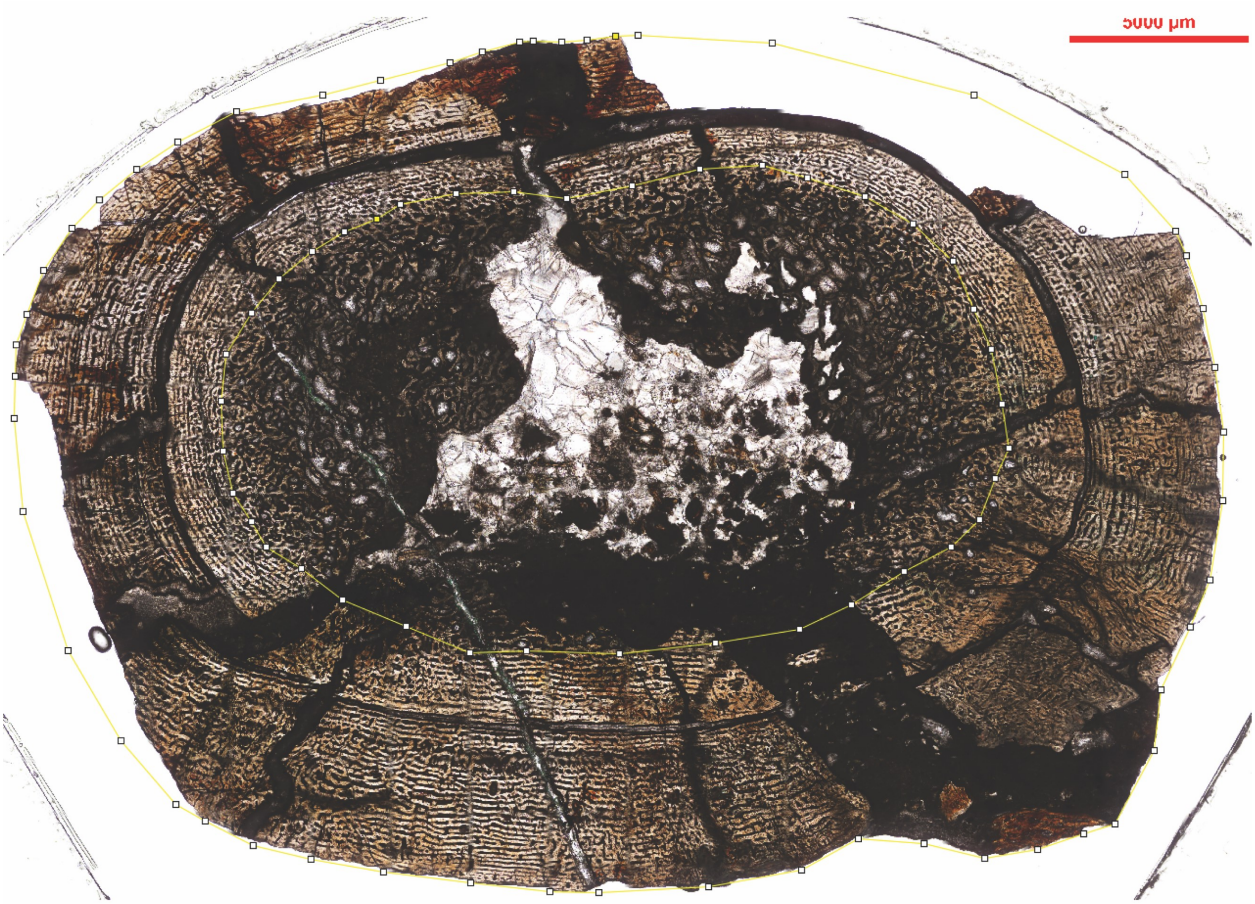

Supplemental Figure 2.6. Cortical thickness measurements of specimen IVPP V 27127. Outer and inner yellow polygons trace the estimated region of compact cortical bone. Measurements were taken using FIJI. Scale bar = 5000 µm.

Supplemental Table 2.2. Table of cranial measurements collected or compiled for Triassic *Lystrosaurus* species.

Taxon	Specimen/ Field Number	BSL (mm)	Locality	Reference
L. murrayi	NMQR 3636	32.08	South Africa	This study
L. murrayi	NMQR 3655	36.29	South Africa	Botha 2020
L. murrayi	BP/I/4011	38.85	South Africa	This study
L. murrayi	BP/I/3904	39.3	South Africa	This study
L. murrayi	BP/1/3904	41	South Africa	Botha 2020
L. murrayi	BP/1/4011	41.81	South Africa	Botha 2020
L. murrayi	NMQR 3915	43.5	South Africa	Botha 2020
L. murrayi	NMQR 3635a	46.33	South Africa	Botha 2020
L. murrayi	SAM-PK-3531	49	South Africa	Botha 2020
Lystrosaurus sp. indet.	SAM-PK-K1396	50.8	South Africa	This study
L. murrayi	GSI 17847	52	India	Ray 2005
L. murrayi	BP/1/4190	53	South Africa	Botha 2020
L. murrayi	BP/I/4190	58.94	South Africa	This study
L. declivis	NMQR 129	59.44	South Africa	Botha 2020
L. murrayi	GSI 17852	59.65	India	Ray 2005
L. declivis	NMQR 624	60.52	South Africa	Botha 2020
L. murrayi	NMQR 351	62.58	South Africa	Botha 2020
L. murrayi	NMQR 3629	66.02	South Africa	This study
L. declivis	NMQR 159	68	South Africa	Botha 2020
L. murrayi	GSI 17854	68.2	India	Ray 2005
L. murrayi	GSI 17855	71.8	India	Ray 2005
L. murrayi	NMQR 3571	72.39	South Africa	Botha 2020
L. declivis	NMQR 738	72.4	South Africa	Botha 2020
L. declivis	NMQR 4039	74.05	South Africa	Botha 2020
L. murrayi	GSI 17856	74.1	India	Ray 2005
L. curvatus	NMQR 4001	74.5	South Africa	Botha 2020
L. murrayi	GSI 17846	75.75	India	Ray 2005
L. murrayi	NMQR 676	76.13	South Africa	Botha 2020
L. murrayi	SAM-PK-K1362	78	South Africa	Botha 2020
Lystrosaurus sp. indet.	BP/I/4340a	78.79	South Africa	This study
L. murrayi	NMQR 721a	79.84	South Africa	Botha 2020
L. declivis	NMQR 158	80	South Africa	Botha 2020
L. declivis	NMQR 4043	80.01	South Africa	Botha 2020
L. murrayi	GSI 17853	80.55	India	Ray 2005
Lystrosaurus sp. indet.	SAM-PK-K103	80.64	South Africa	This study
L. murrayi	GSI 17848	80.9	India	Ray 2005

L. declivis	NMQR 128	80.92	South Africa	Botha 2020
L. curvatus	NMQR 3914	81.23	South Africa	Botha 2020
Lystrosaurus sp. indet.	BP/I/4516	81.45	South Africa	This study
L. murrayi	UR 2690	81.69	South Africa	This study
L. murrayi	BP/1/4030	81.73	South Africa	Botha 2020
L. murrayi	NMQR 4028a	82.16	South Africa	Botha 2020
L. declivis	NMQR 3300	82.39	South Africa	This study
L. murrayi	SAM-PK-K10372	82.73	South Africa	This study
L. murrayi	NMQR 758	82.74	South Africa	Botha 2020
L. murrayi	BMNH 36253	83	South Africa	Botha 2020
L. declivis	NMQR 3999	83	South Africa	Botha 2020
L. murrayi	NMQR 659	83.02	South Africa	This study
L. declivis	NMQR 3737	84.21	South Africa	Botha 2020
L. murrayi	NMQR 1654	84.27	South Africa	This study
Lystrosaurus sp. indet.	NMQR 1648	84.55	South Africa	This study
L. murrayi	NMQR 3927	85.4	South Africa	Botha 2020
L. murrayi	NMQR 4055	86	South Africa	Botha 2020
L. murrayi	GSI 17867	86.05	India	Ray 2005
L. murrayi	NMQR 3541	86.38	South Africa	This study
L. murrayi	NMQR 3547	86.43	South Africa	This study
L. declivis	BP/1/1706	86.45	South Africa	Botha 2020
L. murrayi	TM 115	87	South Africa	Botha 2020
L. murrayi	SAM-PK-K11535	88.15	South Africa	This study
L. murrayi	SAM-PK-K10221	88.38	South Africa	This study
L. declivis	NMQR 721b	88.84	South Africa	Botha 2020
L. declivis	NMQR 640	90.72	South Africa	Botha 2020
L. declivis	BP/1/3908	91	South Africa	Botha 2020
L. murrayi	NMQR 6	91.44	South Africa	Botha 2020
L. murrayi	SAM-PK-K21	91.48	South Africa	This study
L. murrayi	NMQR 29	91.6	South Africa	Botha 2020
L. murrayi	SAM-PK-K8311	92	South Africa	Botha 2020
L. declivis	NMQR 47	92.32	South Africa	Botha 2020
Lystrosaurus sp. indet.	SAM-PK-K8523	92.38	South Africa	This study
Lystrosaurus sp. indet.	BP/I/4626	93.58	South Africa	This study
Lystrosaurus sp. indet.	BP/I/414	93.6	South Africa	This study
L. declivis	NMQR 395	93.66	South Africa	Botha 2020
L. murrayi	ISIR 767	94	India	Ray 2005
L. murrayi	SAM-PK-11186	94.07	South Africa	This study
L. murrayi	BP/1/4344	94.11	South Africa	Botha 2020
L. murrayi	BP/I/4344	94.17	South Africa	This study
L. declivis	BP/1/4275	95	South Africa	Botha 2020

L. declivis	NMQR 660	95.53	South Africa	Botha 2020
L. murrayi	BP/1/3900	96	South Africa	Botha 2020
L. declivis	TM 4113	96	South Africa	Botha 2020
L. murrayi	NMQR 799	96.1	South Africa	Botha 2020
L. murrayi	GSI 17851	96.25	India	Ray 2005
Lystrosaurus sp. indet.	BP/I/5173	96.64	South Africa	This study
L. declivis	BP/I/4343	96.8	South Africa	This study
Lystrosaurus sp. indet.	SAM-PK-11174	96.99	South Africa	This study
L. declivis	NMQR 1655	97.49	South Africa	Botha 2020
L. murrayi	GSI 17863	97.8	India	Ray 2005
Lystrosaurus sp. indet.	BP/I/4802	97.83	South Africa	This study
L. murrayi	SAM-PK-11169	98	South Africa	Botha 2020
L. murrayi	SAM-PK-K1397	98.17	South Africa	This study
L. declivis	NMQR 787	98.18	South Africa	Botha 2020
L. murrayi	NMQR 3691	98.38	South Africa	This study
L. declivis	NMQR 423	98.49	South Africa	Botha 2020
L. murrayi	BP/I/3908	98.69	South Africa	This study
L. murrayi	NMQR 3705	98.91	South Africa	This study
L. murrayi	UWMB 91830	98.92	South Africa	This study
L. murrayi	GSI 17857	99	India	Ray 2005
L. declivis	NMQR 3959a	99	South Africa	Botha 2020
L. declivis	TM 4050	99.19	South Africa	Botha 2020
L. declivis	NMQR 818	99.49	South Africa	Botha 2020
L. declivis	SAM-PK-11525	99.64	South Africa	This study
L. murrayi	NMQR 3581	99.92	South Africa	This study
L. murrayi	BMNH 36224	100	South Africa	Botha 2020
L. murrayi	GSI 17843	100	India	Ray 2005
L. murrayi	NMQR 3480	100.86	South Africa	This study
L. murrayi	BP/I/4798a	100.87	South Africa	This study
L. murrayi	BMNH R5710	101	South Africa	Botha 2020
L. murrayi	BP/1/4798	101	South Africa	Botha 2020
L. murrayi	BP/1/5086a	101	South Africa	Botha 2020
L. declivis	TM 117	101	South Africa	Botha 2020
L. declivis	BP/I/4275	101.04	South Africa	This study
Lystrosaurus sp. indet.	NMQR 3560b	101.05	South Africa	This study
L. declivis	NMQR 42	101.26	South Africa	Botha 2020
L. declivis	NMQR 1	101.36	South Africa	Botha 2020
L. murrayi	SAM-PK-11172	101.43	South Africa	This study
L. murrayi	NMQR 3957	101.54	South Africa	Botha 2020
L. murrayi	BP/1/4217	101.63	South Africa	Botha 2020
L. murrayi	TM 67	102	South Africa	Botha 2020

L. declivis	NMQR 664	102.2	South Africa	Botha 2020
L. murrayi	UR 2691	102.48	South Africa	This study
L. murrayi	BP/I/1269	102.7	South Africa	This study
L. declivis	NMQR 3837	102.72	South Africa	Botha 2020
L. declivis	NMQR 372	102.74	South Africa	Botha 2020
L. murrayi	NMQR 3592	102.88	South Africa	Botha 2020
L. declivis	BP/I/4207	102.95	South Africa	Botha 2020
L. murrayi	BP/1/4039	103	South Africa	Botha 2020
L. murrayi	UMCZ T763	103	South Africa	Botha 2020
L. declivis	NMQR 3560a	103.05	South Africa	This study
L. murrayi	NMQR 37	103.31	South Africa	Botha 2020
L. declivis	SAM-PK-K14	103.89	South Africa	This study
L. declivis	BP/1/4507	103.93	South Africa	Botha 2020
Lystrosaurus sp. indet.	BP/I/4038	104.56	South Africa	This study
L. declivis	BP/1/4314	104.6	South Africa	Botha 2020
L. declivis	NMQR 388	104.73	South Africa	Botha 2020
L. murrayi	NMQR 815a	104.77	South Africa	Botha 2020
L. murrayi	NMQR 4038	104.96	South Africa	Botha 2020
L. hedini	IVPP V18671	105	China	This study
L. murrayi	NMQR 4059	105	South Africa	Botha 2020
L. murrayi	SAM-PK-K1165	105	South Africa	Botha 2020
L. declivis	TM 4049	105	South Africa	Botha 2020
L. murrayi	BP/I/4591	105.12	South Africa	This study
L. declivis	NMQR 32	105.37	South Africa	Botha 2020
L. declivis	BP/1/4343	105.51	South Africa	Botha 2020
Lystrosaurus sp. indet.	SAM-PK-K8519b	105.8	South Africa	This study
L. declivis	NMQR 1382	105.89	South Africa	Botha 2020
L. murrayi	NMQR 2951	105.96	South Africa	Botha 2020
L. declivis	SAM-PK-K10454	105.97	South Africa	Botha 2020
L. murrayi	NMQR 4056	106	South Africa	Botha 2020
L. declivis	TM 164	106	South Africa	Botha 2020
L. murrayi	TM 69	106	South Africa	Botha 2020
L. murrayi	NMQR 3593	106.69	South Africa	Botha 2020
L. declivis	NMQR 618a	106.73	South Africa	Botha 2020
Lystrosaurus sp. indet.	SAM-PK-K1409	106.81	South Africa	This study
L. declivis	BP/I/1368	107.12	South Africa	Botha 2020
L. declivis	BP/I/3915	107.17	South Africa	This study
L. murrayi	UR 2711	107.48	South Africa	This study
L. declivis	NMQR 4041a	107.5	South Africa	This study
L. murrayi	NMQR 3609	107.59	South Africa	Botha 2020
L. murrayi	SAM-PK-K7991	108	South Africa	Botha 2020

L. murrayi	SAM-PK-K10461	108.39	South Africa	Botha 2020
L. murrayi	BP/1/4271	108.4	South Africa	Botha 2020
L. murrayi	BP/I/4271	108.44	South Africa	This study
L. declivis	BP/1/3915	108.55	South Africa	Botha 2020
L. murrayi	BP/I/4276b	108.8	South Africa	This study
L. murrayi	BP/I/3978	109.04	South Africa	This study
L. murrayi	SAM-PK-K10686	109.23	South Africa	Botha 2020
L. murrayi	NMQR 3765	109.41	South Africa	Botha 2020
Lystrosaurus sp. indet.	BP/I/4309	109.62	South Africa	This study
L. declivis	NMQR 3301	109.68	South Africa	This study
L. murrayi	BP/I/4507	109.92	South Africa	Botha 2020
L. declivis	NMQR 116	109.93	South Africa	Botha 2020
L. declivis	BP/1/1368	110	South Africa	Botha 2020
L. murrayi	BPI MN106	110	South Africa	Botha 2020
L. declivis	UR 2506	110.23	South Africa	This study
L. declivis	BP/I/1383	110.31	South Africa	This study
L. murrayi	BP/I/269	110.52	South Africa	This study
Lystrosaurus sp. indet.	BP/I/4345	110.63	South Africa	This study
L. murrayi	BP/1/269	110.65	South Africa	Botha 2020
L. murrayi	SAM-PK-11167	110.89	South Africa	This study
L. murrayi	BP/I/4341	110.92	South Africa	This study
L. murrayi	BP/1/4705	110.98	South Africa	Botha 2020
L. murrayi	NMQR 4057	111	South Africa	Botha 2020
L. declivis	NMQR 3958	111.01	South Africa	This study
Lystrosaurus sp. indet.	BP/I/5731	111.04	South Africa	This study
L. youngi	IVPP V18669	111.11	China	This study
L. declivis	NMQR 3738	111.53	South Africa	Botha 2020
Lystrosaurus sp. indet.	BP/I/4718	111.56	South Africa	This study
L. declivis	NMQR 3759	111.88	South Africa	Botha 2020
L. murrayi	BP/1/468	112	South Africa	Botha 2020
L. murrayi	BP/I/4705	112.12	South Africa	This study
Lystrosaurus sp. indet.	BP/I/1741	112.31	South Africa	This study
L. murrayi	SAM-PK-K10383	112.59	South Africa	Botha 2020
L. murrayi	NMQR 3649	113	South Africa	Botha 2020
L. declivis	TM 139	113	South Africa	Botha 2020
L. murrayi	NMQR 3112	113.01	South Africa	This study
L. declivis	NMQR 12	113.12	South Africa	Botha 2020
L. declivis	NMQR 3239	113.36	South Africa	This study
L. murrayi	NMQR 596	113.43	South Africa	Botha 2020
L. murrayi	NMQR 4153	113.47	South Africa	This study
L. murrayi	SAM-PK-K10466	113.53	South Africa	Botha 2020

L. murrayi	FMNH UC1516	113.75	South Africa	Botha 2020
L. murrayi	SAM-PK-K8567	113.84	South Africa	This study
L. murrayi	SAM-PK-K1459	113.93	South Africa	This study
L. murrayi	UR 2695	113.95	South Africa	This study
L. declivis	BP/1/5086b	114	South Africa	Botha 2020
L. declivis	NMQR 4091	114.1	South Africa	This study
L. murrayi	SAM-PK-3715	114.29	South Africa	This study
Lystrosaurus sp. indet.	BP/I/4340b	114.72	South Africa	This study
L. declivis	NMQR 618b	114.94	South Africa	Botha 2020
L. declivis	FARB 8243	115.1	South Africa	This study
L. declivis	BP/1/1750	115.17	South Africa	Botha 2020
L. murrayi	NMQR 648	115.38	South Africa	Botha 2020
L. murrayi	ISIR 766	115.7	India	Ray 2005
L. declivis	NMQR 3573	115.84	South Africa	This study
L. declivis	BP/1/4211a	115.95	South Africa	Botha 2020
L. murrayi	TM 71	116	South Africa	Botha 2020
L. murrayi	BP/I/4276a	116.28	South Africa	This study
Lystrosaurus sp. indet.	SAM-PK-K1386	116.32	South Africa	This study
L. murrayi	SAM-PK-K1495	116.4	South Africa	This study
L. declivis	NMQR 679	117.7	South Africa	Botha 2020
Lystrosaurus sp. indet.	BP/I/5056	118.16	South Africa	This study
L. declivis	NMQR 4041b	118.22	South Africa	This study
L. declivis	SAM-PK-11184b	118.23	South Africa	This study
L. youngi	IVPP V8532	118.31	China	This study
L. murrayi	BP/1/266	118.4	South Africa	Botha 2020
L. declivis	SAM-PK-K10386	118.42	South Africa	This study
L. declivis	NMQR 375	118.62	South Africa	This study
L. murrayi	UR 2688	118.62	South Africa	This study
L. murrayi	NMQR 725	118.8	South Africa	Botha 2020
L. declivis	FMNH UR2506	118.85	South Africa	Botha 2020
L. murrayi	SAM-PK-K1268	118.89	South Africa	This study
L. declivis	NMQR 815b	118.94	South Africa	Botha 2020
L. declivis	SAM-PK-691	119.11	South Africa	This study
L. declivis	BP/I/5214	119.13	South Africa	This study
L. murrayi	NMQR 4176	119.48	South Africa	This study
L. murrayi	NMQR 5	119.73	South Africa	Botha 2020
L. declivis	NMQR 735	119.73	South Africa	This study
L. declivis	NMQR 161	120.17	South Africa	Botha 2020
Lystrosaurus sp. indet.	SAM-PK-11215	120.24	South Africa	This study
Lystrosaurus sp. indet.	BP/I/4639	120.27	South Africa	This study
L. declivis	SAM-PK-K8566	120.32	South Africa	This study

L. declivis	NMQR 365	120.48	South Africa	Botha 2020
L. murrayi	BP/I/468	120.65	South Africa	This study
Lystrosaurus sp. indet.	SAM-PK-K6	120.71	South Africa	This study
L. murrayi	SAM-PK-3528	120.81	South Africa	This study
L. declivis	SAM-PK-3596	121	South Africa	Botha 2020
L. declivis	NMQR 3917	121.13	South Africa	This study
L. murrayi	GSI 17858	121.2	India	Ray 2005
L. murrayi	UR 2706	121.43	South Africa	This study
L. murrayi	NMQR 3040	121.53	South Africa	Botha 2020
L. declivis	NMQR 3735	121.85	South Africa	This study
L. murrayi	NMQR 3751	121.98	South Africa	This study
L. murrayi	NMQR 3840a	122.09	South Africa	Botha 2020
L. murrayi	BP/I/466	122.18	South Africa	This study
Lystrosaurus sp. indet.	BP/I/4304	122.63	South Africa	This study
L. murrayi	GSI 17860	122.95	India	Ray 2005
L. murrayi	BP/1/3978	123	South Africa	Botha 2020
Lystrosaurus sp. indet.	BP/I/4355	123	South Africa	This study
L. declivis	SAM-PK-11527	123.97	South Africa	This study
L. declivis	SAM-PK-K4800	124.15	South Africa	This study
L. declivis	SAM-PK-K5	124.46	South Africa	This study
Lystrosaurus sp. indet.	FARB 8249	124.48	South Africa	This study
L. declivis	NMQR 132	124.64	South Africa	Botha 2020
L. murrayi	SAM-PK-K1460	124.7	South Africa	This study
L. declivis	NMQR 848	125.01	South Africa	This study
L. youngi	IVPP V18664	125.22	China	This study
L. declivis	NMQR 675	125.75	South Africa	Botha 2020
Lystrosaurus sp. indet.	SAM-PK-K8519a	125.88	South Africa	This study
L. declivis	BMNH 47324	126	South Africa	Botha 2020
L. murrayi	BP/1/4710	126	South Africa	Botha 2020
L. murrayi	TM 33	127	South Africa	Botha 2020
L. murrayi	BP/I/5057	127.29	South Africa	This study
L. murrayi	BP/I/5028	127.65	South Africa	This study
L. murrayi	NMQR 393	127.83	South Africa	Botha 2020
Lystrosaurus sp. indet.	SAM-PK-1272	127.84	South Africa	This study
L. murrayi	NMQR 3539b	128.07	South Africa	Botha 2020
L. declivis	SAM-PK-K11518	128.95	South Africa	This study
L. murrayi	NMQR 2065	129.08	South Africa	Botha 2020
L. declivis	BP/I/267	129.41	South Africa	This study
L. murrayi	NMQR 3960	130	South Africa	Botha 2020
L. murrayi	SAM-PK-4326	130.09	South Africa	This study
L. declivis	NMQR 4028b	130.84	South Africa	Botha 2020

China L. sp.	IVPP V18663	130.9	China	This study
L. declivis	UC 1706	130.93	South Africa	This study
L. murrayi	SAM-PK-K8520	130.95	South Africa	This study
L. murrayi	SAM-PK-K1247	131.03	South Africa	Botha 2020
L. youngi	IVPP V3242	132	China	This study
L. declivis	NMQR 3929	132	South Africa	Botha 2020
Lystrosaurus sp. indet.	SAM-PK-11223	133.65	South Africa	This study
Lystrosaurus sp. indet.	BP/I/4359	133.75	South Africa	This study
L. murrayi	BP/1/5070	134	South Africa	Botha 2020
L. declivis	SAM-PK-3455	134	South Africa	Botha 2020
L. murrayi	NMQR 657	134.38	South Africa	Botha 2020
L. declivis	SAM-PK-K1398	135	South Africa	Botha 2020
L. declivis	BSP 1934-VIII-511	135.86	South Africa	Botha 2020
L. declivis	NMQR 3575	135.86	South Africa	Botha 2020
L. declivis	TM 20	136	South Africa	Botha 2020
L. declivis	NMQR 4096	136.7	South Africa	This study
L. declivis	NMQR 126	136.8	South Africa	Botha 2020
L. declivis	NMQR uncat	137.28	South Africa	This study
L. declivis	NMQR 4145	137.75	South Africa	This study
L. declivis	SAM-PK-11184a	138	South Africa	Botha 2020
L. murrayi	SAM-PK-K26	138.27	South Africa	This study
L. murrayi	NMQR 3539a	138.38	South Africa	Botha 2020
Lystrosaurus sp. indet.	BP/I/1698	138.46	South Africa	This study
Lystrosaurus sp. indet.	BP/I/4702	138.83	South Africa	This study
L. declivis	SAM-PK-K10374	138.95	South Africa	This study
L. murrayi	BP/I/1379	139.12	South Africa	This study
L. murrayi	NMQR 622	139.16	South Africa	This study
L. murrayi	NMQR 4172	139.29	South Africa	This study
L. declivis	NMQR 3545	139.78	South Africa	This study
L. declivis	UR 370	140.54	South Africa	This study
L. declivis	BP/1/1379	140.81	South Africa	Botha 2020
L. declivis	BPI MN109	141	South Africa	Botha 2020
L. murrayi	NMQR 835a	141.48	South Africa	Botha 2020
L. murrayi	BP/I/266	141.91	South Africa	This study
L. murrayi	SAM-PK-K7	142	South Africa	Botha 2020
L. declivis	BMNH 36221	142.45	South Africa	Botha 2020
Lystrosaurus sp. indet.	SAM-PK-K8524	142.57	South Africa	This study
Lystrosaurus sp. indet.	BP/I/4006a	142.62	South Africa	This study
L. declivis	BMNH 36222	143	South Africa	Botha 2020
Lystrosaurus sp. indet.	BP/I/4006b	143.51	South Africa	This study
L. declivis	BP/I/489	143.79	South Africa	This study

L. murrayi	TM 2881	144	South Africa	Botha 2020
L. declivis	TM 4465	144	South Africa	Botha 2020
L. murrayi	SAM-PK-K10385	144.28	South Africa	This study
L. declivis	SAM-PK-K12	144.58	South Africa	This study
L. declivis	BP/1/479	144.67	South Africa	Botha 2020
L. murrayi	NMQR 3963	145	South Africa	Botha 2020
L. declivis	BP/1/477	145.94	South Africa	Botha 2020
L. murrayi	SAM-PK-11181	146	South Africa	Botha 2020
L. murrayi	SAM-PK-K8	146	South Africa	Botha 2020
L. declivis	BP/1/267	146.3	South Africa	Botha 2020
L. declivis	SAM-PK-K10373	146.44	South Africa	This study
L. murrayi	SAM-PK-K10375	146.99	South Africa	This study
L. declivis	BP/I/4798b	147.11	South Africa	This study
L. declivis	NMQR 164	147.24	South Africa	This study
L. murrayi	BP/I/7602	147.39	South Africa	This study
L. declivis	NMQR 3926	147.79	South Africa	This study
L. declivis	BP/1/4624	148	South Africa	Botha 2020
Lystrosaurus sp. indet.	BP/I/5175	148.15	South Africa	This study
L. hedini	IVPP V18654	148.16	China	This study
L. youngi	IVPP V18665	149.07	China	This study
L. declivis	BP/I/4625	149.63	South Africa	This study
L. murrayi	FARB 20882	150.13	South Africa	Botha 2020
Lystrosaurus sp. indet.	BP/I/2240	150.51	South Africa	This study
L. murrayi	NMQR 3565	150.6	South Africa	Botha 2020
L. declivis	BP/I/477	151.1	South Africa	This study
L. declivis	SAM-PK-K1378	151.1	South Africa	Botha 2020
L. murrayi	SAM-PK-K1399	151.61	South Africa	This study
Lystrosaurus sp. indet.	BP/I/4366	153.36	South Africa	This study
L. declivis	NMQR 356	153.56	South Africa	Botha 2020
L. declivis	NMQR 1620	154.86	South Africa	This study
L. declivis	NMQR 4037	156.92	South Africa	This study
Lystrosaurus sp. indet.	SAM-PK-705	157.66	South Africa	This study
L. murrayi	BMNH 1291	159	South Africa	Botha 2020
L. murrayi	SAM-PK-271	159.45	South Africa	This study
China L. sp.	IVPP V18657	159.58	China	This study
Lystrosaurus sp. indet.	SAM-PK-3599	159.61	South Africa	This study
L. murrayi	MHMUK PVR1291	160	South Africa	Botha 2020
L. maccaigi	NMQR 3641	160	South Africa	Botha 2020
China L. sp.	IVPP V10075	160.69	China	This study
L. declivis	NMQR 424	161.29	South Africa	Botha 2020
Lystrosaurus sp. indet.	SAM-PK-11166	161.68	South Africa	This study

L. declivis	SAM-PK-K8013	162.34	South Africa	This study
Lystrosaurus sp. indet.	SAM-PK-K10092	163.14	South Africa	This study
Lystrosaurus sp. indet.	BP/I/4339	163.82	South Africa	This study
China L. sp.	IVPP V18653	165.11	China	This study
China L. sp.	IVPP V18673	165.6	China	This study
L. declivis	NMQR 1866	165.72	South Africa	This study
L. hedini	IVPP V3248	165.75	China	This study
L. declivis	BP/I/4353	166.77	South Africa	This study
L. declivis	FARB 5600	169	South Africa	This study
L. hedini	IVPP RV35012	169.4	China	This study
L. murrayi	NMQR 3559	169.77	South Africa	This study
L. declivis	SAM-PK-K10379	169.78	South Africa	This study
Lystrosaurus sp. indet.	BP/I/5865	170.8	South Africa	This study
L.broomi	IVPP RV390600	170.92	China	This study
China L. sp.	IVPP V4457	171.52	China	This study
L. murrayi	NMQR 3540a	171.64	South Africa	Botha 2020
L. declivis	FARB 7725	172	South Africa	This study
L. declivis	TM 21	173	South Africa	Botha 2020
L. declivis	SAM-PK-K10377	174.62	South Africa	This study
L. declivis	BP/I/878	175.9	South Africa	This study
China L. sp.	XJ/ZAI	175.9	China	This study
Lystrosaurus sp. indet.	SAM-PK-K10	179.29	South Africa	This study
L. declivis	BP/I/2816	180.68	South Africa	This study
China L. sp.	IVPP V18670	184.95	China	This study
L. declivis	NMQR 1485	185	South Africa	Botha 2020
L. declivis	TM 3580	185	South Africa	Botha 2020
L. declivis	NMQR 3181	186.03	South Africa	This study
L. maccaigi	NMQR 3689	186.9	South Africa	Botha 2020
China L. sp.	IVPP 63005-2	187.79	China	This study
China L. sp.	IVPP V3244	189.33	China	This study
L. maccaigi	NMQR 3648	190	South Africa	Botha 2020
L. robustus	IVPP V3246	190.03	China	This study
L. hedini	IVPP V18659	192.9	China	This study
China L. sp.	630040L	193.19	China	This study
Lystrosaurus sp. indet.	BP/I/4717	194.35	South Africa	This study
China L. sp.	63002	194.71	China	This study
L. declivis	BP/1/1754	195.71	South Africa	Botha 2020
L. hedini	IVPP V13462	198.37	China	This study
L. declivis	BP/I/1754	199.43	South Africa	This study
L. murrayi	YPM 2225	200	South Africa	Botha 2020
L. declivis	SAM-PK-3593	203	South Africa	Botha 2020

L. declivis	SAM-PK-K8038	205.59	South Africa	This study
L. robustus	IVPP V3265	205.76	China	This study
L. declivis	SAM-PK-706	206.12	South Africa	This study
L. declivis	BP/I/4624	209	South Africa	This study
China L. sp.	SS-13-2-1	209.69	China	This study
L. hedini	IVPP V18660	209.81	China	This study
L. robustus	IVPP V3247	210.34	China	This study
L. murrayi	BP/1/3236	213	South Africa	Botha 2020
L. robustus	IVPP V3243	215	China	This study
L. hedini	IVPP V18672	218.59	China	This study
L. declivis	NMQR 4027	226	South Africa	Botha 2020
Lystrosaurus sp. indet.	SAM-PK-11234	266	South Africa	This study

Supplemental Table 2.3. Femoral length measurements collected or compiled for Triassic *Lystrosaurus* species.

Taxon	Specimen/ Field Number	Femur Length (mm)	Locality	Reference
L. sp.	19SS14	235	China	This study
L. sp.	19TS12	114	China	This study
L. sp.	19TS3	170	China	This study
L. sp.	19TS5	167	China	This study
L. murrayi	BP/1/4276 LL	66.07	South Africa	This study
L. murrayi	BP/1/4276 UR	103.11	South Africa	This study
L. murrayi	BP/1/4276 UR	103.82	South Africa	This study
L. sp.	BP/1/458	49.64	South Africa	This study
L. sp.	CAS19-4	123	China	This study
L. murrayi	ISIR756	53.77	India	Ray et al. 2005
L. murrayi	ISIR757	68.66	India	Ray et al. 2005
L. murrayi	ISIR758	36.77	India	Ray et al. 2005
L. murrayi	ISIR761	75.69	India	Ray et al. 2005
L. murrayi	ISIR764	90.3	India	Ray et al. 2005
L. murrayi	ISIR765	57.23	India	Ray et al. 2005
L. sp.	IVPP V26542	120	China	Han et al. 2021
L. sp.	IVPP V26543	125	China	Han et al. 2021
L. sp.	IVPP V26544	118	China	Han et al. 2021
L. sp.	IVPP V26545	180	China	Han et al. 2021
L. sp.	IVPP V26546	146	China	Han et al. 2021
L. sp.	IVPP V26547	151	China	Han et al. 2021
L. sp.	IVPP V26548a	192	China	This study
L. sp.	IVPP V27124-6	129	China	This study
L. sp.	IVPP V27124-7	122.38	China	This study

L. sp.	IVPP V27125a	182	China	This study
L. sp.	IVPP V27126a	162	China	This study
L. sp.	IVPP V27127	255	China	This study
L. sp.	NMQR 354	122.94	South Africa	This study
L. sp.	NMQR 3560	83.88	South Africa	This study
L. murrayi	NMQR 3581	103.1	South Africa	This study
L. murrayi	NMQR 3635	27.93	South Africa	This study
L. murrayi	NMQR 3655	34.97	South Africa	This study
L. murrayi	NMQR 3765	101.88	South Africa	This study
L. murrayi	NMQR 3765	103.2	South Africa	This study
L. murrayi	NMQR 3765	103.72	South Africa	This study
L. declivis	NMQR 4041a	96.52	South Africa	This study
L. declivis	NMQR 4041b	97.57	South Africa	This study
L. sp.	NMQR 758	84.32	South Africa	This study
L. hedini	RV35012	142.8	China	This study
L. hedini	RV35012	144.76	China	This study
L. declivis	SAM-PK-11184	115.05	South Africa	This study
L. sp.	SAM-PK-3530	124.96	South Africa	This study
L. murrayi	SAM-PK-8991a	98.16	South Africa	This study
L. murrayi	SAM-PK-8991b	92.72	South Africa	This study
L. murrayi	SAM-PK-K11535	74.58	South Africa	This study
L. sp.	SAM-PK-K1415	92.78	South Africa	This study
L. sp.	SAM-PK-K1415	95.71	South Africa	This study
L. declivis	SAM-PK-K8038	202.18	South Africa	This study
L. sp.	XJ12D	155	China	This study
L. sp.	XJ12L	127	China	This study

Chapter 3. A TEST OF BERGMANN'S RULE IN THE EARLY TRIASSIC: LATITUDE, BODY SIZE, AND SAMPLING IN *LYSTROSAURUS*

Kulik, Z. T., and C. A. Sidor (2022). A test of Bergmann's rule in the Early Triassic: Latitude, body size, and sampling in *Lystrosaurus*. *Paleobiology*, 1–15. https://doi.org/10.1017/pab.2022.25

3.1 ABSTRACT

The ecogeographical rule known as Bergmann's rule suggests that there is a positive relationship between body size and latitude when comparing closely related taxa. The underlying mechanism, or mechanisms, to explain this pattern vary as widely as the taxa that seem to follow it, which has led to skepticism over whether Bergmann's rule should be considered a rule at all. Despite this, Bergmann's rule is widespread among modern birds, mammals, beetles, and some amphibians, but far fewer extinct taxa have been subjected to tests of Bergmann's rule. To test whether Bergmann's rule is detected in extinct taxa, we compared body size proxies in *Lystrosaurus* recovered from Early Triassic-aged strata in Antarctica, South Africa, India, and China. Our results reveal that average body size is largest at mid-northern paleolatitudes (~45°N) instead of the highest southern paleolatitudes (~70°S). Additionally, maximum body size is consistent across northern and southern hemispheres, indicating that Bergmann's rule did not apply for *Lystrosaurus* during the Early Triassic. To test potential sample size biases in our results, we used rarefaction and subsampling to show that only the Karoo Basin is well sampled, and that large individuals are exceedingly rare except in the Turpan-Junggar Basin of Xinjiang, China. Taken together, our results suggest that *Lystrosaurus* had the potential to reach large body sizes in each of the latitudinally widespread tectonic basins studied here, but that local conditions may have allowed

individuals at mid-northern paleolatitudes a greater chance of reaching large size compared to southern congeners that suffered increased mortality at young/small sizes.

3.2 INTRODUCTION

Macroecological patterns in body size are well documented for a wide variety of extant taxa, including endotherms and ectotherms in terrestrial, freshwater, and marine habitats worldwide (Ashton et al. 2000; Belk and Houston 2002; Ashton 2002; Ashton and Feldman 2003; Chown and Gaston 2010; Berke et al. 2013; Angielczyk et al. 2015; Gohli and Voje 2016; Blackburn et al. 2019). Of these, the most commonly observed pattern is Bergmann's rule, after Carl Bergmann, who described a relationship where larger body sizes are seen in species that live in colder climates compared to their smaller-bodied relatives that live in warmer climates (1847; see translation by James 1970). Because the definition of the rule is itself a reformulated translation that has since been reinterpreted by various authors (e.g., Rensch 1938; Mayr 1963; James 1970; Blackburn et al. 1999; Salewski and Watt 2017) and because no underlying mechanism is as widespread as the taxa that seem to follow it, the validity of Bergmann's rule has long been debated (Mayr 1956; McNab 1971; Blackburn et al. 1999; Ashton et al. 2000; Meiri and Dayan 2003; Meiri et al. 2007; Watt et al. 2010; McNab 2010; Salewski and Watt 2017). The classical interpretation of Bergmann's rule is that larger endothermic animals withstand cold temperatures better by having a reduced surface to volume ratio (James 1970). However, many studies have used definitions of Bergmann's rule that do not include a specific physiological mechanism or indeed any explicit underlying process: namely, that body size is positively correlated with latitude (Blackburn and Gaston 1996; Blackburn and Ruggiero 2001; Ashton 2002; Montgomery et al. 2003; Meiri et al. 2004).

Size-latitude relationships are a common test of Bergmann's rule, as climate is assumed to be colder at higher latitudes, although this correlation may be weak at small scales (Mayr 1963; Blackburn et al. 1999) or absent during times in Earth history with reduced temperature gradients from equator to poles. Importantly, latitude does not affect body size directly but is likely to correlate with body size clines because it encompasses more precise predictive variables that fluctuate over temporal and spatial scales to affect body size (reviewed in Yom-Tov and Geffen 2011). Indeed, body size has been shown to vary in response to precipitation (Nwaogu et al. 2018), elevation (Feder et al. 1982; Yu et al. 2019), water depth (Timofeev 2001), seasonality (James 1970; Murphy 1985; Wells et al. 2019), geographic range size (Ashton et al. 2000; Rodriguez et al. 2018), resource availability (McNab 2010; Correll et al. 2016; Brown et al. 2017; Kelly et al. 2018), functional traits (Briscoe et al. 2015), or predation risk and prey size (McNab 1971), with only some correlations supporting a Bergmann-like pattern (e.g., Murphy 1985; Ashton et al. 2000; Timofeev 2001; Briscoe et al. 2015; Correll et al. 2016; Nwaogu et al. 2018; Rodriguez et al. 2018; Yu et al. 2019).

Tests for Bergmann's rule at different taxonomic scales can also give different results, with interspecific analyses obscuring intraspecific patterns that may be better explained by the specific variables mentioned above, rather than latitude alone (e.g., Ashton et al. 2000; Freckleton et al. 2003; Gohli and Voje 2016; Pallarés et al. 2019; Romano et al. 2021). Nonetheless, modern birds, mammals, and salamanders generally show support for Bergmann's rule when average body sizes of numerous species are compared across a wide latitudinal range (mammals: Ashton et al. 2000; Meiri et al. 2004; birds: Blackburn and Gaston 1996; salamanders: Ashton 2002). Modern turtles and frogs also follow a Bergmann-like pattern, although species sampling is comparatively scarce (Ashton 2002; Ashton and Feldman 2003).

Extant squamates tend to show the converse of Bergmann's rule, that body size decreases in colder climates (Ashton and Feldman 2003), however, others argue that no spatial pattern in body size is seen (Pincheira-Donoso and Meiri 2013; Slavenko et al. 2019). Interestingly, many more taxa should follow Bergmann's rule, according to estimates using ancestral state reconstructions among major tetrapod groups (de Queiroz and Ashton 2004). This provocative result may imply that the tendency to develop Bergmann-like clines is a shared pattern that is deeply nested in the evolutionary history of endothermic and ectothermic tetrapods (de Queiroz and Ashton 2004).

3.2.1 *Bergmann's rule in the Fossil Record*

While Bergmann's rule is certainly widespread among extant taxa, comparatively few investigations have looked for similar results in the fossil record. Pterosaurs show the converse of Bergmann's rule during the Cretaceous and do not follow size-latitude clines during the Triassic–Jurassic (Villabolos et al. 2017). Bivalve size distributions remain remarkably consistent across a global latitudinal distribution during the Miocene–Recent (Roy et al. 2000). Similar investigations that focus on comparisons between extant and extinct members of the same clade within the same latitudinal region approximate tests for Bergmann's rule from a climatically driven standpoint but do not test for size-latitude patterns outright. For example, comparisons between Eocene–Recent Antarctic penguins, Pleistocene–Recent coyotes across North America, and equids, canids, and sciurids from the Oligo-Miocene of the northwest United States test for climate-driven patterns in body size (Jadwiszczak 2001; Orcutt and Hopkins 2013; Meachen et al. 2014). These studies, while not a direct comparison of latitudinally-driven changes in body size, indicate that penguin average body size tends to be larger in extinct taxa

but that the underlying mechanism may be due to an adaptive radiation rather than warmer climates (Jadwiszczak 2001). Body size trends are highly variable among North American mammals studied thus far, with coyotes showing a decrease from larger than Recent average size across the Pleistocene/Holocene boundary, perhaps due to species interactions and niche partitioning (Meachen et al. 2014). Equid, canid, and sciurid body size variation during the Oligo–Miocene show no consistent relationship with climate variables, nor were trends similar between orders (Orcutt and Hopkins 2013). Taken together, investigations into the potential drivers of body size patterns in the fossil record have yielded highly variable results. For the few taxa that have been studied during the Cenozoic, inferred climate variables do not have significant relationships to body size variation, counter to what has been shown in modern ecosystems. Indeed, times in Earth history with a decreased temperature gradient from equator-to-pole may have removed key factors underlying Bergmann's rule. One extreme example of this is the earliest Triassic, where elevated CO_2 levels, globally high sea level, and ice-free polar regions intensified global climate extremes across the supercontinent of Pangea (Kidder and Worsley 2004; Winguth et al. 2015; Mancuso et al. 2021).

A prime candidate for a test of Bergmann's rule in the fossil record is *Lystrosaurus*, a non-mammalian synapsid that survived the end-Permian mass extinction and rose to remarkable abundance across much of Pangea during the Early Triassic (King, 1990; Grine et al. 2006). Indeed, *Lystrosaurus* is exceptional among fossil tetrapods because it is a globally distributed genus known from a relatively short time interval (~3 MY). Fossils of *Lystrosaurus* have been recovered in Early Triassic-aged strata in South Africa, Antarctica, Mongolia, Russia, China, India, and possibly Australia and Mozambique (e.g., Tripathi and Puri 1961; Colbert 1974; Sun 1980; Thulborn 1990; Gubin and Sinitza 1993; Liu et al. 2002; Ray 2005; Botha and Smith

2007; Araujo et al. 2017; Viglietti et al. 2021) (Fig. 1). Besides a near-global distribution, *Lystrosaurus* is also remarkably abundant, especially in South Africa, where over 2500 specimens are cataloged into museum collections (Smith et al. 2012).

Here, we examine whether body size proxies vary predictably with paleolatitude in Triassic species of *Lystrosaurus*. Our sample includes nearly 500 specimens recovered from four tectonic basins that span a range of paleolatitudes from approximately 73–55° S and ~45° N (van Hinsbergen et al. 2015; Yang et al. 2021) (Fig. 1). This sample spans the entirety of all known Early Triassic-aged deposits but unfortunately *Lystrosaurus*-bearing strata from equatorial regions are lacking. If *Lystrosaurus* followed a size-latitude pattern consistent with Bergmann's rule, the largest specimens would be expected from the highest southern paleolatitudes (i.e., the Transantarctic Basin of Antarctica). If some other body size cline is detected, this could indicate that *Lystrosaurus* is an exception to the rule, along with modern lizards and snakes. If, however, no size-latitude pattern is detected, sampling inconsistencies between Early Triassic tectonic basins could play a role in overprinting potential patterns. Finally, a failure to detect body size clines in *Lystrosaurus* could also imply a previously unrecognized macroevolutionary consequence of climatic warming.

3.3 Data Collection and Analysis

3.3.1 *Distribution of* **Lystrosaurus** *Species Across Pangea*

Lystrosaurus is found in Early Triassic-aged strata on every continent except North and South America (Tripathi and Puri 1961; Colbert 1974; Sun 1980; Thulborn 1990; Gubin and Sinitza 1993; Liu et al. 2002; Ray 2005; Botha and Smith 2007; Araujo et al. 2017; Viglietti et al. 2021). Species-specific distributions are more clearly defined from southern Pangean deposits

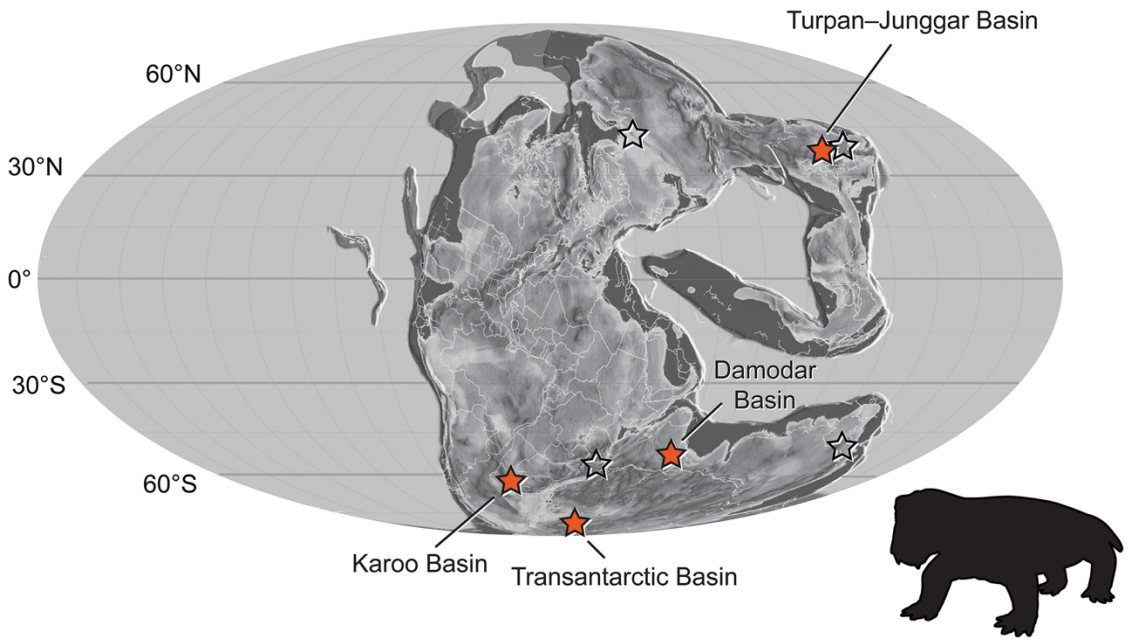

Figure 3.1. Geographic distribution of *Lystrosaurus* fossils sampled. Paleogeographic map of the Early Triassic with estimated locations of tectonic basins denoted by stars, sampled localities are highlighted in orange, unsampled localities are transparent. Paleomap modified from Scotese (2016). *Lystrosaurus* silhouette from Phylopic.org.

where the most recent systematic appraisal of *Lystrosaurus* recognized four valid species in South Africa: *Lystrosaurus maccaigi*, *L. curvatus*, *L. murrayi*, and *L. declivis* (Grine et al. 2006). These four species have been used in numerous studies since (e.g., Botha and Smith, 2007; Botha-Brink et al., 2016; Botha 2020). All four species occur in varying abundances across southern Pangea except for *L. maccaigi* which is only found in South Africa and Antarctica (Colbert 1974; Peecook et al. 2019), and *L. declivis* which is currently only recognized from South Africa and India (Gupta and Das 2011).

Within the Karoo Basin of South Africa, *Lystrosaurus curvatus* is the rarest species followed by *L. maccaigi*. These species are locally considered Permian taxa but likely survived during the extinction interval based on in situ specimens found in strata within the lithologic boundary of the vertebrate-defined Permo-Triassic boundary (Botha-Brink et al. 2014; Viglietti et al. 2021). Additionally, *L. maccaigi* and *L. curvatus* are found in the lower Fremouw Formation of Antarctica, indicating that these species persisted at higher latitudes in the Early Triassic (Colbert 1974; Collinson et al. 2006; Peecook et al. 2019).

In contrast to the sparse occurrences of *L. maccaigi and L. curvatus*, thousands of specimens of *L. murrayi* and *L. declivis* have been recovered from the lowermost Triassic of the Karoo Basin, the more abundant *L. declivis* giving name to the assemblage zone that typifies the faunal assemblage immediately after the end-Permian mass extinction (Botha and Smith 2020). *Lystrosaurus murrayi* is also known in Antarctica and India (Peecook et al. 2019; Colbert 1974; Ray 2005). Two specimens referred to *L. curvatus* and one to *L. declivis* have also been recovered from the Panchet Formation in the Damodar Basin of India, further suggesting the cosmopolitan distribution of all four species across southern Pangea (Gupta and Das 2011).

In the greater Turpan-Junggar Basin of Xinjiang, China, numerous species of *Lystrosaurus* have been described, including *L. youngi, L. robustus*, *L. latifrons,* and *L. hedini,* which has also been found in Mongolia (Gubin and Sinitza 1993; Sun 1964, 1973; Young 1939; Yuan and Young 1934; Liu et al. 2002). Cosgriff et al. (1982) suggested that some of the northern Pangean forms were likely synonymous with *Lystrosaurus murrayi*. More recently, work by Camp (2010) and Kulik et al. (2021), has shown that Chinese specimens have significantly different cranial morphologies compared to South African specimens. Therefore, it is unlikely that northern Pangean species are synonymous with southern species. Furthermore, is it not currently possible to provide a reliable taxonomic assignment to Chinese specimens as additional work is needed to clarify the number of valid taxa there, as well as in Russia (Surkov et al. 2005). For our analysis, we refer to all species recovered from China as *Lystrosaurus sp.*

3.3.2 ***Body Size Proxies***

We gathered cranial measurements from 482 skulls in order to compare body size proxies from Early Triassic specimens of *Lystrosaurus*. Nine specimens were from the Transantarctic Basin of Antarctica, 411 were from the Karoo Basin of South Africa, 27 were from the Damodar Basin of India, and 35 were from the Turpan-Junggar Basin of China (see supplement for associated data). Specimens were selected to best represent the maximum distribution of *Lystrosaurus* skull size from all known Early Triassic localities. Paleolatitude was estimated from tectonic plate reconstructions made available through the online calculator www.paleolatitude.org developed by van Hinsbergen et al. (2015) and range from approximately 73°–55° S and ~45° N (van Hinsbergen et al. 2015; Yang et al. 2021). These ranges were reconstructed from the basins preserving Early Triassic *Lystrosaurus*, but importantly lack

records from low paleolatitudes (Romano et al. 2020). Indeed, the Triassic terrestrial fossil record is exceedingly sparse from low paleolatitudes, which complicates our understanding of Pangean species distributions but does not preclude an assessment of body sizes at high-southern and mid-northern paleolatitudes.

We selected cranial measurements that were easily identifiable, reproducible, and most often free of encasing matrix (i.e., the interorbital region and snout are often prepared because they provide taxonomically informative details for species-level identification). As shown in Figure 3.2, these include: (1) basal skull length, as measured from the anterior extremity of the snout to the occipital condyle, (2) minimum interorbital width, and (3) tusk diameter at its point of eruption from the maxilla (averaged when both tusks could be measured). When skulls were not sufficiently prepared or were incomplete, we measured the dorsal snout length, as a midline horizontal line from the anterior-most point of the parietal foramen to the anterior extent of the premaxilla, and/or dorsal skull length, as a midline horizontal line from the anterior extent of the premaxilla to the posterior end of the parietal. Linear regressions were computed based on complete and prepared specimens of the four southern Pangean species to estimate basal skull length in specimens that were incomplete or not completely prepared. Skulls that were crushed, distorted, or too fragmentary were excluded from our analysis.

Measurements were taken using Mitutoyo digital calipers (±0.02mm) at the following institutions: American Museum of Natural History, New York, USA; Evolutionary Studies Institute, (formerly Bernard Price Institute for Paleontological Research), University of the Witwatersrand, Johannesburg, South Africa; The Field Museum of Natural History, Chicago, Illinois, USA; Institute of Vertebrate Paleontology and Paleoanthropology, Chinese Academy of Sciences, Beijing, China; National Museum, Bloemfontein, South Africa; Iziko, The South

African Museum, Cape Town, South Africa. Measurement data were also compiled from a survey of the literature (Ray 2005; Botha 2020; Gupta and Das 2011; see supplemental data). All subsequent data manipulations and visualizations were carried out in R (2022.02.0).

3.3.3 ***Testing for Bergmann's rule***

We assessed whether *Lystrosaurus* body size proxies varied with paleolatitude by comparing average basal skull length and average tusk diameter between interspecific samples binned into the four tectonic basins included in our study (Fig. 3). Interspecific averages could be influenced by species-specific body size distributions in *Lystrosaurus*, particularly because each species overlaps in its body size range with at least one other species. For example, *Lystrosaurus murrayi* has a maximum known size of 21.3 cm (BP/1/ 3236) whereas *L. curvatus* has a maximum known size of 20 cm (BP/1/ 3976). To account for species specific differences in body size, we standardized basal skull length and tusk diameter as a proportion of the maximum known size per species. We treated the unidentified southern Pangean specimens as a unique species (*Lystrosaurus sp. indet.*) which corresponds to a grouping of small skulls that are most likely unidentifiable to the species level because they lack developed diagnostic features. Similarly, we treated Chinese *L. sp.* as a separate species and computed proportional skull and tusk size accordingly.

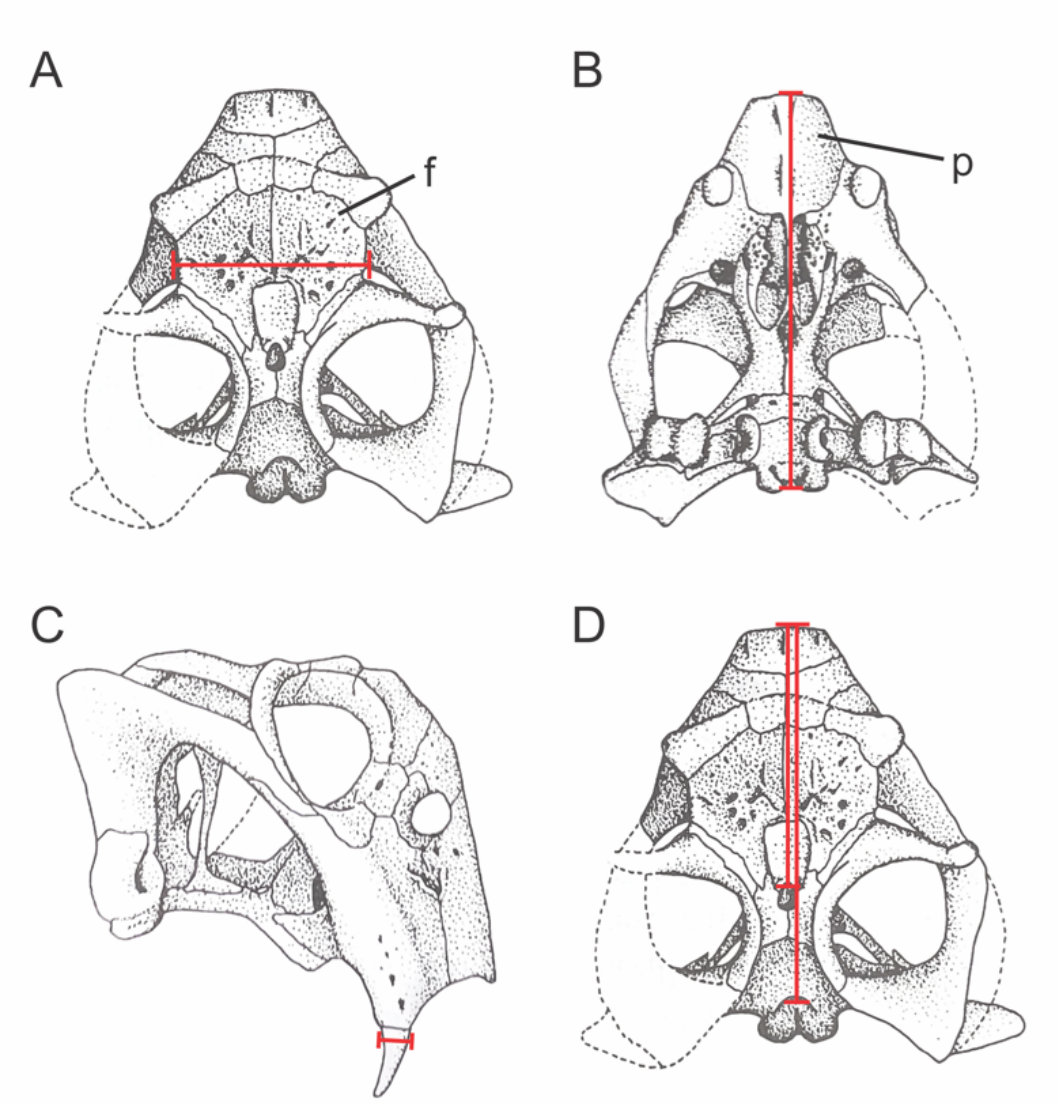

Figure 3.2. Cranial measurements used to estimate body size in *Lystrosaurus*. **A**, minimum interorbital width. **B**, basal skull length. **C**, tusk diameter at eruption. **D**, dorsal snout length and dorsal skull length were measured from incompletely prepared or broken specimens. Abbreviations: f, frontal; pm, premaxilla. Skull drawings adapted from King (1990).

3.4 RESULTS

Considering both raw and standardized body size across tectonic basins, *Lystrosaurus* body size proxies do not vary with paleolatitude in a pattern that is consistent with Bergmann's rule (Fig. 3). The largest average skull and tusk sizes are from *Lystrosaurus* specimens from the Turpan-Junggar Basin, which have an estimated paleolatitude of ~45° N (Yang et al. 2021). Indeed, average basal skull length and tusk diameter are between 16–17% larger in the Turpan-Junggar Basin compared to southern congeners. However, when only the tectonic basins in the southern hemisphere are considered, average skull and tusk size increase towards the pole (Fig. 3). These results, however, are not statistically significant at high paleolatitudes between the Karoo (~55–65°S) and Transantarctic Basin (~65–70°S) ($t = 0.87124$, $df = 8.0759$, $p = 0.4088$). Interestingly, mean tusk diameter and basal skull length are significantly smaller in the Damodar Basin when compared to the Karoo dataset (tusk: $t = -8.4281$, $df = 37.01$, $p < 0.05$; skull: $t = -7.0031$, $df = 37.384$, $p < 0.05$).

From these results, it could be possible that intraspecific differences in maximum size could be driving the pattern of large specimens (i.e., large species) in high southern paleolatitudes. To address this, we compared species-specific average body size across southern Pangean tectonic basins and show that Bergmann's rule is not detected (Fig. 3.4). Median body size remains constant across southern Pangean species, except for large *Lystrosaurus maccaigi* from the Transantarctic basin, which are much larger than the median size from the Karoo basin. However, maximum size is remarkably similar across both basins. Indeed, interspecific maximum size is comparable across the Transantarctic, Karoo, and Turpan-Junggar basins (between 22-28 cm) indicating that *Lystrosaurus* species in both the northern and southern

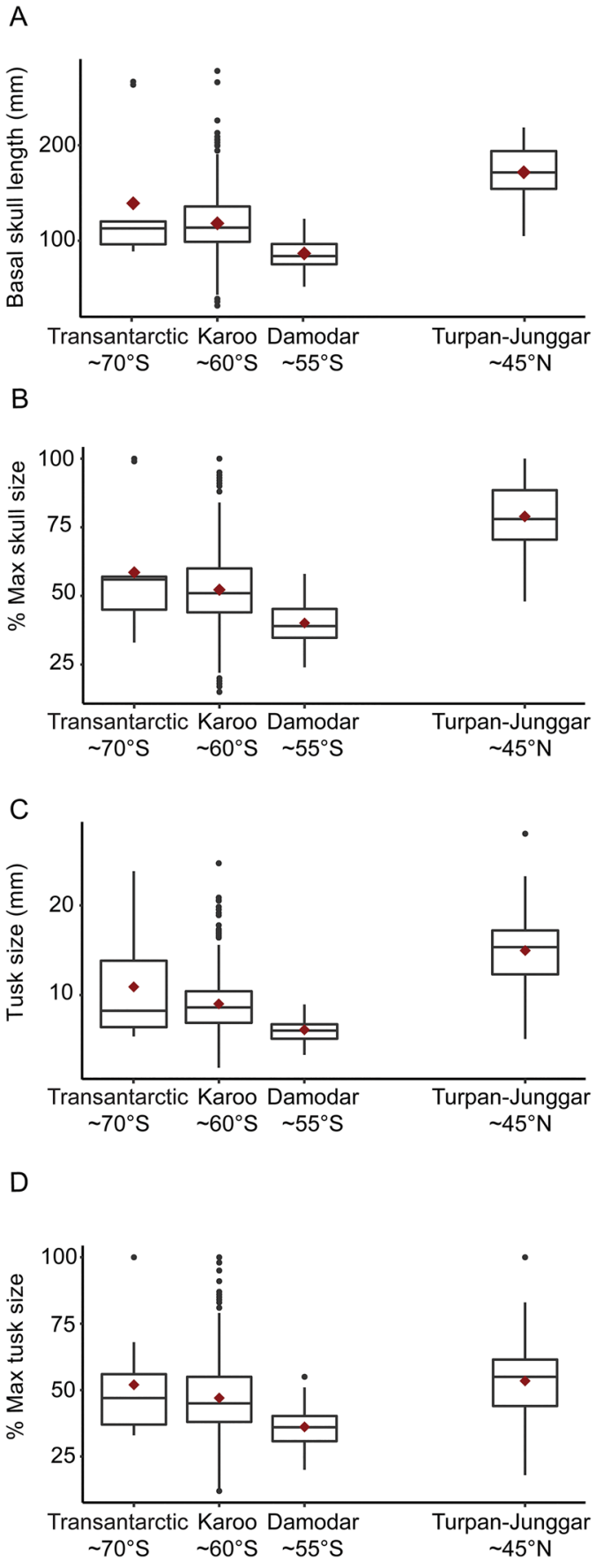
A
Basal skull length (mm)
200
100
Transantarctic ~70°S
Karoo ~60°S
Damodar ~55°S
Turpan-Junggar ~45°N
B
% Max skull size
100
75
50
25
Transantarctic ~70°S
Karoo ~60°S
Damodar ~55°S
Turpan-Junggar ~45°N
C
Tusk size (mm)
20
10
Transantarctic ~70°S
Karoo ~60°S
Damodar ~55°S
Turpan-Junggar ~45°N
D
% Max tusk size
100
75
50
25
Transantarctic ~70°S
Karoo ~60°S
Damodar ~55°S
Turpan-Junggar ~45°N

Figure 3.3. Plots comparing *Lystrosaurus* size and geographic position using: **A**, basal skull length; **B**, standardized basal skull length as a percent of maximum size; **C**, tusk diameter; **D**, standardized tusk diameter. *Lystrosaurus* does not follow a pattern that is consistent with Bergmann's rule. Skull size is significantly larger in the mid-latitude Turpan-Junggar Basin, as well as between the Karoo and Damodar Basin. Red diamonds and gray bars indicate the mean and median values, respectively.

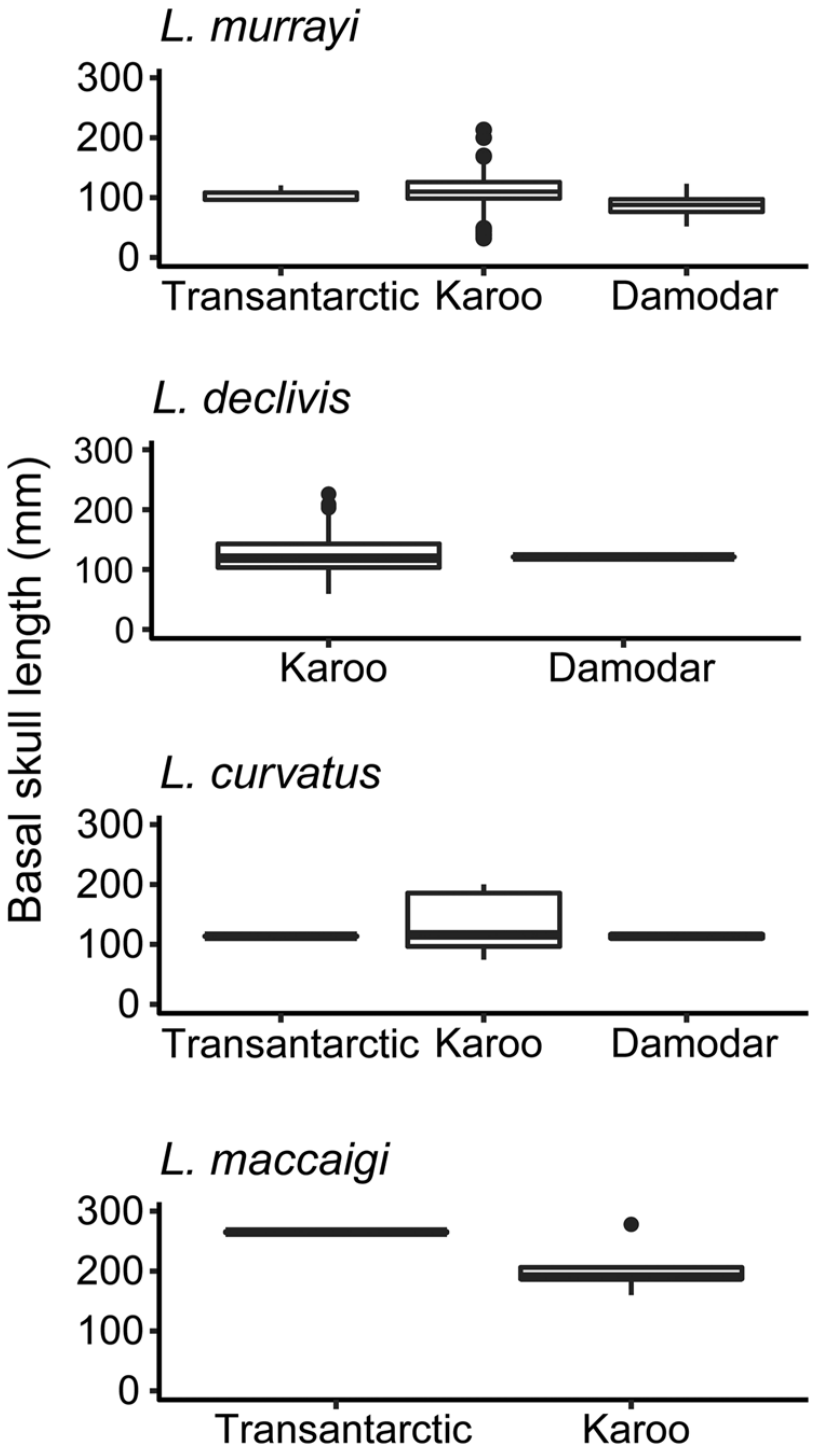
L. murrayi
300
200
100
0
Transantarctic
Karoo
Damodar
L. declivis
Basal skull length (mm)
300
200
100
0
Karoo
Damodar
L. curvatus
300
200
100
0
Transantarctic
Karoo
Damodar
L. maccaigi
300
200
100
0
Transantarctic
Karoo

Figure 3.4. Plots comparing skull length in four species of *Lystrosaurus* against geographic position. At the species level, median body size remains constant between Triassic basins, except for *Lystrosaurus maccaigi*, note that the outlier from the Karoo Basin is approximately the same size as the individuals from the Transantarctic Basin.

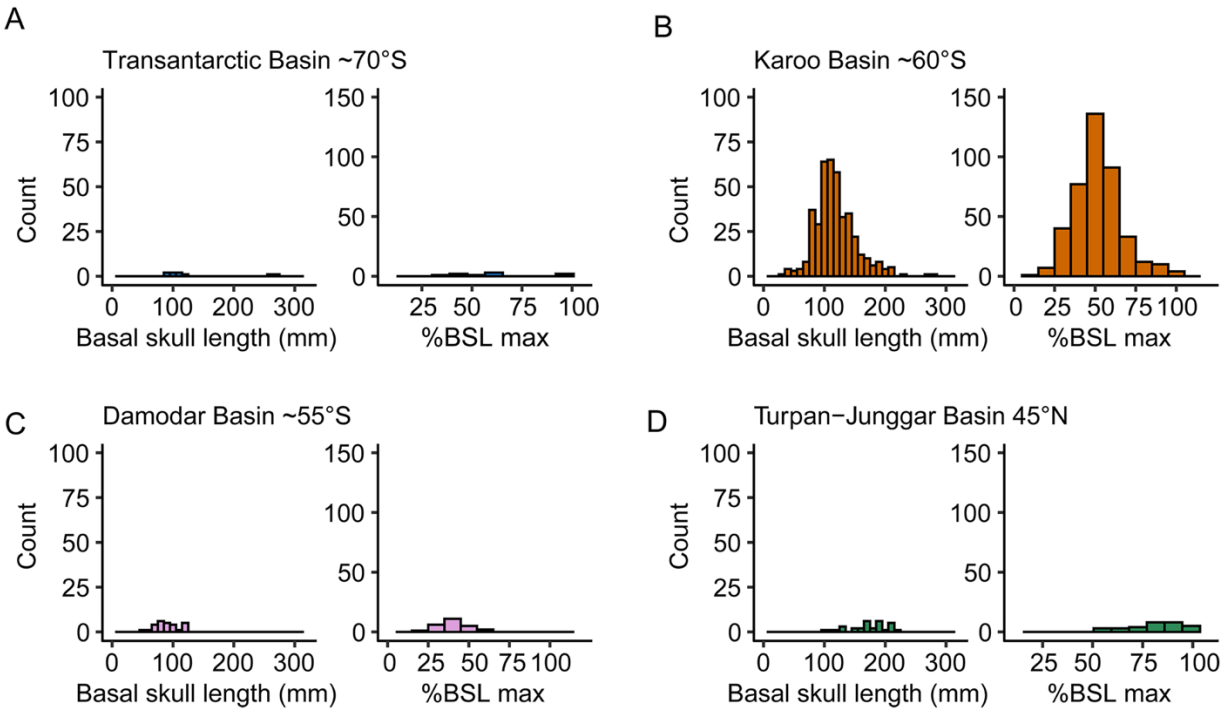

Figure 3.5. Distributions of skull size of *Lystrosaurus* collected from four geographic areas. **A**, interspecific *Lystrosaurus* skull size and proportional skull size in the Transantarctic Basin. **B**, normally distributed skull size in the Karoo Basin; **C**, right-skewed distribution in the Damodar Basin, and **D**, left-skewed in the Turpan-Junggar Basin when basal skull length is standardized as a proportion of the maximum known size per species.

hemispheres could reach similar large sizes (Figs. 3, 5). However, the frequency of large *Lystrosaurus* specimens is highest in the northern hemisphere, as most sampled individuals are larger than ~50% maximum known size (Fig. 3.5). This is in contrast to the Karoo Basin where the highest frequency of skulls is less than 50% maximum known size. Importantly, the Karoo Basin dataset is an order of magnitude larger than those of the other basins which prompts us to consider the effects that different sample sizes have on average body size in *Lystrosaurus*.

3.4.1 *Assessing Sampling Bias Through Resampling*

Despite being one of the most abundant terrestrial fossils found in Early-Triassic-aged strata, substantial differences exist in the number of *Lystrosaurus* specimens recovered outside of the Karoo Basin. To assess how different sample sizes could be affecting our results, we subsampled the Karoo Basin dataset to the size of the other basins, respectively. We then tested for statistically significant differences between the down-sampled Karoo dataset and the remaining datasets from the other tectonic basins. In addition, we also calculated the probability of recovering the largest known skull when the Karoo dataset was down-sampled to further demonstrate the rarity of large sizes known from the Karoo Basin. We found that there is a 7% probability of recovering the maximum known skull size when the Karoo Basin dataset is reduced to the sample size of the Damodar or Turpan-Junggar basins and only a 2% probability of recovering the largest individual when the Karoo is down-sampled to the size of the Transantarctic Basin. We then tested whether average body size proxies (i.e., basal skull length and tusk diameter) were significantly different between the down-sampled Karoo dataset and the datasets from other tectonic basins using Welch's t-test of unequal variance. Average skull and

tusk size were similarly not significantly larger between the Transantarctic Basin and down-sampled Karoo Basin (t = -0.89094, df = 8.0035, p = 0.399), consistent with the raw and standardized results reported above. In addition, body size proxies from the Damodar Basin remained significantly smaller when compared to the down-sampled Karoo dataset (t = 7.5418, df = 26.176, $p > 0.05$). These results indicate a significant difference in body size between basins at relatively high southern paleolatitudes (~50–65° S) but not between these basins and the most poleward sample in our dataset, which is not consistent with the predictions of Bergmann's rule. However, comparisons between down-sampled results remove much of the available data. Therefore, we employed rarefaction methods to extrapolate body size abundance at larger sample sizes.

3.4.2 *Assessing Sampling Bias Using Rarefaction*

To test the effects that different sample size had on body size distributions without reducing sample sizes to the smallest dataset in our results, we employed rarefaction methods originally developed to assess species diversity from unequal sample sizes. This provides a new approach to estimate whether body sizes are likely to remain large if more specimens are recovered from the Turpan-Junggar Basin, or conversely, specimens are likely to remain small if more are recovered from the Damodar Basin. To investigate whether body size distributions are likely to remain consistent when sample sizes are increased, diversity metrics (i.e., richness, Shannon diversity, and Simpson diversity) were used to calculate rarefaction curves using the R-package iNEXT (Hsieh et al. 2016). This method was originally developed to extrapolate species diversity from unequal sample sizes and is preferred over traditional rarefaction methods because it does not reduce sample sizes. Importantly, diversity metric calculations are iterated over

numerous sample sizes and are typically reliable to twice that of the reference sample (Jost 2012). Unfortunately, this does not allow comparisons between equal sample sizes in our dataset as the doubled Transantarctic Basin sample size is less than the reference sample size of the remaining datasets.

In our application of these rarefaction metrics, rather than thinking of richness as a measure of the number of species within a population, we treat it as the number of individuals at a given size class within a population. With this in mind, we made the following adjustments to our data. First, we binned *Lystrosaurus* skull sizes into 25 size classes using 10 mm increments, from 21–270 mm. Next, we calculated the interspecific abundances of each size class within each basin. This allowed us to compare body size abundance between basins, analogous to traditional diversity metrics that compare species abundances between sites. Our goal was to be able to determine whether each tectonic basin had reached its asymptote in the number of body size classes filled.

Sample-size based rarefaction curves estimates the number of body size classes that would be filled if larger sample sizes were collected. Our results indicate that skull sizes do not readily span the full range of sizes known for *Lystrosaurus* in any of the four basins studied here (Fig. 3.6). Of the 25 size classes generated by *Lystrosaurus* skull size, none of the richness estimates reach the expected asymptote (Fig. 3.6). The Karoo Basin comes closest to the asymptote with 21 size classes filled in the reference sample. In the remaining basins, only a small portion of size classes are filled in the reference and extrapolated sample, indicating that sampling is sparse overall. The wide confidence intervals in the rarefaction curves for the Damodar and Transantarctic basins further indicate that small sample size is skewing the

distribution of body sizes in those basins (Fig. 3.6). The current sample also makes it impossible to extrapolate what sample size is needed for the asymptotes to be reached.

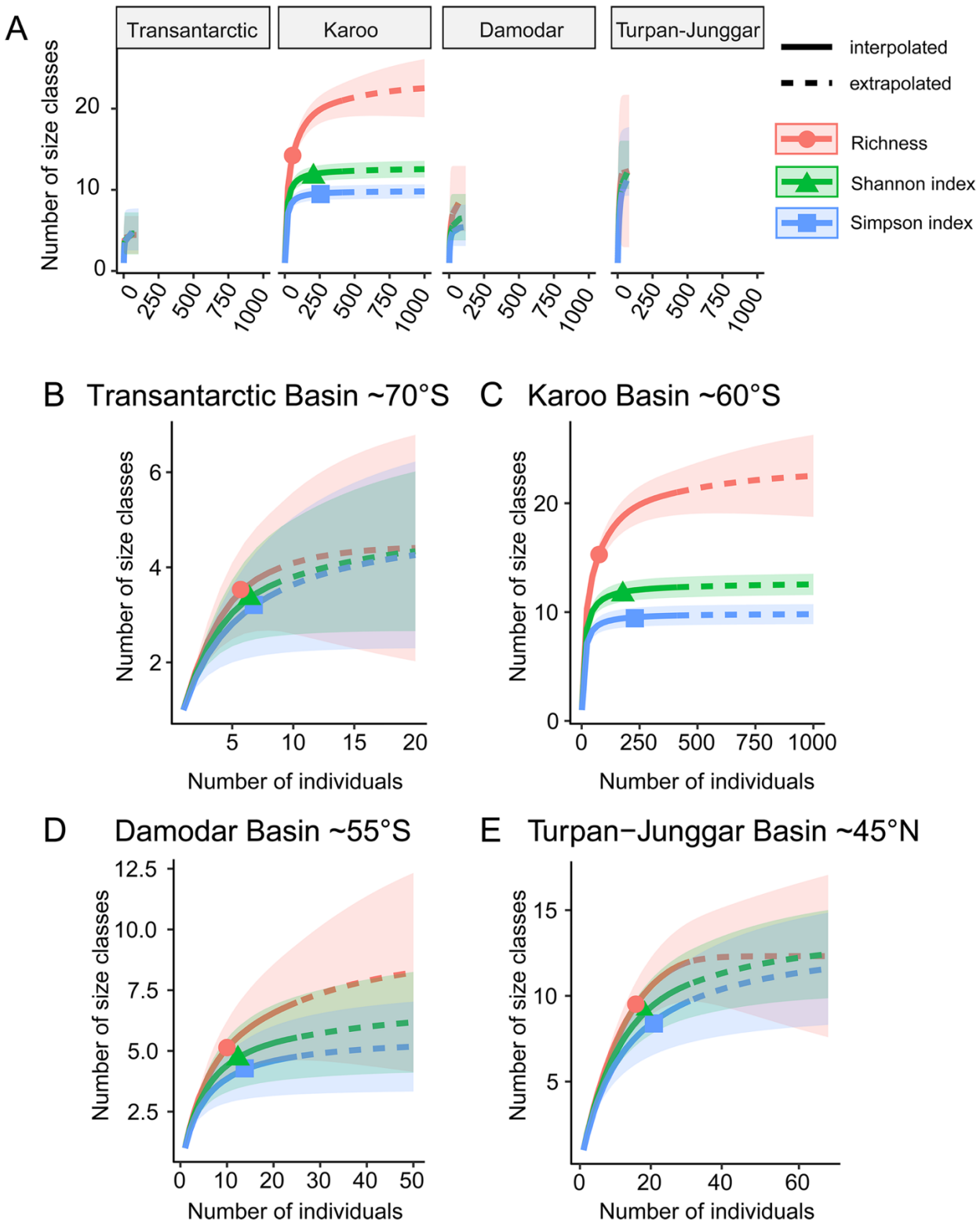
A
Transantarctic
Karoo
Damodar
Turpan-Junggar
Number of size classes
interpolated
extrapolated
Richness
Shannon index
Simpson index
B Transantarctic Basin ~70°S
C Karoo Basin ~60°S
D Damodar Basin ~55°S
E Turpan−Junggar Basin ~45°N
Number of individuals

Figure 3.6. Plots comparing rarefaction curves estimating the number of body size categories that are filled by fossil specimens in each tectonic basin studied here. **A**, summary of rarefaction curves for each basin, scaled to extrapolate twice that of the reference sample. **B**–**E**, rarefaction curves for each tectonic basin. Sample-size based rarefaction curves indicate that all *Lystrosaurus* specimens collected from Early Triassic tectonic basins fail to capture the total expected diversity of *Lystrosaurus* body sizes. In **A**–**E**, the solid lines represent the total number of size classes that are filled by at least one individual in the reference sample, and the extrapolated dotted line shows how many additional size classes would be filled at larger sample sizes with 95% confidence intervals. Note that extrapolated sample sizes are scaled based on the size of the reference sample. Colored lines indicate the diversity metric as either richness (red), Shannon diversity index (green), or Simpson diversity index (blue).

With so many size classes left empty in our data, we cannot reliably estimate body size distributions at larger sample sizes. Instead, we can compare the frequency and skew of body sizes from the four tectonic basins (Fig. 3.5) and rarefaction curves (Fig. 3.6), to see that specimens recovered from the Transantarctic Basin are either large or quite small, whereas specimens from the Damodar Basin tend to be small, and in the Turpan-Junggar Basin, specimens are quite large. Taken together, our results indicate that additional sampling efforts outside of the Karoo Basin will improve the accuracy of average body size estimates within each basin as well as the accuracy of what sample size is needed to reach rarefied asymptotes of body size abundances. Furthermore, our resampling and rarefaction results indicate that average body size estimates are likely to change with the addition of new specimens outside the Karoo Basin, but that maximum body size estimates are less likely to change, as maximum known skull size is comparable across northern and southern tectonic basins, regardless of paleolatitude. These results imply that Bergmann's rule did not apply for *Lystrosaurus* during the Early Triassic.

3.5 DISCUSSION

The myriad drivers suggested to underly Bergmann's rule in modern ecosystems makes it difficult to narrow down mechanisms that could have affected body size distributions and body size clines in *Lystrosaurus* in the fossil record. In addition to sample size differences, local environmental differences within each tectonic basin could explain why body size distributions are left or right skewed which can influence body size clines more broadly. Furthermore, physiological interpretations and thermal tolerances inferred for *Lystrosaurus* could also help to explain the potential trend of large body size in southern polar regions. As outlined below, we consider these potential drivers of *Lystrosaurus* body size clines and discuss some of the unique considerations of size-latitude assessments in the fossil record.

There is considerable debate on the environmental conditions inferred during the Permian-Triassic (Tabor et al. 2017; Li et al. 2017; Thomas et al. 2011; Yang et al. 2021). This complicates tests for Bergmann's rule using specific environmental indicators. Seasonally dry, subhumid to semiarid conditions have been inferred for the mid-Induan lower Olenekian Jiucaiyuan Formation in the Turpan-Junngar Basin (Yang et al. 2021). Seasonally dry conditions are132ivaled during the extinction interval in the Karoo Basin, however, aridity estimates are highly variable (e.g., Smith and Botha-Brink, 2014; Tabor et al. 2017, Li et al. 2017). Despite differing reports for environmental conditions in the Karoo Basin, ecosystem instability is widespread across Pangea and began in the latest Permian and continued into the Early Triassic. For example, macrofloral fossils indicate increased environmental stress in the *Glossopteris* forests of Antarctica (Gulbranson et al. 2021) and fossilized charcoal shows evidence of wildfires in northwestern China (Wan et al. 2021).

Considering the disturbed and highly turbulent ecosystems of the Earliest Triassic, local environmental conditions within each tectonic basin could have provided different resources for *Lystrosaurus* to exploit, which could explain why similar maximum sizes are observed across assemblages in the northern and southern hemisphere, as well as the highest frequency of large individuals in subhumid to semiarid environments inferred for the Turpan-Junggar Basin (Yang et al. 2021). This interpretation is consistent with McNab's (2010) resource rule, which predicts that the quality and availability of resources will have a stronger effect on body size clines than latitude or temperature. It follows that temperature and climate dictate resource availability and primary productivity (McNab 2010). Since paleoclimates are inferred to be more favorable and therefore could have provided increased food availability for *Lystrosaurus* in the Turpan-Junggar Basin, we might expect to find additional large individuals with renewed sampling in this area.

The presence of large individuals in Antarctica during the Early Triassic might also be explained by more favorable environments outside of the Karoo and Damodar basins, but specific climate estimates are limited.

An important consideration in climate and resource-related influences on body size is the physiology inferred for *Lystrosaurus*. A heterothermic endothermic physiology has been suggested based on histological analyses of hard tissues (Botha 2020; Whitney and Sidor 2020; Kulik et al. 2021; Han et al. 2021). This flexible physiology could have allowed *Lystrosaurus* to weather extreme ecosystem instability, combined with its broad habitat and thermal tolerances (Retallack et al. 2003; Liu et al. 2021), burrowing lifestyle (Botha-Brink 2017), and inferred generalist diet of tough plant material (e.g., Jasinoski et al. 2009, Jasinoski et al. 2014). Histological evidence from the long bones of specimens from South Africa, India, and China indicate that none of the sampled individuals had reached skeletal maturity at death (Botha 2020; Kulik et al. 2021). Further, the intrinsically high rate of growth inferred from the bone tissue composition indicates that *Lystrosaurus* had the ability to reach large size and did so in the Turpan-Junggar Basin (Kulik et al. 2021), but that southern hemisphere assemblages suffered increased mortality at young/small sizes in the Karoo and Damodar basins (Botha 2020).

As demonstrated in our results, differences in sample size also affects estimates of average body size between tectonic basins. The relative abundance of large bodied *Lystrosaurus* from China could reflect more favorable environmental conditions in the Turpan-Junggar Basin during the Early Triassic. However, we might expect the right-skewed body size distribution to change to a normal distribution when more specimens are recovered (Fig. 3.5). This is also true for the Transantarctic Basin, which is so sparsely sampled that no pattern is evident in the body size distribution (Fig. 3.5). Overall, it is rare to record extremes of extant taxa, so it is likely even

rarer to find fossils that are extremely small or large (Blackburn and Gaston 1994). Indeed, from our results, it is rare to find a wide distribution of body sizes at all, as the number of missing size classes from our rarefaction analyses indicates that the true shape of basin-specific body size distributions is largely unknown outside of the Karoo Basin.

From the classical interpretation of Bergmann's rule with respect to cold climates, it is possible that the heterothermic endothermic physiology reconstructed for *Lystrosaurus* (based on the interpretation of hard tissues), could have allowed natural selection to act on individuals to impact growth rates, life history, and lifespan at different paleolatitudes leading to variation in body size (Botha 2020; Whitney and Sidor 2020; Kulik et al. 2021; Han et al. 2021; Grigg et al. 2021). However, cold climates, akin to current Antarctic conditions, were not present at the poles during the Early Triassic (Boucot et al. 2013) so any potential body size trend in southern Pangea is not directly comparable to the energetic benefit of large body size at cold, high latitude climates as classically interpreted for Bergmann's rule. Indeed, global warming caused severe dampening of the latitudinal temperature gradient and is thought to have permitted the migration of terrestrial tetrapods into southern polar regions during the Early Triassic (Collinson and Hammer 2007; Fröbisch et al. 2010). In the absence of polar ice caps, it is possible that the comparatively cooler climate conditions in the highest southern regions could have allowed individuals to reach larger body size, as large archosauriforms are also known from the Early Triassic of Antarctica (Smith et al. 2011). The characteristic of large-bodied Triassic taxa in present day Antarctica could have resulted from a release of constraints operating in mid-southern paleolatitudes to reduce body size (i.e., high mortality at small size), possibly due to increased resource quality and availability in temperate polar regions (Fröbisch et al 2010, Romano et al. 2020).

A similar migration in the northern hemisphere may not have been necessary as paleoclimate estimates indicate warm, subhumid to semiarid environments for the mid-paleolatitudes (Yang et al. 2021; Boucot et al. 2013). The possibility that Bergmann's rule could operate across different latitudinal regions within each hemisphere cannot be ruled out, nor can it be tested, as the scarcity of terrestrial fossils from paleoequatorial regions makes it impossible to assess Bergmann's rule in the northern hemisphere alone (Romano et al. 2020).

A unique consideration when testing Bergmann's rule in the fossil record is the temporal scale that the sampled assemblages encompass. Age-estimates for the terrestrial Permian/Triassic boundary are highly debated, especially in the Karoo Basin (e.g., Gastaldo et al. 2020; Botha et al. 2020), which raises the possibility that samples of *Lystrosaurus* within each basin represent different—and potentially non-overlapping—intervals of geologic time. Geochemical age estimates generated by independent working groups reveal that the terrestrial extinction event is decoupled from the end-Permian marine extinction event in the Karoo (Botha et al. 2020; Gastaldo et al. 2020; Viglietti et al. 2021). Further, U-Pb age estimates from the same localities in the Karoo Basin have recovered different dates, either placing the base of *Lystrosaurus declivis* Assemblage Zone in the latest Permian (Gastaldo et al. 2020) or in the Early Triassic after the lithological change taken to signify the Permian/Triassic boundary (Botha et al. 2020). Age assessments for the Permian-Triassic boundary in China place specimens recovered from the Jiucaiyuan Formation as upper Induan-lower Olenekian (Yang et al. 2021). However, the remaining historical collection from the wider Turpan-Junggar Basin has not been correlated to this datum. In Antarctica and India, vertebrate biochronology suggests that both the Lower Fremouw and Panchet formations are Early Triassic in age, but age-dates are not available

(Collinson et al. 2006). Taken together, the possibility that our results include body size data from Permian specimens cannot be entirely ruled out.

Although our results do not recognize a Bergmann's rule body size distribution in *Lystrosaurus*, other geographically widespread tetrapods, such as *Diictodon* and *Dicynodon* during the Permian, might be more amenable to this type of analysis. If body size varies predictably with paleolatitude for other Permian or Triassic taxa, this might suggest that our results are hampered by latitudinal range or small sample sizes in some geographic areas. Alternatively, repeated failures to detect Bergmann-like patterns during times in Earth history with drastically different global temperature regimes could indicate that Bergmann's rule is only valid for the ice-house conditions of the ~Recent. This has been suggested by neontologists who notice a phenotypic change in body size of modern vertebrates due to anthropogenic climate change (Yom-Tov and Geffen 2011; McCoy 2012; Goldenburg et al. 2022). In sum, additional investigations of Bergmann's rule in the fossil record are critical for understanding how well patterns in the past can inform our understanding of the present.

3.6 ACKNOWLEDGEMENTS

We thank the following curators, collections managers, and colleagues for their help in providing museum collections access and support: Zaituna Skosan, Claire Browning, Christian Kammerer, Roger Smith, Jennifer Botha, Elize Butler, Bernhard Zipfel, Bruce Rubidge, Sifelani Jirah, Viktor Radermacher, Carl Mehling, Mark Norell, Ken Angielczyk, Jun Liu, and Alida Bailleul.

We acknowledge research funding from NSF EAR 1713787 and ANT 1341304 (to CAS) and University of Washington Department of Biology Iuvo, Walker, and Snyder awards (to ZTK).

3.7 Data Availability Statement

Data available from the Dryad Digital Repository: https://doi.org/10.5061/dryad. j3tx95xhk.

3.8 Literature Cited

Allen, B. J., P. B. Wignall, D. J. Hill, E. E. Saupe, and A. M. Dunhill. 2020. The latitudinal diversity gradient of tetrapods across the Permo-Triassic mass extinction and recovery interval. Proceedings of the Royal Society B: Biological Sciences 287(1929):20201125. https://doi.org/10.1098/rspb.2020.1125.

Angielczyk, K. D., and C. F. Kammerer. 2018. Non-mammalian synapsids: the deep roots of the mammalian family tree. Pp. 117–198. *In* F. Zachos, and R. Asher, eds. Mammalian Evolution, Diversity and Systematics. De Gruyter, Berlin.

Angielczyk, K. D., R. W. Burroughs, and C. R. Feldman. 2015. Do turtles follow the rules? Latitudinal gradients in species richness, body size, and geographic range area of the world's turtles. Journal of Experimental Zoology Part B: Molecular and Developmental Evolution 324(3):270–94. https://doi.org/10.1002/jez.b.22602.

Araújo, R., R. M. H. Smith, S. Tolan, K. D. Angielczyk, J. L. Crowley, D. Milisse, and J. Mugabe. 2020. Biostratigraphic refinement of tetrapod-bearing beds from the Metangula graben (Niassa province, Mozambique). New radiometric dating and the first Lower Triassic tetrapod fossils from Mozambique. Palaeontologia Africana, 56-58.

Ashton, K. G. 2002. Do amphibians follow Bergmann's rule? Canadian Journal of Zoology 80(4):708–16. https://doi.org/10.1139/z02-049.

Ashton, K. G., and C. R. Feldman. 2003. Bergmann's rule in nonavian reptiles: Turtles follow it, lizards and snakes reverse it. Evolution 57(5):1151–63. https://doi.org/10.1111/j.0014-3820.2003.tb00324.x.

Ashton, K. G., M. C. Tracy, and A. de Queiroz. 2000. Is Bergmann's rule valid for mammals? The American Naturalist 156(4):390–415. https://doi.org/10.1086/303400.

Belk, M. C., and D. D Houston. 2002. Bergmann's rule in ectotherms: A test using freshwater fishes. The American Naturalist 160(6):803–8.

Bergmann, C. 1847. Uber die verhaltnisse der warmeokonomie der thiere zu uber grosso. Vol. 3. Gottinger studien.

Berke, S. K., D. Jablonski, A. Z. Krug, K. Roy, and A. Tomasovych. 2013. Beyond Bergmann's rule: Size–latitude relationships in marine 137ivalvia world-wide. Global Ecology and Biogeography 22(2):173–83. https://doi.org/10.1111/j.1466-8238.2012.00775.x.

Blackburn, T. M., and K. J. Gaston. 1994. Animal body size distributions: Patterns, mechanisms and implications. Trends in Ecology & Evolution 9(12):471–74. https://doi.org/10.1016/0169-5347(94)90311-5.

—— 1996. Spatial patterns in the body sizes of bird species in the new world. Oikos 77(3):436–46. https://doi.org/10.2307/3545933.

Blackburn, T. M., and A. Ruggiero. 2001. Latitude, elevation and body mass variation in Andean passerine birds. Global Ecology and Biogeography 10(3):245–59.
Blackburn, T. M., K. J. Gaston, and N. Loder. 1999. Geographic gradients in body size: A clarification of Bergmann's rule. Diversity and Distributions 5(4):165–74. https://doi.org/10.1046/j.1472-4642.1999.00046.x.
Blackburn, T. M., D. W. Redding, and E. E. Dyer. 2019. Bergmann's rule in alien birds. Ecography 42(1):102–10. https://doi.org/10.1111/ecog.03750.
Botha-Brink, J. 2017. Burrowing in *Lystrosaurus*: Preadaptation to a postextinction environment? Journal of Vertebrate Paleontology 37(5):e1365080. https://doi.org/10.1080/02724634.2017.1365080.
Botha, J. 2020. The paleobiology and paleoecology of South African *Lystrosaurus*. PeerJ 8:e10408. https://doi.org/10.7717/peerj.10408.
Botha, J., and R. M. H. Smith. 2007. *Lystrosaurus* species composition across the Permo–Triassic boundary in the Karoo Basin of South Africa. Lethaia 40(2):125–37. https://doi.org/10.1111/j.1502-3931.2007.00011.x.
—— 2020. Biostratigraphy of the *Lystrosaurus declivis* Assemblage Zone (Beaufort Group, Karoo Supergroup), South Africa. South African Journal of Geology 123:207–216.
Botha-Brink, J., A. K. Huttenlocker, and S. P. Modesto. 2014. Vertebrate paleontology of Nooitgedacht 68: A *Lystrosaurus maccaigi*-rich Permo-Triassic boundary locality in South Africa. *In* Early Evolutionary History of the Synapsida, edited by C. F. Kammerer, K. D. Angielczyk, and J. Fröbisch, 289–304. Vertebrate Paleobiology and Paleoanthropology. Dordrecht: Springer Netherlands. https://doi.org/10.1007/978-94-007-6841-3_17.
Botha-Brink, J., D. Codron, A. K. Huttenlocker, K. D. Angielczyk, and M. Ruta. 2016. Breeding young as a survival strategy during earth's greatest mass extinction. Scientific Reports 6(1). https://doi.org/10.1038/srep24053.
Botha, J., A. K. Huttenlocker, R. M.H. Smith, R. Prevec, P. Viglietti, and S. P. Modesto. 2020. New geochemical and palaeontological data from the Permian–Triassic boundary in the South African Karoo Basin test the synchronicity of terrestrial and marine extinctions. Palaeogeography, Palaeoclimatology, Palaeoecology 540:109467. https://doi.org/10.1016/j.palaeo.2019.109467.
Boucot, A. J., C. Xu, C. R. Scotese, and R. J. Morley. 2013. Phanerozoic Paleoclimate: An Atlas of Lithologic Indicators of Climate. Tulsa, Oklahoma, U.S.A.: SEPM (Society for Sedimentary Geology). https://doi.org/10.2110/sepmcsp.11.
Briscoe, N. J., A. Krockenberger, K. A. Handasyde, and M. R. Kearney. 2015. Bergmann meets Scholander: Geographical variation in body size and insulation in the koala is related to climate. Journal of Biogeography 42(4): 791–802.
Brown, J. S., B. P. Kotler, and W. P. Porter. 2017. How foraging allometries and resource dynamics could explain Bergmann's rule and the body-size diet relationship in mammals. Oikos 126(2). https://doi.org/10.1111/oik.03468.
Camp, J., and J. Liu. 2011. The taxonomy and cranial morphology of Chinese *Lystrosaurus*. [Abstract] Supplement to online Journal of Vertebrate Paleontology. *In* 71st Annual Meeting Society of Vertebrate Paleontology 82.
Chao, A., and L. Jost. 2012. Coverage-based rarefaction and extrapolation: standardizing samples by completeness rather than size. Ecology 93(12):2533–47. https://doi.org/10.1890/11-1952.1.

Chown, S. L., and K. J. Gaston. 2010. Body size variation in insects: A macroecological perspective. Biological Reviews 85(1):139–69. https://doi.org/10.1111/j.1469-185X.2009.00097.x.
Colbert, E. H. 1974. *Lystrosaurus* from Antarctica. American Museum Novitates 2535:1–44.
Collinson, J. W., and W. R. Hammer. 2007. Migration of Triassic tetrapods to Antarctica. P. 3. *In* A. K. Cooper, and C. R. Raymond, eds. Antarctica: A keystone in a changing world – online proceedings of the 10th ISAES X.
Collinson, J. W., W. R. Hammer, R. A. Askin, and D. H. Elliot. 2006. Permian-Triassic boundary in the central Transantarctic Mountains, Antarctica. GSA Bulletin 118:747–763.
Correll, R. A., T. A. A. Prowse, and G. J. Prideaux. 2016. Lean-season primary productivity and heat dissipation as key drivers of geographic body-size variation in a widespread marsupial. Ecography 39(1):77–86. https://doi.org/10.1111/ecog.01243.
Cosgriff, J. W., W. R. Hammer, and W. J. Ryan. 1982. The Pangaean reptile, *Lystrosaurus maccaigi*, in the Lower Triassic of Antarctica. Journal of Paleontology 56(2): 371–85.
Dunne, E. M., R. A. Close, D. J. Button, N. Brocklehurst, D. D. Cashmore, G. T. Lloyd, and R. J. Butler. 2018. Diversity change during the rise of tetrapods and the impact of the 'Carboniferous rainforest collapse.' Proceedings of the Royal Society B: Biological Sciences 285(1872):20172730. https://doi.org/10.1098/rspb.2017.2730.
Elliot, D. H., C. M. Fanning, J. L. Isbell, and S. R.W. Hulett. 2017. The Permo-Triassic Gondwana sequence, Central Transantarctic Mountains, Antarctica: Zircon geochronology, provenance, and basin evolution. Geosphere 13(1):155–78. https://doi.org/10.1130/GES01345.1.
Feder, M. E., T. J. Papenfuss, and D. B. Wake. 1982. Body size and elevation in neotropical salamanders. Copeia 1982(1):186–88. https://doi.org/10.2307/1444288.
Freckleton, R. P., P. H. Harvey, and M. Pagel. 2003. Bergmann's rule and body size in mammals. The American Naturalist 161(5):821–25. https://doi.org/10.1086/374346.
Fröbisch, J., K. D. Angielczyk, and C. A. Sidor. 2010. The Triassic dicynodont *Kombuisia* (Synapsida, Anomodontia) from Antarctica, a refuge from the terrestrial Permo-Triassic mass extinction. Naturwissenschaften 97:187-196.
Gastaldo, R. A., S. L. Kamo, J. Neveling, J. W. Geissman, C. V. Looy, and A. M. Martini. 2020. The base of the *Lystrosaurus* Assemblage Zone, Karoo Basin, predates the End-Permian marine extinction. Nature Communications 11:1428. https://doi.org/10.1038/s41467-020-15243-7.
Gohli, J., and K. L. Voje. 2016. An interspecific assessment of Bergmann's rule in 22 mammalian families. BMC Evolutionary Biology 16(1). https://doi.org/10.1186/s12862-016-0778-x.
Goldenberg, J., K. Bisschop, L. D'Alba, and M. D. Shawkey. 2022. The link between body size, colouration and thermoregulation and their integration into ecogeographical rules: A critical appraisal in light of climate change. Oikos. https://doi.org/10.1111/oik.09152.
Grigg, G., J. Nowack, J. E. P. W. Bicudo, N. C. Bal, H. N. Woodward, and R. S. Seymour. 2021. Whole-body endothermy: Ancient, homologous and widespread among the ancestors of mammals, birds and crocodylians. Biological Reviews, brv.12822. https://doi.org/10.1111/brv.12822.
Grine, F. E., C. A. Forster, M. A. Cluver, and J. A. Georgi. 2006. Cranial variability, ontogeny and taxonomy of *Lystrosaurus* from the Karoo Basin of South Africa. *In* M. T. Carrano,

T. Gaudin, R. Blob, and J. Wible, eds. Amniote Paleobiology: Perspectives on the evolution of mammals, birds, and reptiles. University of Chicago Press, Chicago.
Gubin, Y. M., and S. M. Sinitza. 1993. Triassic terrestrial tetrapods of Mongolia and the geological structure of the Sain-Sar-Bulak locality. *In* The Nonmarine Triassic, 3:169–70. New Mexico Museum of Natural History and Science Bulletin.
Gulbranson, E., M. Mellum, V. Corti, A. Dahlseid, B. Atkinson, P. Ryberg, and G. Cornamusini. 2021. Paleoclimate-induced stress on polar forested ecosystems prior to the Permian–Triassic mass extinction. Preprint. https://doi.org/10.21203/rs.3.rs-1108556/v1.
Gupta, A., and D. P. Das. 2011. "Report of *Lystrosaurus* cf. c*urvatus* and *L.* cf. *declivis* from the Early Triassic Panchet Formation, Damodar Valley, West Bengal, India and its Implications. Indian Journal of Geosciences 65:119–30.
Han, F., Q. Zhao, and J. Liu. 2021. Preliminary bone histological analysis of *Lystrosaurus* (Therapsida: Dicynodontia) from the Lower Triassic of North China, and its implication for lifestyle and environments after the end-Permian extinction. PLOS ONE 16(3):e0248681. https://doi.org/10.1371/journal.pone.0248681.
Hinsbergen, D. J. J. van, L. V. de Groot, S. J. van Schaik, W. Spakman, P. K. Bijl, A. Sluijs, C. G. Langereis, and H. Brinkhuis. 2015. A paleolatitude calculator for paleoclimate studies. PLOS ONE 10(6):e0126946. https://doi.org/10.1371/journal.pone.0126946.
Hsieh, T. C., K. H. Ma, and A. Chao. 2016. INEXT: An R package for rarefaction and extrapolation of species diversity (HILL Numbers). Edited by Greg McInerny. Methods in Ecology and Evolution 7(12):1451–56. https://doi.org/10.1111/2041-210X.12613.
Jadwiszczak, P. 2001. Body size in Eocene Antarctic Penguins. Polish Polar Research 22(2):147–58.
James, F. C. 1970. Geographic size variation in birds and its relationship to climate. Ecology 51(3):365–90. https://doi.org/10.2307/1935374.
Jasinoski, S. C., E. J. Rayfield, and A. Chinsamy. 2009. Comparative feeding biomechanics of *Lystrosaurus* and the generalized Dicynodont *Oudenodon*. The Anatomical Record: Advances in Integrative Anatomy and Evolutionary Biology 292(6):862–74. https://doi.org/10.1002/ar.20906.
Jasinoski, S. C., M. A. Cluver, A. Chinsamy, and B. D. Reddy. 2014. Anatomical Plasticity in the Snout of Lystrosaurus. *In* Early Evolutionary History of the Synapsida, edited by C. F. Kammerer, K. D. Angielczyk, and J. Fröbisch, 139–49. Vertebrate Paleobiology and Paleoanthropology. Dordrecht: Springer Netherlands. https://doi.org/10.1007/978-94-007-6841-3_8.
Kammerer, C. F., K. D. Angielczyk, and J. Fröbisch. 2011. A comprehensive taxonomic revision of *Dicynodon* (Therapsida, Anomodontia) and its implications for dicynodont phylogeny, biogeography, and biostratigraphy. Journal of Vertebrate Paleontology 31:1–158. https://doi.org/10.1080/02724634.2011.627074.
Kelly, R. M., R. Friedman, and S. E. Santana. 2018. Primary productivity explains size variation across the pallid bat's western geographic range. Functional Ecology 32(6):1520–30. https://doi.org/10.1111/1365-2435.13092.
Kidder, D. L., and T. R. Worsley. 2004. Causes and consequences of extreme Permo-Triassic warming to globally equable climate and relation to the Permo-Triassic extinction and recovery. Palaeogeography, Palaeoclimatology, Palaeoecology 203(3–4):207–37. https://doi.org/10.1016/S0031-0182(03)00667-9.
King, G. 1990. The dicynodonts: a study in palaeobiology. Chapman and Hall, New York.

Kulik, Z. T, J. K. Lungmus, K. D. Angielczyk, and C. A. Sidor. 2021. Living fast in the Triassic: new data on life history in *Lystrosaurus* (Therapsida: Dicynodontia) from northeastern Pangea. PLOS ONE 16(11):e0259369. https://doi.org/10.1371/ journal.pone.0259369

Li, J., R. A. Gastaldo, J. Neveling, and J. W. Geissman. 2017. Siltstones across the *Daptocephalus* (*Dicynodon*) and *Lystrosaurus* Assemblage Zones, Karoo Basin, South Africa, show no evidence for aridification. Journal of sedimentary research 87(6):653–71. Https://doi.org/10.2110/jsr.2017.35.

Liu, J., J. L. Li, and Z. W. Cheng. 2002. The *Lystrosaurus* fossils from Xinjiang and their bearing on the terrestrial Permian Triassic boundary. Vertebrata Pal Asiatica 40(4):267–75.

Liu, J., F. Abdala, K. D. Angielczyk, and C. A. Sidor. 2021. Tetrapod Turnover during the Permo-Triassic Transition explained by temperature change. Earth-Science Reviews, 103886. https://doi.org/10.1016/j.earscirev.2021.103886.

Mancuso, A. C., B. L. D. Horn, C. A. Benavente, C. L. Schultz, and R. B. Irmis. 2021. The paleoclimatic context for South American Triassic vertebrate evolution. Journal of South American Earth Sciences 110:103321. https://doi.org/10.1016/j.jsames.2021.103321.

Mayr, E. 1956. Geographical character gradients and climatic adaptation. Evolution 10(1):105–8.

—— 1963. Animal species and evolution. Cambridge, MA: Harvard University Press.

McCoy, D. E. 2012. Connecticut birds and climate change: Bergmann's rule in the fourth dimension. Northeastern Naturalist 19(2):323–34.

McNab, B. K. 1971. On the ecological significance of Bergmann's rule. Ecology 52(5):845–54. https://doi.org/10.2307/1936032.

—— 2010. Geographic and temporal correlations of mammalian size reconsidered: A resource rule. Oecologia 164 (1):13–23. https://doi.org/10.1007/s00442-010-1621-5.

Meachen, J. A., A. C. Janowicz, J. E. Avery, and R. W. Sadleir. 2014. Ecological changes in coyotes (*Canis latrans*) in response to the ice age megafaunal extinctions. PLOS ONE 9(12):e116041. https://doi.org/10.1371/journal.pone.0116041.

Meiri, S., and T. Dayan. 2003. On the validity of Bergmann's rule. Journal of Biogeography 30(3):331–51. https://doi.org/10.1046/j.1365-2699.2003.00837.x.

Meiri, S., T. Dayan, and D. Simberloff. 2004. Carnivores, biases and Bergmann's rule. Biological Journal of the Linnean Society 81(4):579–88. https://doi.org/10.1111/j.1095-8312.2004.00310.x.

Meiri, S., Y. Yom-Tov, and E. Geffen. 2007. "What Determines Conformity to Bergmann's Rule?" *Global Ecology and Biogeography* 16(6):788–94. https://doi.org/10.1111/j.1466-8238.2007.00330.x.

Montgomery, C. E., S. P. Mackessy, and J. C. Moore. 2003. Body size variation in the Texas horned lizard, *Phrynosoma cornutum*, from central Mexico to Colorado. Journal of Herpetology 37(3):550–53.

Murphy, E. C. 1985. Bergmann's rule, seasonality, and geographic variation in body size of house sparrows. Evolution 39(6):1327–34. https://doi.org/10.1111/j.1558-5646.1985.tb05698.x.

Nwaogu, C. J., B. I. Tieleman, K. Bitrus, and W. Cresswell. 2018. Temperature and aridity determine body size conformity to Bergmann's rule independent of latitudinal differences in a tropical environment. Journal of Ornithology 159(4):1053–62. https://doi.org/10.1007/s10336-018-1574-8.

Orcutt, J. D., and S. S. B. Hopkins. 2013. Oligo-Miocene climate change and mammal body-size evolution in the northwest United States: A test of Bergmann's rule. Paleobiology 39(4):648–61. https://doi.org/10.1666/13006.

Pallarés, S., M. Lai, P. Abellán, I. Ribera, and D. Sánchez-Fernández. 2019. An interspecific test of Bergmann's rule reveals inconsistent body size patterns across several lineages of water beetles (Coleoptera: Dytiscidae). Ecological Entomology 44(2):249–54. https://doi.org/10.1111/een.12701.

Peecook, B. R., R. M. H. Smith, and C. A. Sidor. 2019. A novel archosauromorph from Antarctica and an updated review of a high-latitude vertebrate assemblage in the wake of the end-Permian mass extinction. Journal of Vertebrate Paleontology 38(6):e1536664. https://doi.org/10.1080/02724634.2018.1536664.

Pincheira-Donoso, D., and S. Meiri. 2013. An intercontinental analysis of climate-driven body size clines in reptiles: no support for patterns, no signals of processes. Evolutionary Biology 40(4):562–78. https://doi.org/10.1007/s11692-013-9232-9.

Queiroz, A. de, and K. G. Ashton. 2004. The phylogeny of a species-level tendency: species heritability and possible deep origins of Bergmann's rule in tetrapods. Evolution 58(8):1674–84. https://doi.org/10.1111/j.0014-3820.2004.tb00453.x.

Ray, S. 2005. *Lystrosaurus* (Therapsida, Dicynodontia) from India: Taxonomy, relative growth and cranial dimorphism. Journal of Systematic Palaeontology 3(2):203–21. https://doi.org/10.1017/S1477201905001574.

Ray, S., A. Chinsamy, and S. Bandyopadhyay. 2005. *Lystrosaurus murrayi* (Therapsida, Dicynodontia): Bone histology, growth and lifestyle adaptations. Palaeontology 48(6):1169–85. https://doi.org/10.1111/j.1475-4983.2005.00513.x.

Rensch, B. 1938. Some problems of geographical variation and species-formation. Proceedings of the Linnean Society of London 150(4):275–85. https://doi.org/10.1111/j.1095-8312.1938.tb00182k.x.

Retallack, G. J., R. M.H. Smith, and P. D. Ward. 2003. Vertebrate extinction across Permian–Triassic boundary in Karoo Basin, South Africa. Geological Society of America Bulletin 115:1133–1152. https://doi.org/10.1130/B25215.1.

Rodríguez, M. Á., M. Á. Olalla-Tárraga, and B. A. Hawkins. 2008. Bergmann's rule and the geography of mammal body size in the western hemisphere. Global Ecology and Biogeography 17(2):274–83. https://doi.org/10.1111/j.1466-8238.2007.00363.x.

Romano, M., M. Bernardi, F. M. Petti, B. Rubidge, J. Hancox, and M. J. Benton. 2020. Early Triassic terrestrial tetrapod fauna: A review. Earth-Science Reviews 210(103331):1–40. https://doi.org/10.1016/j.earscirev.2020.103331.

Romano, A., R. Séchaud, and A. Roulin. 2021. Generalized evidence for Bergmann's rule: Body size variation in a cosmopolitan owl genus. Journal of Biogeography 48(1):51–63. https://doi.org/10.1111/jbi.13981.

Roy, K., D. Jablonski, and K. K. Martien. 2000. Invariant size–frequency distributions along a latitudinal gradient in marine bivalves. Proceedings of the National Academy of Sciences 97(24):13150–55. https://doi.org/10.1073/pnas.97.24.13150.

Scotese, C. R. 2016. PALEOMAP PaleoAtlas for Gplates and the PaleoData Plotter Program. Version
2. PALEOMAP Project. http://www.earthbyte. org/paleomap-paleoatlas-for-gplates/.

Salewski, V., and C. Watt. 2017. Bergmann's rule: A biophysiological rule examined in birds. Oikos 126(2). https://doi.org/10.1111/oik.03698.

Slavenko, A., A. Feldman, A. Allison, A. M. Bauer, M. Böhm, L. Chirio, G. R. Colli, et al. 2019. Global patterns of body size evolution in squamate reptiles are not driven by climate. Global Ecology and Biogeography 28(4):471–83. https://doi.org/10.1111/geb.12868.

Smith, N. D., J. R. Crandall, S. M. Hellert, W. R. Hammer, and P. J. Makovicky. 2011. Anatomy and affinities of large Archosauromorphs from the Lower Fremouw Formation (Early Triassic) of Antarctica. Journal of Vertebrate Paleontology 31(4):784–97. https://doi.org/10.1080/02724634.2011.586662.

Smith, R. M. H., and J. Botha-Brink. 2014. Anatomy of a mass extinction: sedimentological and taphonomic evidence for drought-induced die-offs at the Permo-Triassic boundary in the main Karoo Basin, South Africa. Palaeogeography, Palaeoclimatology, Palaeoecology 396:99–118.

Smith, R. M. H., B. S. Rubidge, and M. van der Walt. 2012. Therapsid biodiversity patterns and paleoenvironments of the Karoo Basin, South Africa (pp. 31-63) *In* The Forerunners of Mammals. Indiana University Press.

Sun, A.-L. 1964. Preliminary Report on a new species of *Lystrosaurus* of Sinkiang. Vertebrata Pal Asiatica 8:216–17.

—— 1973. Permo-Triassic Dicynodonts from Turfan, Sinkiang. Permo-Triassic Vertebrate Fossils of the Turfan Basin, 53–68.

—— 1980. Late Permian and Triassic terrestrial tetrapods of North China. Vertebrata PalAsiatica XVIII (2): 11.

Surkov, M. V., N. N. Kalandadze, and M. J. Benton. 2005. *Lystrosaurus georgi*, a dicynodont from the Lower Triassic of Russia. Journal of Vertebrate Paleontology 25(2):402–13. https://doi.org/10.1671/0272-4634(2005)025[0402:LGADFT]2.0.CO;2.

Tabor, N. J., C. A. Sidor, R. M. H. Smith, S. J. Nesbitt, and K. D. Angielczyk. 2017. Paleosols of the Permian-Triassic: Proxies for rainfall, climate change and major changes in terrestrial tetrapod diversity. Journal of Vertebrate Paleontology 37:240–53. https://doi.org/10.1080/02724634.2017.1415211.

Thomas, S. G., N. J. Tabor, W. Yang, T. S. Myers, Y. Yang, and D. Wang. 2011. Palaeosol stratigraphy across the Permian–Triassic Boundary, Bogda Mountains, NW China: Implications for palaeoenvironmental transition through Earth's largest mass extinction. Palaeogeography, Palaeoclimatology, Palaeoecology 308:41–64. https://doi.org/10.1016/j.palaeo.2010.10.037.

Thulborn, R. A. 1990. Mammal-like reptiles of Australia. Memoirs of the Queensland Museum 28:1–169.

Timofeev, S F. 2001. Bergmann's principle and deep-water gigantism in marine crustaceans. Biology Bulletin 28(6):646–50.

Tripathi, C., and S. N. Puri. 1961. On the remains of *Lystrosaurus* from the Panchets of the Raniganj coalfield. Records of the Geological Survey of India 89:407–19.

Viglietti, P. A., R. B. J. Benson, R. M. H. Smith, J. Botha, C. F. Kammerer, Z. Skosan, E. Butler, et al. 2021. Evidence from South Africa for a protracted end-Permian extinction on land. Proceedings of the National Academy of Sciences 118(17):e2017045118. https://doi.org/10.1073/pnas.2017045118.

Villabolos, F., M. A. Olalla-Tarraga, C. M. Vieira, N. D. Mazzei, and L. M. Bini. 2017. Spatial dimension of body size evolution in Pterosauria: Bergmann's rule does not drive Cope's rule. Evolutionary Ecology Research. https://doi.org/10.5061/DRYAD.N0310.

Wan, M.-L., W. Yang, S. Wan, and J. Wang. 2021. Wildfires in the Early Triassic of Northeastern Pangaea: Evidence from fossil charcoal in the Bogda Mountains, Northwestern China. Palaeoworld 30(4):593–601. https://doi.org/10.1016/j.palwor.2021.07.002.
Watt, C., S. Mitchell, and V. Salewski. 2010. Bergmann's rule; a concept cluster? Oikos 119(1):89–100. https://doi.org/10.1111/j.1600-0706.2009.17959.x.
Wells, J. C., M. A. Saunders, A. S. Lea, M. Cortina-Borja, and M. K. Shirley. 2019. Beyond Bergmann's rule: Global variability in human body composition is associated with annual average precipitation and annual temperature volatility. American Journal of Physical Anthropology 170(1):75–87. https://doi.org/10.1002/ajpa.23890.
Whitney, M. R., and C. A. Sidor. 2020. Evidence of torpor in the tusks of *Lystrosaurus* from the Early Triassic of Antarctica. Communications Biology 3(1):1–6.
Winguth, A. M. E., C. A. Shields, and C. Winguth. 2015. Transition into a Hothouse World at the Permian–Triassic Boundary—A Model Study. Palaeogeography, Palaeoclimatology, Palaeoecology 440:316–27. https://doi.org/10.1016/j.palaeo.2015.09.008.
Yang, W., M. Wan, J. L. Crowley, J. Wang, X. Luo, N. Tabor, K. D. Angielczyk, et al. 2021. Paleoenvironmental and paleoclimatic evolution and cyclo- and chrono-stratigraphy of upper Permian–Lower Triassic fluvial-lacustrine deposits in Bogda mountains, NW China — implications for diachronous plant evolution across the Permian–Triassic boundary. Earth-Science Reviews 222:103741. https://doi.org/10.1016/j.earscirev.2021.103741.
Yom-Tov, Y., and E. Geffen. 2011. Recent spatial and temporal changes in body size of terrestrial vertebrates: Probable causes and pitfalls. Biological Reviews 86(2):531–41. https://doi.org/10.1111/j.1469-185X.2010.00168.x.
Young, C. C. 1939. Additional Dicynodontia remains from Sinkiang. Bulletin of the Geological Society of China 19:111–36.
Yuan, P. L., and C. C. Young. 1934. On the occurrence of *Lystrosaurus* in Sinkiang. Bulletin of the Geological Society of China 13(1):575–80. https://doi.org/10.1111/j.1755-6724.1934.mp13001029.x.
Yu, T. L., D. L. Wang, M. Busam, and T. H. Deng. 2019. Altitudinal variation in body size in *Bufo minshanicus* supports Bergmann's rule. Evolutionary Ecology 33(3):449–60. https://doi.org/10.1007/s10682-019-09984-1.

3.9 Supplementary Dataset

Description of dataset

These data were generated to compare body size and paleolatitude in *Lystrosaurus* from four tectonic basins that host Early Triassic strata. 482 specimens were measured by Zoe Kulik or compiled from the literature. Cranial measurements, including basal skull length (BSL) and tusk diameter, were used as body size proxies and are reported as raw and standardized

measurements. Measurements were standardized as percent of maximum known size for each species, respectively. Paleolatitude was estimated from tectonic plate reconstructions made available through the online calculator www.paleolatitude.org. Please contact the corresponding author for further details (zkulik@uw.edu).

File Description: Species identification, raw and standardized cranial measurements, and geographic location of specimens included in this analysis.

Number of variables: 9

Number of rows: 482

Species: Species identification

Accession Number: Accession number for each catalogued fossil specimen, or currently uncatalogued fossil specimen included in this study. Uncatalogued specimens are denoted by their respective museum code (e.g., uncat AMNH)

BSL (mm): Basal skull length measured in millimeters.

Std.BSL: Standardized basal skull length as the proportion of species-specific maximum known size, or percent of maximum known size reported for each species of *Lystrosaurus* included in our analysis.

Tusk Diameter: Diameter (in millimeters) of tusk at eruption from the maxilla. Values were averaged when both tusks could be measured.

Std.Tusk: Standardized tusk diameter as the proportion of species-specific maximum known tusk size, or the percent of maximum known size reported for each species of *Lystrosaurus* included in our analysis.

Paleolatitude: estimated paleolatitude

Basin: geographic location of fossil collection

Reference: Citation information for cranial measurements that were compiled from a survey of the literature

Methodological Information

Cranial measurements were taken using Mitutoyo digital calipers (±0.02mm).

Supplemental Table 3.1. Cranial measurements compiled for Early Triassic *Lystrosaurus*.

Species	Accession Number	BSL (mm)	Std. BSL	Tusk Diameter (mm)	Std. Tusk	Paleolat.	Basin	Reference
murrayi	NMQR 3636	32.08	0.15	1.90	0.12	-60.00	Karoo	This study
murrayi	NMQR 3655	36.29	0.17	2.21	0.13	-60.00	Karoo	This study
murrayi	BP/1/4011	38.85	0.18	2.39	0.15	-60.00	Karoo	This study
murrayi	BP/1/3904	39.30	0.18	2.42	0.15	-60.00	Karoo	This study
murrayi	NMQR 3915	43.50	0.20	2.73	0.17	-60.00	Karoo	This study
murrayi	NMQR 3635a	46.33	0.22	2.93	0.18	-60.00	Karoo	Botha 2020

murrayi	SAM-PK-3531	49.00	0.23	3.12	0.19	-60.00	Karoo	Botha 2020
sp. indet.	SAM-PK-K1396	50.80	0.19	3.93	0.16	-60.00	Karoo	This study
murrayi	GSI 17847	52.00	0.24	3.34	0.20	-55.00	Damodar	Ray 2005
murrayi	BP/1/4190	58.94	0.28	3.65	0.22	-60.00	Karoo	This study
declivis	NMQR 129	59.44	0.26	5.24	0.26	-60.00	Karoo	Botha 2020
murrayi	GSI 17852	59.65	0.28	3.89	0.24	-55.00	Damodar	Ray 2005
declivis	NMQR 624	60.52	0.27	4.50	0.23	-60.00	Karoo	Botha 2020
murrayi	NMQR 351	62.58	0.29	4.10	0.25	-60.00	Karoo	Botha 2020
murrayi	NMQR 3629	66.02	0.31	4.35	0.26	-60.00	Karoo	This study
declivis	NMQR 159	68.00	0.30	5.84	0.29	-60.00	Karoo	Botha 2020
murrayi	GSI 17854	68.20	0.32	4.51	0.27	-55.00	Damodar	Ray 2005
murrayi	GSI 17855	71.80	0.34	4.76	0.29	-55.00	Damodar	Ray 2005
murrayi	NMQR 3571a	72.39	0.34	4.81	0.29	-60.00	Karoo	Botha 2020
declivis	NMQR 738	72.40	0.32	6.15	0.31	-60.00	Karoo	Botha 2020
declivis	NMQR 4039	74.05	0.33	6.27	0.32	-60.00	Karoo	Botha 2020
murrayi	GSI 17856	74.10	0.35	4.93	0.30	-55.00	Damodar	Ray 2005
sp. indet.	BP/1/458	74.37	0.28	5.35	0.22	-60.00	Karoo	This study
sp. indet.	FARB 21411	74.49	0.28	5.40	0.22	-55.00	Damodar	This study
curvatus	NMQR 4001	74.50	0.65	3.20	0.19	-60.00	Karoo	Botha 2020
sp. indet.	SAM-PK-K16	74.84	0.28	5.55	0.22	-60.00	Karoo	This study
sp. indet.	SAM-PK-K1496	75.03	0.28	5.63	0.23	-60.00	Karoo	This study
sp. indet.	BP/1/415	75.51	0.28	5.83	0.24	-60.00	Karoo	This study
murrayi	GSI 17846	75.75	0.36	5.05	0.31	-55.00	Damodar	Ray 2005
murrayi	NMQR 676	76.13	0.36	5.08	0.31	-60.00	Karoo	This study
sp. indet.	SAM-PK-K1266	76.44	0.29	6.22	0.25	-60.00	Karoo	This study
sp. indet.	BP/1/1699	76.79	0.29	6.37	0.26	-60.00	Karoo	This study
sp. indet.	SAM-PK-K15	77.06	0.29	6.48	0.26	-60.00	Karoo	This study
sp. indet.	FARB 8250	77.20	0.29	6.54	0.26	-60.00	Karoo	This study
murrayi	GSI 17865	77.40	0.36	5.17	0.31	-55.00	Damodar	Ray 2005
murrayi	SAM-PK-K1362	78.00	0.37	5.21	0.32	-60.00	Karoo	Botha 2020
sp. indet.	BP/1/4340a	78.79	0.30	7.18	0.29	-60.00	Karoo	This study
murrayi	NMQR 3635b	79.01	0.37	5.28	0.32	-60.00	Karoo	This study
murrayi	BP/1/3904	79.61	0.37	5.33	0.32	-60.00	Karoo	This study
murrayi	NMQR 721a	79.84	0.37	5.34	0.33	-60.00	Karoo	Botha 2020
declivis	NMQR 158	80.00	0.35	6.69	0.34	-60.00	Karoo	Botha 2020
declivis	NMQR 4043	80.01	0.35	6.69	0.34	-60.00	Karoo	Botha 2020

murrayi	GSI 17853	80.55	0.38	5.39	0.33	-55.00	Damodar	Ray 2005
sp. indet.	SAM-PK-K103	80.64	0.30	6.59	0.27	-60.00	Karoo	This study
sp. indet.	BP/1/476	80.74	0.30	8.03	0.33	-60.00	Karoo	This study
murrayi	GSI 17848	80.90	0.38	8.95	0.55	-55.00	Damodar	Ray 2005
murrayi	GSI 17848	80.90	0.38	5.42	0.33	-55.00	Damodar	Ray 2005
declivis	NMQR 128	80.92	0.36	6.75	0.34	-60.00	Karoo	Botha 2020
sp. indet.	SAM-PK-K11537	81.24	0.31	8.24	0.33	-60.00	Karoo	This study
sp. indet.	SAM-PK-K1479	81.29	0.31	8.26	0.33	-60.00	Karoo	This study
sp. indet.	BP/1/4516	81.45	0.31	6.74	0.27	-60.00	Karoo	This study
murrayi	UR 2690	81.69	0.38	6.43	0.39	-60.00	Karoo	This study
murrayi	BP/1/4030	81.73	0.38	6.77	0.41	-60.00	Karoo	Botha 2020
sp. indet.	uncat AMNH	81.88	0.31	8.51	0.34	-55.00	Damodar	This study
murrayi	NMQR 4028a	82.16	0.39	5.51	0.34	-60.00	Karoo	Botha 2020
declivis	NMQR 3300	82.39	0.36	6.17	0.31	-60.00	Karoo	This study
murrayi	SAM-PK-K10372	82.73	0.39	6.44	0.39	-60.00	Karoo	This study
murrayi	NMQR 758	82.74	0.39	5.55	0.34	-60.00	Karoo	Botha 2020
sp. indet.	BP/1/3234	82.95	0.31	8.96	0.36	-60.00	Karoo	This study
murrayi	BMNH 36253	83.00	0.39	5.57	0.34	-60.00	Karoo	Botha 2020
declivis	NMQR 3999	83.00	0.37	6.90	0.35	-60.00	Karoo	Botha 2020
murrayi	NMQR 659	83.02	0.39	4.80	0.29	-60.00	Karoo	This study
sp. indet.	BP/1/4315	83.36	0.31	9.13	0.37	-60.00	Karoo	This study
declivis	NMQR 3737	84.21	0.37	6.98	0.35	-60.00	Karoo	Botha 2020
murrayi	NMQR 1654	84.27	0.40	6.80	0.41	-60.00	Karoo	This study
sp. indet.	NMQR 1648	84.55	0.32	10.56	0.43	-60.00	Karoo	This study
sp. indet.	SAM-PK-K102	84.64	0.32	9.67	0.39	-60.00	Karoo	This study
sp. indet.	BP/1/444	84.76	0.32	9.72	0.39	-60.00	Karoo	This study
sp. indet.	SAM-PK-K1501	85.00	0.32	9.82	0.40	-60.00	Karoo	This study
sp. indet.	SAM-PK-K1408	85.21	0.32	9.91	0.40	-60.00	Karoo	This study
murrayi	NMQR 3927a	85.40	0.40	5.74	0.35	-60.00	Karoo	This study
sp. indet.	BP/1/1137	85.45	0.32	6.31	0.26	-60.00	Karoo	This study
murrayi	NMQR 4055	86.00	0.40	5.79	0.35	-60.00	Karoo	Botha 2020
murrayi	GSI 17867	86.05	0.40	5.79	0.35	-55.00	Damodar	Ray 2005
murrayi	NMQR 3541	86.38	0.41	6.00	0.37	-60.00	Karoo	This study
murrayi	NMQR 3547	86.43	0.41	8.68	0.53	-60.00	Karoo	This study
murrayi	TM 115	87.00	0.41	5.86	0.36	-60.00	Karoo	Botha 2020

sp. indet.	SAM-PK-K1379	87.18	0.33	13.89	0.56	-60.00	Karoo	This study
murrayi	SAM-PK-K11535	88.15	0.41	5.42	0.33	-60.00	Karoo	This study
sp. indet.	SAM-PK-K1265	88.25	0.33	17.16	0.69	-60.00	Karoo	This study
sp. indet.	SAM-PK-K100	88.37	0.33	4.16	0.17	-60.00	Karoo	This study
murrayi	SAM-PK-K10221	88.38	0.41	5.96	0.36	-60.00	Karoo	This study
declivis	NMQR 721b	88.84	0.39	7.31	0.37	-60.00	Karoo	Botha 2020
sp. indet.	FARB 9363	89.01	0.33	11.51	0.47	-70.00	Transantarctic	This study
murrayi	GSI 17866	89.40	0.42	6.03	0.37	-55.00	Damodar	This study
murrayi	GSI 17849	89.65	0.42	6.05	0.37	-55.00	Damodar	Ray 2005
declivis	NMQR 640	90.72	0.40	7.44	0.38	-60.00	Karoo	Botha 2020
murrayi	NMQR 6	91.44	0.43	6.18	0.38	-60.00	Karoo	Botha 2020
murrayi	SAM-PK-K21	91.48	0.43	6.18	0.38	-60.00	Karoo	This study
murrayi	NMQR 29	91.60	0.43	6.19	0.38	-60.00	Karoo	Botha 2020
murrayi	SAM-PK-K8311	92.00	0.43	6.22	0.38	-60.00	Karoo	Botha 2020
declivis	NMQR 47	92.32	0.41	7.55	0.38	-60.00	Karoo	Botha 2020
sp. indet.	SAM-PK-K8523	92.38	0.35	7.20	0.29	-60.00	Karoo	This study
declivis	NMQR 4043	92.88	0.41	11.65	0.59	-60.00	Karoo	This study
murrayi	GSI 17859	93.00	0.44	6.29	0.38	-55.00	Damodar	Ray 2005
declivis	NMQR 618a	93.10	0.41	11.03	0.56	-60.00	Karoo	This study
sp. indet.	BP/1/4626	93.58	0.35	7.88	0.32	-60.00	Karoo	This study
sp. indet.	BP/1/414	93.60	0.35	9.47	0.38	-60.00	Karoo	Botha 2020
curvatus	BP/1/457	93.75	0.47	9.05	0.53	-60.00	Karoo	This study
curvatus	SAM-PK-K27	93.75	0.47	4.16	0.24	-60.00	Karoo	This study
murrayi	ISIR 767	94.00	0.44	6.36	0.39	-55.00	Damodar	Ray 2005
murrayi	SAM-PK-11186	94.07	0.44	4.87	0.30	-60.00	Karoo	This study
murrayi	BP/1/4344	94.17	0.44	7.36	0.45	-60.00	Karoo	This study
sp. indet.	SAM-PK-K2	94.36	0.35	13.76	0.56	-60.00	Karoo	This study
sp. indet.	FARB 9310	94.53	0.36	13.83	0.56	-70.00	Transantarctic	This study
declivis	NMQR 660	95.53	0.42	16.81	0.85	-60.00	Karoo	Botha 2020
murrayi	BP/1/3900	96.00	0.45	6.51	0.40	-60.00	Karoo	Botha 2020
declivis	TM 4113	96.00	0.42	7.81	0.39	-60.00	Karoo	Botha 2020
murrayi	NMQR 799	96.10	0.45	6.51	0.40	-60.00	Karoo	Botha 2020
murrayi	GSI 17851	96.25	0.45	6.52	0.40	-55.00	Damodar	Ray 2005
murrayi	FMNH uncat	96.36	0.45	5.39	0.33	-70.00	Transantarctic	This study

murrayi	uncat	96.36	0.45	6.53	0.40	-70.00	Transantarctic	This study
curvatus	BP/1/1746	96.54	0.48	5.04	0.29	-60.00	Karoo	This study
sp. indet.	BP/1/5173	96.64	0.36	7.54	0.31	-60.00	Karoo	This study
declivis	BP/1/4343	96.80	0.43	6.31	0.32	-60.00	Karoo	This study
sp. indet.	SAM-PK-11174	96.99	0.36	7.57	0.31	-60.00	Karoo	This study
declivis	NMQR 1655	97.49	0.43	7.92	0.40	-60.00	Karoo	Botha 2020
murrayi	GSI 17863	97.80	0.46	6.64	0.40	-55.00	Damodar	Ray 2005
sp. indet.	BP/1/4802	97.83	0.37	6.12	0.25	-60.00	Karoo	This study
declivis	NMQR 423	97.99	0.43	6.73	0.34	-60.00	Karoo	This study
murrayi	SAM-PK-11169	98.00	0.46	6.65	0.41	-60.00	Karoo	Botha 2020
murrayi	SAM-PK-K1397	98.17	0.46	7.16	0.44	-60.00	Karoo	This study
declivis	NMQR 787a	98.18	0.43	7.97	0.40	-60.00	Karoo	Botha 2020
murrayi	NMQR 3691	98.38	0.46	4.20	0.26	-60.00	Karoo	This study
declivis	BP/1/3908	98.69	0.44	6.38	0.32	-60.00	Karoo	This study
murrayi	NMQR 3705	98.91	0.46	9.52	0.58	-60.00	Karoo	This study
murrayi	UWMB 91830	98.92	0.46	6.72	0.41	-60.00	Karoo	This study
declivis	NMQR 3959a	99.00	0.44	8.02	0.40	-60.00	Karoo	Botha 2020
murrayi	GSI 17857	99.00	0.46	6.72	0.41	-55.00	Damodar	Ray 2005
declivis	TM 4050	99.19	0.44	8.04	0.41	-60.00	Karoo	Botha 2020
declivis	BP/1/1706	99.44	0.44	7.28	0.37	-60.00	Karoo	This study
declivis	NMQR 818	99.49	0.44	8.06	0.41	-60.00	Karoo	Botha 2020
declivis	SAM-PK-11525	99.64	0.44	8.07	0.41	-60.00	Karoo	This study
murrayi	NMQR 3581a	99.92	0.47	6.79	0.41	-60.00	Karoo	This study
murrayi	BMNH 36224	100.00	0.47	6.79	0.41	-60.00	Karoo	Botha 2020
murrayi	GSI 17843	100.00	0.47	6.79	0.41	-55.00	Damodar	Ray 2005
curvatus	BP/1/481	100.66	0.50	6.73	0.39	-60.00	Karoo	This study
murrayi	NMQR 3480	100.86	0.47	6.07	0.37	-60.00	Karoo	This study
murrayi	BP/1/4798	100.87	0.47	6.72	0.41	-60.00	Karoo	This study
murrayi	BP/1/4798a	100.87	0.47	6.86	0.42	-60.00	Karoo	This study
murrayi	NMQR 815a	100.90	0.47	6.86	0.42	-60.00	Karoo	This study
murrayi	BMNH R5710	101.00	0.47	6.87	0.42	-60.00	Karoo	Botha 2020
murrayi	BP/1/5086a	101.00	0.47	6.87	0.42	-60.00	Karoo	Botha 2020
declivis	TM 117	101.00	0.45	8.16	0.41	-60.00	Karoo	Botha 2020
declivis	BP/1/4275	101.04	0.45	6.29	0.32	-60.00	Karoo	This study
sp. indet.	NMQR 3560b	101.05	0.38	8.51	0.34	-60.00	Karoo	This study

murrayi	NMQR 3592	101.24	0.48	7.23	0.44	-60.00	Karoo	This study
declivis	NMQR 42	101.26	0.45	8.18	0.41	-60.00	Karoo	Botha 2020
declivis	NMQR 1	101.36	0.45	8.19	0.41	-60.00	Karoo	This study
murrayi	SAM-PK-11172	101.43	0.48	8.70	0.53	-60.00	Karoo	This study
murrayi	NMQR 3957	101.54	0.48	6.91	0.42	-60.00	Karoo	Botha 2020
murrayi	BP/1/4217	101.63	0.48	6.91	0.42	-60.00	Karoo	Botha 2020
murrayi	SAM-PK-K8	101.96	0.48	10.19	0.62	-60.00	Karoo	This study
murrayi	TM 67	102.00	0.48	6.94	0.42	-60.00	Karoo	Botha 2020
declivis	NMQR 664	102.20	0.45	8.25	0.42	-60.00	Karoo	Botha 2020
declivis	NMQR 395	102.23	0.45	6.80	0.34	-60.00	Karoo	This study
murrayi	UR 2691	102.48	0.48	8.99	0.55	-60.00	Karoo	This study
murrayi	BP/1/1269	102.70	0.48	6.65	0.41	-60.00	Karoo	This study
declivis	NMQR 3837	102.72	0.45	8.29	0.42	-60.00	Karoo	Botha 2020
declivis	NMQR 372	102.74	0.45	8.29	0.42	-60.00	Karoo	Botha 2020
declivis	UR 2709	102.92	0.48	8.30	0.42	-60.00	Karoo	This study
declivis	BP/1/4207	102.95	0.46	8.08	0.41	-60.00	Karoo	Botha 2020
murrayi	BP/1/4039	103.00	0.48	7.01	0.43	-60.00	Karoo	Botha 2020
murrayi	SAM-PK-K1165	103.00	0.48	6.99	0.43	-60.00	Karoo	This study
murrayi	UMCZ T763	103.00	0.48	7.01	0.43	-60.00	Karoo	Botha 2020
declivis	NMQR 3560a	103.05	0.46	8.31	0.42	-60.00	Karoo	This study
murrayi	NMQR 37	103.31	0.49	7.03	0.43	-60.00	Karoo	Botha 2020
declivis	SAM-PK-K14	103.89	0.46	8.88	0.45	-60.00	Karoo	This study
declivis	BP/1/4507	103.93	0.46	8.37	0.42	-60.00	Karoo	Botha 2020
sp. indet.	BP/1/4038	104.56	0.39	8.16	0.33	-60.00	Karoo	This study
declivis	BP/1/4314	104.60	0.46	8.42	0.42	-60.00	Karoo	Botha 2020
declivis	NMQR 388	104.73	0.46	8.43	0.42	-60.00	Karoo	Botha 2020
murrayi	NMQR 4038	104.96	0.49	7.15	0.44	-60.00	Karoo	Botha 2020
murrayi	NMQR 4059	105.00	0.49	7.15	0.44	-60.00	Karoo	Botha 2020
China L. sp.	IVPP V18671	105.00	0.48	7.80	0.28	45.00	Turpan-Junggar	This study
declivis	TM 4049	105.00	0.46	8.45	0.43	-60.00	Karoo	Botha 2020
murrayi	BP/1/4591	105.12	0.49	5.46	0.33	-60.00	Karoo	This study
declivis	NMQR 32	105.37	0.47	8.47	0.43	-60.00	Karoo	Botha 2020
declivis	BP/1/4343	105.51	0.47	8.48	0.43	-60.00	Karoo	Botha 2020
sp. indet.	SAM-PK-K8519(B)	105.80	0.40	7.25	0.29	-60.00	Karoo	This study
declivis	NMQR 1382	105.89	0.47	8.51	0.43	-60.00	Karoo	Botha 2020
murrayi	NMQR 2951	105.96	0.50	7.22	0.44	-60.00	Karoo	Botha 2020
declivis	SAM-PK-K10454	105.97	0.47	8.51	0.43	-60.00	Karoo	Botha 2020

murrayi	NMQR 4056	106.00	0.50	7.23	0.44	-60.00	Karoo	Botha 2020
declivis	TM 164	106.00	0.47	8.52	0.43	-60.00	Karoo	Botha 2020
murrayi	TM 69	106.00	0.50	7.23	0.44	-60.00	Karoo	Botha 2020
murrayi	NMQR 3593	106.10	0.50	7.23	0.44	-60.00	Karoo	This study
murrayi	SAM-PK-K7991	106.22	0.50	8.37	0.51	-60.00	Karoo	This study
sp. indet.	SAM-PK-K1409	106.81	0.40	8.78	0.36	-60.00	Karoo	This study
curvatus	AG/RCF/04/22	107.00		5.80		-55.00	Damodar	Gupta and Das 2011
declivis	BP/1/1368	107.12	0.47	7.26	0.37	-60.00	Karoo	Botha 2020
declivis	BP/1/3915	107.17	0.47	9.01	0.45	-60.00	Karoo	This study
murrayi	UR 2711	107.48	0.50	10.63	0.65	-60.00	Karoo	This study
declivis	NMQR 4041a	107.50	0.48	8.62	0.43	-60.00	Karoo	This study
murrayi	NMQR 3609	107.59	0.51	7.34	0.45	-60.00	Karoo	Botha 2020
murrayi	NMQR 3581b	108.18	0.51	5.99	0.37	-60.00	Karoo	This study
murrayi	SAM-PK-K10461	108.39	0.51	7.40	0.45	-60.00	Karoo	Botha 2020
murrayi	BP/1/4271	108.44	0.51	5.52	0.34	-60.00	Karoo	This study
murrayi	BP/1/4276 UR	108.80	0.51	9.05	0.55	-60.00	Karoo	This study
murrayi	NMQR 3539c	108.98	0.51	9.03	0.55	-60.00	Karoo	This study
murrayi	SAM-PK-K10686	109.23	0.51	7.46	0.45	-60.00	Karoo	Botha 2020
murrayi	NMQR 3765	109.41	0.51	7.47	0.46	-60.00	Karoo	This study
sp. indet.	BP/1/4309	109.62	0.41	9.55	0.39	-60.00	Karoo	This study
declivis	NMQR 3301	109.68	0.49	10.53	0.53	-60.00	Karoo	This study
murrayi	BP/1/4507	109.92	0.52	9.58	0.58	-60.00	Karoo	Botha 2020
declivis	NMQR 116	109.93	0.49	8.79	0.44	-60.00	Karoo	This study
declivis	BP/1/1368	110.00	0.49	8.80	0.44	-60.00	Karoo	Botha 2020
murrayi	BPI MN106	110.00	0.52	7.51	0.46	-60.00	Karoo	Botha 2020
declivis	UR 2506	110.23	0.49	10.48	0.53	-60.00	Karoo	This study
declivis	BP/1/1383	110.31	0.49	16.41	0.83	-60.00	Karoo	This study
murrayi	BP/1/269	110.52	0.52	7.36	0.45	-60.00	Karoo	This study
sp. indet.	BP/1/2815	110.60	0.42	20.59	0.83	-60.00	Karoo	This study
sp. indet.	BP/1/4345	110.63	0.42	8.64	0.35	-60.00	Karoo	This study
murrayi	SAM-PK-11167	110.89	0.52	7.58	0.46	-60.00	Karoo	This study
murrayi	BP/1/4341	110.92	0.52	5.57	0.34	-60.00	Karoo	This study
murrayi	NMQR 4057	111.00	0.52	7.59	0.46	-60.00	Karoo	Botha 2020
declivis	NMQR 3958	111.01	0.49	8.87	0.45	-60.00	Karoo	This study
sp. indet.	BP/1/5731	111.04	0.42	8.07	0.33	-60.00	Karoo	This study

China L. sp.	IVPP V18669	111.11	0.51	8.50	0.30	45.00	Turpan-Junggar	This study
declivis	NMQR 3738	111.53	0.49	8.91	0.45	-60.00	Karoo	This study
sp. indet.	BP/1/4718	111.56	0.42	8.04	0.33	-60.00	Karoo	This study
declivis	NMQR 3759	111.88	0.50	8.93	0.45	-60.00	Karoo	This study
murrayi	SAM-PK-K10383	111.90	0.53	9.81	0.60	-60.00	Karoo	This study
murrayi	BP/1/4705	112.12	0.53	3.43	0.21	-60.00	Karoo	This study
sp. indet.	BP/1/1741	112.31	0.42	5.91	0.24	-60.00	Karoo	This study
curvatus	NMQR 3914	112.40	0.56	7.82	0.46	-60.00	Karoo	This study
curvatus	FARB 9515	112.98	0.56	6.43	0.37	-70.00	Transantarctic	This study
declivis	TM 139	113.00	0.50	9.01	0.45	-60.00	Karoo	Botha 2020
murrayi	NMQR 3112	113.01	0.53	6.15	0.37	-60.00	Karoo	This study
declivis	NMQR 12	113.12	0.50	9.02	0.45	-60.00	Karoo	This study
declivis	NMQR 3239	113.36	0.50	8.81	0.44	-60.00	Karoo	This study
murrayi	NMQR 596	113.43	0.53	7.76	0.47	-60.00	Karoo	Botha 2020
murrayi	NMQR 4153	113.47	0.53	6.84	0.42	-60.00	Karoo	This study
murrayi	SAM-PK-K10466	113.53	0.53	7.77	0.47	-60.00	Karoo	Botha 2020
murrayi	FMNH UC1516	113.75	0.53	7.78	0.47	-60.00	Karoo	Botha 2020
murrayi	SAM-PK-K8567	113.84	0.53	6.66	0.41	-60.00	Karoo	This study
murrayi	SAM-PK-K1459	113.93	0.53	6.27	0.38	-60.00	Karoo	This study
murrayi	UR 2695a	113.95	0.53	8.90	0.54	-60.00	Karoo	This study
murrayi	UR 2695b	113.95	0.53	7.80	0.48	-60.00	Karoo	This study
declivis	BP/1/5086b	114.00	0.50	8.63	0.43	-60.00	Karoo	Botha 2020
curvatus	FARB 24205	114.10	0.57	6.31	0.37	-70.00	Transantarctic	This study
declivis	NMQR 4091	114.10	0.50	9.09	0.46	-60.00	Karoo	This study
murrayi	SAM-PK-3715	114.29	0.54	6.87	0.42	-60.00	Karoo	This study
sp. indet.	BP/1/4340b	114.72	0.43	7.59	0.31	-60.00	Karoo	This study
declivis	NMQR 618b	114.94	0.51	9.15	0.46	-60.00	Karoo	Botha 2020
declivis	FARB 8243	115.10	0.51	6.33	0.32	-60.00	Karoo	This study
declivis	BP/1/1750	115.17	0.51	9.16	0.46	-60.00	Karoo	Botha 2020
murrayi	NMQR 648	115.38	0.54	7.90	0.48	-60.00	Karoo	Botha 2020
murrayi	ISIR 766	115.70	0.54	7.93	0.48	-55.00	Damodar	Ray 2005
declivis	NMQR 3573	115.84	0.51	9.27	0.47	-60.00	Karoo	This study
curvatus	SAM-PK-K1403	115.86	0.58	6.77	0.39	-60.00	Karoo	This study
declivis	BP/1/4211a	115.95	0.51	9.22	0.46	-60.00	Karoo	Botha 2020
murrayi	TM 71	116.00	0.54	7.95	0.48	-60.00	Karoo	Botha 2020

murrayi	NMQR 3960a	116.18	0.55	7.41	0.45	-60.00	Karoo	This study
murrayi	BP/1/4276 LL	116.28	0.55	7.23	0.44	-60.00	Karoo	This study
sp. indet.	SAM-PK-K1386	116.32	0.44	9.09	0.37	-60.00	Karoo	This study
murrayi	SAM-PK-K1495	116.40	0.55	7.80	0.48	-60.00	Karoo	This study
declivis	NMQR 679	117.70	0.52	9.34	0.47	-60.00	Karoo	Botha 2020
sp. indet.	BP/1/5056	118.16	0.44	9.23	0.37	-60.00	Karoo	This study
declivis	NMQR 4041b	118.22	0.52	9.38	0.47	-60.00	Karoo	This study
declivis	SAM-PK-11184b	118.23	0.52	9.38	0.47	-60.00	Karoo	This study
China L. sp.	IVPP V8532	118.31	0.54	5.12	0.18	45.00	Turpan-Junggar	This study
murrayi	BP/1/266	118.40	0.56	8.12	0.49	-60.00	Karoo	Botha 2020
declivis	SAM-PK-K10386	118.42	0.52	8.77	0.44	-60.00	Karoo	This study
murrayi	SAM-PK-K7	118.61	0.56	6.33	0.39	-60.00	Karoo	This study
declivis	NMQR 375	118.62	0.52	9.41	0.47	-60.00	Karoo	This study
murrayi	UR 2688	118.62	0.56	6.88	0.42	-60.00	Karoo	This study
murrayi	NMQR 725	118.80	0.56	8.15	0.50	-60.00	Karoo	Botha 2020
declivis	FMNH UR2506	118.85	0.53	9.42	0.47	-60.00	Karoo	Botha 2020
murrayi	SAM-PK-K1268	118.89	0.56	5.64	0.34	-60.00	Karoo	This study
declivis	NMQR 815b	118.94	0.53	9.43	0.48	-60.00	Karoo	Botha 2020
declivis	SAM-PK-691	119.11	0.53	8.18	0.41	-60.00	Karoo	This study
declivis	BP/1/5214	119.13	0.53	17.33	0.87	-60.00	Karoo	This study
declivis	SAM-PK-3596	119.30	0.53	9.42	0.47	-60.00	Karoo	Botha 2020
murrayi	NMQR 4176	119.48	0.56	10.53	0.64	-60.00	Karoo	This study
murrayi	NMQR 5	119.73	0.56	8.22	0.50	-60.00	Karoo	Botha 2020
declivis	NMQR 735	119.73	0.53	9.48	0.48	-60.00	Karoo	This study
curvatus	D–2/93	120.00		5.00		-55.00	Damodar	Gupta and Das 2011
declivis	NMQR 161	120.17	0.53	9.51	0.48	-60.00	Karoo	Botha 2020
murrayi	UWBM 95525	120.23	0.56	8.25	0.50	-70.00	Transantarctic	This study
sp. indet.	SAM-PK-11215	120.24	0.45	9.40	0.38	-60.00	Karoo	This study
sp. indet.	BP/1/4639	120.27	0.45	8.33	0.34	-60.00	Karoo	Botha 2020
declivis	SAM-PK-K8566	120.32	0.53	7.17	0.36	-60.00	Karoo	This study
sp. indet.	BP/1/5866	120.37	0.45	24.70	1.00	-60.00	Karoo	This study
declivis	NMQR 365	120.48	0.53	9.54	0.48	-60.00	Karoo	This study
murrayi	BP/1/468	120.65	0.57	5.49	0.33	-60.00	Karoo	This study

sp. indet.	SAM-PK-K6	120.71	0.45	8.66	0.35	-60.00	Karoo	Botha 2020
murrayi	SAM-PK-3528	120.81	0.57	9.48	0.58	-60.00	Karoo	This study
declivis	K60/732	121.00	0.54	6.00	0.35	-55.00	Damodar	Gupta and Das 2011
declivis	NMQR 3917	121.13	0.54	9.58	0.48	-60.00	Karoo	This study
murrayi	GSI 17858	121.20	0.57	8.32	0.51	-55.00	Damodar	Ray 2005
murrayi	UR 2706	121.43	0.57	9.85	0.60	-60.00	Karoo	This study
murrayi	NMQR 3040	121.53	0.57	8.34	0.51	-60.00	Karoo	Botha 2020
declivis	NMQR 3735	121.85	0.54	9.63	0.49	-60.00	Karoo	This study
murrayi	NMQR 3751	121.98	0.57	8.38	0.51	-60.00	Karoo	This study
murrayi	NMQR 3751	121.98	0.57	7.78	0.47	-60.00	Karoo	This study
murrayi	NMQR 3765	122.01	0.57	8.67	0.53	-60.00	Karoo	This study
murrayi	NMQR 3840a	122.09	0.57	8.39	0.51	-60.00	Karoo	Botha 2020
murrayi	BP/1/466	122.18	0.57	8.51	0.52	-60.00	Karoo	This study
sp. indet.	BP/1/4304	122.63	0.46	9.58	0.39	-60.00	Karoo	This study
murrayi	NMQR 3649	122.66	0.58	5.48	0.33	-60.00	Karoo	This study
murrayi	GSI 17860	122.95	0.58	8.45	0.51	-55.00	Damodar	Ray 2005
murrayi	BP/1/3978	123.00	0.58	8.45	0.51	-60.00	Karoo	Botha 2020
sp. indet.	BP/1/4355	123.00	0.46	10.47	0.42	-60.00	Karoo	This study
declivis	SAM-PK-11527	123.97	0.55	9.78	0.49	-60.00	Karoo	This study
declivis	SAM-PK-K4800	124.15	0.55	8.06	0.41	-60.00	Karoo	This study
declivis	SAM-PK-K5	124.46	0.55	10.86	0.55	-60.00	Karoo	This study
sp. indet.	FARB 8249	124.48	0.47	7.20	0.29	-60.00	Karoo	This study
declivis	NMQR 132	124.64	0.55	9.83	0.50	-60.00	Karoo	Botha 2020
murrayi	SAM-PK-K1460	124.70	0.59	8.39	0.51	-60.00	Karoo	This study
declivis	NMQR 848	125.01	0.55	9.86	0.50	-60.00	Karoo	This study
China L. sp.	IVPP V18664	125.22	0.57	10.99	0.39	45.00	Turpan-Junggar	This study
declivis	NMQR 675	125.75	0.56	9.91	0.50	-60.00	Karoo	This study
sp. indet.	SAM-PK-K8519(A)	125.88	0.47	8.72	0.35	-60.00	Karoo	This study
declivis	BMNH 47324	126.00	0.56	9.92	0.50	-60.00	Karoo	Botha 2020
murrayi	BP/1/4710	126.00	0.59	8.67	0.53	-60.00	Karoo	Botha 2020
murrayi	TM 33	127.00	0.60	8.74	0.53	-60.00	Karoo	Botha 2020
murrayi	BP/1/5057	127.29	0.60	9.59	0.58	-60.00	Karoo	This study
murrayi	BP/1/5028	127.65	0.60	11.29	0.69	-60.00	Karoo	This study
murrayi	NMQR 721c	127.81	0.60	7.72	0.47	-60.00	Karoo	This study
murrayi	NMQR 393	127.83	0.60	8.80	0.54	-60.00	Karoo	This study
sp. indet.	SAM-PK-1272	127.84	0.48	9.99	0.40	-60.00	Karoo	Botha 2020

murrayi	NMQR 3539b	128.07	0.60	8.82	0.54	-60.00	Karoo	Botha 2020
murrayi	UR 2689	128.77	0.60	9.61	0.59	-60.00	Karoo	This study
declivis	SAM-PK-3455	128.83	0.57	10.12	0.51	-60.00	Karoo	This study
declivis	SAM-PK-K11518	128.95	0.57	10.59	0.53	-60.00	Karoo	This study
murrayi	NMQR 2065	129.08	0.61	8.89	0.54	-60.00	Karoo	Botha 2020
declivis	BP/1/267	129.41	0.57	10.30	0.52	-60.00	Karoo	This study
murrayi	NMQR 3960b	130.00	0.61	8.95	0.55	-60.00	Karoo	Botha 2020
murrayi	NMQR 3927b	130.07	0.61	7.68	0.47	-60.00	Karoo	This study
murrayi	SAM-PK-4326	130.09	0.61	11.28	0.69	-60.00	Karoo	This study
murrayi	NMQR 3540	130.74	0.61	9.82	0.60	-60.00	Karoo	This study
declivis	NMQR 4028b	130.84	0.58	10.27	0.52	-60.00	Karoo	Botha 2020
China L. sp.	IVPP V18663	130.90	0.60	8.32	0.30	45.00	Turpan-Junggar	This study
declivis	UC 1706	130.93	0.58	11.81	0.60	-60.00	Karoo	This study
murrayi	SAM-PK-K8520	130.95	0.61	7.95	0.48	-60.00	Karoo	This study
murrayi	SAM-PK-K1247	131.03	0.62	9.03	0.55	-60.00	Karoo	Botha 2020
curvatus	SAM-PK-K8014	131.62	0.66	8.95	0.52	-60.00	Karoo	This study
China L. sp.	IVPP V3242	132.00	0.60	8.20	0.29	45.00	Turpan-Junggar	This study
declivis	NMQR 3929	132.00	0.58	10.35	0.52	-60.00	Karoo	This study
sp. indet.	SAM-PK-11223	133.65	0.50	10.45	0.42	-60.00	Karoo	This study
sp. indet.	BP/1/4359	133.75	0.50	10.42	0.42	-60.00	Karoo	This study
murrayi	BP/1/5070	134.00	0.63	9.24	0.56	-60.00	Karoo	Botha 2020
declivis	SAM-PK-3455	134.00	0.59	10.49	0.53	-60.00	Karoo	Botha 2020
murrayi	NMQR 657	134.38	0.63	9.27	0.56	-60.00	Karoo	Botha 2020
declivis	SAM-PK-K1398	135.00	0.60	9.40	0.47	-60.00	Karoo	Botha 2020
declivis	BSP 1934-VIII-511	135.86	0.60	10.62	0.54	-60.00	Karoo	Botha 2020
declivis	NMQR 3575	135.86	0.60	10.62	0.54	-60.00	Karoo	Botha 2020
declivis	TM 20	136.00	0.60	10.63	0.54	-60.00	Karoo	Botha 2020
murrayi	NMQR 3571b	136.62	0.64	6.39	0.39	-60.00	Karoo	This study
declivis	NMQR 4096	136.70	0.60	10.68	0.54	-60.00	Karoo	This study
declivis	NMQR 126	136.80	0.61	10.69	0.54	-60.00	Karoo	Botha 2020
declivis	NMQR uncat	137.28	0.61	9.65	0.49	-60.00	Karoo	This study
declivis	NMQR 4145	137.75	0.61	10.75	0.54	-60.00	Karoo	This study

declivis	SAM-PK-11184a	138.00	0.61	10.77	0.54	-60.00	Karoo	Botha 2020
murrayi	SAM-PK-K26	138.27	0.65	8.63	0.53	-60.00	Karoo	This study
murrayi	NMQR 3539a	138.38	0.65	9.56	0.58	-60.00	Karoo	Botha 2020
sp. indet.	BP/1/1698	138.46	0.52	12.07	0.49	-60.00	Karoo	This study
sp. indet.	BP/1/4702	138.83	0.52	14.63	0.59	-60.00	Karoo	This study
declivis	SAM-PK-K10374	138.95	0.61	10.74	0.54	-60.00	Karoo	This study
murrayi	NMQR 622	139.16	0.65	8.56	0.52	-60.00	Karoo	This study
murrayi	NMQR 4172	139.29	0.65	9.46	0.58	-60.00	Karoo	This study
declivis	NMQR 3545	139.78	0.62	14.36	0.72	-60.00	Karoo	This study
declivis	UR 370	140.54	0.62	11.48	0.58	-60.00	Karoo	This study
declivis	BP/1/1379	140.81	0.62	10.57	0.53	-60.00	Karoo	Botha 2020
declivis	BPI MN109	141.00	0.62	10.98	0.55	-60.00	Karoo	Botha 2020
murrayi	BP/1/266	141.91	0.67	10.85	0.66	-60.00	Karoo	This study
murrayi	SAM-PK-K7	142.00	0.67	9.82	0.60	-60.00	Karoo	Botha 2020
declivis	BMNH 36221	142.45	0.63	11.08	0.56	-60.00	Karoo	Botha 2020
sp. indet.	SAM-PK-K8524	142.57	0.54	9.98	0.40	-60.00	Karoo	This study
sp. indet.	BP/1/4006a	142.62	0.54	10.03	0.41	-60.00	Karoo	This study
declivis	BMNH 36222	143.00	0.63	11.12	0.56	-60.00	Karoo	Botha 2020
sp. indet.	BP/1/4006b	143.51	0.54	9.53	0.39	-60.00	Karoo	This study
curvatus	SAM-PK-K4	143.60	0.72	11.65	0.68	-60.00	Karoo	This study
declivis	BP/1/489	143.79	0.64	19.84	1.00	-60.00	Karoo	This study
murrayi	TM 2881	144.00	0.68	9.96	0.61	-60.00	Karoo	Botha 2020
declivis	TM 4465	144.00	0.64	11.19	0.56	-60.00	Karoo	Botha 2020
murrayi	SAM-PK-K10385	144.28	0.68	7.71	0.47	-60.00	Karoo	This study
declivis	SAM-PK-K12	144.58	0.64	8.02	0.40	-60.00	Karoo	This study
declivis	BP/1/479	144.67	0.64	11.24	0.57	-60.00	Karoo	Botha 2020
murrayi	NMQR 3963	145.00	0.68	10.03	0.61	-60.00	Karoo	Botha 2020
declivis	NMQR 787b	145.41	0.64	11.29	0.57	-60.00	Karoo	This study
murrayi	SAM-PK-11181	146.00	0.69	10.11	0.62	-60.00	Karoo	Botha 2020
murrayi	SAM-PK-K8	146.00	0.69	10.11	0.62	-60.00	Karoo	This study
declivis	BP/1/267	146.30	0.65	11.35	0.57	-60.00	Karoo	Botha 2020
declivis	SAM-PK-K10373	146.44	0.65	13.37	0.67	-60.00	Karoo	This study
murrayi	SAM-PK-K10375	146.99	0.69	11.77	0.72	-60.00	Karoo	This study
declivis	BP/1/4798b	147.11	0.65	13.53	0.68	-60.00	Karoo	This study
declivis	NMQR 164	147.24	0.65	11.42	0.58	-60.00	Karoo	This study

murrayi	BP/1/7602	147.39	0.69	9.92	0.60	-60.00	Karoo	This study
declivis	NMQR 3926	147.79	0.65	11.46	0.58	-60.00	Karoo	This study
declivis	BP/1/4624a	148.00	0.65	11.47	0.58	-60.00	Karoo	Botha 2020
sp. indet.	BP/1/5175	148.15	0.56	9.27	0.38	-60.00	Karoo	This study
China L. sp.	IVPP V18654	148.16	0.68	19.30	0.69	45.00	Turpan-Junggar	This study
China L. sp.	IVPP V18665	149.07	0.68	9.34	0.33	45.00	Turpan-Junggar	This study
declivis	BP/1/4625	149.63	0.66	10.85	0.55	-60.00	Karoo	This study
murrayi	FARB 20882	150.13	0.70	11.63	0.71	-60.00	Karoo	This study
sp. indet.	BP/1/2240	150.51	0.57	10.37	0.42	-60.00	Karoo	Botha 2020
murrayi	NMQR 3565	150.60	0.71	10.44	0.64	-60.00	Karoo	Botha 2020
declivis	BP/1/477	151.10	0.67	10.73	0.54	-60.00	Karoo	This study
declivis	SAM-PK-K1378	151.10	0.67	11.69	0.59	-60.00	Karoo	Botha 2020
murrayi	SAM-PK-K1399	151.61	0.71	11.68	0.71	-60.00	Karoo	This study
sp. indet.	BP/1/4366	153.36	0.58	9.30	0.38	-60.00	Karoo	This study
declivis	NMQR 356	153.56	0.68	11.87	0.60	-60.00	Karoo	Botha 2020
declivis	NMQR 1620	154.86	0.69	10.86	0.55	-60.00	Karoo	This study
declivis	NMQR 4037	156.92	0.69	12.10	0.61	-60.00	Karoo	This study
sp. indet.	SAM-PK-705	157.66	0.59	13.70	0.55	-60.00	Karoo	This study
murrayi	BMNH 1291	159.00	0.75	11.04	0.67	-60.00	Karoo	Botha 2020
murrayi	SAM-PK-271	159.45	0.75	10.77	0.66	-60.00	Karoo	This study
murrayi	NMQR 835a	159.55	0.75	12.29	0.75	-60.00	Karoo	This study
China L. sp.	IVPP V18657	159.58	0.73	9.27	0.33	45.00	Turpan-Junggar	This study
sp. indet.	SAM-PK-3599	159.61	0.60	12.49	0.51	-60.00	Karoo	This study
murrayi	MHMUK PVR1291	160.00	0.75	11.11	0.68	-60.00	Karoo	This study
maccaigi	NMQR 3641	160.00	0.60			-60.00	Karoo	Botha 2020
China L. sp.	IVPP V10075	160.69	0.74	23.25	0.83	45.00	Turpan-Junggar	This study
sp. indet.	SAM-PK-11166	161.68	0.61	12.66	0.51	-60.00	Karoo	This study
declivis	SAM-PK-K8013	162.34	0.72	10.48	0.53	-60.00	Karoo	This study
sp. indet.	SAM-PK-K10092	163.14	0.61	13.70	0.55	-60.00	Karoo	This study
sp. indet.	BP/1/4339	163.82	0.62	12.79	0.52	-60.00	Karoo	This study
China L. sp.	IVPP V18653	165.11	0.76	18.70	0.67	45.00	Turpan-Junggar	This study
China L. sp.	IVPP V18673	165.60	0.76	16.25	0.58	45.00	Turpan-Junggar	This study
declivis	NMQR 1866	165.72	0.73	14.47	0.73	-60.00	Karoo	This study

China L. sp.	IVPP V3248	165.75	0.76	14.88	0.53	45.00	Turpan-Junggar	This study
declivis	BP/1/4353	166.77	0.74	15.60	0.79	-60.00	Karoo	This study
murrayi	NMQR 3540a	168.47	0.79	9.27	0.56	-60.00	Karoo	This study
declivis	FARB 5600	169.00	0.75	12.76	0.64	-60.00	Karoo	This study
China L. sp.	IVPP RV35012	169.40	0.77	14.71	0.53	45.00	Turpan-Junggar	This study
murrayi	NMQR 3559	169.77	0.80	16.41	1.00	-60.00	Karoo	This study
declivis	SAM-PK-K10379	169.78	0.75	14.44	0.73	-60.00	Karoo	This study
sp. indet.	BP/1/5865	170.80	0.64	13.54	0.55	-60.00	Karoo	This study
China L. sp.	IVPP RV390600	170.92	0.78	14.88	0.53	45.00	Turpan-Junggar	This study
China L. sp.	IVPP V4457	171.52	0.78	15.06	0.54	45.00	Turpan-Junggar	This study
declivis	FARB 7725	172.00	0.76	11.62	0.59	-60.00	Karoo	This study
declivis	TM 21	173.00	0.77	13.23	0.67	-60.00	Karoo	Botha 2020
declivis	SAM-PK-K10377	174.62	0.77	18.91	0.95	-60.00	Karoo	This study
China L. sp.	XJ/ZAI	175.90	0.80	14.27	0.51	45.00	Turpan-Junggar	This study
declivis	BP/1/878	175.90	0.78	13.20	0.67	-60.00	Karoo	This study
sp. indet.	SAM-PK-K10	179.29	0.67	16.59	0.67	-60.00	Karoo	This study
declivis	BP/1/2816	180.68	0.80	7.53	0.38	-60.00	Karoo	This study
declivis	NMQR 424	180.70	0.80	13.78	0.69	-60.00	Karoo	This study
China L. sp.	IVPP V18670	184.95	0.85	16.37	0.58	45.00	Turpan-Junggar	This study
declivis	NMQR 1485	185.00	0.82	14.08	0.71	-60.00	Karoo	Botha 2020
declivis	TM 3580	185.00	0.82	14.08	0.71	-60.00	Karoo	Botha 2020
curvatus	BP/1/4048	185.58	0.93	11.03	0.64	-60.00	Karoo	This study
declivis	NMQR 3181	186.03	0.82	13.75	0.69	-60.00	Karoo	This study
maccaigi	NMQR 3689	186.90	0.70			-60.00	Karoo	This study
China L. sp.	IVPP 63005-2	187.79	0.86	15.54	0.56	45.00	Turpan-Junggar	This study
curvatus	BP/1/464	188.77	0.94	16.81	0.98	-60.00	Karoo	This study
China L. sp.	IVPP V3244	189.33	0.87	15.99	0.57	45.00	Turpan-Junggar	This study
curvatus	SAM-PK-7843	189.64	0.95	13.89	0.81	-60.00	Karoo	This study
maccaigi	NMQR 3648	190.00	0.71			-60.00	Karoo	Botha 2020
China L. sp.	IVPP V3246	190.03	0.87	14.55	0.52	45.00	Turpan-Junggar	This study
declivis	NMQR 3738	190.80	0.84	14.49	0.73	-60.00	Karoo	This study
China L. sp.	IVPP V18659	192.90	0.88	17.78	0.64	45.00	Turpan-Junggar	This study
China L. sp.	630040L	193.19	0.88	15.20	0.54	45.00	Turpan-Junggar	This study

sp. indet.	BP/1/4717	194.35	0.73	17.79	0.72	-60.00	Karoo	This study
China L. sp.	V63002	194.71	0.89	16.07	0.57	45.00	Turpan-Junggar	This study
China L. sp.	IVPP V13462	198.37	0.91	17.91	0.64	45.00	Turpan-Junggar	This study
declivis	BP/1/1754	199.43	0.88	13.24	0.67	-60.00	Karoo	This study
murrayi	YPM 2225	200.00	0.94	13.99	0.85	-60.00	Karoo	Botha 2020
curvatus	BP/1/3976	200.14	1.00	17.16	1.00	-60.00	Karoo	This study
declivis	SAM-PK-3593	203.00	0.90	15.35	0.77	-60.00	Karoo	Botha 2020
declivis	SAM-PK-K8038	205.59	0.91	19.54	0.98	-60.00	Karoo	This study
China L. sp.	IVPP V3265	205.76	0.94	16.65	0.59	45.00	Turpan-Junggar	This study
maccaigi	BP/I/879	206.06	0.60	20.52	0.71	-60.00	Karoo	This study
declivis	SAM-PK-706	206.12	0.91	14.38	0.72	-60.00	Karoo	This study
declivis	BP/1/4624b	209.00	0.92	10.37	0.52	-60.00	Karoo	This study
China L. sp.	SS-13-2-1	209.69	0.96	20.50	0.73	45.00	Turpan-Junggar	This study
China L. sp.	IVPP V18660	209.81	0.96	18.73	0.67	45.00	Turpan-Junggar	This study
China L. sp.	IVPP V3247	210.34	0.96	16.45	0.59	45.00	Turpan-Junggar	This study
murrayi	BP/1/3236	213.00	1.00	14.93	0.91	-60.00	Karoo	Botha 2020
China L. sp.	IVPP V3243	215.00	0.98	15.35	0.55	45.00	Turpan-Junggar	This study
China L. sp.	IVPP V18672	218.59	1.00	28.00	1.00	45.00	Turpan-Junggar	This study
declivis	NMQR 4027	226.00	1.00	16.96	0.86	-60.00	Karoo	Botha 2020
maccaigi	WSU 0974	263.33	0.99	16.21	0.68	-70.00	Transantarctic	This study
sp. indet.	SAM-PK-11234	266.00	1.00	20.87	0.84	-60.00	Karoo	This study
maccaigi	FARB 24200	266.57	1.00	23.81	1.00	-70.00	Transantarctic	This study
maccaigi	SAM-PK-K9958	277.86	0.93	19.16	0.66	-60.00	Karoo	This study
China L. sp.	IVPP V3263			9.85	0.35	45.00	Turpan-Junggar	This study
China L. sp.	IVPP V18668			13.65	0.49	45.00	Turpan-Junggar	This study
China L. sp.	XJ12/ZAI			15.94	0.57	45.00	Turpan-Junggar	This study
China L. sp.	IVPP V83025			20.71	0.74	45.00	Turpan-Junggar	This study

Chapter 4. DIVERGENT GROWTH TRAJECTORIES REVEALED THROUGH HISTOLOGICAL ANALYSES OF *SCALENODON ANGUSTIFRONS* AND *LUANGWA DRYSDALLI* (CYNODONTIA: TRAVERSODONTIDAE) FROM THE ANISIAN MANDA BEDS OF TANZANIA

4.1 ABSTRACT

This study reports the first bone tissue composition from a temporally and spatially constrained assemblage of cynodont species that were thin sectioned to assess whether size and developmental stage are correlated in two closely related traversodontids species, *Scalenodon* and *Luangwa*. Sixteen femora were sampled, eight from each species, respectively, from size ranges that span the smallest to largest available femora in collections housed at the Burke Museum. *Luangwa* femoral histology is characterized by parallel-fiber dominated woven-parallel bone with extensive endosteally deposited bone, which I interpret as adaptation for fossoriality. In contrast, *Scalenodon* femoral histology shows highly variable tissue composition with respect to element size, indicating that growth was developmentally plastic in this species. Interestingly, femoral cortices are similarly thick in *Scalenodon*. However, these thick cortices were achieved via highly disorganized woven-dominated tissue that was directed periosteally, unlike the more organized and mineralized endosteal tissue seen in *Luangwa*. From these results, I review the evolution of traversodontid growth trajectories, summarize growth trajectories known for cynodont species more broadly, and comment on histological sampling intensity, or lack thereof, in order to contextualize the validity of different developmental strategies known for cynodont species that have been analyzed thus far.

4.2 INTRODUCTION

The fossil record of non-mammalian cynodonts reveals that multiple mammalian traits originated among Permian-Triassic species. Indeed, unlike the evolution of some other major clades (e.g., Tetrapoda, Aves), the origin of mammals does not coincide with a major morphological change, but rather a series of more and more mammal-like transitional forms (Sidor and Hopson, 1998). Mammalian traits that evolved in Permo-Triassic cynodont species include a bony secondary palate that separates oral and nasal passages, an attachment point to the vertebral column made up of double occipital condyles, multi-cusped teeth that precisely occlude, a more upright and parasagittal stance, and a regionalized vertebral column with a separate thoracic region with lumbar region that lacks ribs (Hopson, 1969; Jenkins, 1973; Crompton, 1963, Crompton et al., 1972; Kemp, 1980; Sidor and Hopson, 1998; Jones et al., 2018). The evolution of these skeletal features has been hypothesized to be related to the evolution of a more mammal-like physiology and growth trajectory but directly assessing life history and physiology in extinct species is notoriously difficult.

Bone histology is a prime method for assessing rates of growth in the fossil record and provides critical insight into growth trajectories and physiological inferences in extinct taxa. Histological analyses of bone tissue composition have been instrumental in reconstructing the biology of multiple synapsid subclades (e.g., Huttenlocker and Rega, 2012; Chinsamy-Turan, 2012; Ray and Botha-Brink, 2012; Hurum and Chinsamy-Turan, 2012; Botha-Brink et al., 2012; Botha and Huttenlocker, 2021). Indeed, previous hypotheses link the evolution of mammal-like growth patterns (i.e., rapid postnatal growth that plateaus abruptly at sexual/skeletal maturity) as a consequence of the evolution of other mammalian traits like maternal care, live birth, and lactation (de Ricqlès, 1974; McNab, 1978; Hopson, 1973, 2012; Farmer, 2000; Koteja, 2000;

Luo et al., 2004; Kemp, 2006). However, assessing growth trajectories requires an understanding of which developmental stages have been preserved from the cynodont fossil record. In other words, are both juveniles and adults preserved? Without these details, the timing of the onset of life history tradeoffs, the duration and rate of growth during development, and whether growth strategies are constrained or highly flexible, remain unclear.

The fossil assemblage of the Anisian Manda Beds of Tanzania provides an exceptional opportunity to assess growth, longevity, and life history patterns in cynodonts as at least six species co-occur in the mid-upper Lifua Member. Undescribed cranial remains temporarily housed at the Burke Museum are attributed to *Scalenodon angustifrons*, *Mandagomphodon attridgei*, *Luangwa drysdalli*, *Aleodon brachyrhamphus*, and *Cricodon metabolus*. Historical collections of *C. metabolus*, *S. angustifrons*, *A. brachyrhamphus* and other fossils originally collected by Stockley in the 1930's were described by Crompton (1955). *Mandagomphodon hirschoni* was described by Hopson (2014) and is one of three species of traversodontids previously assigned to *Scalenodon* that has since been generically re-assigned. For a complete review of traversodontid taxonomy see Liu and Abdala (2014). Importantly, *M. attridgei* and *M. hirschoni* lack associated postcranial remains, whereas the remaining four species are known from skulls, associated skeletons, or referable isolated elements (see descriptions below).

To assess whether size/age correlations and life history patterns are reflected in a histologic sample of cynodont femora, we are working under the hypothesis that life history is adaptive within a species in ways that can be linked to variation in an individual's environment (herein considered extrinsic factors) and that phylogenetic affinity (herein considered one of many intrinsic factors) can influence ecology, body size, and other intrinsic factors that influence growth rates. By controlling for paleoenvironment and by sampling the bone histology of close

relatives (e.g., *S. angustifrons* and *L. drysdalli*, Fig. 4.1), differential life histories can be recognized in the extinct forerunners of mammals. By extension, if size/age correlations are born out in the multitaxic histological sample, then growth trajectories can be elucidated for these contemporaneous traversodontids species. If, however, histological differences in bone tissue composition are not detected between close relatives, then the hypothesis that early diverging traversodontids shared a characteristic growth trajectory would gain support. Lastly, if size and age are not correlated among individuals, this would either provide evidence that a complete ontogenetic trajectory is not preserved (i.e., if only juvenile tissue types are seen), or that highly variable developmental trajectories existed in some cynodonts, which has been shown in the bone histology of the early dinosauriform *Asilisaurus kongwe* from the Manda Beds (Griffin and Nesbitt, 2016a).

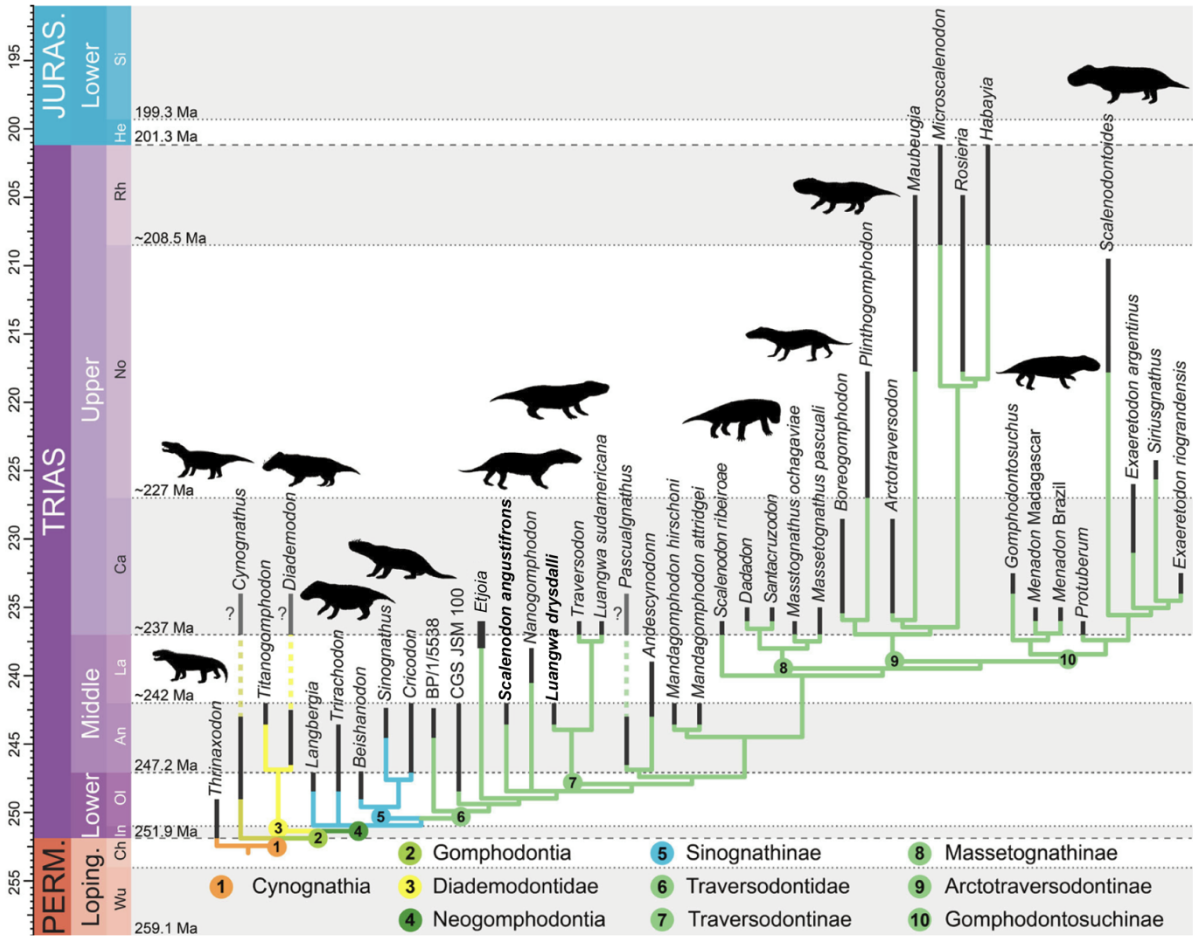

Figure 4.1. Cladogram of Traversodontidae, adapted from Hendrickx et al. (2020). The two histologically sampled species, *S. angustifrons* and *L. drysdalli*, co-occur in the Anisian Manda Beds of Tanzania and are highlighted in bold.

4.2.1 ***Background on Cynodont Paleobiology***

The earliest nonmammaliaform cynodonts (herein referred to as cynodonts) are known from the upper Permian Beaufort Group of South Africa's Karoo Basin and their equivalent strata in Russia (Hopson, 1969; Botha, Abdala, and Smith 2007; Botha-Brink et al., 2012). Their fossil record extends into the Lower Cretaceous of Russia and documents a major radiation of herbivorous-omnivorous forms during Middle-Late Triassic times (Hopson, 1969; Hendrickx et al., 2020; Tatarinov and Matchenko, 1999). The earliest cynodonts are small-bodied Permian insectivorous or carnivorous species that are characterized by a long series of multicusped teeth (e.g., *Abdalodon*, *Dvinia*, *Charrasognathus*) (Abdala et al., 2021; Huttenlocker and Sidor, 2020). However, these early diverging forms also possess cynodont hallmarks that are considered to be related to improvements in oral food processing and mastication, including: flared zygomatic arches, a masseteric fossa on the dentary, a small reflected lamina on the angular, and complex cusps on a long row of cheek teeth (Barghusen, 1968; Hopson, 1969).

The remaining radiation of cynodonts form a monophyletic group called Eucynodontia. *Galesaurus* and *Thrinaxodon*, which are among the earliest representative of this clade, are known from the Early Triassic of South Africa and were small, insectivorous forms often found in, or in close association to burrows, suggesting a fossorial lifestyle (Hopson, 1969; Botha-Brink, et al., 2012; Groenewald et al., 2001).

By Middle Triassic times, eucynodonts had radiated into two major divisions, the Cynognathia and the Probainognathia. The cynognathian fossil record from Africa and South America show a diversification into large and ecologically diverse species, including very large carnivores such as *Cynognathus* (skull = 415 mm in length) and the medium-large omnivorous and herbivorous group known as the Gomphodontia (sensu Abdala and Ribiero, 2003).

Gomphodontians include the families Diademodontidae, Trirachodontidae, and Traversodontidae, and are characterized by highly specialized transversely expanded postcanine teeth (Crompton, 1972; Hendrickx et al., 2020).

During the Middle-Late Triassic, Traversodontidae diversified into a major radiation with over 20 genus-level taxa known from Africa, South America, North America, and Europe (Abdala and Ribiero, 2010; Liu and Abdala, 2014; Tolchard et al., 2021). As key components of paleocommunities across Pangea, traversodontids became the most taxonomically and geographically diverse clade of cynodonts during the Triassic (Abdala and Gaetano, 2018). Such a radiation can partly be explained by their diverse dental morphologies which enabled them to occupy different ecological niches (Crompton, 1972; Hendrickx et al, 2020).

Traversodontids have transversely expanded gomphodont postcanine teeth enabling precise occlusion (Sues, 2000) and each taxon can be differentiated by a combination of cusps, crests, and basins positioned on the crowns and along the tooth row. Compared to trirachodontids or diademodontids, traversodontid postcanines lack accessory ridges on the transverse crest and do not have well-developed cingula bounding the crown (Hendrickx et al., 2020). Traversodontids are also generally characterized by the absence of sectorial (i.e., blade-like) postcanines, with only some small or early diverging species having a reduced number retained at the posterior end of the toothrow, (e.g., *Etjoia*, *Andescynodon*, *Massetognathus*, and *Boreogomphodon*) (Goni and Goin, 1988; Liu and Sues, 2010; Sues and Hopson, 2010; Hendrickx et al., 2020). Sectorial teeth are plesiomorphic for Eucynodontia and are retained in the other two gomphodont radiations represented by members of Diademodontidae and Trirachodontidae (Hendrickx, et al., 2019).

Dental microwear patterns have been used to reconstruct the diet of various traversodontid species but no consensus has formed with respect to which taxa were obligately herbivorous. Hendrickx et al. (2020) summarized gomphodont dental evolution and suggested that the loss of sectorial upper and lower postcanines and the development of conical and transversely expanded gomphodont upper and lower postcanines in basal-most gomphodonts was likely the result of shifting feeding strategies, from a carnivorous diet in basal-most cynognathians (i.e., *Cynognathus*) to an omnivorous feeding ecology in basal gomphodonts (Crompton, 1972; Hopson and Kitching, 1972; Gow, 1978). Hendrickx et al., (2020) also suggested that the loss of shearing planes between upper and lower postcanines in taxa more derived than *Diademodon* could be interpreted as a shift towards omnivorous, carnivorous or insectivorous diets. In trirachodontids, (e.g., *Trirachodon* and *Langbergia*) an inferred carnivorous or insectivorous diet is further evidenced by the development additional lingual and labial cingula covered in cuspules (Gow, 1987; Crompton,1972; Hopson, 2005).

While toothrow simplification characterizes basal-most traversodontids due to the loss of sectorial postcanines, deep lingual and labial basins on the postcanines as well as shearing planes between upper and lower teeth are also characteristic of traversodontid dentition (Crompton, 1972). These features have led paleontologists to interpret traversodontid feeding ecologies as plant dominated (Hendrickx et al., 2020). However, like other gomphodonts, basal-most traversodontids like *L. drysdalli* retained serrated canines, which could either be interpreted as a plesiomorphy from shared ancestry with trirachodontids with serrated teeth, or as an adaptation to better capture prey or process food more efficiently. Furthermore, ontogenetic shifts in dietary ecology are not well understood for traversodontids. Recent insights from cranial dimensions, sutural complexity, and microwear patterns of the largest traversodont species known from South

America, *Exaeretodon argentinus* (skull = 459.9 mm in length), reveal that smaller individuals had a crushing-dominated feeding style that transitioned into a chewing-dominated feeding style at large size (Wynd, et al., 2022). Those authors suggested that *E. argentinus* likely shifted from a faunivorous to plant-dominated diet during development, a pattern that may be more widespread among traversodontids. This hypothesis awaits further testing as microwear analysis has been performed on few traversodontids and gomphodonts more broadly.

4.2.2 ***Problems with Inferred Cynodont Growth Trajectories***

Numerous cynodont species that have been histologically sampled are limited to small sample sizes, often of unstandardized elements at unknown lengths and sometimes of unknown element type or taxonomic assignment (Fig. 4.2, de Ricqlès 1969, de Ricqlès 1974; Chinsamy and Abdala 2008; Botha-Brink et al. 2012; Veiga et al., 2018). Inferring macroevolutionary shifts in growth strategies from such an incomplete sample is tenuous. Not only are previous claims based on poorly controlled samples of disparate elements, previous authors have overlooked the effects of ecology, environment, and phylogeny on bone tissue microstructure and instead focus largely on physiological or life history implications (Ray et al., 2004; Botha and Chinsamy, 2004; Botha and Chinsamy, 2005; Chinsamy and Hurum, 2006; Botha-Brink et al., 2018). This calls into question the validity of some previously inferred cynodont growth strategies that have been assessed from isolated, individual elements. Growth trajectories cannot be confidently assessed from this type of sample as histological variation occurs within a single element and across the skeleton (de Margerie et al., 2002; Woodward et al., 2014; Prondvai et al., 2018). Inter- and intra-bone histovariation must be addressed with increased sample sizes and

increased clarity of element size to robustly reconstruct life history patterns and growth strategies in the mammalian stem.

In addition, previous efforts to reconstruct cynodont growth trajectories largely focused on the presence or absence of rapidly growing fibrolamellar or woven-parallel-fibered tissue. This is an inadequate reconstruction of growth trajectories since the presence of fibrolamellar bone is not indicative of sustained rapid growth, but rather the ability to grow rapidly. In fact, fibrolamellar bone has been seen in early tetrapods, reptiles, non-avian dinosaurs, and in sphenacodontid-grade pelycosaurs suggesting that fibrolamellar/woven-parallel bone may be plesiomorphic for tetrapoda (Curry, 1999; Cubo et al., 2005; Woodward et al., 2014; Shelton and Sander, 2017; Whitney et al., 2022).

Instead, the proportion of rapidly growing tissue over the entirety of an animal's growth period at various stages of maturity is a better measure of growth strategy, but this requires a histologic sample that spans multiple sizes and inferred growth stages from species that experienced the same relative environmental conditions. Another useful indicator of growth strategy is the presence of periodic LAGs in rapidly growing tissue that can be used to estimated absolute age. The number of factors that cause animals to arrest growth differs from seasonal, endogenous circadian effects (e.g., Köhler et al., 2012) and from stressful life history events like birth, hatching, or weaning (e.g., Nacarino-Meneses and Köhler, 2018). Only with a large, comprehensive histological sample can the nuances of which growth marks (if any) correspond to non-cyclical or cyclical arrests be clarified.

4.2.3 *Previous Histological Analyses of Coeval Cynodont Species*

Two previous histological studies have made comparisons between coeval cynodont species. One study performed by Botha-Brink and Chinsamy (2000) investigated the growth strategies of two sister taxa from the Triassic of South Africa. *Diademodon*, an inferred herbivore, showed vascularized fibrolamellar bone with periodic cessations in growth. Its coeval close relative, *Cynognathus*, an inferred carnivore, showed continuous vascularized fibrolamellar bone. These authors concluded that a physiological difference might explain the different growth strategies in these taxa of similar adult size. Alternatively, they suggested that an herbivorous diet may have left *Diademodon* more susceptible to seasonally available food resources whereas carnivory in *Cynognathus* could mitigate this effect (Botha-Brink and Chinsamy, 2000). However, not all *Diademodon* samples preserve cyclical growth marks, suggesting that ontogenetic variation in growth rate may explain the absence of growth marks in some small, rapidly growing individuals (Kulik, pers. obs.). Taken together, there is some evidence that seasonal environmental changes affected bone growth in *Diademodon*, but the extent to which this effect is seen in other extinct cynognathian genera is unclear without a larger sample size.

In another assessment of coeval cynodont growth, Botha and Chinsamy (2005) documented sustained rapid growth in *Thrinaxodon* which was later compared by Butler et al., (2019) to the prolonged phase of moderately paced parallel-fibered bone in *Galesaurus*. However, neither of these previous reports were able to constrain a histological sample to a precise geographic area and instead sampled broadly within time bins, therefore local paleoclimatic effects on bone tissue composition could not be controlled.

The current work represents the third study to assess coeval species from a histological perspective and leverages a large sample size that can be confidently constrained one geographic

area and geologic era from the Anisian Manda Beds of Tanzania. No other examples exist in the cynodont literature where relatively large samples are gathered from size series of coeval (but not necessarily co-occurring) cynodont postcrania to reconstruct growth strategies and life history patterns (Fig. 4.2).

4.2.4 *Effects on Bone Morphogenesis*

Since the 1950's the number of histological analyses aimed at understanding the various effects that ontogeny, physiology, environmental conditions, and phylogenetic ancestry have on bone tissue organization has increased dramatically (Enlow and Brown, 1958; Francillon-Vieillot et al., 1990; Horner et al., 1999; Starck and Chinsamy, 2002; de Margerie et al., 2002; Cubo et al., 2005; Cubo et al., 2012, 2008; de Margerie et al., 2004; Nacarino-Meneses et al., 2016; Jordana et al., 2016; Padian and de Ricqlès, 2020). In addition to life history, many of these authors attempted to tease apart the influences that exist in bone micro-composition due to intra-bone, inter-bone, intraspecific, ontogenetic, phylogenetic, and environmental variation (Padian et al., 2013; Buffrénil et al., 2021; Cubo et al., 2021).

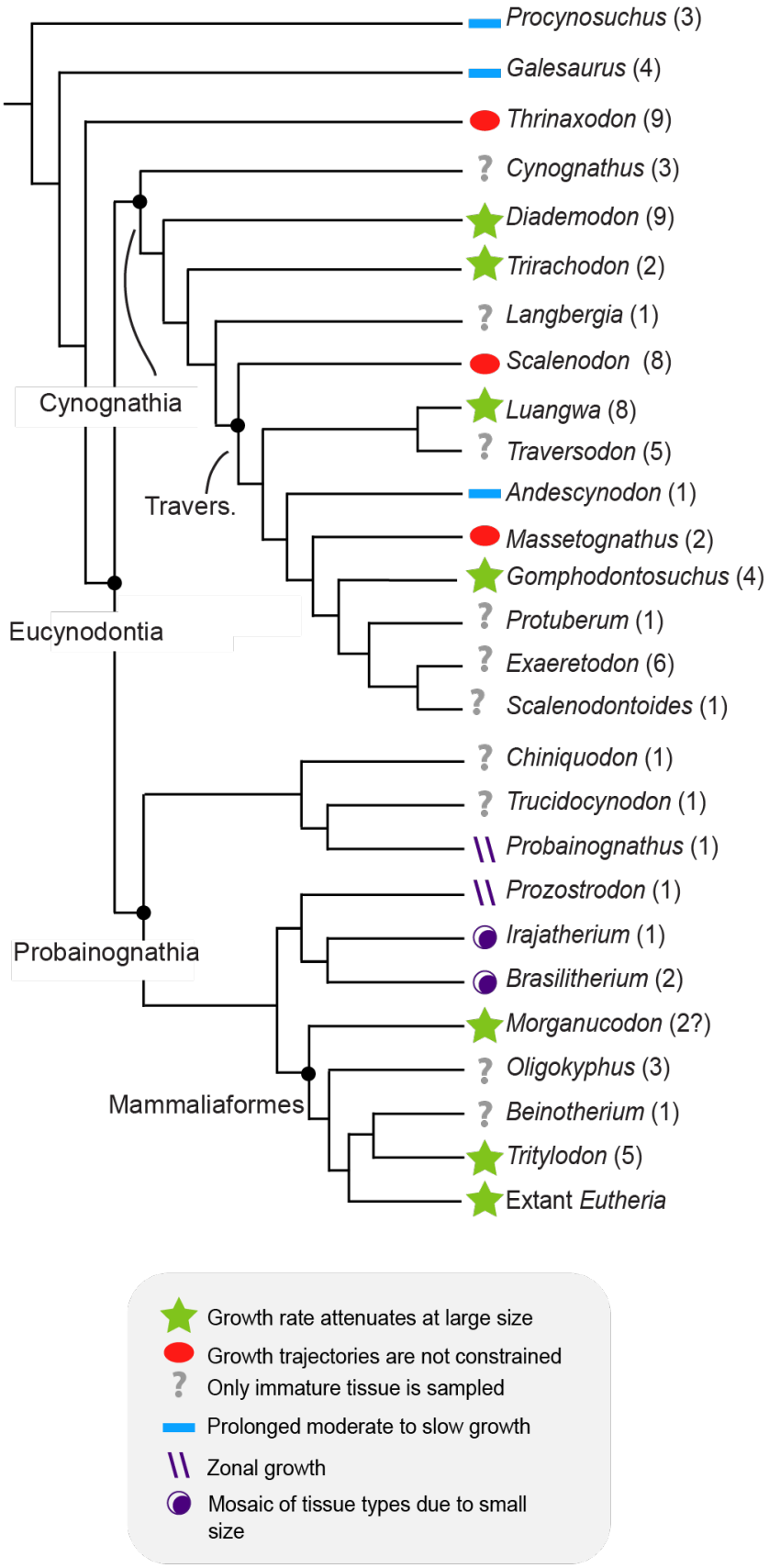
Procynosuchus (3)
Galesaurus (4)
Thrinaxodon (9)
Cynognathus (3)
Diademodon (9)
Trirachodon (2)
Langbergia (1)
Scalenodon (8)
Luangwa (8)
Traversodon (5)
Andescynodon (1)
Massetognathus (2)
Gomphodontosuchus (4)
Protuberum (1)
Exaeretodon (6)
Scalenodontoides (1)
Chiniquodon (1)
Trucidocynodon (1)
Probainognathus (1)
Prozostrodon (1)
Irajatherium (1)
Brasilitherium (2)
Morganucodon (2?)
Oligokyphus (3)
Beinotherium (1)
Tritylodon (5)
Extant Eutheria
Cynognathia
Travers.
Eucynodontia
Probainognathia
Mammaliaformes
Growth rate attenuates at large size
Growth trajectories are not constrained
Only immature tissue is sampled
Prolonged moderate to slow growth
Zonal growth
Mosaic of tissue types due to small size

Figure 4.2. Cladogram of histologically sampled cynodonts compiled from the literature and from this study. The number of histologically sampled individuals are shown in parentheses. The presence of peripheral slow growing tissue is indicated by a green star. Growth trajectories that are unconstrained, either due to poor sampling coverage or due to highly plastic growth are indicated by a red oval. Question marks denote species where only immature bone tissue has been sampled. Blue dashes indicate slow or moderately paced growth that is not dominated by a woven-parallel complex. Purple backslashes denote zonal growth strategies that do no attenuate at large size. Purple crescents indicate a mosaic of tissue types (i.e., woven-, parallel-fibered, and lamellar bone) that compose the cortices of very small species. For more information on the specific tissue types and elements sampled, see 4.11 Supplementary Data Table 1. Abbreviations: Travers., Traversodontidae.

Some generalizations can be made with respect to body size. For example, small mammals show a distinctive growth pattern that is less vascularized than larger mammals (e.g., Weaver et al., 2022). Despite lower vascularity, many small mammals grow rapidly and abruptly stop growing in a matter of weeks (Case, 1978; Harvey et al., 1991; Lui and Baron, 2011; however, see bathyerids; Montoya-Sanhueza and Chinsamy, 2017). A short growth period is a result of small body size, shorter lifespan, and faster reproductive rates in these animals (Case, 1978; Ricklefs et al., 1996). By contrast, larger bodied animals have a prolonged period of rapid growth but reach sexual maturity in a matter of months to one year (Jordana et al., 2016; Nacarino-Meneses et al., 2016a; Nacarino-Meneses et al, 2016b; Nacarino-Meneses and Köhler, 2018; Köhler et al., in press). From this difference in growth phase, one can expect larger animals to be more susceptible to external factors affecting tissue formation since they take longer to reach maturity. By contrast, smaller animals stop growing well before one year and are thus not as susceptible to factors influencing appositional bone tissue organization but are generally as equally susceptible to remodeling and restructuring of perimedular bone.

The extent to which co-variation between body size and: (i) ecology, (ii) shared ancestry, or (iii) environmental fluctuation affects growth strategy across mammalian diversity is poorly known. However, comprehensive histological sampling of mammalian orders has grown in recent years and was summarized by Buffrénil et al. (2021). Namely, ruminants, bovids, equids, primates, and humans represent the majority of large-bodied histological studies (Buffrénil et al., 2021). While some patterns have emerged, such as extensive Haversian remodeling among primates (reviewed in Buffrénil et al., 2021), the broader effects of ontogeny, ecology, and phylogeny on bone tissue microstructure in extant mammals remains underexplored. With so few living mammals histologically sampled, can we expect mammal-like growth trajectories across

disparate mammal clades? Of the non-mammalian synapsids that have been sampled, are we instead seeing individual variation instead of a changing growth strategy? Determining what variation exists in the bone tissue microstructure of living mammals of known body sizes, ecologies, life history, and growth rates will shed light on the variation that can be expected in fossil thin-sections.

4.2.5 *Histological Insights of Non-mammaliaform Cynodont Paleobiology*

Over the past 60+ years, twenty-five species of non-mammalian cynodonts have been histologically sampled and described in the literature (Fig. 4.2; de Ricqlès, 1969; Botha-Brink and Chinsamy, 2000, 2004, 2005; Ray et al., 2004; Chinsamy and Hurum, 2006; Chinsamy and Abdala, 2008; Botha-Brink et al., 2012, 2018; Veiga et al., 2018; Butler et al., 2019; Botha and Huttenlocker, 2021; Garcia Marsà et al., 2022). Previous studies have focused on early diverging members (e.g., *Procynosuchus*, *Thrinaxodon*, *Galesaurus*) to provide insights into the growth rates and developmental patterns that might have contributed to the survival of the cynodont lineage through the end-Permian mass extinction (de Ricqlès, 1969; Botha and Chinsamy, 2005; Butler et al., 2019). These include histological analyses of a clavicle, radius, and rib of three individuals referable to *Procynosuchus sp.* that were first described by Ray et al., (2004) and show a transition from fibrolamellar bone in the deep cortex to lamellar zonal bone in the middle and outer cortices of this basal form. The maintenance of slow growing lamellar bone interrupted by multiple LAGs in these small-bodied individuals indicates that skeletal growth proceeded slowly and was cyclically interrupted, likely due to endogenous circadian cycles that have been shown to coincide with unfavorable periods of the year when skeletal growth arrests in extant mammalian taxa (Castanet, 2004; Köhler et al., 2012, Köhler et al., in press).

The epicynodonts *Galesaurus* and *Thrinaxodon* were histologically sampled from multiple elements of associated individuals to evaluate histovariation across the skeleton throughout ontogeny (de Ricqlès, 1969; Botha and Chinsamy, 2005; Butler et al., 2019). *Thrinaxodon* histology documents a shift from fibrolamellar bone to peripheral parallel-fibered bone from elements between 42%–97% maximum known size. The predominance of lamellar zonal tissue indicates a prolonged phase of slow growth. The abrupt transition from fibrolamellar tissue to lamellar bone has been suggested to coincide with the life history tradeoff from growth to reproduction (Botha and Chinsamy, 2005). However, the proportion of this slow growing tissue does not scale with element size, so the timing of when in ontogeny the shift towards slow growth does not seem to be well-constrained in *Thrinaxodon*, which may have afforded an advantageously flexible developmental strategy that enabled its survival during fluctuating climates of the Early Triassic or its ability to reach the Antarctic portion of southern Pangea (which *Galesaurus* didn't seem to do) (Botha-Brink et al., 2012). *Thrinaxodon* also documents a growth strategy that is not regularly interrupted by growth marks, unlike *Procynosuchus*, suggesting that growth proceeded at a rapid rate throughout early ontogeny until the life history tradeoff towards reproduction occurred. In contrast, *Galesaurus* osteohistology documents parallel-fibered bone that transitions to peripheral lamellar zonal tissue, indicating that growth proceeded slowly and over a prolonged period of time before skeletal maturity was reached (Butler et al., 2019).

Cynognathian osteohistology represent the first group of cynodonts to demonstrate physiological differences related to growth strategy driven by dietary niche (Botha-Brink and Chinsamy, 2000). For example, *Cynognathus* femora are composed of sustained rapidly deposited woven-parallel tissue whereas the co-occurring and similarly large *Diademodon*

femora recovered from the same horizons in the South African Karoo Basin document cyclical growth marks in an otherwise woven-parallel complex. In *Diademodon*, growth marks become increasingly closely spaced in large individuals and represent attainment of skeletal maturity in the form of a thin EFS (Botha and Chinsamy, 2000). Importantly, histologically sampled specimens of *Diademodon* were collected from three locations (Rouxville, Aliwal North, and Lady Frere), whereas *Cynognathus* specimens were collected from Aliwal North. Therefore, these specimens do not come from the same localities or stratigraphic horizons.

Other gomphodont species that have been sampled include the South American *Andescynodon*, which is characterized by lamellar tissue throughout the middle and outer cortex of an isolated femur (Abdala and Chinsamy, 2008). *Andescynodon* is an early diverging traversodont with a small-medium body size (estimated skull length = 90 mm), which may explain the slow rate of skeletal growth indicated by the femur. Medium bodied species from South America include *Massetognathus pascuali* (maximum skull = 205 mm in length; Abdala and Chinsamy. 2008) where smaller femora show slow-growing tissue. However, a recent report by Garcia Marsa et al. (2022), revealed intraspecific variation in bone tissue composition from continuous rapid growth at death shown in distinctly longer *M. pascuali* femora than those sampled by Abdala and Chinsamy (2008). This result indicates a decoupling between element size and histological changes at the age/size at sexual maturity.

More derived traversodontids that have been histologically sampled include *Traversodon*, *Protuberum*, *Exaeretodon* and *Scalenodontoides* and do not appear to have experienced cyclical growth (Botha et al., 2012). However, the individuals that were sampled had not passed their most rapid phase of early growth. As such, they may have shown shifts to slow peripheral

growth later in life, similar to that seen in *Thrinaxodon* or *Massetognathus*, but limited sampling precludes this assessment with confidence.

Taken together, the variability in growth strategies demonstrated by gomphodontian species suggests that growth trajectories cannot be predicted by phylogenetic affinity, body size, or inferred dietary niche, but rather, each species is responding to the unique combination of extrinsic and intrinsic pressures to influence the rate of growth and the timing of when in ontogeny a shift towards slow growth begins. It is clear that many species experienced sustained rapid growth in early ontogeny that eventually plateaus to a slower rate, likely at the onset of reproductive maturity. However, from the available descriptions of cynodont histology from previous studies, the potential correlation between the onset of sexual/skeletal maturity and element size has not been robustly documented. This is a result of sporadic histological sampling across the skeleton, across geographic areas, across species, and across geologic time zones, where non-standardized and isolated elements were thin-sectioned (either due to limitations imposed by preserving type material, or from limited recovered specimens, Fig. 4.2).

To investigate if size and age are correlated in cynodonts and subsequently draw conclusions from inferred growth strategies, I compiled a histologic sample that controls for element by sampling femora and associated tibiae referable to two species that co-occur in the Anisian Manda Beds of Tanzania. Specimens that cover the widest possible femoral size range were selected and include multiple individuals within size classes. However, because this sample is primarily derived from isolated and fragmentary femora that are not associations of skeletons, it is impossible to completely rule out the possibility that other cynodont species may be represented in this data.

4.2.6 *Institutional Abbreviations—*

NMT, National Museum of Tanzania, Dar es Salaam, Tanzania; **UMZC**, University of Cambridge Museum of Zoology, Cambridge, United Kingdom; **BPI**, Evolutionary Studies Institute, University of the Witwatersrand, Johannesburg, South Africa.

4.3 MATERIALS AND METHODS

4.3.1 *Geologic Setting*

4.3.1.1 **Study Area—**In 2007, a team of paleontologists and sedimentologists from the University of Washington, Field Museum of Natural History, and Virginia Tech began a long-term project to document the geology and paleontology of the Permo-Triassic basins in Tanzania and Zambia (Sidor and Nesbitt, 2018). Expeditions to the Ruhuhu Basin of southern Tanzania happened five times over the span of ten years where two bone-bearing intervals were identified from: 1) a bonebed in the lowermost Lifua member and 2) numerous localities in the middle-upper Lifua member. Both intervals have been the subject of ongoing research to document the taphonomy, sedimentology, and faunal assemblages and have led to important discoveries that have reshaped our understanding of dinosaur origins (Griffin and Nesbit, 2016; Nesbitt et al., 2017), and have contributed perspectives on the non-uniform effects of the end-Permian extinction and recovery at regional scales across southern Africa (Sidor et al., 2013).

The lowermost and mid-upper bone-bearing intervals in the Manda Beds are hosted in floodplain mudrocks deposited along river floodplains that flowed from the Ruhuhu rift scarps into a series of subsiding basins under warm, seasonally wet climates (Smith et al., 2018). However, a sharp contrast in bonebed characteristics occurs within this fluvio-lacustrine paleoenvironment and is well illustrated by the different taphonomic histories, faunal

assemblages, and paleoenvironments that are captured from lowermost to middle-upper Lifua strata (Fig. 4.3).

4.3.2 *Field-based Observations of Lifua Member Fossil Localities*

The lower Lifua Member occurrence (locality Z183) is a fossil-rich bonebed that hosts hundreds of remains of a unique, large-bodied dicynodont referable to *Dolichuranus*. Fossils range in size from inferred juvenile to adult and are preserved in fine matrix in close association, suggesting that animals were buried rapidly near or at the site of death (Smith et al., 2018).

In stark contrast to the in-situ material from the lower Lifua Member, most of the fossils from the mid-upper Lifua Member were collected from shallow exposures or remains that have weathered out onto the surface. Fossils were often found in laterally extensive sheets of mudstone with calcareous nodules with similar taphonomic signatures of disarticulated and weathered elements that are encased in calcareous or micritic material. Channel sandstones below and above the mid-upper Lifua fossiliferous mudstone intervals have different lithologies and geometries; the lower is filled with laterally accreted trough-cross bedded fine sands whereas the upper unit has vertically accreted tabular medium-grained sandstones and reworked conglomeratic nodules (Smith et al., 2018).

From these field-based observations, Smith et al. (2018) interpreted the depositional environment of the mid-upper Lifua fossil-bearing localities as having accumulated around distal floodplain pond deposits between meander belts. Compared to the underlying Kingori Sandstone Formation, the Lifua Member lithology documents a shift towards increasing rainfall and ephemeral ponds that likely hosted the diversity of cynodonts and other Anisian vertebrate fauna.

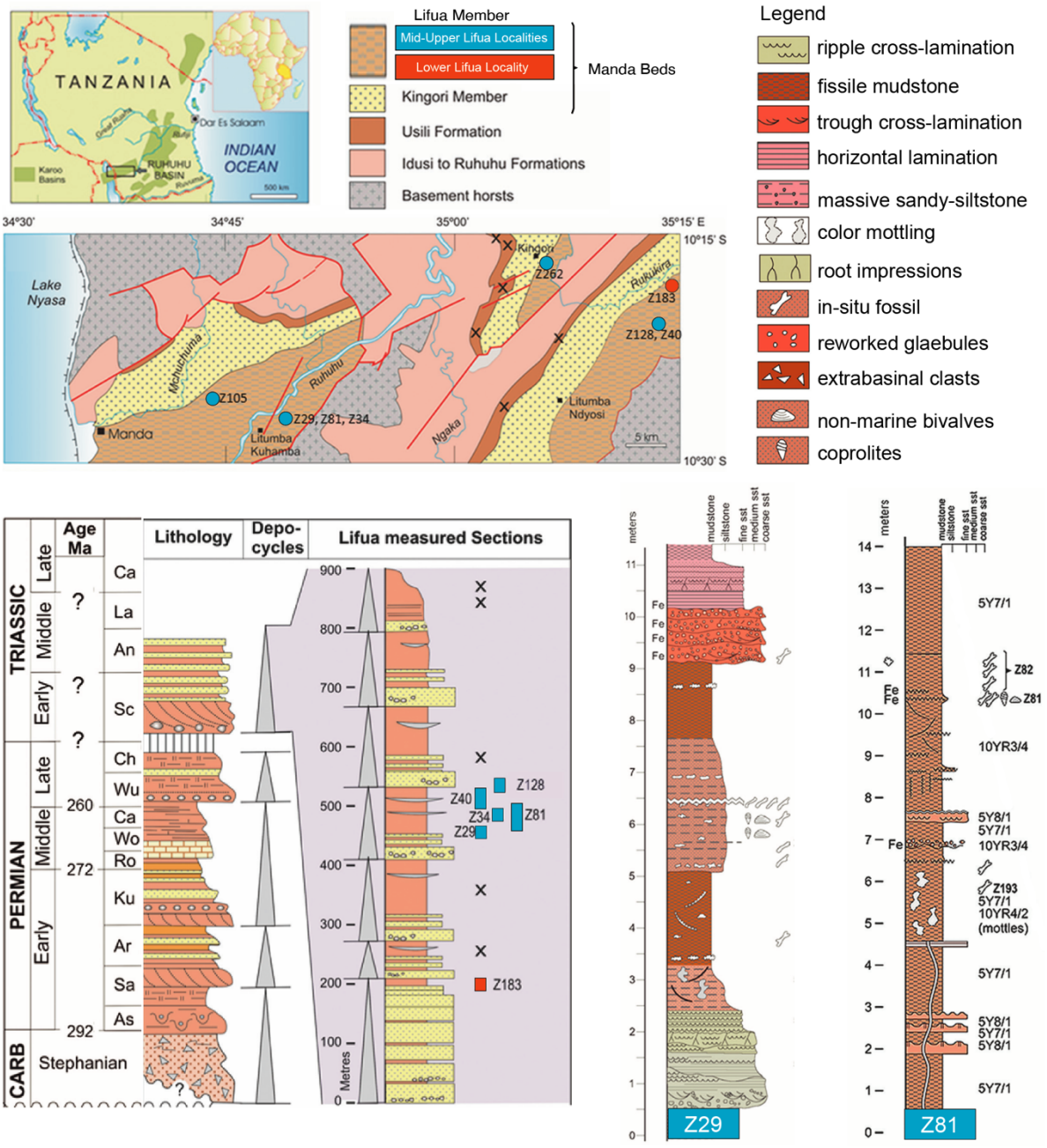

Figure 4.3. Stratigraphic, lithologic, and geographic context of the Anisian Lifua Member fossil localities, adapted from Smith et al., (2018). Mid-Upper Lifua fossil localities are highlighted in blue whereas the lowermost (Z183) locality is in orange.

Due to the heavily vegetated areas between the isolated and patchy outcrops, these localities cannot be precisely placed in stratigraphic context, but appear to be within tens of meters of each other stratigraphically, near the middle of the member. From these localities, numerous vertebrate remains have been recovered, including cynodonts (e.g., *Scalenodon angustifrons*, *Mandagomphodon hirschoni*, *Mandagomphodon attridgei*, *Luangwa drysdalli*, *Aleodon brachyrhamphus*, *Cricodon metabolus*) (Hopson, 2014; Crompton, 1955), archosauromorphs (e.g., *Stenaulorhynchus stockleyi*, *Parringtonia gracilis*, *Nundasuchus songeaensis*, *Mandasuchus tanyauchen*, *Mambawakale ruhuhu*, and *Asilisaurus kongwe*) (Nesbitt et al., 2014; Werning and Nesbitt, 2016; Nesbitt and Butler, 2012; Butler et al., 2017; Nesbitt et al., 2020; Butler et al., 2022), and dicynodonts (*e.g., Sangusaurus parringtonii*) (Angielczyk et al., 2017; Kammerer et al., 2018) . Invertebrate burrows and nonmarine bivalves also co-occur.

Ten localities (Z29, Z51, Z80, Z81, Z126, Z129, Z131, Z134, Z138, and Z185) host cynodont fossils that were used in this study. Each of these isolated outcrops are from a fluvio-lacustrine mudstone-sandstone sequence that have been extensively described by Smith et al., (2018). Specifically, localities Z29, Z34, Z126, Z128, and Z129 share similar host lithologies of thin, laterally extensive sheets of calcareous nodules that cap a bed of reddish-brown silty mudstone. Z81 similarly hosts a pedogenically modified floodplain mudstone with heavily calcified, semi-articulated to articulated skeletons of *Scalenodon angustifrons*, along with rhynchosaurs, archosaurs, and isolated dicynodont elements. Z051 is equivalent to Z041 which was discussed in Nesbitt et al. (2014) as the type locality of the archosaur *Nundasuchus songeaensis*. Localities Z80 and Z131-Z185 are awaiting further descriptions.

Interestingly, Z29 and Z81 host an abundance of small and large-sized remains of *S. angustifrons.* It is unclear why this species aggregated or was concentrated more so than the other cynodont species known from the Lifua Member. Smith et al. (2018) discussed the possibility that as a gregarious herbivore, similar to *Trirachodon* from the nearby Karoo Basin, *Scalenodon* sheltered underground in communal mounds around watering holes (Groenewald et al., 2001). In a review of bonebed accumulation methods in the Upper Cretaceous Two Medicine Formation of Montana, Rogers (1990) concluded that drought was the most plausible agent that caused animals to aggregate around shrinking watering holes, in contrast to lithologic or taphonomic causal agents that move fossilized animals post-mortem. Indeed, water dependency has a strong effect on the behavior of modern savannah mammals during droughts (Shipman, 1995) which could have acted in the same way to concentrate *Scalenodon* populations around shrinking ponds, as discussed in Smith et al. (2018).

4.3.3 ***Identification of Isolated Femora***

Femora were identified using a combination of associated individuals from collections housed at the Burke Museum that were collected from the Manda Beds and the nearby Luangwa Basin in Zambia. Associations were used to refer isolated femora to *Scalenodon angustifrons* and *Cricodon metabolus*. Isolated femora were referred to *Luangwa drysdalli* based on distinct femoral morphologies figured in Kemp (1980) that are discussed in detail below. Lastly, isolated femora were referred to *Aleodon brachyrhamphus* from comparisons to South American species *A. cromptoni* (Martinelli et al., 2017) and from discussions with Christian Kammerer (pers. comm., 2023). A detailed description of the associations of various Manda Bed cynodont specimens follows.

Isolated cranial and postcranial fossils have been assigned to six cynodont species from collections housed at the Burke Museum. These include (i) associations of cranial and postcranial remains of *Scalenodon angustifrons* (NMT RB581, NMT RB731, and NMT RB564) (ii) associations of teeth and postcranial remains for *Cricodon metabolus* and associated skeletons from the nearby Ntawere Formation of northeastern Zambia (Sidor and Hopson, 2018), (iii) isolated skulls, associations of partial mandibles and skulls with postcranial remains and isolated femora referable to *Aleodon brachyrhamphus*, (iv) isolated partial skulls and isolated femora referable to *Luangwa drysdalli* (e.g., NMT RB565, NMT RB1491, NMT RB58, NMT RB59,), and (v) isolated skulls of *Mandagomphodon hirschoni* and *M. attridgei* (Hopson, 2014). Therefore, the referral of femora is limited to only the four species that have associated postcranial remains (e.g., Fig. 4.4; *S. angustifrons*, Sidor and Hopson, 2018;fig.9, *C. metabolus*, and Fig. 4;.5 *A. brachyrhamphus*) or descriptions of isolated postcranial remains (e.g. Fig. 4.6, *L. drysdalli*) so the possibility that *Mandagomphodon* femora are represented in this sample cannot be ruled out. However, the available sample of over 80 femora permits the assessment of different femoral morphologies that conform to four of the six known cynodont species, outlined below.

The femoral anatomy of *Luangwa drysdalli* (Fig. 4.6) shares the most similarities with *S. angustifrons* (Fig. 4.4) but notable differences in the development of the lesser trochanter and medial condyle permit discriminating between the two. However, no associations of cranial and postcranial remains have been recovered from the Manda Beds and the only figured specimen of a femur referable to *L. drysdalli* is a composite reconstruction in Kemp (1980). Therefore, isolated femora are tentatively referred to *L. drysdalli* using the combination of morphological features described below. In addition, histological details such

as the prevalence of parallel-fibered bone and the triangular aspect of the femoral midshaft in thin-section provide additional features to identify *L. drysdalli* femora from those of *S. angustifrons*.

In *S. angustifrons,* the distal articular surface of the femur lacks a well-developed patellar groove, leaving a smooth dorsal surface of the distal profile (Fig. 4.4E). This is unlike the condition seen in *Cricodon metabolus*, where the distal profile is dorso-ventrally flattened and a gentle constriction separates equidimensional medial and lateral condyles (Crompton, 1955; Sidor and Hopson, 2018). In *S. angustifrons*, the lateral distal condyle is substantially larger than the medial condyle (Fig. 4.4E). The medial condyle extends ventrally, in-line with the medial side of the shaft and does not hook laterally, like the condition seen in *Luangwa drysdalli* (Kemp, 1980). Femora referable to *Aleodon brachyrhamphus* at similar sizes to *S. angustifrons* femora (NMT RB581, NMT RB864, and NMT RB564) have larger, more robust, and rectangular shafts. Isolated proximal femora referable to *A. brachyrhamphus* have distinct profiles with a T-shaped greater trochanter that has an anterior expansion (Fig. 4.5C). The head of the femur is very pronounced and rounded (Fig. 4.5A). In ventral view, the lesser trochanter bounds a deep adductor fossa (Fig. 4.5B). On its proximal end, the lesser trochanter has a rugosity that appears as though a flap of bone wraps medially around the site of muscle attachment (Fig. 4.5B). When *S. angustifrons* is compared to the distal profile of a complete femur referable to *A. brachyrhamphus* (NMT RB353, NMT RB1463), the medio-lateral width of the articular surface is substantially longer in *A. brachyrhamphus* than in *S. angustifrons* or *L. drysdalli*. Moreover, in *A. brachyrhamphus*, the lateral condyle is antero-posteriorly deep whereas the medial condyle is thinner and more gracile (Kulik, pers. obs.).

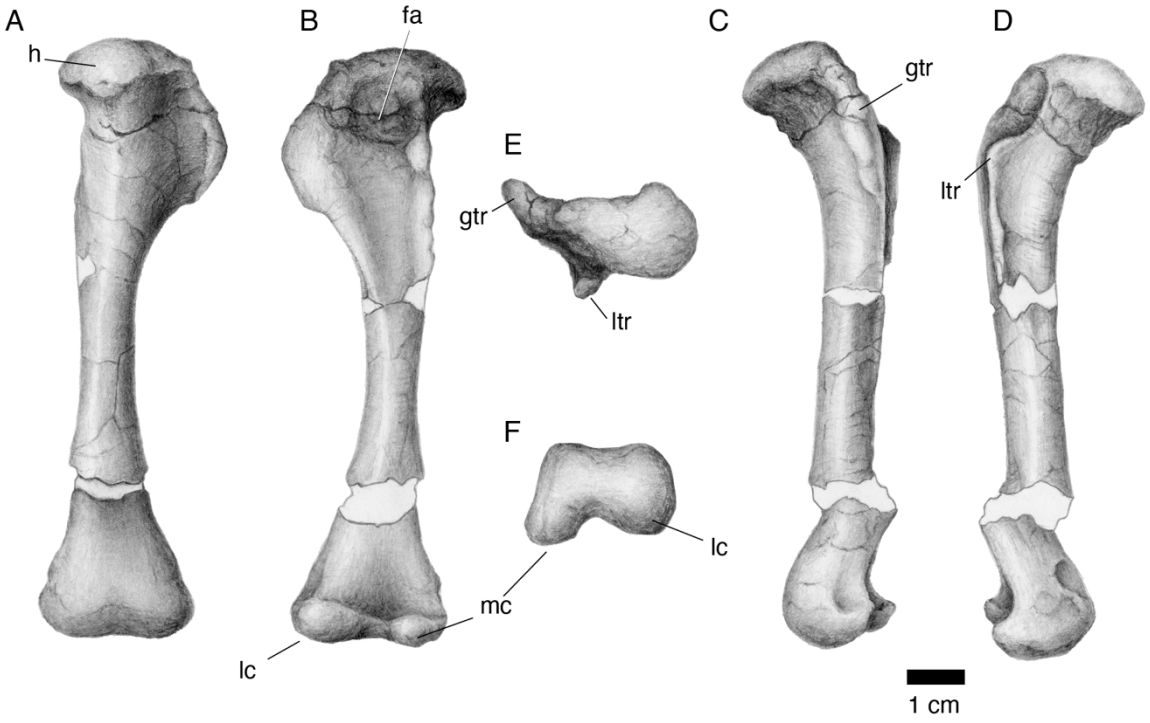

Figure 4.4. Femur of *cf. Scalenodon angustifrons* (NMT RB564). Complete left femur in **A**, dorsal, **B**, ventral, **C**, lateral, **D**, medial, **E**, proximal, and **F** distal views. **Abbreviations**: **fa**, adductor fossa; **gtr**, greater trochanter; **h**, head of femur; **lc**, lateral condyle; **ltr**, lesser trochanter; **mc**, medial condyle. Scale bar equals 1 cm.

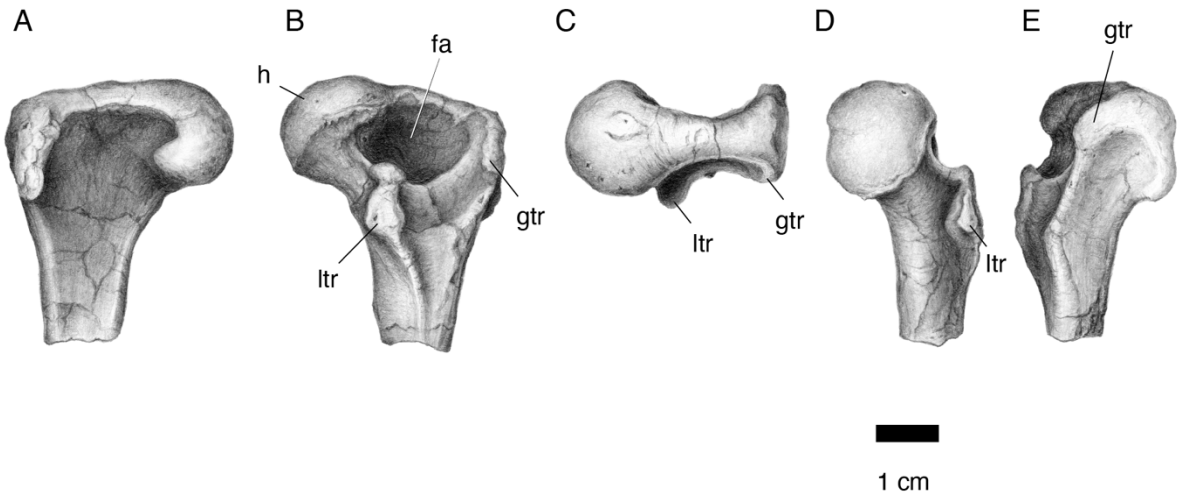

Figure 4.5. Femur of *cf. Aleodon brachyrhamphus* (NMT RB1447). Proximal right femur in **A**, dorsal, **B**, ventral, **C**, proximal, **D**, medial, and **E**, lateral views. **Abbreviations**: **fa**, adductor fossa; **gtr**, greater trochanter; **h**, head of femur; **ltr**, lesser trochanter. Scale bar equals 1 cm.

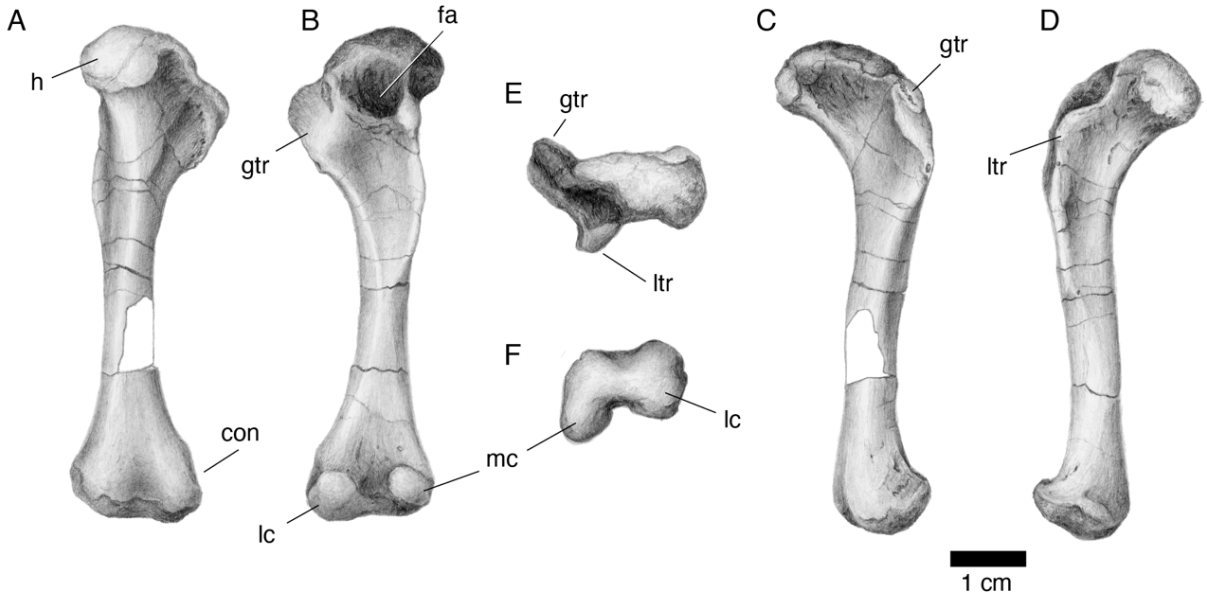

Figure 4.6. Femur of *cf. Luangwa drysdalli* (NMT RB1491). Complete left femur in **A**, dorsal, **B**, ventral, **C**, lateral, **D**, medial, **E**, proximal, and **F** distal views. **Abbreviations**: **con**, constriction surrounding distal shaft; **fa**, adductor fossa; **gtr**, greater trochanter; **h**, head of femur; **lc**, lateral condyle; **ltr**, lesser trochanter; **mc**, medial condyle. Scale bar equals 1 cm.

4.3.4 ***Body Size Estimation***

To contextualize potential size/age correlations in this histologic sample, measurements of the remaining femora referable to *S. angustifrons* and *L. drysdalli* that were not thin-sectioned were collected (Tables 4.1 and 4.2). Many of these femora are incompletely preserved, which prompted length estimates based on minimum dorsal midshaft diameter (MSD). This measurement was not available for all elements due to preservation of isolated distal or proximal ends. Therefore, I also measured the dorso-ventral depth of the lateral condyle to generate length estimates for incomplete distal ends and the dorso-ventral depth of the femoral head for proximal ends (Tables 4.1 and 4.2). Length estimates were combined to provide a range of femoral lengths between 43–128 mm in *L. drysdalli* and 61–123 mm in *S. angustifrons*.

Variation exists in this sample that can be attributed to either taphonomic, ontogenetic, phylogenetic, or intraspecific differences in morphology. For example, intraspecific variation in complete *S. angustifrons* femora, indicates that the width of the midshaft remains relatively constant as you move proximally, until the greater trochanter is expressed. In contrast, the dorsal width of the distal end increases substantially, from 8.6 mm wide at the midshaft to 15.74 mm at the distalmost shaft. Therefore, isolated distal shafts may contribute to larger femoral estimates. This was minimized by using the depth of the lateral condyle (discussed above). Variation in the robusticity of distal condyles is also observed, but their general morphology and aspect remain consistent.

In *L. drysdalli*, there is minimal morphological variation in the femora, as midshaft diameters scale relatively predictably as length increases (Table 4.2). In contrast to *S. angustifrons*, distal shaft diameter remains relatively consistent. However, L. *drysdalli*

femoral midshafts increase substantially as you move proximally, due to the prominent expression of the greater trochanter.

4.3.5 *Thin Section Preparation*

Thin sections were made following standard osteohistological techniques outlined in Lamm (2013). Transverse cross-sections at or near the mid-diaphyses were stabilized with Paleobond and cut on a high-precision diamond-edged saw (Isomet 1000). These pieces were then mold and cast using Moldstar silicone rubber and Smooth-on plastic resin to create research quality replicas. The casts were then glued to the remaining un-imbedded proximal and/or distal ends of the specimen to preserve its 3-dimensional morphology for future research.

Sectioned midshafts were embedded in Epothin Epoxy/Resin 2, sectioned to a thickness of approximately 2 mm on a high-precision diamond-edged saw (Isomet 1000) and glued to glass slides using Devcon 2-Ton epoxy. Prior to 2020, slides were ground on a Metaserv 3000 lapidary plate until the specimen was 80 μm thick or until optical clarity was reached. From 2021 onward, slides were ground to optical clarity using an automated lapidary plate (Exakt 400CS). High magnification and composite images were taken using a Nikon Eclipse LV100POL microscope under plain and cross-polarized light with a lambda filter. Composite images were processed using Nikon NIS-Elements AR (version 5.20.02) imaging software.

Ontogenetic maturity was assessed through bone tissue composition, articular surface texture and morphology, and size compared to other cynodont specimens from the mid-upper Lifua Member. Specimens were placed into three size classes based on maximum femoral length, epiphyseal surface ossification, and changes in bone tissue composition. Size class I corresponds to femoral lengths that are less than 50% max, size class II is represented by

elements between 50–75% max length, and size class III includes specimens that are greater than 75% max length. The dimensions of the two species overlap as the maximum estimated size of *S. angustifrons*, and *L. drysdalli* are between 100–120 mm. However, there are some differences in the robustness and gracility of midshaft measurements when compared to estimates or known femoral lengths. For example, *L. drysdalli* femora have an average midshaft width to length ratio of 0.092 and are more gracile than *S. angustifrons* (average MSD/L = 0.11) at the same size.

Specimens in size class I have poorly formed joint surfaces and show very spongey and pitted surfaces indicative of epiphyseal cartilage attachment in immature individuals (Griffin et al., 2020). By comparison, the joint surfaces of elements in size II and III are more robustly built and more completely ossified, although slight pitting remains on the distal surface of elements from size class II. The relative degree of epiphyseal surface ossification combined with histological features is well correlated for *L. drysdalli* and *S. angustifrons*.

4.3.6 ***Cortical Thickness***

Cross-sectional area of near-midshaft femoral thin sections was used to calculate cortical thickness (K), expressed as the proportional diameter of the medullary cavity relative to the total diameter of the bone cross-section. Bone wall thickness measurements facilitate comparisons to other taxa and are used to infer bone robusticity and lifestyle (Buffrénil , et al., 2021). The proportional cortical thickness based on area (K_A), and diameter (K_D) (Currey and Alexander, 1985) are reported (see supplementary data). Measurements were taken in FIJI (v2.3.0/1.539).

4.4 SYSTEMATIC PALEONTOLOGY

THERAPSIDA Broom, 1905

CYNODONTIA Owen, 1861

TRAVERSODONTIDAE Huene, 1936

SCALENODON ANGUSTIFRONS Crompton, 1955

Holotype– UCMZ 120B, an incomplete skull with two incomplete dentaries.

Diagnosis: Modified from Crompton (1955): transversely ovate maxillary postcanine teeth with a broader labial portion in the antero-posterior direction than the lingual portion; a near vertical inner wall of the labial cusp that extends across the crown in the antero-posterior direction, essentially dividing the crown in two parts; a deep excavation in the anterior region of the crown; mandibular postcanine teeth having two main cusps (a labial and lingual cusp) that steeply arise from the anterior region of the crown; a broad heel with a cingulum that extends from the labial cusp to wrap posteromedially around the heel.

Referred Material—NMT RB581, a mostly articulated skeleton including the skull with lower jaws, at least 26 articulated vertebrae, articulated partial scapula, coracoid, complete right humerus, and proximal ulna, proximal left humerus, complete left femur (thin-sectioned), distal right femur, parts of both tibiae and fibulae, several ribs, and unprepared pieces. NMT RB731, a partial skeleton including a skull and occluded mandible, a complete right humerus, distal left humerus articulated with a proximal radius and ulna, complete right femur (thin-sectioned), partial proximal tibia, numerous caudal vertebrae and other

unprepared elements. For a complete list of isolated femora referred to *S. angustifrons*, see Table 4.1.

Taxonomic Note—This survey of 33 (at minimum) referable femora, five of which are from associations of 3 individuals (i.e., NMT RB581, NMTRB731, NMT RB564), suggests that the following features are characteristic of the species: the adductor fossa is shallow, the lesser trochanter is a short, flat shelf of muscle attachment that is visible in proximal profile, the medial condyle is dorso-ventrally taller than the lateral condyle and extends ventrally, in-line with the medial side of the shaft, femoral midshafts are square and primarily composed of well-vascularized woven-dominated woven-parallel tissue.

Description—The following description is based primarily on NMT RB581 and NMT RB731, which represent femora between 96–99 mm long in NMT RB581, and 102 mm long in NMT RB731, compared to the entire sample (see Table 4.1). There is some morphological variation in the femora, namely that smaller femora or more gracile. However, even elements that are approaching maximum known length and are between 96–102 mm long, midshaft diameters, true (i.e., taken from complete specimens) vary from 9– 13.25 mm.

In *S. angustifrons* (Fig. 4.4), the head of the femur is comma-shaped and tapers laterally towards the greater trochanter in proximal view. The anteromedial border of the head makes up the largest and most rounded portion of the head whereas the articulating surface flattens between the head and the greater trochanter. In ventral view (Fig. 4.4B), the greater trochanter is long and squared off ventrally, with a thin, dorsally curved profile. On the ventral surface, the greater trochanter creates a broad, flat surface that is slightly depressed where it reaches the

lesser trochanter. The lesser trochanter is developed into a short, flat shelf that makes up the medial border of the adductor fossa which has a gently curved and shallow surface for muscle attachment. This is unlike the condition in *Luangwa* and *Aleodon*, which have a sharp adductor fossa with a large basin and prominent lesser trochanter.

The shaft of the femur has a square cross-sectional profile at the midshaft. The distal profile of the femur has a smooth and rounded articulating surface with little to no development of a patellar groove (Fig. 4.4A). The distal profiles of both femora of NMT RB581 have substantially larger lateral condyles than medial condyles (Fig. 4.4F). The medial condyle is dorso-ventrally taller, and extends ventrally, in-line with the medial side of the shaft. In addition, NMT RB864 and NMT RB564 are unlike the femora referable to the other cynodont species recovered from the Manda Beds, as noted below.

4.4.1 ***Osteohistology of S. angustifrons***

The following histological descriptions of *S. angustifrons* include a general overview of the bone histology that characterize each sectioned specimen, with subsequent descriptions that detail the bone tissue composition and vascular organization of each thin section, beginning with the smallest element sectioned based on the dorsal width of the midshaft. Each thin section was made in the transverse plane nearest to, or at the midshaft, depending on specimen preservation. Elements that were diagenetically altered to the point where histological details were obscured are not included.

Eight femora and two tibiae referable to *S. angustifrons* were thin sectioned from a size range that spans 61.23-123 mm femoral length (Fig. 4.7A–H). The smallest individual is approximately 50% maximum size whereas the rest of the histologically sectioned femora are

>75%max size. Therefore, no individuals from size class I are present, and only one individual is represented by size class II. *S. angustifrons* is characterized by highly vascularized woven-dominant woven-parallel tissue that is present in all elements that were sectioned. Unlike *L. drysdalli*, *Scalenodon* does not have discrete growth phases and does not follow a stereotyped pattern where vascular density or composition changes as elements increase in size. Instead, femora between 90–123 mm in length display moderately to highly vascularized primary tissue. In some individuals, peripheral tissue abruptly shifts to parallel-fibered tissue, and one instance of a well-developed outer circumferential layer or EFS in an individual with an estimated femoral length of ~100 mm. However, similarly sized and substantially larger femora show continued, rapid growth at death, indicating a developmentally plastic growth pattern within the species. Similar to *L. drysdalli*, medullary expansion and remodeling has removed the earliest phases of growth in this sample, but unlike *L. drysdalli*, the predominance of woven-dominated and highly vascularized tissue seen throughout *Scalenodon* elements suggests that *Scalenodon* had a higher intrinsic rate of growth than its close relative. Furthermore, intraspecific variation in femoral size and histological tissue reflective of skeletal maturity indicate that size is a poor predictor of ontogenetic status in *S. angustifrons*.

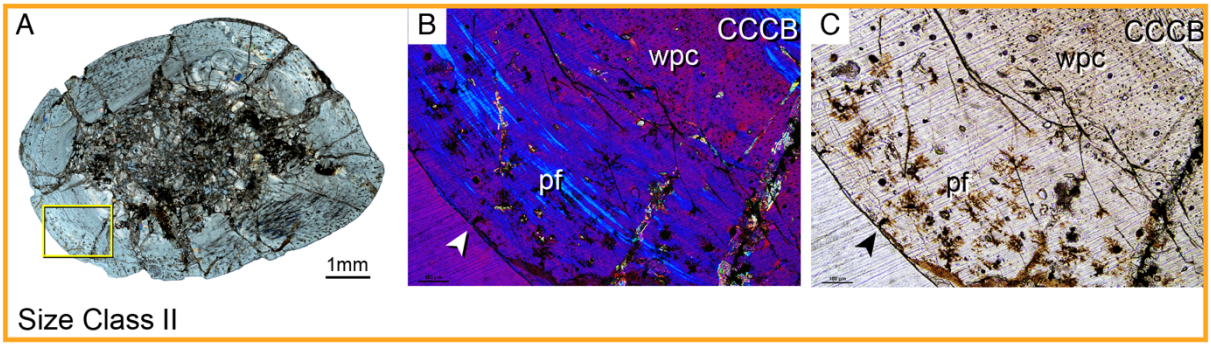
A
1mm
B
CCCB
wpc
pf
C
CCCB
wpc
pf
Size Class II

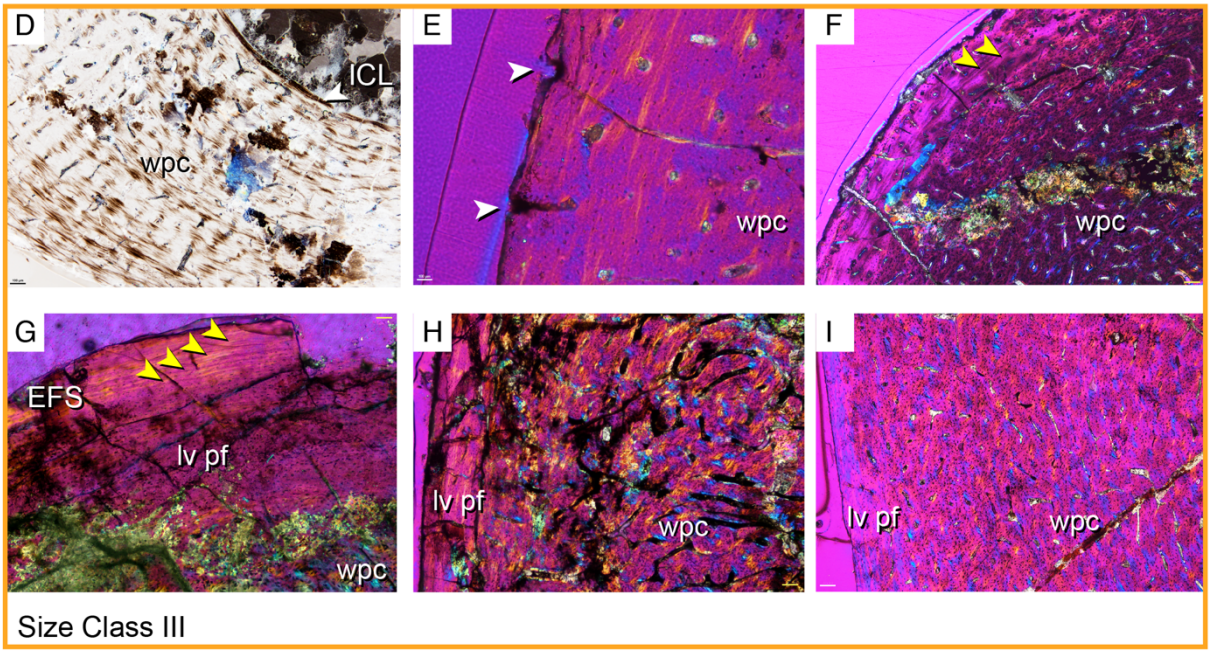
D
ICL
wpc
E
wpc
F
wpc
G
EFS
lv pf
wpc
H
lv pf
wpc
I
lv pf
wpc
Size Class III

Figure 4.7. Osteohistology of *Scalenodon angustifrons* femora from Size Class II and III show compact cortices composed of varying degrees of woven and parallel-fibered bone as the dominant tissue. Size class II (50-75%max length) is represented by one individual (NMT RB860) seen in transverse cross-section in **A**, yellow box indicates higher magnification of cortex seen in **B**, in cross polarized light with a lambda filter, and **C**, plain polarized light. Size class III (>75%max length) is characterized by a woven-parallel complex with highly variable peripheral tissue (**D**-**I**). **D**, inverted cross-polarized image highlights the woven-parallel complex and ICL of NMT RB860. **E**, simple vascular canals open to the subperiosteal surface in NMT RB863, indicating growth at not stopped prior to death. **F**, 2 peripheral LAGs (yellow arrows) indicate a temporary cessation in growth in NMT RB862. **G**, NMT RB864 shows a well-developed EFS with at least 4 closely spaced LAGs (yellow arrows), whereas NMT RB866 (**H**) and NMT RB731 (**I**) show poorly vascularized peripheral parallel-fibered bone. **Abbreviations**: **CCCB**, compact coarse cancellous bone; **EFS**, external fundamental system; **ICL**, inner circumferential layer; **pf**, parallel-fibered bone, **lv pf**, low-vascular parallel-fibered bone; **wpc**, woven-parallel complex. Scale bars equal 1 mm in **A**, 100 μm in **B**-**I**. Image **D** is inverted cross-polarized light. Images **E**-**I** are in cross-polarized light with a lambda filter.

A small, dorsoventrally crushed distal femur (NMT RB860; 61.2 mm in length) has a slightly porous articular surface that appears partially ossified. A distally shifted transverse thin section is composed of CCCB in the deepest cortex (Fig. 4.8A). A reversal line separates the CCCB from a thin region of woven-bone that quickly grades into parallel-fibered bone more peripherally. Small, simple vascular canals sit within this moderately fast-growing bone tissue which changes to more woven-dominated tissue at the subperiosteal edge. Here, vascular canals increase in density in some regions of the cortex, indicating that this individual died while actively growing.

A partial distal femur (NMT RB863; 94.93 mm estimated length) has a poorly ossified epiphyseal surface. On the distal articular surface, open vascular canals are visible to the naked eye and represent areas of cartilage attachment. The distally shifted thin section has a much thinner cortex compared to true midshaft sections, and the medullary cavity is completely infilled with trabeculae. A reversal line separates the drifted medullary cavity from the cortex that is composed of small, longitudinal canals in the woven-parallel complex. This tissue continues to the subperiosteal edge, indicating that this individual had not passed through its most active phase of growth prior to death.

A distal femur (NMT RB862; 95.01 mm estimated length) has a partially ossified articular surface with a slightly rugose and pitted texture. In thin section, the femur consists of a thick cortex composed of plexiform vascular canals that grade into more organized, sparsely vascularized tissue at the periphery (Fig. 4.8B). The deepest cortex is composed of a very thin ICL of avascular parallel-fibered bone. The remaining deep and middle cortex is composed of large, plexiform canals in a fibrolamellar complex. Vascular canal size and density decrease drastically near the periphery. Two closely spaced LAGs are traceable in this peripheral tissue

but do not coincide with the decrease in vascularity. Instead, the LAGs sit in sparsely vascularized parallel-fibered matrix. Small simple vascular canals and primary osteons remain open along the subperiosteal edge, indicating that this individual had passed its most rapid phase of growth prior to death but had not reached skeletal maturity.

A distal femur (NMT RB1075; 97.57 mm estimated length) has a partially ossified articular surface that is incompletely preserved and slightly pitted. A transverse near-midshaft section shows a shift from low to high vascular density in a woven-dominated woven-parallel complex (Fig. 4.8C). The deepest cortex is damaged from infilling mineral precipitates. Where preserved, small islands of CCCB and large resorption cavities are present, likely as a result of the slightly distal position of the transverse section. This remodeled tissue is bounded by a reversal line that separates deep CCCB from peripheral sub-plexiform vascular canals in a woven-dominated matrix in the middle cortex. Vascular density increases peripherally, similar to what is seen in *L. drysdalli* from size class II. In the outer cortex, vascular canals have a reticular organization, with long radial canals that extend to the subperiosteal edge, indicating that this individual died during its most active phase of growth.

A complete femur (NMT RB581; 95.84 mm in length) from nearly complete but disarticulated skeleton has well-ossified articular surfaces. In thin section, a thick cortex is heavily micro-cracked but is composed entirely of primary woven-fibered tissue with small, longitudinal vascular canals (Fig. 4.8D). The deepest cortex is composed of a thin ICL of avascular parallel-fibered bone that surrounds the irregularly shaped medullary cavity. Small fingers of trabeculae are present along the ventral surface of the shaft. Large resorption cavities occur in the deepest cortex. The remainder of the cortex is composed of consistently rapidly deposited woven bone. Longitudinal primary osteons are well-organized and anastomose

slightly. Due to the poor preservation of this specimen, the subperiosteal edge is partially incomplete. Where preserved, simple vascular canals open to the subperiosteal surface, indicating that this individual had not reached skeletal maturity prior to death.

A distal femur (NMT RB864; 96.79 mm estimated length) has a well- ossified articular surface with a slight rugose texture. This element was thin sectioned near the mid-diaphysis to reveal a thick cortex composed of longitudinal canals in the woven-parallel complex that abruptly changes to avascular parallel-fibered and lamellar bone with at least 4 closely spaced LAGs in an EFS (Fig. 4.8E). The EFS changes in thickness around the periphery but remains avascular along the subperiosteal edge, indicating that this individual had reached skeletal maturity prior to death. In the deepest cortex, the endosteal edge has been remodeled and is composed of a thick ICL compared to other *Scalenodon* femora examined here. The deep cortex grades from highly vascularized longitudinal and sub-plexiform tissue to a more organized primary tissue of small longitudinal canals in the woven-parallel complex until growth plateaus at skeletal maturity.

An association of a proximal femur (NMT RB379.A; 98.21 mm estimated length), complete tibia (NMT RB379.B) (in 4 pieces), distal tibia (NMT RB379.C), and other fragmentary unidentifiable elements is referred to *S. angustifrons*. The articular surfaces of the femur and tibiae are well ossified. The midshafts of both tibiae were sectioned to reveal a flat, ovate cross-section with three major tissue types. The medullary cavity is loosely filled with trabeculae that have broken post-mortem (Fig. 4.8F). The true midshaft thin section (NMT RB379.B) is composed of primary tissue with highly vascularized longitudinal to sub-plexiform vascular canals in the woven-parallel complex. The endosteal margin is remodeled and small patches of an ICL are preserved between areas of mineral precipitation. In the distally shifted

transverse section, the endosteal edge is more remodeled and consists of a nearly continuous band of CCCB. More peripherally, primary parallel-fibered bone composes the middle cortex. This tissue is poorly vascularized, with small, longitudinal canals and simple canals. Some areas are avascular. The outer cortex transitions into higher vascularized tissue, with longitudinal and anastomosing vascular canals surrounded by woven and parallel-fibered bone. In both tibiae, vascular canals open to the subperiosteal edge indicating that this individual died while actively growing.

A complete femur (NMT RB731; 102.42 mm in length) from an associated skull and skeleton reveals a thick cortex that is almost entirely composed of plexiform vascular canals (Fig. 4.8G). The inner medullary cavity has a remodeled endosteal edge that is composed of what would have likely been a continuous layer of CCCB, but much of the medullary cavity and innermost cortex is broken. The tissue composition shifts to highly vascularized, plexiform canals in woven-dominated bone in the deep and middle cortex. More peripherally, the vascular density decreases and becomes more organized in anastomosing longitudinal canals in the woven-parallel complex. The outermost subperiosteal tissue shows a marked transition to avascular, parallel-fibered to lamellar bone. This abrupt shift to slow indicates that this individual had passed its most rapid phase of growth prior to death but would likely have continued growing at a slow pace.

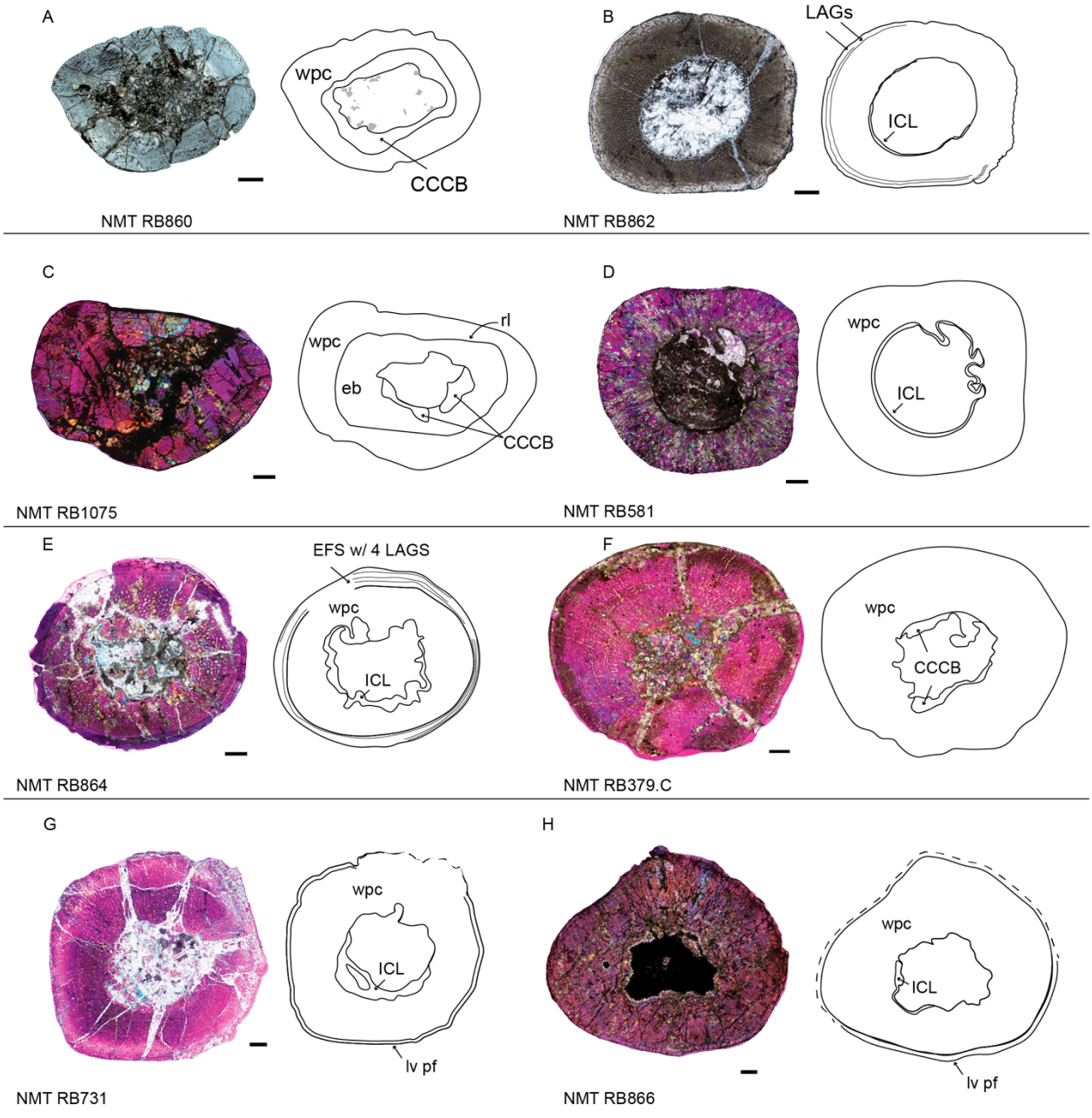
A
wpc
CCCB
NMT RB860
B
LAGs
ICL
NMT RB862
C
rl
wpc
eb
CCCB
NMT RB1075
D
wpc
ICL
NMT RB581
E
EFS w/ 4 LAGS
wpc
ICL
NMT RB864
F
wpc
CCCB
NMT RB379.C
G
wpc
ICL
lv pf
NMT RB731
H
wpc
ICL
lv pf
NMT RB866

Figure 4.8. Transverse midshaft thin sections and interpretive drawings for all *Scalenodon angustifrons* femora included in the sample, arranged in increasing midshaft diameter (**AH**). All but specimen **A** (NMT RB860) have estimated lengths >75% maximum known size and demonstrate remarkable variation in bone tissue composition. Some specimens are underdeveloped (e.g., **C**, **D**, **F**), others show shifts to slower growth (e.g., **G**, **H**) or temporary arrests in growth (e.g., **B**), and one individual is skeletally mature (**E**). Images were taken in cross-polarized light in **A**, plane-polarized light in **B**, and cross-polarized light with a lambda filter in **C**–**H**. Scale bars equal 1 mm. **Abbreviations: CCCB**, compact coarse cancellous bone; **eb**, endosteal bone; **ICL**, inner circumferential layer; **LAG**, line of arrested growth; **lv pf**, low-vascular parallel-fibered bone; **rl**, reversal line; **wpc**, woven-parallel-complex.

The largest partial distal femur (NMT RB866; 123 mm estimated length) has a well-ossified articular surface. In thin section, a thick, heavily micro-cracked cortex is composed of highly vascularized primary tissue that grades from disorganized plexiform canals in the deep cortex to more organized longitudinal and radial canals in the outer cortex (Fig. 4.8H). Much of the cortex consists of woven-parallel tissue. However, the endosteal edge has been remodeled and has an irregular edge with a thin ICL of avascular parallel-fibered bone. Resorption cavities and immature secondary osteons are common in the deepest cortex. More peripherally, primary osteons are densely distributed until the bone tissue shifts along the outermost periosteal edge. Here, vascular canals are small simple canals in a parallel-fibered matrix, indicating that this individual had passed its most rapid phase of growth prior to death but would have likely continued to grow at a slower pace until skeletal maturity was reached.

LUANGWA DRYSDALLI Brink, 1963

Holotype— BPI 3727, a skull with associated dentaries.

Diagnosis—There is no modern diagnosis for the genus, but the following several features have been noted by Brink (1963) and Abdala, and SaTeixeira (2004) in *L. drysdalli* and *L. sudamericana*: oval upper postcanines with an anterolabial cingulum (shared with other African traversodontid species), presence of a posterior cingulum in the upper postcanines, anterior cingulum in front of the transverse crest in the lower postcanines, short snout, large orbits and short temporal region.

Referred Material—NMT RB93, a partial right side of skull preserving the upper postcanine toothrow. NMT RB58, snout and occluded lower jaws, postcanine teeth are not exposed. NMT RB59, snout and occluded mandible with exposed postcanine teeth in labial view. See Table 4.2 for a complete list of referred femora.

Taxonomic Note—There are no definitive associations of cranial and postcranial remains of *L. drysdalli* in collections housed at the Burke Museum nor are there figured or described skeletons that include a description of the hindlimb (e.g., Abdala and Smith, 2009). However, the referral of isolated femora based on Kemp (1980) permit the assignment of 18 femora to *L. drysdalli* at minimum. Features that may be diagnostic of the genus include: prominent lesser trochanter, deep adductor fossa bordered by prominent lesser trochanter having a large, tear-dropped shaped site of attachment, medially deflected greater trochanter with a squared-off ventral border, dorso-ventrally elongated medial condyle that hooks laterally.

Description—The following description is based primarily on complete femora NMT RB1491 and NMT RB565, representing 68 and 77.5 mm in length, compared to the rest of the sample (see Table 4.2). There is minimal morphological variation in the femora, as midshaft diameters scale relatively predictably as length increases. However, in contrast to *S. angustifrons*, L. *drysdalli* femoral midshafts increase substantially as you move proximally, from the prominent expression of the greater trochanter. The distal shaft diameter remains relatively consistent, at least among complete elements that are available (e.g., NMT RB1491, NMT RB565, NMT RB1078).

In proximal view, the head of the femur bears a broad articular surface that is expanded on the medial side to make up a well-defined head, like in *S. angustifrons* and other cynodonts. The proximal profile of the head is constricted slightly, at the point of attachment with the lesser trochanter that occurs below the articular surface on the ventral shaft. The articular surface continues to taper laterally towards the greater trochanter, at which point, a sharp, medially directed angle separates the surface of the greater trochanter from the rest of the head as the trochanter curves medio-dorsally (Fig. 4.5A). This sharp deflected angle of the greater trochanter is unlike the condition seen in *S. angustifrons*. Furthermore, the greater trochanter is relatively more robust than in *S. angustifrons* and bears a sharper, squared-off distal contact with the metaphysis (Fig. 4.5B). In lateral view (Fig. 4.5C), the greater trochanter is wider than in *S. angustifrons* and similarly contributes to a broad, flat ventral surface.

On the ventral side, the lesser trochanter is very well-developed and contributes to a deep adductor fossa that is bordered by a shelf that extends from the lateral contact of the lesser trochanter to the rest of the proximal shaft. The lesser trochanter has a tear-drop shaped surface for muscle attachment that is well-ossified. It continues as a long fin down the ventral surface of the shaft and gently tapers at the midshaft. In cross-sectional profile, *L. drysdalli* femora are sub-triangular with the medial edge of the midshaft making up the apex of the triangle.

In distal view (Fig. 4.5F), the medial and lateral condyles are separated by a broad and flat patellar groove that is slightly more developed than in *S. angustifrons*. Distal femora referable to *L. drysdalli* can be identified based on the morphology of the medial condyle that bears a well-rounded surface that hooks laterally. The lateral condyle is similarly well-

developed as a rounded articular surface but is considerably larger than the medial head and is equidimensional in distal profile. The distal articular surface of *cf. L. drysdalli* femora is separated from the rest of the metaphysis by a constriction that encircles the distalmost shaft (Fig. 4.5B), which is unlike the condition in *S. angustifrons* where the metaphysis merges seamlessly with the articular surface.

4.4.2 ***Osteohistology of cf. L. drysdalli***

The following histological descriptions of *L. drysdalli* include a general overview of the bone histology that characterize each sectioned specimen, with subsequent descriptions that detail the bone tissue composition and vascular organization of each thin section, beginning with the smallest element sectioned based on the dorsal width of the midshaft. Each thin section was made in the transverse plane nearest to, or at the midshaft, depending on specimen preservation. *L. drysdalli* is characterized by a multiphased growth trajectory that starts out with longitudinal and oblique vascular canals in parallel-fibered tissue in the earliest record of growth from individuals in size class I (Fig. 4.9A-C). This tissue is subsequently eroded during expansion of the medullary cavity later in ontogeny. As the element increases in size, endosteal and periosteal bone deposition simultaneously increase the cortical thickness. In individuals in size class I and II, perimedullar bone deposition composed of poorly vascularized parallel-fibered bone concentrically reduces the lumen of the medullary cavity, followed by an ICL of avascular parallel-lamellar tissue (Fig. 4.9C, E). Periosteally directed bone is characterized by a shift to higher vascular areas in a woven-parallel complex. In most specimens, a mid-cortical reversal line indicates where peripherally directed tissue is separated from endosteally directed growth (Figs. 4.9, 4.10). Due to the placement of each thin section along the shaft, and

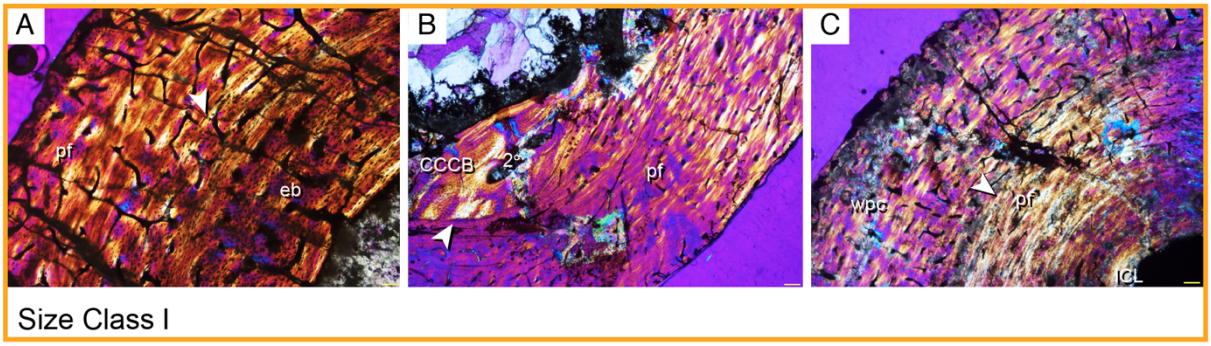

Size Class I

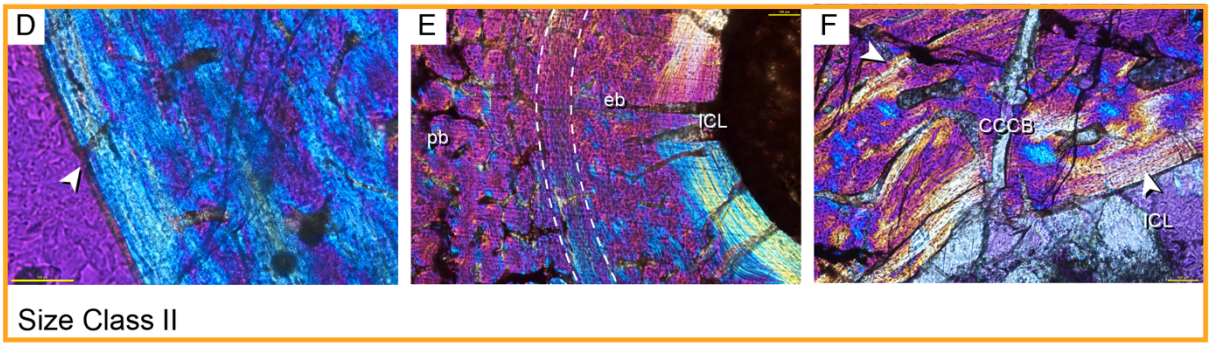

Size Class II

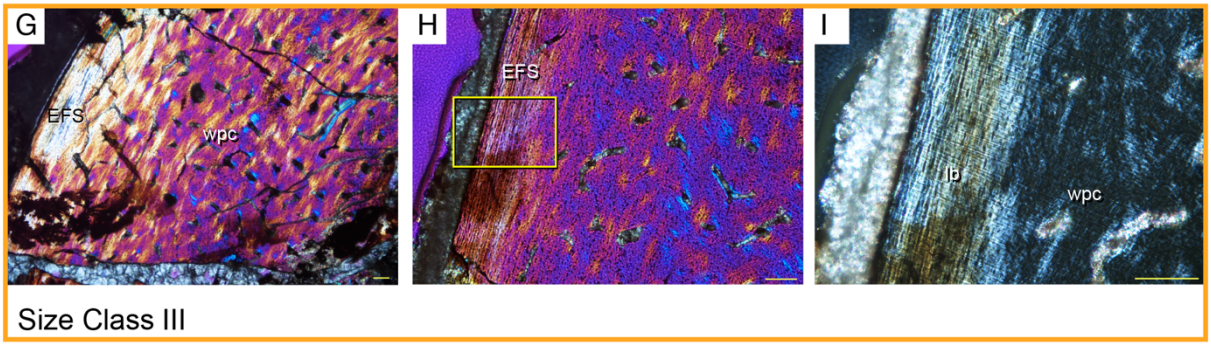

Size Class III

Figure 4.9. Osteohistology of *cf. Luangwa drysdalli* femora from Size Classes I, II, and III show primary bone tissue composed of parallel-fibered bone as the dominant tissue type, indicating sustained moderately paced growth that plateaus at large size. Size Class I (**A**-**C**) shows poorly organized vascular canals in **A**, (NMT RB1078), **B**, (NMT RB894) and **C** (NMT RB1080), with reversal lines (white arrows) separating periosteal deposition from endosteally directed deposition and remodeling of the medullary cavity. Size Class II (**DF**) shows sustained growth with open vascular canals seen in **D** (NMT RB1072) and is also characterized by restructuring of the inner cortex by endosteal bone separated by a with a thick ICL in **E** (NMT RB1071), and CCCB followed by an ICL in **F** (NMT RB1072). Size Class III is represented by one individual (NMT RB882) that shows a well-developed EFS of lamellar tissue in **G** and **H**. Magnification of lamellar bone seen in cross-polarized light in **I**. **Abbreviations**: **CCCB**, compact coarse cancellous bone; **EFS**, external fundamental system; **ICL**, inner circumferential layer; **pf**, parallel-fibered bone, **lv pf**, low-vascular parallel-fibered bone; **wpc**, woven-parallel complex, **2º**, secondary osteon. Scale bars equal 100 μm.

intraspecific histovariation in the degree of medullary expansion, the proportion of perimedular parallel-fibered tissue compared to the outer woven-parallel tissue varies between specimens. In large individuals, vascular density decreases towards the periphery followed by an abrupt shift to avascular tissue in the EFS/OCL of lamellar tissue, indicative of skeletal maturity.

Eight individuals referable to *L. drysdalli* were sampled from a size range that spans 43.5–128.7 mm femoral length (Fig. 4.10A-H). Size class I is characterized by individuals that are less than 50% maximum known length (4.2–6.5 mm) and include specimens NMT RB1078, NMT RB1080, NMT RB894, and NMT RB565 (Fig. 4.10A-C). Size class II includes individuals between 50–75% maximum diameter (7.4–9.7 mm) and includes specimens NMT RB1071, NMT RB1072, and NMT RB1073 (Fig. 4.10D-F). Finally, specimen NMT RB882 has a midshaft diameter of 13.54 and represents the largest individual in our sample that was skeletally mature prior to death (Fig. 4.10.G-H).

The degree of articular surface ossification appears to be well-correlated with size in *L. drysdalli*. Individuals from size class I show poorly ossified epiphyseal surfaces with extremely porous trabecular bone exposed on proximal and distal ends indicating cartilaginous caps. The one individual from size class II that is complete provides some preliminary evidence that the proximal articular surface ossifies earlier than the distal surface, but a larger sample size is needed to confirm this possible trend.

A very small complete right femur (NMT BR1078; 43.5 mm length) is preserved in three parts and represents the smallest element in this species and in the entire sample. Its ends are not ossified, leaving very porous and spongey proximal and distal surfaces. A transverse midshaft thin section reveals a cortex composed of parallel-fibered dominated woven-parallel bone (Fig. 4.9A, Fig. 4.10A). A thin ICL surrounds the eroded and remodeled endosteal edge. In the middle

stratum, the dominant tissue type is parallel-fibered bone, but large lacunar morphologies and densely packed cellular spaces indicate that woven-bone contributes to the cortex. Throughout the cortex, there are slight modulations in the proportion of vascularized and less vascularized bands in the cortex suggesting that growth rates were not consistent or high throughout early ontogeny. Furthermore, a reversal line separates what appears to be endosteally directed parallel-fibered bone (Fig. 4.9A). Anastomosing longitudinal canals continue peripherally throughout the middle and outer cortex and open to the subperiosteal surface indicating that this individual had not passed its most rapid phase of growth prior to death.

Three associated hind limb elements represent the second smallest individual in this sample. The proximal and distal articular surfaces are incompletely ossified in the right tibia (NMT RB1080.C; 50.48 mm in length), distal right femur (NMT RB1080.B; 55.45 mm estimated length), and complete but broken left femur (NMT RB1080.A; 58.57 mm in length). Specimen 1080.B was sectioned and is composed of a thick cortex that shifts from poorly vascularized parallel-fibered dominated tissue in the deep cortex to reticular canals in a woven-parallel complex more peripherally, separated by a reversal line (Fig. 4.10B). Reticular vascular canals increase in vascular area periosteally and open to the subperiosteal edge, indicating that this individual died while actively growing.

An associated complete tibia (NMT RB1080.C) is broken in three parts. The midshaft segment was thin sectioned to reveal a thick cortex composed of three tissue types. The deepest cortex has been remodeled and consists of a thick ICL of parallel-fibered bone. A reversal line separates this tissue from poorly vascularized, parallel-fibered bone in the deep-middle cortex. A reversal line marks a substantial increase in vascular density that continues more peripherally (Fig. 4.9C). Here, woven-parallel bone surrounds radially anastomosing primary osteons that

extend to the subperiosteal surface leaving a scalloped edge (Fig. 4.9C). This individual had not passed through its most rapid phase of growth prior to death and indeed shows sustained periosteally directed growth.

A small proximal femur (NMT RB894; 58.09 mm in estimated length) has a partially ossified articular surface with open vascular canals. In thin section, the same tissue types as seen in the larger NMT RB565 are also seen here (described below). However, a clear reversal line separates the deep remodeled endosteal tissue from primary periosteal growth (Fig. 4.9B, Fig. 4.10C).

The cortex of a complete left femur (NMT RB565; 67.65 mm in length) is composed of parallel-fibered bone with longitudinal vascular canals that anastomose throughout the cortex (Fig.4.10D). This individual has partially ossified articular surfaces. The distal surface ossified earlier in ontogeny and has a smooth face whereas the proximal end has a rugose texture of open vascular canals. In thin section, the deepest cortex has been remodeled and has left an irregular endosteal edge lined by a thin ICL of avascular parallel-fibered bone. Secondary osteons and resorption cavities are present in this deep region of the cortex and are clustered near the muscle scar of the lesser trochanter. The remodeled tissue is bounded by a reversal line that separates the remainder of the periosteally deposited tissue composed of parallel-fibered bone that is moderately well-vascularized with simple canals and longitudinal primary osteons. Vascular canals open to the subperiosteal edge indicating that this individual died while still in its most rapid phase of growth.

A nearly complete right femur (NMT RB1072; 81.94 mm estimated length) was thin-sectioned near the transverse midshaft using the distal piece. The proximal epiphyseal surface has not been prepared but appears partially ossified, whereas the distal articular surface has a

slightly porous texture indicative of a cartilage cap. The cortex of a transverse distal shaft of this femur is predominantly composed of parallel-fibered bone that decreases in vascular density towards the subperiosteal edge (Fig.4.10E). The deepest cortical tissue is composed of CCCB that has been remodeled and eroded by an ICL of parallel-fibered bone (Fig. 4.9F). A reversal line separates the CCCB from the periosteal parallel-fibered tissue that continues, uninterrupted, until the subperiosteal edge (Fig. 4.9F). Vascular density decreases periosteally, indicating that this individual had a prolonged phase of relatively rapid growth that slowed prior to death but had not reached skeletal maturity.

A similarly sized and possibly associated tibia (NMT RB1073) has a poorly ossified articular surface. A transverse section from the proximal tibia is composed of a thick cortex consisting of sub-plexiform vascular canals in the woven-parallel complex (Fig.4.10F). The medullary cavity is small and is free of trabeculae. The endosteal margin is irregular and shows two cortical drifts in the parallel-fibered bone that comprise the remodeled endosteal edge. The remainder of the cortex is composed of parallel-fibered dominated woven-parallel complex that is interrupted by one mid-cortical reversal line that marks a shift towards large periosteally accreting anastomosing canals. Vascular canals continue in a poorly organized and anastomosing organization towards the subperiosteal edge but reduce locally in some regions of the outer cortex. This mosaic of tissue continues to the subperiosteal edge, indicating that this induvial died during its most rapid phase of growth.

The nearly complete left femur (NMT RB 1071; 84.64 mm estimated length) has smooth, well-ossified proximal and distal articular surfaces. The transverse mid-shaft is composed of parallel-fibered bone that shifts in vascular density from endosteal to periosteal edges (Fig.4.10G). This individual shows evidence of sustained, prolonged growth that increased as the

individual grew larger, that likely would have continued if the animal had not died. The deepest endosteal tissue has been removed and remodeled and consists of a thick ICL of avascular lamellar bone. The remainder of the deep cortex is composed of endosteally deposited poorly vascularized parallel-fibered bone that is separated from periosteally directed growth by a thick annulus of poorly vascularized tissue (Fig. 4.9E). Vascular canal size increases immediately following the annulus in the middle cortex that transitions to reticular, well-vascularized canals that readily anastomose. More peripherally, vascular density decreases but some radially oriented canals open to the subperiosteal edge, indicating that this individual had not completely stopped growing at the time of death but had passed its most rapid phase of growth.

The cortex of the largest distal femur (NMT RB882; 128.74 mm estimated length) in this sample has been damaged and partially exploded from mineral growth that has completely infilled the medullary cavity (Fig. 4.10H). The articular surface appears well-ossified, with a slightly rugose texture. In thin section, the medullary cavity is infilled with small islands of broken trabeculae. The intact endosteal edge has been remodeled and consist of an irregular edge of ICL composed of parallel-fibered to lamellar bone. The remaining cortex is composed of well vascularized longitudinal canals in woven-parallel tissue that is dominated by parallel-fibered bone (Fig. 4.9G). The outermost subperiosteal edge shifts to lamellar bone comprising an EFS, indicating that this individual had passed its most rapid phase of growth prior and had reached skeletal maturity prior to death (Fig. 4.9H, I).

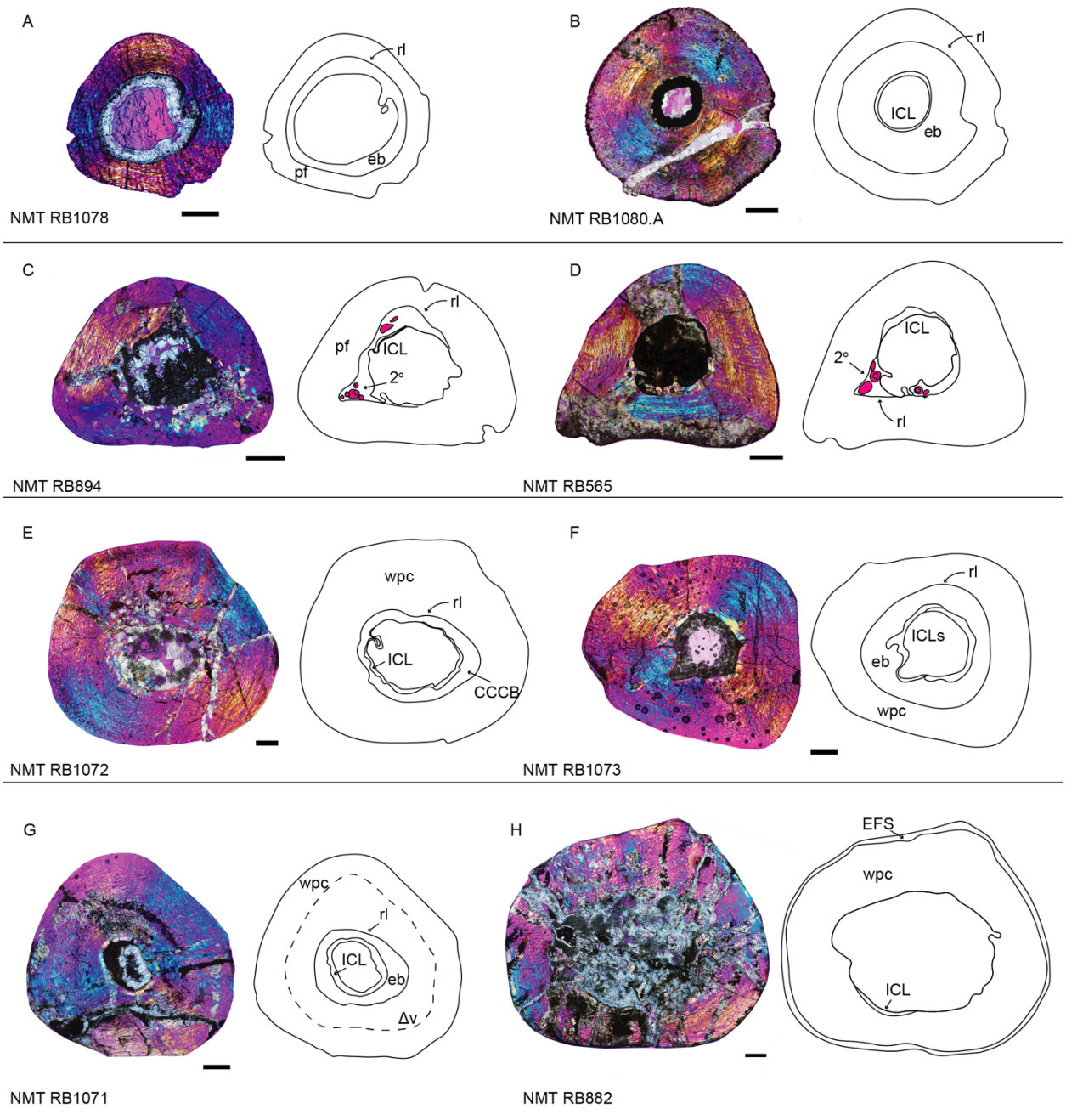
A
rl
eb
pf
NMT RB1078
B
rl
ICL
eb
NMT RB1080.A
C
rl
pf
ICL
2°
NMT RB894
D
ICL
2°
rl
NMT RB565
E
wpc
rl
ICL
CCCB
NMT RB1072
F
rl
ICLs
eb
wpc
NMT RB1073
G
wpc
rl
ICL
eb
Δv
NMT RB1071
H
EFS
wpc
ICL
NMT RB882

Figure 4.10. Transverse midshaft thin sections and interpretive drawings for all *cf. Luangwa drysdalli* femora included in the sample, arranged in increasing midshaft diameter (**A-H**). **A-C** represent size class I (<50%max femoral length), **DG**, represent size class II (50-75%max femoral length), and **H**, corresponds to size class III (>75% max femoral length). As elements increase in size, endosteal and periosteally deposited bone thicken the primary parallel-fibered dominated wpc until vascular density decreases peripherally (e.g., **G**) and an avascular EFS forms at large size (**H**). All images were taken in cross-polarized light with a lambda filter. Scale bars equal 1 mm. **Abbreviations: 2º**, secondary osteon; **Δv**, decreased vascular density and canal size; **CCCB**, compact coarse cancellous bone; **eb**, endosteal bone; **ICL**, inner circumferential layer; **LAG**, line of arrested growth; **lv pf**, low-vascular parallel-fibered bone; **rl**, reversal line; **wpc**, woven-parallel-complex.

4.5 RESULTS

4.5.1 *Bone Tissue Composition of Luangwa and Scalenodon*

Bone tissue textures seen in skeletally mature *L. drysdalli* and *S. angustifrons* conform to the three-stratum structure pattern described in a review of extant mammal histology by Buffrénil et al. (2021) and the "sandwich" pattern described by Weaver et al. (2022) in small (e.g., <5kg) eutherian and metatherian mammals. The three-stratum structure is formed by a central layer that comprises fast-growing primary periosteal tissue. It may also include compact, coarse cancellous bone (CCCB, sensu Enlow, 1963) that formed at the metaphyseal level earlier in ontogeny and was maintained and compacted during growth to reach the diaphyseal region (Fig. 4.9A, C, F; Fig. 4.10C, D). As shown in Figures 4.9 and 4.10, central strata formed by CCCB is bordered by reversal lines on either side.

The inner stratum is composed of organized, endosteally directed parallel-fibered to lamellar bone, termed the inner circumferential layer (ICL). The outer stratum consists of slow-growing parallel-fibered to lamellar tissue that is completely avascular, termed the outer circumferential layer (OCL) or external fundamental system (EFS). This peripheral tissue is not bound by a reversal line, but closely spaced LAGs can also occur within an EFS. Importantly, this peripheral tissue is indicative of skeletal maturity and represents the final smoothing of the periosteum whereby no additional apposition growth occurs.

When CCCB is not present in the central stratum, a reversal line separates the ICL from primary periosteal growth, as illustrated in Fig. 4.10A-C, D. Taken together, the local morphogenesis of the femoral shaft is a complex process in which more than one episode of medullary expansion and resorption may occur.

Despite their relatively close phylogenetic relationship, primary periosteal bone tissue differs between *L. drysdalli* and *S. angustifrons*. Primary periosteal bone tissue generally consists of parallel-fibered bone in *L. drysdalli* whereas a woven-parallel complex with disorganized vascular canals is seen in *S. angustifrons*. However, parallel- and woven-fibered bone can occur simultaneously and often in different proportions within the same section, forming a spectrum of tissue types that can be difficult to define. Here, I follow the terminology outlined in Francillion-Veilliot (1990) with updates to bone matrix terminology described in Buffrénil et al., (2021). For a detailed review of bone tissue terminology see Chapter 2.3.3 (*Bone Histology Terminology* from Kulik et al., 2021).

4.6 DISCUSSION

4.6.1 *Growth Trajectories in Traversodontidae*

Almost all fossil cynodont species that have been thin-sectioned thus far show thick, compact cortices composed of primary, rapidly-deposited bone tissue (de Ricqlès, 1969; Botha and Chinsamy, 2000, 2004, 2005; Ray et al., 2004; Chinsamy and Hurum, 2006; Chinsamy and Abdala, 2008; Botha-Brink et al., 2012, 2018; Veiga et al., 2018; Butler et al., 2019; Botha and Huttenlocker, 2021; Garcia Marsà et al., 2022). However, the current sample lacks sufficient coverage of growth stages and of histovariation within growth stages, leading to unresolved size/age correlations. This ultimately results in uncertainty surrounding the timing and speed of life history shifts in cynodonts. Sporadic, both in terms of taxonomic sampling and in terms of ontogenetic sampling, in addition to non-standardized histologic sampling of elements across the skeleton, complicates and limits assessments of growth strategies in traversodontids, in particular (Fig. 4.2). Here, the hindlimb osteohistology of *Luangwa* and *Scalenodon* provide a more

comprehensive ontogenetic sample to contextualize growth patterns for traversodontids and affords a new perspective on the evolution of cynodont growth trajectories.

In all size classes studied here, there is little to no Haversian remodeling of the cortex, and if present, resorption cavities and occasional secondary osteons are restricted to the inner cortex. However, the medullary cavity shows signs of expansion and remodeling and is rarely infilled with trabeculae. A shift towards poorly vascularized or avascular peripheral parallel-fibered to lamellar tissue is present in some individuals, suggesting that asymptotic growth was achieved in both species via sustained rapid growth. In *Luangwa*, growth was directed in both the periosteal and endosteal directions at a slower rate than what has been reported for other traversodontids at similar body sizes and proceeded in a fairly stereotyped pattern throughout the size series studied here.

By contrast, *Scalenodon*, while also growing in a sustained and even more rapid fashion than *Luangwa*, shows little to no correlation between size and bone tissue composition, as nearly all of the femora correspond to elements at similar estimated lengths (Fig. 4.11). It is difficult to rule out whether this is due to the accidental inclusion of *Mandagomphodon* femora or otherwise yet undescribed cynodont species from the Manda Beds. Despite this limitation, at least within associated cranial and femoral remains, *S. angustifrons* is characterized by highly vascularized, poorly organized, rapidly deposited tissue, unlike *L. drysdalli*.

In addition, the thickness of *Scalenodon* femoral cortices is almost entirely due to periosteally directed deposition, in contrast to the combined endosteally and periosteally directed growth in *Luangwa*. Both species are considered medium-sized fossorial animals (Liu and Abdala, 2014; Groenewald et al., 2001). Generally, fossorial animals have thick cortices with open medullary spaces (Buffrénil et al., 2021, Montoya-Sanhueza et al., 2017) which is reflected

in the thick cortices seen in both species studied here (Supplementary Table 4.1). It appears that *Scalenodon* was able to achieve thick cortices via sustained rapidly deposited tissue whereas *Luangwa* femora grew at slightly slower rates and were thickened via periosteal and endosteally directed deposition.

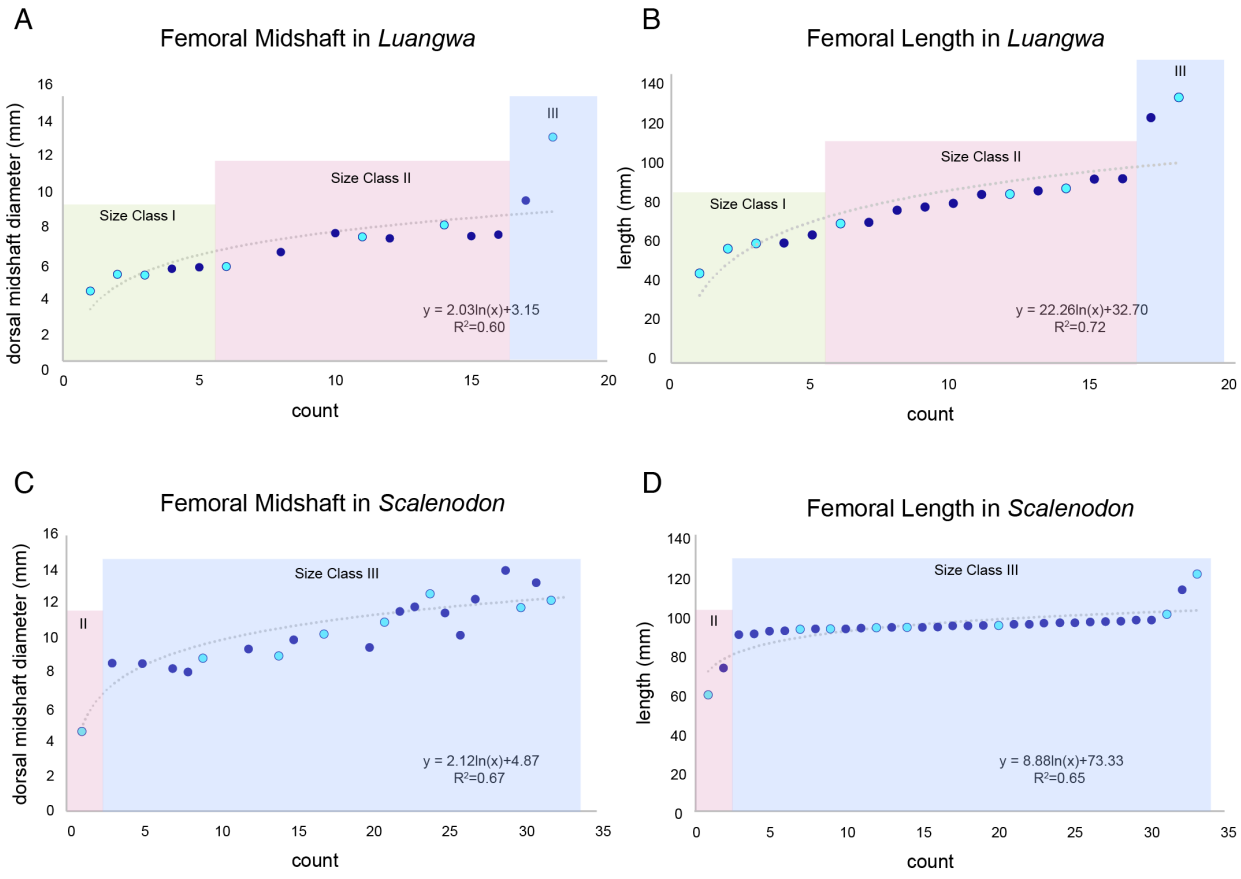

Figure 4.11. Logarithmic trend lines fitted to femoral midshaft and estimated length measurements in *Luangwa* and *Scalenodon* indicate weak asymptotic growth in *Luangwa* whereas *Scalenodon* femora are very similar in length (except for some small and large outliers) but show highly variable midshaft diameters. Each blue dot represents one femur in this sample with cyan colors highlighting histologically sampled individuals and dark blue dots representing unsampled individuals. Size Classes calculated from maximum femoral length for each species, respectively include <50% max length in Size Class I, 5075% max length in Size Class II, and >75% max length in Size Class III.

4.6.2 ***Developmental Plasticity in Scalenodon***

The growth pattern of *Scalenodon angustifrons* is characterized by initial rapid growth that plateaus at skeletal maturity in one of the femora sampled here (NMT RB864). The prevalence of woven-parallel bone tissue throughout the majority (or entirety; NMT RB581) of the cortex suggests an uninterrupted rapid rate of bone deposition throughout ontogeny. However, only NMT RB864 shows attainment of skeletal maturity whereas two other individuals show shifts to slower growth (NMT RB731 and NMT RB866) and yet another individual (NMT RB862) shows at least two LAGs near the outermost cortex. Such variability between individuals of the same size class indicates that histological and skeletal markers of maturity are decoupled for *Scalenodon angustifrons*; six sectioned femora are estimated to be 94–100 mm long and have similarly developed articular surfaces, but only one is histologically mature. Rather than following a developmental pattern whereby bone tissue composition changes from fast to slow growth in elements that are approaching maximum known size (estimated maximum femoral length for *Scalenodon* is 123 mm), *S. angustifrons* likely had a polymorphic developmental trajectory because equivalently sized femora reveal different developmental stages.

It is possible that variability in bone tissue composition is due to sampling other species that matured at smaller size. However, *Mandagomphodon*, while not known from postrcranial remains, overlaps in skull size with *Scalenodon* (dentary = 118.3 mm estimated length; Hopson, 2014), suggesting that femora should be of similar size. It is also possible that other, yet undescribed, cynodont species are represented in this sample. However, no substantial variation in femoral morphology suggests a new morphotype, nor are there

associations of cranial and postcranial remains provide clarity on more minute or nuanced morphological variation at the genus or species level.

Variability in development is well-demonstrated in extant vertebrates, and similar variability in morphology and growth trajectory has been observed in early dinosaurs and non-dinosaurian dinosauromorphs (e.g., Griffin and Nesbitt, 2016a; Barta et al., 2022), and is often interpreted as sexual dimorphism. However, using ontogenetic sequence analyses of non-avian dinosaurs and their closest extant relatives, Griffin and Nesbitt (2016b) hypothesized that anomalously high variation in postnatal development is plesiomorphic for dinosaurs and not a reflection of sexual dimorphism. From a histological perspective, the same high level of variation in developmental plasticity is seen from *Scalenodon* growth trajectories. However, ontogenetic sequence analysis that combines morphological and histological changes in skeletal growth are not available for *Scalenodon* as many of the thin-sectioned elements are incompletely preserved. Despite this limitation, additional evidence for intraspecific variation in bone tissue composition has also been reported in *Massetognathus pascuali*, where smaller femora show slow-growing tissue compared to distinctly longer femora that record continuous rapid growth at death (Garcia Marsà et al., 2022; Abdala and Chinsamy, 2008). This suggests that highly variable developmental plasticity evolved in parallel among Triassic archosaurs and synapsids. Alternatively, developmental plasticity may be plesiomorphic for Amniota more broadly, but additional studies that correlate size, age, and morphology across a large sample of individuals at different developmental stages is needed to test this hypothesis.

Taken together, these results challenge presumed correlations between element size and developmental stage for cynodonts, as neither size nor external morphology effectively predict sexual or skeletal maturity for *Scalenodon*. Further, this result may help to explain why skeletal

maturity is rarely captured in cynodont fossils (de Ricqlès, 1969; Botha and Chinsamy, 2000, 2004, 2005; Ray et al., 2004; Chinsamy and Hurum, 2006; Chinsamy and Abdala, 2008; Botha-Brink et al., 2012, 2018; Veiga et al., 2018; Butler et al., 2019; Garcia Marsà et al., 2022). Other plausible explanations for a lack of more frequent histological evidence for maturity in cynodonts include: sparse histological sampling across taxa, across the skeleton, and across inferred ontogenetic series; scarcity of skeletally mature adults in the fossil record, high mortality prior to attainment of skeletal maturity; or other biases in the fossil record. I explore some of these factors below. However, they are not mutually exclusive, which underscores the need for better histological sampling to increase taxonomic, skeletal, and size sampling, in order to more comprehensively capture growth patterns in the fossil record. In addition, the results presented here underscore the need for iterative histological sampling of elements within the same size class to interpret the growth patterns of extinct taxa more accurately.

4.6.3 *Rarity of Histologically Mature Permo-Triassic Cynodonts*

Numerous factors influence the probability of recovering skeletally mature individuals from osteohistological analyses, including biological, taphonomic, and sampling biases. From a biological standpoint, cynodonts have determinate growth as evidence by attenuating size and the presence of an EFS in a handful of species (Fig. 4.2). Therefore, we should expect to recover skeletally mature individuals if the biases of the fossil record have not filtered out these individuals. One of the only ways to overcome taphonomic biases is to target histological analyses from large numbers of individuals that have been collected from the same locality. However, fossils are rare and consumptively sampling numerous individuals may not be available or possible due to curatorial constraints. When large sample sizes are

available, they have their own inherent limitations as they can either be derived from multiple elements that were sectioned from the same individual, or derived from isolated and incomplete elements from multiple individuals (as is the case with this sample). When large sample sizes are possible, for example in the case of the hadrosaur *Maiasaura peeblesorum*, skeletally mature tissue is still rare and present in only five of the fifty tibiae that were thin-sectioned (Woodward et al., 2015).

That an EFS is found in one individual each of *S. angustifrons* and *L. drysdalli*, from a sample of eighteen sectioned femora represents nearly the same 'recovery rate' as in *Maisaura*. However, considering that all but one femur are within the same size range of 90–123 mm long for the *Scalenodon* sample, this points to a biological rarity caused by polymorphic growth trajectory.

4.6.4 *Age-Structure of the Multitaxic Manda Bed Assemblage*

The dinosauriform *Asilisaurus kongwe* and the rhynchosaur *Stenaulorhynchus stockleyi* are two other tetrapods that have been histologically sampled that co-occur with the cynodonts examined here, and histological data from these reptiles can further contextualize the biological vs. taphonomic bias on mature tissue types in this fossil assemblage. The bone histology of *Asilisaurus kongwe* shows highly polymorphic growth, indicating that size and age are similarly poorly correlated, as in *Scalenodon* (Griffin and Nesbitt, 2016a). The tibia and femur of one individual of *Stenaulorhynchus stockleyi* indicate that skeletal maturity was reached prior to death via slow and cyclical growth (Werning and Nesbitt, 2016). Little insight is gained from this comparison because of the underlying growth rates that each species displays: *S. stockleyi* has a slower rate of growth that arrested regularly throughout ontogeny whereas *A.*

kongwe, *L. drysdalli*, and *S. angustifrons* all show non-cyclical fast growth until death or skeletal maturity.

Therefore, the differences in bone tissue from Manda vertebrate tissues described thus far are likely due to physiological differences in the slower metabolic rate of non-archosauriform archosauromorphs compared to faster rates inferred for dinosauriforms and cynodonts (Huttenlocker and Farmer, 2017). However, *Luangwa* likely had an elevated metabolic rate similar to *Scalenodon* and *Asilisaurus* but shows a "typical" or constrained growth trajectory of moderately paced growth that attenuates at large size. This suggests that the scarcity of mature tissue types is driven by developmentally plastic growth strategies demonstrated in *Scalenodon* (and *Asilisaurus*) which could be a result of a faster pace of life history in these species. What drives a faster pace is difficult to determine, but from theoretical evolutionary models conducted by Marty et al., (2011), age at maturation can be decelerated when extrinsic mortality is high, which can be driven by poor environmental conditions exacerbated by high density-populations. Indeed, *Scalenodon* represents the most abundant cynodont species in mid-upper Lifua localities and aggregations of animals are suggested to have accumulated in large numbers around shrinking ponds, reflective of a stressful environmental (Smith et al., 2018).

The rate of skeletal growth is difficult to determine for *Scalenodon* (and *Luangwa*) because cyclical growth marks used to estimate absolute age are not recorded in any of the individuals sampled thus far, nor are they present in *A. kongwe* (Griffin and Nesbitt, 2016a). If it were possible to measure the absolute age of cynodont species, growth models could estimate the speed of growth and the length of developmental stages for cynodonts. In the absence of these data, we can assess whether asymptotic growth curves using element size characterize the cynodont femora (Fig. 4.11). However, this is only a visualization of how element size increases

in this histologic sample and therefore cannot be used to determine the age when life history shifts occurred in these species. Using both dorsal midshaft diameter and estimated femoral length, a weak asymptote is reached in *Luangwa* but is complicated by large individuals (Fig. 4.11. A, B), whereas element size is almost entirely constrained to a single size class for *Scalenodon* (Fig. 4.11 C, D). That histological markers of maturity are so rarely shown in this large size either indicates that a taphonomic bias removed larger elements from the sample, or that *Scalenodon* suffered from high rates of mortality at this size. Rhynchosaur elements are recovered from the same localities and are substantially larger and more robust that *Scalenodon* remains, suggesting that mortality rates drive the size spectrum and growth strategy seen in *Scalenodon*.

4.6.5 ***Adaptations to Fossoriality***

Despite their similar size, femora referable to *Luangwa* have distinctively larger muscle insertion sites, fossae, and trochanters compared to *Scalenodon*, and in combination with thick cortices composed of endosteally directed parallel-fibered bone, these features suggest that *Luangwa* was adapted for fossoriality. Thick and more mineralized bone tissue (i.e., parallel-fibered bone) withstand impact loads better than woven-fibered tissue and commonly compose the cortices of fossorial animals such as the cape dunerat and naked molerat akin to the pattern described for *Luangwa* (Montoya-Sanheuza et al., 2017, 2021). Interestingly, in the naked-mole rat, fluorochrome injected dyes were retained in both the endosteal and subperiosteal regions of the cortex over a period of 7 months, indicating that bone turnover and resorption rates are very low for this species (Montoya-Sanhueza et al., 2021). Bone turnover is similarly low in *Luangwa* femora, but deep areas of secondary remodeling in the inner cortex of some individuals in this

sample provide evidence that *Luangwa* may have had a slightly higher demand for calcium mobilization compared to extant fossorial mammals.

Thick, compact cortices in extant fossorial and inferred fossorial fossil species contrasts with observations made on surface dwelling animals which show pronounced bone loss with aging, especially in the perimedullary region (e.g., Bonucci and Ballanti, 2014; Cerroni et al., 2000; Duque & Watanabe, 2011; Frost & Jee, 1992). Low levels of perimedullar bone remodeling and maintenance of thick, compact cortices supports the hypothesis that *L. drysdalli* femoral cortices reflect a fossorial or subterranean lifestyle. However, *Scalenodon* has similarly thick cortices compared to *Luangwa* but achieved these thicknesses via periosteally directed growth that was much more vascularized. Moreover, much of the perimedullary region shows signs of remodeling and resorption in *Scalenodon*. From the current sample, *Scalenodon* cortices do not show the same degree of fossorial adaptation, despite having similarly thick cortices (see Supplemental Table 4.1). Future work can explore this hypothesis through comparisons of cortical vascular density and other histometric variables shown to correlate with lifestyle inference that are widely used in paleobiology (Buffrénil et al., 2021; Amson and Muizon, 2018; Quemeneur et al., 2013).

4.6.6 ***Shifts in bone composition and life history in extant mammals***

Due to a lack of growth marks in this sample, it is difficult to assess the age or developmental stage when growth rates slowed in *Scalenodon* and *Luangwa*. Indeed, a prerequisite for reliable skeletochronology in fossil taxa is the correlation of bone tissue transitions with life history events in closely related extant species with known life history and age of sexual maturity. Fluorochrome labelling studies provide detailed data on the

development of lone bone cortices of extant mammal species and have been used to infer the age at sexual maturity in closely related fossil species (Nacarino-Meneses et al., 2018; Köhler et al., in press). For example, rabbits typically reach sexual maturity by age 6–7 months and females become pregnant between 8–12 months (Broekhuizen and Maaskamp, 1981). Descriptions by Pazzaglia et al., (2015) of femoral cortices of rabbits aged 1.5 months to 7.5 years show that in early growth stages the bone cortex consists of a woven-parallel complex with longitudinal primary osteons. By the age of 6 months, the cortical matrix turns into parallel-fibered bone with simple vascular canals and longitudinal primary osteons. Growth proceeds as scarcely vascularized tissue in older individuals, and the peripheral cortex of adults is composed of a poorly vascularized or avascular parallel-fibered tissue, bordered by a thin layer of lamellar bone in an EFS (Pazzaglia et al., 2015). This pattern matches the bone tissue in *Scalenodon*, *Luangwa*, and most other cynodonts, however, the duration of each stage of bone deposition is difficult to correlate between rabbits and cynodonts without broader taxonomic labelling studies on mammals with slower paces of life history. Currently, other mammal species with available fluorochrome labeling details include the mouse lemur, *Microcebus* (Castanet et al., 2004), the naked mole-rat (Montoya-Sanhueza et al., 2021), a latitudinally widespread sample of ruminants (Köhler et al., 2012, Calderon et al., 2021), and the onager, *Equus hemionus* (Nacarino-Meneses et al., 2016). Future work should investigate histomorphological changes related to life history in mammals that have prolonged phases of growth before sexual maturity.

4.6.7 ***The Evolution of Growth Strategies in Cynodonts***

The ability to grow rapidly, as evidenced by the production of fibrolamellar or woven-parallel bone, is widespread in Synapsida (Shelton and Sander, 2017; Huttenlocker and Rega,

2012; Kulik et al., 2021; Huttenlocker and Botha, 2013; Huttenlocker and Botha, 2021), suggesting that this bone tissue type extends deep into the amniote lineage and may even be an innovation of Tetrapoda (Whitney et al., 2022). However, when comparing bone tissue in a phylogenetic context in Cynodontia, patterns emerge that afford a reappraisal of the evolution of cynodont growth strategies (Fig. 4.12). These interpretations must be prefaced with the reminder that growth occurs at different rates throughout the skeleton and that intraskeletal variation in the development of an EFS, number of LAGs, and degree of remodeling is highly variable (Castanet et al., 2004; de Margerie et al., 2004; Buffrénil et al., 2021). With that said, the basal-most cynodont that has been histologically sampled (*Procynosuchus*) reveals that growth occurred over a prolonged phase of slow, seasonally interrupted growth (Ray et al., 2004).

Eucynodont species that survived the EPME or diversified in the earliest Triassic have growth trajectories that start out quickly and then transition to peripheral slow-growing tissue, with little correlation between element size and maturity status (e.g., *Thrinaxodon*) suggesting that polymorphic growth and developmental plasticity was selected for during the extinction interval, at least among species that have been histologically sampled (Botha and Chinsamy, 2005; Butler et al., 2019). This developmental plasticity appears to be somewhat constrained in Diademodontidae and Trirachodontidae that experience cyclically arrested growth in an otherwise woven-parallel complex in early ontogeny that transitions to peripheral parallel-fibered bone. For example, *Diademodon*, *Trirachodon*, and *Langbergia* show cyclical growth marks in cortices composed of parallel-fibered bone (Botha and Chinsamy, 2000; Botha and Chinsamy, 2004; Botha-Brink et al., 2012) indicating that the stock lineage that gave rise to traversodontids grew unlike modern mammals and had extended, moderately paced growth to reach large size. Non-traversodont gomphodontian species were also susceptible to seasonal fluctuations reflected

by cyclical LAGs, possibly due to highly variable environmental conditions in Induan and Olenekian post-extinction environments (Botha and Chinsamy, 2000; Botha-Brink et al., 2012).

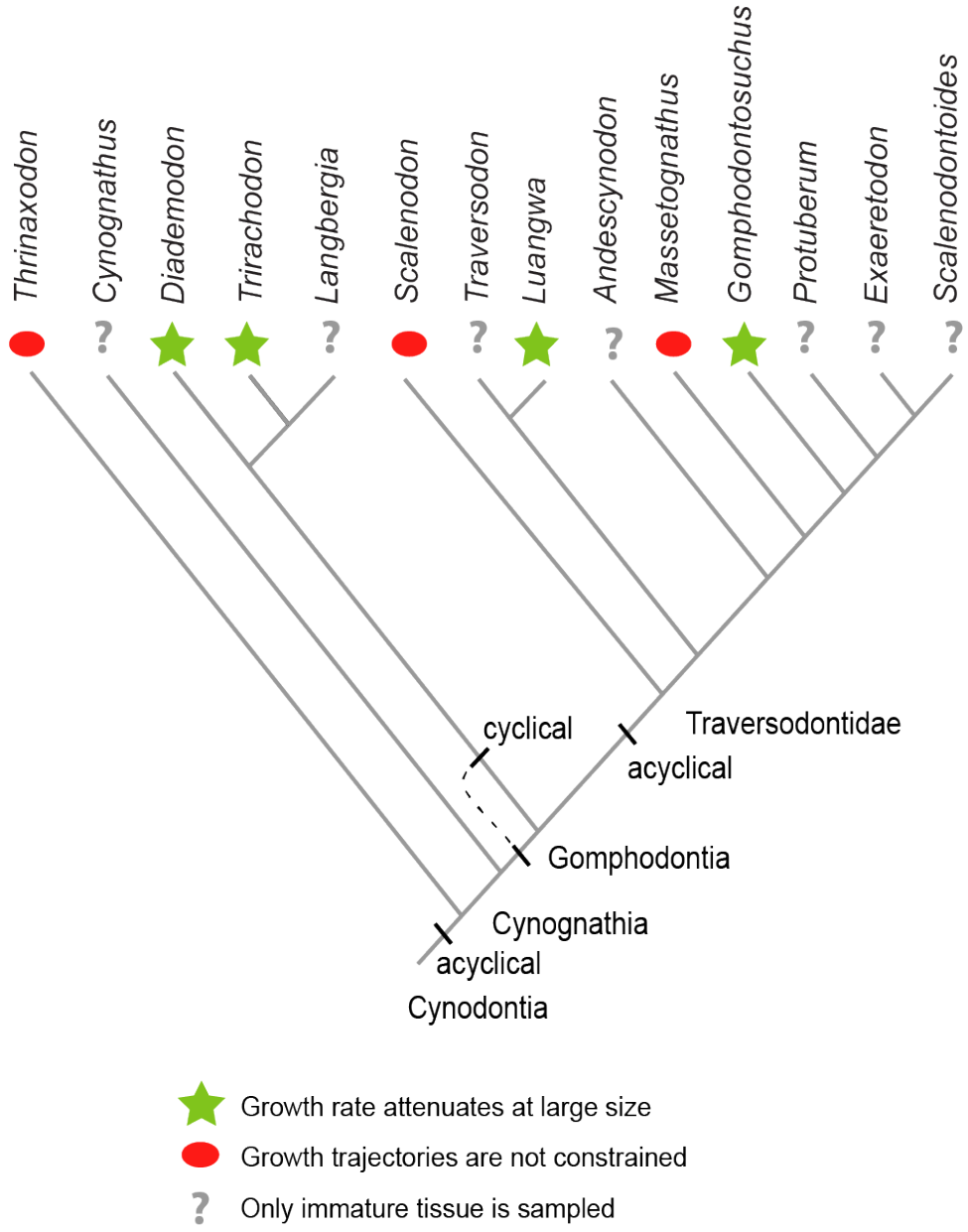

Figure 4.12. Cladogram of trends in traversodontid growth strategies. Diet, body size, and phylogenetic relatedness do not explain the variable growth trajectories documented in species that have been histologically sampled whereas inferences are not available from samples derived from immature tissue.

During the Middle–Late Triassic, traversodontids that have been sampled from southern African and South American Ladinian–Carnian deposits show acyclical, moderately to rapidly deposited tissue throughout early ontogeny, but very few species provide insight into growth strategies as only immature tissue has been sampled thus far (e.g., *Traversodon*, *Protuberum*, *Exaeretodon*, and *Scalenodontoides*) (de Ricqlès, 1969; Botha-Brink et al., 2012; Veiga et al., 2018). In comparison, the growth strategy for the Anisian species *Scalenodon* reflects the highest degree of developmental polymorphism which may also be echoed in *Massetognathus* (Carnian) and possibly *Andescynodon* (Anisian–Ladinian; however, only one individual that grew unusually slowly has been sampled for *Andescynodon*). In stark contrast, the coeval Anisian species *Luangwa* provides the most compelling evidence of attenuating growth in traversodontids that occurred via moderately rapid growth until skeletal maturity was reached.

4.7 CONCLUSIONS

Here, differences in growth rate and growth strategy between two coeval traversodont species from the Anisian of Tanzania are revealed through femoral histology. Initial moderately paced growth abruptly transitions to avascular lamellar tissue indicating that skeletal maturity was reached via sustained growth rates in *L. drysdalli*. In contrast, the femoral histology of *S. angustifrons* is composed of disorganized, well-vascularized woven-parallel tissue that: arrests in at least one individual, shows peripheral slow growth in other individuals, or sustained rapid growth in another still, all within the same size class, indicating that histological details and element size are poorly correlated in this species.

From this sample derived from penecontemporaneous strata that experienced seasonal droughts during the Anisian (Smith et al., 2018), differences in growth rate and growth strategy

among individuals cannot be attributed to differences in paleoenvironment or phylogenetic affinity, and instead suggest inherent biological differences. If future works confirms the histological differences of these two species, I hypothesize that their divergent growth strategies are driven by increased mortality risk for *Scalenodon* that resulted in highly variable developmental trajectories and poor correlation between size and age.

The sustained and relatively rapid growth demonstrated in *Luangwa* strongly suggests that development occurred during a prolonged phase of moderately paced parallel-fibered dominated woven-parallel bone. These results also reveal that cortices were buttressed with endosteally directed parallel-fibered bone as an adaptation to fossoriarility. Coupled with the well-developed muscle attachment sites, larger trochanters and fossae, and thick cortices for impact loading, the differences in bone composition between *Luangwa* and *Scalenodon* may be driven by different ecological roles. However, *Scalenodon* has equally thick cortices, but achieved thick bones via periosteally directed bone that is not as compact, and instead is composed of disorganized vascular canals in a woven-fibered matrix.

Finally, evidence of a stereotyped growth strategy, where size and histological details are fairly well-correlated in *Luangwa*, contributes new insights into the evolution of constrained growth strategies outside the immediate ancestors of mammals and provides evidence that species in cynodont side branches evolved growth patterns and adaptations to fossoriality akin to extant small burrowing mammals alive today.

4.8 ACKNOWLEDGEMENTS

I thank the 2007 and 2012 field crews to Tanzania. Fossils were collected with support from NGS 7787-05, NGS 8962-11, and NSF EAR-1337569 (to C. A. Sidor), NSF DBI-

0306158 (to K. D. Angielczyk). Lianna Marilao is thanked for her expert assistance in making thin-sections and Kimberly Schoenberger is thanked for helping with data collection. Sophia Powers and Julia Ricks are thanked for their heroic efforts to catalogue and inventory the Tanzanian and Zambian fossil collections temporarily housed at the Burke Museum. Fossils were curated, prepared, and photographed by Mike Rich, Craig Abramson, Gary Livingston, Bruce Crowley, Kelsie Abrams, Katie Anderson, Bob Masek, and other volunteers from the Burke prep lab. Scientific illustrations were drawn by Crystal Shin with support from the UW Walker Family and Hoag Awards (to Z. T. Kulik). I thank members of my reading committee, Drs. C. A. Sidor, T. Popowics, G. P. Wilson Mantilla, A. K. Huttenlocker, for providing detailed feedback to help improve this work. I also thank Drs. B. M. Gee, M. R. Whitney, and Y. Haridy for their advice, histology brainstorming sessions, feedback, and reviews throughout the various stages of this project and its many drafts.

4.9 Literature Cited

Abdala, F., & Gaetano, L. C. (2018). The Late Triassic Record of Cynodonts: Time of Innovations in the Mammalian Lineage. In L. H. Tanner (Ed.), *The Late Triassic World: Earth in a Time of Transition* (pp. 407–445). Springer International Publishing. https://doi.org/10.1007/978-3-319-68009-5_11

Abdala, F., & Giannini, N. P. (2002). Chiniquodontid cynodonts: Systematic and morphometric considerations. *Palaeontology*, *45*(6), 1151–1170. https://doi.org/10.1111/1475-4983.00280

Abdala, F., & Ribeiro, A. M. (2003). A new traversodontid cynodont from the Santa Maria Formation (Ladinian-Carnian) of southern Brazil, with a phylogenetic analysis of Gondwanan traversodontids. *Zoological Journal of the Linnean Society*, *139*(4), 529–545.

Abdala, F., & Ribeiro, A. M. (2010). Distribution and diversity patterns of Triassic cynodonts (Therapsida, Cynodontia) in Gondwana. *Palaeogeography, Palaeoclimatology, Palaeoecology*, *286*(3–4), 202–217. https://doi.org/10.1016/j.palaeo.2010.01.011

Abdala, F., & SaTeixeira, A. M. (2004). A traversodontid cynodont of African affinity in the South American Triassic. http://wiredspace.wits.ac.za/handle/10539/15955

Amson, E., & de Muizon, G. (2018). Evolutionary adaptation to aquatic lifestyle in extinct sloths can lead to systemic alteration of bone structure. *Proceedings of the Royal Society B: Biological Sciences*, *285*(270).

Barghusen, H. R. (1968). The lower jaw of cynodonts (Reptilia, Therapsida) and the evolutionary origin of mammal-like adductor jaw musculature.

Barrett, P. M., Nesbitt, S. J., & Peecook, B. R. (2015). A large-bodied silesaurid from the Lifua Member of the Manda beds (Middle Triassic) of Tanzania and its implications for body-size evolution in Dinosauromorpha. *Gondwana Research*, *27*(3), 925–931. https://doi.org/10.1016/j.gr.2013.12.015

Barta, D. E., Griffin, C. T., & Norell, M. A. (2022). Osteohistology of a Triassic dinosaur population reveals highly variable growth trajectories typified early dinosaur ontogeny. *Scientific Reports*, *12*(1), Article 1. https://doi.org/10.1038/s41598-022-22216-x

Bonucci, E., & Ballanti, P. (2014). Osteoporosis—Bone Remodeling and Animal Models. *Toxicologic Pathology*, *42*(6), 957–969. https://doi.org/10.1177/0192623313512428

Botha, J., & Chinsamy, A. (2000). Growth Patterns Deduced from the Bone Histology of the Cynodonts *Diademodon* and *Cynognathus*. *Journal of Vertebrate Paleontology*, *20*(4), 705–711.

Botha-Brink, J., Abdala, F., & Chinsamy, A. (2012). The Radiation and Osteohistology of Nonmammaliaform Cynodonts. In *Forerunners of mammals: Radiation, histology, biology* (p. 223). Indiana University Press.

Botha, J., & Chinsamy, A. (2004). Growth and life habits of the Triassic cynodont *Trirachodon*, inferred from bone histology. *Acta Palaeontologica Polonica*, *49*(4).

Botha, J., & Chinsamy, A. (2005). Growth Patterns of *Thrinaxodon liorhinus*, a Non-Mammalian Cynodont from the Lower Triassic of South Africa. *Palaeontology*, *48*(2), 385–394. https://doi.org/10.1111/j.1475-4983.2005.00447.x

Botha, J., & Huttenlocker, A. K. (2021). Nonmammalian Synapsids. In *Vertebrate Skeletal Histology and Paleohistology* (p. 550). CRC Press, Taylor & Francis Group. https://www.taylorfrancis.com/books/9781351189590

Botha, J., Abdala, F., & Smith, R. (2007). The oldest cynodont: New clues on the origin and early diversification of the Cynodontia. *Zoological Journal of the Linnean Society*, *149*(3), 477–492.

Broekhuizen, S., & Maaskamp, F. (1981). Annual production of young in European hares (*Lepus europaeus*) in the Netherlands. *Journal of Zoology*, *193*(4), 499–516. https://doi.org/10.1111/j.1469-7998.1981.tb01500.x

Buffrénil, V. de, Ricqlès, A. de, Zylberberg, L., & Padian, K. (Eds.). (2021). *Vertebrate skeletal histology and paleohistology*. CRC Press, Taylor & Francis Group.

Butler, E., Abdala, F., & Botha-Brink, J. (2019). Postcranial morphology of the Early Triassic epicynodont *Galesaurus planiceps* (Owen) from the Karoo Basin, South Africa. *Papers in Palaeontology*, *5*(1), 1–32. https://doi.org/10.1002/spp2.1220

Butler, R. J., Fernandez, V., Nesbitt, S. J., Leite, J. V., & Gower, D. J. (2022). A new pseudosuchian archosaur, *Mambawakale ruhuhu* gen. Et sp. Nov., from the Middle Triassic Manda Beds of Tanzania. *Royal Society Open Science*, *9*(2), 211622. https://doi.org/10.1098/rsos.211622

Butler, R. J., Nesbitt, S. J., Charig, A. J., Gower, D. J., & Barrett, P. M. (2017). *Mandasuchus tanyauchen* , gen. Et sp. Nov., a pseudosuchian archosaur from the Manda Beds (?Middle

Triassic) of Tanzania. *Journal of Vertebrate Paleontology*, *37*(sup1), 96–121. https://doi.org/10.1080/02724634.2017.1343728

Calderón, T., Arnold, W., Stalder, G., Painer, J., & Köhler, M. (2021). Labelling experiments in red deer provide a general model for early bone growth dynamics in ruminants. *Scientific Reports*, *11*(1), Article 1. https://doi.org/10.1038/s41598-021-93547-4

Cerroni, A. M., Tomlinson, G. A., Turnquist, J. E., & Grynpas, M. D. (2000). Bone mineral density, osteopenia, and osteoporosis in the rhesus macaques of Cayo Santiago. *American Journal of Physical Anthropology*, *113*(3), 389–410. https://doi.org/10.1002/1096-8644(200011)113:3<389::AID-AJPA9>3.0.CO;2-I

Chinsamy, A., & Abdala, F. (2008). Palaeobiological implications of the bone microstructure of South American traversodontids (Therapsida: Cynodontia). *South African Journal of Science*, *104*(5–6), 225–230.

Chinsamy, A., & Hurum, J. H. (2006). Bone microstructure and growth patterns of early mammals. *ACTA PALAEONTOLOGICA POLONICA*, 14.

Crompton, A. W. (1955). On some Triassic cynodonts from Tanganyika. *Proceedings of the Zoological Society of London*, *125*(3–4), 617–669. https://doi.org/10.1111/j.1096-3642.1955.tb00620.x

Crompton, A. W. (1963). The Evolution of the Mammalian Jaw. *Society for the Study of Evolution*, *17*, 10.

Crompton, A. W., & Jenkins, F. A. (1973). Mammals from Reptiles: A Review of Mammalian Origins. *Annual Review of Earth and Planetary Sciences*, *1*(1), 131–155. https://doi.org/10.1146/annurev.ea.01.050173.001023

Crompton, A. W., Joysey, K. A., & Kemp, T. S. (1972). The evolution of the jaw articulation of cynodonts. *Studies in Vertebrate Evolution*, *17*, 21.

Cubo, J., Legendre, L., & Laurin, M. (2021). Phylogenetic Signal in Bone Histology. In V. de Buffrénil, A. J. de Ricqlès, K. Padian, & L. Zylberberg (Eds.), *Vertebrate Skeletal Histology and Paleohistology* (1st ed.). CRC Press, Taylor & Francis Group. https://doi.org/10.1201/9781351189590

Cubo, J., Legendre, P., De Ricqlès, A., Montes, L., De Margerie, E., Castanet, J., & Desdevises, Y. (2008). Phylogenetic, functional, and structural components of variation in bone growth rate of amniotes: Evolution of bone growth patterns in amniotes. *Evolution & Development*, *10*(2), 217–227. https://doi.org/10.1111/j.1525-142X.2008.00229.x

Cubo, J., Ponton, F., Laurin, M., De Margerie, E., & Castanet, J. (2005). Phylogenetic Signal in Bone Microstructure of Sauropsids. *Systematic Biology*, *54*(4), 562–574. https://doi.org/10.1080/10635150591003461

Curry, K. A. (1999). Ontogenetic histology of *Apatosaurus* (Dinosauria: Sauropoda): New insights on growth rates and longevity. *Journal of Vertebrate Paleontology*, *19*(4), 654–665.

de Margerie, E., Cubo, J., & Castanet, J. (2002). Bone typology and growth rate: Testing and quantifying 'Amprino's rule' in the mallard (*Anas platyrhynchos*). *Comptes Rendus Biologies*, *325*(3), 221–230. https://doi.org/10.1016/S1631-0691(02)01429-4

de Margerie, E., Robin, J.-P., Verrier, D., Cubo, J., Groscolas, R., & Castanet, J. (2004). Assessing a relationship between bone microstructure and growth rate: A fluorescent labelling study in the king penguin chick (*Aptenodytes patagonicus*). *Journal of Experimental Biology*, *207*(5), 869–879. https://doi.org/10.1242/jeb.00841

de Ricqlès, A. (1969). Recherches paleohistologiques sur les os longs des tetrapodes; II, Quelques observations sur la structure des os longs des theriodontes. *Annales de paléontologie. Vertébrés*, *55*(1), 52.
de Ricqlès, A. (1974). Evolution of Endothermy: Histological Evidence. *Evolutionary Theory*, *1*(2), 51–80.
Duque, G., & Watanabe, K. (2011). *Osteoporosis Research: Animal Models*. Springer Science & Business Media.
Enlow, D. H. 1963. Principles of bone remodeling: an account of post-natal growth and remodeling processes in long bones and the mandible. Charles C. Thomas, Springfield, IL.
Enlow, D. H., and S. O. Brown. 1958. A comparative histological study of fossil and recent bone tissues. III. Texas Journal of Science 10:187–230.
Farmer, C. G. (2000). Parental Care: The Key to Understanding Endothermy and Other Convergent Features in Birds and Mammals. The American Naturalist, 155(3), 326–334. https://doi.org/10.1086/303323
Filippini, F., Abdala, F., & Cassini, G. (2022). Body mass estimation in Triassic cynodonts from Argentina based on limb variables. Acta Palaeontologica Polonica, 67. https://doi.org/10.4202/app.00919.2021
Francillon-Vieillot, H., de Buffrénil, V., Castanet, J., Géraudie, J., Meunier, F. J., Sire, J. Y., Zylberberg, L., & de Ricqlès, A. (1990). Microstructure and Mineralization of Vertebrate Skeletal Tissues. In J. G. Carter (Ed.), *Short Courses in Geology* (pp. 175–234). American Geophysical Union. https://doi.org/10.1029/SC005p0175
Garcia Marsà, J. A., Agnolín, F. L., & Novas, F. E. (2022). Comparative bone microstructure of two non-mammaliaform cynodonts from the Late Triassic (Carnian) Chañares formation of Northwestern Argentina. *Historical Biology*, *0*(0), 1–11. https://doi.org/10.1080/08912963.2022.2149332
Germain, D., and M. Laurin. 2005. Microanatomy of the Radius and Lifestyle in Amniotes (Vertebrata, Tetrapoda). Zoologica Scripta 34 (4): 335–50. https://doi.org/10.1111/j.1463-6409.2005.00198.x.
Goñi, R., & Goin, F. J. (1988). Morfologia Dentaria y Biomecanica Masticatoria de los Cinodontes (Reptilia, Therapsida) del Triasico Argentino: I Andescynodon Mendozensis Bonaparte (Traversodontidae) (No. 2). *25*(2), Article 2. https://www.ameghiniana.org.ar/index.php/ameghiniana/article/view/1905
Gow, C. E. (1978). The advent of herbivory in certain reptilian lineages during the Triassic. http://hdl.handle.net/10539/16256
Griffin, C. T., & Nesbitt, S. J. (2016a). The femoral ontogeny and long bone histology of the Middle Triassic (?late Anisian) dinosauriform *Asilisaurus kongwe* and implications for the growth of early dinosaurs. *Journal of Vertebrate Paleontology*, *36*(3), e1111224. https://doi.org/10.1080/02724634.2016.1111224
Griffin, C. T., & Nesbitt, S. J. (2016b). Anomalously high variation in postnatal development is ancestral for dinosaurs but lost in birds. *Proceedings of the National Academy of Sciences*, *113*(51), 14757–14762. https://doi.org/10.1073/pnas.1613813113
Griffin, C. T., Stefanic, C. M., Lessner, E. J., Riegler, M., Formoso, K., Koeller, K., & Nesbitt, S. J. (2020). Assessing ontogenetic maturity in extinct saurian reptiles. *Biological Reviews*, 56.

Groenewald, G. H., Welman, J., & Maceachern, J. A. (2001). Vertebrate Burrow Complexes from the Early Triassic Cynognathus Zone (Driekoppen Formation, Beaufort Group) of the Karoo Basin, South Africa. *PALAIOS*, *16*(2), 148–160. https://doi.org/10.1669/0883-1351(2001)016<0148:VBCFTE>2.0.CO;2

Harvey, P. H., Pagel, M. D., & Rees, J. A. (1991). Mammalian Metabolism and Life Histories. *The American Naturalist*, *137*(4), 556–566. https://doi.org/10.1086/285183

Hendrickx, C., Abdala, F., & Choiniere, J. (2016). Postcanine microstructure in *Cricodon metabolus*, a Middle Triassic gomphodont cynodont from south-eastern Africa. *Palaeontology*, *59*(6), 851–861. https://doi.org/10.1111/pala.12263

Hendrickx, C., Abdala, F., & Choiniere, J. N. (2019). A proposed terminology for the dentition of gomphodont cynodonts and dental morphology in Diademodontidae and Trirachodontidae. *PeerJ*, *7*, e6752. https://doi.org/10.7717/peerj.6752

Hendrickx, C., Gaetano, L. C., Choiniere, J. N., Mocke, H., & Abdala, F. (2020). A new traversodontid cynodont with a peculiar postcanine dentition from the Middle/Late Triassic of Namibia and dental evolution in basal gomphodonts. *Journal of Systematic Palaeontology*, *18*(20), 1669–1706. https://doi.org/10.1080/14772019.2020.1804470

Hopson, J. A. (1969). The Origin and Adaptive Radiation Of Mammal-Like Reptiles and Nontherian Mammals*. *Annals of the New York Academy of Sciences*, *167*(1), 199–216. https://doi.org/10.1111/j.1749-6632.1969.tb20445.x

Hopson, J. A. (1973). Endothermy, Small Size, and the Origin of Mammalian Reproduction. *The American Naturalist*, *107*(955), 446–452. https://doi.org/10.1086/282846

Hopson, J. A. (2005). A juvenile gomphodont cynodont specimen from the Cynognathus Assemblage Zone of South Africa: implications for the origin of gomphodont postcanine morphology. *Palaeontologia africana*, *41*, 53-66.

Hopson, J. A. (2012). The Role of Foraging Mode in the Origin of Therapsids: Implications for the Origin of Mammalian Endothermy. *Fieldiana Life and Earth Sciences*, *2012*(5), 126–148. https://doi.org/10.3158/2158-5520-5.1.126

Hopson, J. A. (2014). The Traversodontid Cynodont Mandagomphodon hirschsoni from the Middle Triassic of the Ruhuhu Valley, Tanzania. In C. F. Kammerer, K. D. Angielczyk, & J. Fröbisch (Eds.), *Early Evolutionary History of the Synapsida* (pp. 233–253). Springer Netherlands. https://doi.org/10.1007/978-94-007-6841-3_14

Hopson, J. A., & Kitching, J. W. (1972). A revised classification of cynodonts (Reptilia; Therapsida) *Palaeontol. Afr.* 14:71–85.

Horner, J. R., de Ricqlès , A., & Padian, K. (1999). Variation in dinosaur skeletochronology indicators: Implications for age assessment and physiology. Paleobiology, 25(3), 295–304.

Hurum, J. H., & Chinsamy-Turan, A. (2012). The Radiation, Bone Histology, and Biology of Early Mammals. In *Forerunners of mammals: Radiation, histology, biology* (p. 249). Indiana University Press.

Huttenlocker, A. K., & Farmer, C. G. (2017). Bone Microvasculature Tracks Red Blood Cell Size Diminution in Triassic Mammal and Dinosaur Forerunners. *Current Biology*, *27*(1), 48–54. https://doi.org/10.1016/j.cub.2016.10.012

Huttenlocker, A. K., & Rega, E. (2012). The Paleobiology and Bone Microstructure of Pelycosaurian- Grade Synapsids. In *Forerunners of mammals: Radiation, histology, biology* (p. 91). Indiana University Press.

Huttenlocker, A. K., & Sidor, C. A. (2020). A Basal Nonmammaliaform Cynodont from the Permian of Zambia and the Origins of Mammalian Endocranial and Postcranial Anatomy. *Journal of Vertebrate Paleontology*, *40*(5), e1827413. https://doi.org/10.1080/02724634.2020.1827413

Jee, W. S., & Frost, H. M. (1992). Skeletal adaptations during growth. *Triangle; the Sandoz Journal of Medical Science*, *31*(2/3), 77–88.

Jenkins Jr., F. A. (1973). The functional anatomy and evolution of the mammalian humero-ulnar articulation. *American Journal of Anatomy*, *137*(3), 281–297. https://doi.org/10.1002/aja.1001370304

Jones, K. E., Angielczyk, K. D., Polly, P. D., Head, J. J., Fernandez, V., Lungmus, J. K., Tulga, S., & Pierce, S. E. (2018). Fossils reveal the complex evolutionary history of the mammalian regionalized spine. *Science*, *361*(6408), 1249–1252. https://doi.org/10.1126/science.aar3126

Jordana, X., Marín-Moratalla, N., Moncunill-Solè, B., Nacarino-Meneses, C., & Köhler, M. (2016). Ontogenetic changes in the histological features of zonal bone tissue of ruminants: A quantitative approach. *Comptes Rendus Palevol*, *15*(1), 255–266. https://doi.org/10.1016/j.crpv.2015.03.008

Kammerer, C. F., Angielczyk, K. D., & Nesbitt, S. J. (2018). Novel hind limb morphology in a kannemeyeriiform dicynodont from the Manda Beds (Songea Group, Ruhuhu Basin) of Tanzania. *Journal of Vertebrate Paleontology*, *37*(sup1), 178–188. https://doi.org/10.1080/02724634.2017.1309422

Kemp, T. S. (1980). Aspects of the structure and functional anatomy of the Middle Triassic cynodont *Luangwa*. *Journal of Zoology*, *191*(2), 193–239. https://doi.org/10.1111/j.1469-7998.1980.tb01456.x

Kemp, T. S. (2006). The origin of higher taxa: Macroevolutionary processes, and the case of the mammals: Origin of higher taxa. *Acta Zoologica*, *88*(1), 3–22. https://doi.org/10.1111/j.1463-6395.2007.00248.x

Köhler, M., Marín-Moratalla, N., Jordana, X., & Aanes, R. (2012). Seasonal bone growth and physiology in endotherms shed light on dinosaur physiology. *Nature*, *487*(7407), 358–361. https://doi.org/10.1038/nature11264

Köhler, M., Nacarino-Meneses, C., Quintana Cardona, J., Arnold, W., Stalder, G., Suchentrunk, F., & Moyà-Solà, S. (in press). Insular giant leporid matured later than predicted by scaling. *iScience.*

Koteja, P. (2000). Energy assimilation, parental care and the evolution of endothermy. *Proceedings of the Royal Society of London. Series B: Biological Sciences*, *267*(1442), 479–484. https://doi.org/10.1098/rspb.2000.1025

Kozlowski, J. (1996). Optimal allocation of resources explains interspecific life-history patterns in animals with indeterminate growth. *Proceedings of the Royal Society of London. Series B: Biological Sciences*, *263*(1370), 559–566. https://doi.org/10.1098/rspb.1996.0084

Kulik, Z. T., Lungmus, J. K., Angielczyk, K. D., & Sidor, C. A. (2021). Living fast in the Triassic: New data on life history in *Lystrosaurus* (Therapsida: Dicynodontia) from northeastern Pangea. *PLOS ONE*. https://doi.org/e0259369

Liu, J., & Abdala, F. (2014). Phylogeny and Taxonomy of the Traversodontidae. In C. F. Kammerer, K. D. Angielczyk, & J. Fröbisch (Eds.), *Early Evolutionary History of the Synapsida* (pp. 255–279). Springer Netherlands. https://doi.org/10.1007/978-94-007-6841-3_15

Liu, J., & Sues, H.-D. (2009). Dentition and tooth replacement of *Boreogomphodon* (Cynodontia: Traversodontidae) from the Upper Triassic of North Carolina, USA. Vertebrata PalAsiatica 48:169–184.

Lui, J. C., & Baron, J. (2011). Mechanisms Limiting Body Growth in Mammals. *Endocrine Reviews*, *32*(3), 422–440. https://doi.org/10.1210/er.2011-0001

Luo, Z.-X., Kielan-Jaworowska, Z., & Cifelli, R. L. (2004). Evolution of Dental Replacement in Mammals. *Bulletin of Carnegie Museum of Natural History*, *36*, 159–175. https://doi.org/10.2992/0145-9058(2004)36[159:EODRIM]2.0.CO;2

Marín-Moratalla, N., Cubo, J., Jordana, X., Moncunill-Solé, B., & Köhler, M. (2014). Correlation of quantitative bone histology data with life history and climate: A phylogenetic approach: Bone histology in bovids. *Biological Journal of the Linnean Society*, *112*(4), 678–687. https://doi.org/10.1111/bij.12302

Marín-Moratalla, N., Jordana, X., & Köhler, M. (2013). Bone histology as an approach to providing data on certain key life history traits in mammals: Implications for conservation biology. *Mammalian Biology*, *78*(6), 422–429. https://doi.org/10.1016/j.mambio.2013.07.079

Martinelli, A. G., Kammerer, C. F., Melo, T. P., Paes Neto, V. D., Ribeiro, A. M., Da-Rosa, Á. A. S., Schultz, C. L., & Soares, M. B. (2017). The African cynodont *Aleodon* (Cynodontia, Probainognathia) in the Triassic of southern Brazil and its biostratigraphic significance. *PLOS ONE*, *12*(6), e0177948. https://doi.org/10.1371/journal.pone.0177948

Marty, L., Dieckmann, U., Rochet, M.-J., & Ernande, B. (2011). Impact of Environmental Covariation in Growth and Mortality on Evolving Maturation Reaction Norms. *The American Naturalist*, *177*(4), E98–E118. https://doi.org/10.1086/658988

McNab, B. K. (1978). The Evolution of Endothermy in the Phylogeny of Mammals. *The American Naturalist*, *112*(983), 1–21. https://www.jstor.org/stable/2460134

Montoya-Sanhueza, G., & Chinsamy, A. (2017). Long bone histology of the subterranean rodent *Bathyergus suillus* (Bathyergidae): Ontogenetic pattern of cortical bone thickening. *Journal of Anatomy*, *230*(2), 203–233. https://doi.org/10.1111/joa.12547

Montoya-Sanhueza, G., Bennett, N. C., Oosthuizen, M. K., Dengler-Crish, C. M., & Chinsamy, A. (2021). Bone remodeling in the longest living rodent, the naked mole-rat: Interelement variation and the effects of reproduction. *Journal of Anatomy*, *239*(1), 81–100. https://doi.org/10.1111/joa.13404

Nacarino-Meneses, C., & Köhler, M. (2018). Limb bone histology records birth in mammals. *PLOS ONE*, *13*(6), e0198511. https://doi.org/10.1371/journal.pone.0198511

Nacarino-Meneses, C., Jordana, X., & Köhler, M. (2016a). First approach to bone histology and skeletochronology of *Equus hemionus*. *Comptes Rendus Palevol*, *15*(1), 267–277. https://doi.org/10.1016/j.crpv.2015.02.005

Nacarino-Meneses, C., Jordana, X., & Köhler, M. (2016b). Histological variability in the limb bones of the Asiatic wild ass and its significance for life history inferences. *PeerJ*, *4*, e2580. https://doi.org/10.7717/peerj.2580

Nesbitt, S. J., Butler, R. J., Ezcurra, M. D., Barrett, P. M., Stocker, M. R., Angielczyk, K. D., Smith, R. M. H., Sidor, C. A., Niedźwiedzki, G., Sennikov, A. G., & Charig, A. J. (2017). The earliest bird-line archosaurs and the assembly of the dinosaur body plan. *Nature*, *544*(7651), 484–487. https://doi.org/10.1038/nature22037

Nesbitt, S. J., Butler, R. J., Ezcurra, M. D., Charig, A. J., & Barrett, P. M. (2017). The anatomy of *Teleocrater rhadinus*, an early avemetatarsalian from the lower portion of the Lifua

Member of the Manda Beds (Middle Triassic). *Journal of Vertebrate Paleontology*, *37*(sup1), 142–177. https://doi.org/10.1080/02724634.2017.1396539
Nesbitt, S. J., Langer, M. C., & Ezcurra, M. D. (2020). The Anatomy of *Asilisaurus kongwe*, a Dinosauriform from the Lifua Member of the Manda Beds (Middle Triassic) of Africa. *The Anatomical Record*, *303*(4), 813–873. https://doi.org/10.1002/ar.24287
Nesbitt, S. J., Sidor, C. A., Angielczyk, K. D., Smith, R. M. H., & Tsuji, L. A. (2014). A new archosaur from the Manda Beds (Anisian, Middle Triassic) of southern Tanzania and its implications for character state optimizations at Archosauria and Pseudosuchia. *Journal of Vertebrate Paleontology*, *34*(6), 1357–1382. https://doi.org/10.1080/02724634.2014.859622
Padian, K., & de Ricqlès, A. (2020). Inferring the physiological regimes of extinct vertebrates: Methods, limits and framework. *Philosophical Transactions of the Royal Society B: Biological Sciences*, *375*(1793), 20190147. https://doi.org/10.1098/rstb.2019.0147
Padian, K., & Lamm, E.-T. (Eds.). (2013). *Bone histology of fossil tetrapods: Advancing methods, analysis, and interpretation*. University of California Press.
Pazzaglia, U. E., Sibilia, V., Congiu, T., Pagani, F., Ravanelli, M., & Zarattini, G. (2015). Setup of a bone aging experimental model in the rabbit comparing changes in cortical and trabecular bone: Morphological and morphometric study in the femur. *Journal of Morphology*, *276*(7), 733–747. https://doi.org/10.1002/jmor.20374
Prondvai, E., Godefroit, P., Adriaens, D., & Hu, D.-Y. (2018). Intraskeletal histovariability, allometric growth patterns, and their functional implications in bird-like dinosaurs. *Scientific Reports*, *8*(1), 258. https://doi.org/10.1038/s41598-017-18218-9
Prondvai, E., Stein, K. H. W., de Ricqlès, A., & Cubo, J. (2014). Development-based revision of bone tissue classification: The importance of semantics for science. *Biological Journal of the Linnean Society*, *112*(4), 799–816. https://doi.org/10.1111/bij.12323
Quemeneur, S., de Buffrénil, V., & Laurin, M. (2013). Microanatomy of the amniote femur and inference of lifestyle in limbed vertebrates. *Biological Journal of the Linnean Society*, *109*(3), 644–655. https://doi.org/10.1111/bij.12066
Ray, S., Botha, J., & Chinsamy, A. (2004). Bone histology and growth patterns of some nonmammalian therapsids. *Journal of Vertebrate Paleontology*, *24*(3), 634–648. https://doi.org/10.1671/0272-4634(2004)024[0634:BHAGPO]2.0.CO;2
Ricklefs, R. E., Konarzewski, M., & Daan, S. (1996). The Relationship between Basal Metabolic Rate and Daily Energy Expenditure in Birds and Mammals. *The American Naturalist*, *147*(6), 1047–1071. https://doi.org/10.1086/285892
Rogers, R. R. (1990). Taphonomy of Three Dinosaur Bone Beds in the Upper Cretaceous Two Medicine Formation of Northwestern Montana: Evidence for Drought-Related Mortality. *PALAIOS*, *5*(5), 394. https://doi.org/10.2307/3514834
Shelton, C. D., & Sander, P. M. (2017). Long bone histology of *Ophiacodon* reveals the geologically earliest occurrence of fibrolamellar bone in the mammalian stem lineage. *Comptes Rendus Palevol*, *16*(4), 397–424. https://doi.org/10.1016/j.crpv.2017.02.002
Shipman, P. (1975). Implications of drought for vertebrate fossil assemblages. *Nature*, *257*(5528), Article 5528. https://doi.org/10.1038/257667a0
Sidor, C. A., & Hopson, J. A. (1998). Ghost lineages and "mammalness": Assessing the temporal pattern of character acquisition in the Synapsida. *Paleobiology*, *24*(2), 254–273. https://doi.org/10.1666/0094-8373(1998)024[0254:GLAATT]2.3.CO;2

Sidor, C. A., & Hopson, J. A. (2018). *Cricodon metabolus* (Cynodontia: Gomphodontia) from the Triassic Ntawere Formation of northeastern Zambia: patterns of tooth replacement and a systematic review of the Trirachodontidae. *Journal of Vertebrate Paleontology*, *37*(sup1), 39–64. https://doi.org/10.1080/02724634.2017.1410485

Sidor, C. A., & Nesbitt, S. J. (2018). Introduction to vertebrate and climatic evolution in the Triassic Rift Basins of Tanzania and Zambia. *Journal of Vertebrate Paleontology*, *37*(sup1), 1–7. https://doi.org/10.1080/02724634.2017.1420661

Sidor, C. A., Vilhena, D. A., Angielczyk, K. D., Huttenlocker, A. K., Nesbitt, S. J., Peecoock, B. R., & Tsuji, L. A. (2013). Provincialization of terrestrial faunas following the end-Permian mass extinction. *Proceedings of the National Academy of Science*, *110*(20), 8129–8133.

Smith, R. M. H., Sidor, C. A., Angielczyk, K. D., Nesbitt, S. J., & Tabor, N. J. (2018). Taphonomy and paleoenvironments of Middle Triassic bone accumulations in the Lifua Member of the Manda Beds, Songea Group (Ruhuhu Basin), Tanzania. *Journal of Vertebrate Paleontology*, *37*(sup1), 65–79. https://doi.org/10.1080/02724634.2017.1415915

Sues, H.-D. 2000. Evolution of herbivory in terrestrial vertebrates: perspectives from the fossil record. Cambridge University Press, Cambridge, UK, 256 pp.

Sues, H.-D., & Hopson, J. A. (2010). Anatomy and phylogenetic relationships of *Boreogomphodon jeffersoni* (Cynodontia: Gomphodontia) from the Upper Triassic of Virginia. *Journal of* Vertebrate Paleontology, 30(4), 1202–1220. https://doi.org/10.1080/02724634.2010.483545

Tabor, N. J., Sidor, C. A., Smith, R. M. H., Nesbitt, S. J., & Angielczyk, K. D. (2017). Paleosols of the Permian-Triassic: Proxies for rainfall, climate change and major changes in terrestrial tetrapod diversity. Journal of Vertebrate Paleontology, 37(sup1), 240–253. https://doi.org/10.1080/02724634.2017.1415211

Tatarinov, L. P., & Matchenko, E. N. (1999). A find of an aberrant tritylodont (Reptilia, Cynodontia) in the Lower Cretaceous of the Kemerovo Region. Paleontological Journal, 33(4), 422-428.

Tolchard, F., Kammerer, C. F., Butler, R. J., Hendrickx, C., Benoit, J., Abdala, F., & Choiniere, J. N. (2021). A new large gomphodont from the Triassic of South Africa and its implications for Gondwanan biostratigraphy. *Journal of Vertebrate Paleontology*, *41*(2), e1929265. https://doi.org/10.1080/02724634.2021.1929265

Tsuji, L. A. (2017). *Mandaphon nadra*, gen. Et sp. Nov., a new procolophonid from the Manda Beds of Tanzania. *Journal of Vertebrate Paleontology*, *37*(sup1), 80–87.

Weaver, L. N., Fulghum, H. Z., Grossnickle, D. M., Brightly, W. H., Kulik, Z. T., Wilson Mantilla, G. P., & Whitney, M. R. (2022). Multituberculate Mammals Show Evidence of a Life History Strategy Similar to That of Placentals, Not Marsupials. *The American Naturalist*, 000–000. https://doi.org/10.1086/720410

Werning, S., & Nesbitt, S. J. (2016). Bone histology and growth in *Stenaulorhynchus stockleyi* (Archosauromorpha: Rhynchosauria) from the Middle Triassic of the Ruhuhu Basin of Tanzania. *Comptes Rendus Palevol*, *15*(1), 163–175. https://doi.org/10.1016/j.crpv.2015.03.004

Whitney, M. R., Otoo, B. K. A., Angielczyk, K. D., & Pierce, S. E. (2022). Fossil bone histology reveals ancient origins for rapid juvenile growth in tetrapods. *Communications Biology*, *5*(1), Article 1. https://doi.org/10.1038/s42003-022-04079-0

Wynd, B. M., Peecook, B. R., Whitney, M. R., & Sidor, C. A. (2017). The first occurrence of *Cynognathus crateronotus* (Cynodontia: Cynognathia) in Tanzania and Zambia, with implications for the age and biostratigraphic correlation of Triassic strata in southern Pangea. *Journal of Vertebrate Paleontology*, *37*(sup1), 228–239. https://doi.org/10.1080/02724634.2017.1421548

Wynd, B., Abdala, F., & Nesbitt, S. J. (2022). Ontogenetic growth in the crania of *Exaeretodon argentinus* (Synapsida: Cynodontia) captures a dietary shift. *PeerJ*, 10, e14196. https://doi.org/10.7717/peerj.14196

4.10 TABLES

Table 4.1. Measurement data and localities details of referable *Scalenodon angustifrons* femora. All measurements in mm. Minimum dorsal midshaft diameter (MSD), proximal and distal dorsal shaft diameters (PSD, DSD), femoral head depth, preserved length, estimated length, proportional length, and proportional midshaft diameter are reported. Histologically sampled individuals, size classes based on estimated length, and preservation details are also noted.

Spec. No	Loc.	Taxon	Element	MSD	PSD	Head depth	DSD	Length pres.	Estimated length	%Max FEM L	%Max FEM MSD	Histo ?	Size Class	Preservation
NMT RB860	Z029	*cf. Scalenodon*	Femur	4.62	-	-	7.69	23.16	61.23	50%	33%	yes	II	distal end and midshaft
NMT RB1453	Z029	*cf. Scalenodon*	Femur	-	10.78	12.06	-	34.72	75.11	61%	-		III	prox head only
NMT RB564	Z198	*Scalenodon angustifrons*	Femur	8.58	9.21	16.64	15.74	92.1	92.10	75%	61%		III	complete, broken
NMT RB1520	Z080	*cf. Scalenodon*	Femur	-	-	11.3		32.43	92.49	75%	-		III	prox head only
NMT RB564	Z198	*Scalenodon angustifrons*	Femur	8.57	10.35	14.82	11.18	93.95	93.95	76%	61%		III	complete and associated
NMT RB1456	Z029	*cf. Scalenodon*	Femur	-	6.91	10.44	-	22.62	94.01	76%	-		III	head and shaft
NMT RB863	Z029	*cf. Scalenodon*	Femur	8.27	-	-	13.43	42.49	94.93	77%	59%	yes	III	distal end; R fem
NMT RB1530	Z196	*cf. Scalenodon*	Femur	8.07	9.71	14.91	10.84	94.97	94.97	77%	58%		III	complete
NMT RB862	Z029	*cf. Scalenodon*	Femur	8.87	-	-	10.91	38.06	95.01	77%	63%	yes	III	distal end; R fem
NMT RB1451	Z029	*cf. Scalenodon*	Femur	-	8.84	14.05	-	34.36	95.12	77%	-		III	prox head and neck only
NMT RB1522	Z096	*cf. Scalenodon*	Femur	13.9	-	18.89	-	95.49	95.49	78%	99%		III	complete, matrix encrusted
NMT RB1075	Z029	*cf. Scalenodon*	Femur	9.41	-	-	12.66	26.87	95.57	78%	67%	yes	III	distal end
NMT RB1500	Z081	*cf. Scalenodon*	Femur	-	11.02	16.21	33.48	35.16	95.78	78%	-		III	proximal R femur
NMT RB581	Z80	*Scalenodon angustifrons*	Femur	9	-	15.97	-	95.84	95.84	78%	64%	yes	III	complete, thin-sectioned
NMT RB1501	Z081	*cf. Scalenodon*	Femur	9.94	13.02	13.58	-	46.88	95.89	78%	71%		III	proximal L femur

NMT RB1499	Z081	*cf. Scalenodon*	Femur	-	12.7	17.03	-	39.8	96.03	78%	-		III	proximal R femur
NMT RB1469	Z029	*cf. Scalenodon*	Femur	10.27	-	-	13.65	30.94	96.61	79%	74%		III	distal end with shaft
NMT RB1506	Z081	*cf. Scalenodon*	Femur	-	13.12	19.17	-	35.86	96.68	79%	-		III	proximal L femur
NMT RB1467	Z029	*cf. Scalenodon*	Femur	-	-	-	12.5	30.72	96.77	79%	-		III	distal head
NMT BRB864	Z029	*cf. Scalenodon*	Femur	9.5	-	-	14.44	43.79	96.79	79%	68%	yes	III	distal end; R fem
NMT RB1505	Z081	*cf. Scalenodon*	Femur	10.96	15.71	17.26	-	56.18	97.33	79%	78%		III	proximal L femur
NMT RB1514	Z081	*cf. Scalenodon*	Femur	11.59	-	-	16.4	49.35	97.39	79%	83%		III	proximal R femur
NMT RB883	Z081	*cf. Scalenodon*	Femur	11.85	-	-	14.67	43.47	98.04	80%	85%	yes (altered)	III	dist end; R fem
NMT RB1510	Z081	*cf. Scalenodon*	Femur	12.62	-	-	17.86	48.63	98.12	80%	90%		III	distal R femur
NMT RB379A	Z029	*cf. Scalenodon*	Femur	11.49	14.73	20.04	-	45.36	98.21	80%	82%		III	prox; L
NMT RB581	Z80	*Scalenodon angustifrons*	Femur	10.21	-	17.2	-	98.57	98.57	80%	73%		III	nearly complete, broken
NMT RB1513	Z081	*cf. Scalenodon*	Femur	12.3	-	-	20.01	42.69	98.74	80%	88%		III	distasl R femur
NMT RB1466	Z029	*cf. Scalenodon*	Femur	-	-	-	13.36	27.1	98.89	80%	-		III	distal head
NMT RB1504	Z081	*cf. Scalenodon*	Femur	13.97	-	14.4	-	77.71	99.48	81%	100%		III	proximal R femur
NMT RB1543	Z198	*cf. Scalenodon*	Femur	11.81	-	17.75	-	99.62	99.62	81%	85%		III	complete and broken
NMT RB731	Z081	*Scalenodon angustifrons*	Femur	13.25	14.59	39.12	15.33	102.42	102.42	83%	95%	yes	III	complete
NMT RB1074	Z029	*cf. Scalenodon*	Femur	12.22	-	-	17.05	39.8	115.00	93%	87%		III	dist end; L fem
NMT RB866	Z029	*cf. Scalenodon*	Femur	-	-	-	19.87	-	123.00	100%	-	yes	III	distal end; R fem

Table 4.2. Measurement data and locality details of referable *Luangwa drysdalli* femora. All measurements in mm. Minimum dorsal midshaft diameter (MSD), proximal and distal dorsal shaft diameters (PSD, DSD), femoral head depth, preserved length, estimated length, proportional length, and proportional midshaft diameter are reported. Histologically sampled individuals, size classes based on estimated length, and preservation details are also noted.

Spec. No	Loc.	Taxon	Element	MSD	PSD	Head depth	DSD	Length pres.	Estimated Length	%Max FEML	%MaxFEM MSD	Size Class	Histo?	Preservation
NMT RB1078	Z129	*cf. Luangwa*	Femur	4.24	6.58	4.68	5.44	43.54	43.54	34%	31%	I	yes	complete; R fem
NMT RB1080.B	Z138	*cf. Luangwa*	Femur	5.26	6.06		7.06	39.94	55.47	43%	39%	I	yes	distal end to prox shaft
NMT RB1080.A	Z138	*cf. Luangwa*	Femur	5.93	8.43	8.82	9.36	58.57	58.57	45%	44%	I		complete, 2 pieces
NMT RB894	Z029	*cf. Luangwa*	Femur	5.21	5.91	8.59	-	28.58	58.09	45%	38%	I	yes	prox end
NMT RB1488	Z183	*cf. Luangwa*	Femur	5.58	7.81	8.72	7.37	58.25	58.25	45%	41%	I		complete
NMT RB378	Z029	*cf. Luangwa*	Femur	5.67	9.53	9.71	10.5	62.09	62.09	48%	42%	I		complete
NMT RB565	Z131	*cf. Luangwa*	Femur	5.73	9.47	10.1	9.17	67.65	67.65	53%	42%	II	yes	complete
NMT RB1495	Z127	*cf. Luangwa*	Femur	-	-	-	10.82	20.83	68.19	53%	-	II		distal L femur
NMT RB1076	Z029	*cf. Luangwa*	Femur	6.59	-	-	11.9	25.26	74.00	57%	49%	II		distal end
NMT RB1464	Z029	*cf. Luangwa*	Femur	-	-	-	12.77	33.67	75.72	59%	-	II		distal end
NMT RB1491	Z127	*cf. Luangwa*	Femur	7.73	12.5	12.19	13.35	77.5	77.50	60%	57%	II		L complete
NMT RB1494	Z127	*cf. Luangwa*	Femur	7.52	11.65	12.04	-	39.66	81.76	64%	56%	II		prox head; R
NMT RB1072	Z134	*cf. Luangwa*	Femur	7.43	10.8	13.24	13.41	70.95	81.94	64%	55%	II	yes	R dist and prox ends, incomplete
NMT RB1541	Z129	*cf. Luangwa*	Femur	-	-	13.93		-	83.46	65%	-	II		prox head only
NMT RB1071.A	Z134	*cf. Luangwa*	Femur	8.23	8.81	12.95	12.98	89.38	84.64	66%	61%	II	yes	prox and distal ends, incomplete
NMT RB1492	Z127	*cf. Luangwa*	Femur	7.57	10.57	-	-	49.32	89.19	69%	56%	II		prox head and shaft; head is eroded; L
NMT RB1493	Z127	*cf. Luangwa*	Femur	7.65	9.89	15.07	-	60.15	89.42	69%	56%	II		prox head and fractured shaft
NMT RB1460	Z029	*cf. Luangwa*	Femur	9.72	-	-	-	46.26	118.91	92%	72%	III		distal end with shaft
NMT RB882	Z081	*cf. Luangwa*	Femur	13.54	-	-	15.37	47.07	128.74	100%	100%	III	yes	distal end

4.11 SUPPLEMENTARY DATA

Supplemental Table 4.2. Literature review of Cynodont growth strategies, bone tissue types, and elements sampled. Element length, midshaft diameter, and percentage of maximum size are reported, however the method used to calculate maximum size is not standardized across studies nor is it always reported. Tissue types are reported from the largest and presumably most mature specimen from each specimen. Abbreviations: LB, lamellar bone; PFB, parallel-fibered bone; WPC, woven-parallel complex; WB, woven-fibered bone; GM, growth mark; EFS, external fundamental system. Measurements are in mm.

Taxon	Specimen no.	Element	Length	MSD	%Max Size	Growth pattern	Tissue(s) reported from largest element	Source
Andescynodon mendozensis	PVL 3836	femur	80-90		80	Prolonged slow growth	LB	Chinsamy and Abdala, 2008
Beinotherium yunnanenses	43.1.1.T	femur				only immature tissue	WB in WPC	de Ricqlès , 1969
Brasilitherium riograndensis	UFRGS-PV-1308-T	femur				Mosaic due to small size	Mosaic of WPC, PFB, and LB	Botha-Brink, et al., 2018
Brasilitherium riograndensis	UFRGS-PV-1043-T	femur				Mosaic due to small size	Mosaic of WPC, PFB, and LB	Botha-Brink, et al., 2018
Brasilitherium riograndensis	UFRGS-PV-1308-T	fibula				Mosaic due to small size	Mosaic of WPC, PFB, and LB	Botha-Brink, et al., 2018
Brasilitherium riograndensis	UFRGS-PV-1308-T	radius				Mosaic due to small size	Mosaic of WPC, PFB, and LB	Botha-Brink, et al., 2018
Brasilitherium riograndensis	UFRGS-PV-1308-T	tibia				Mosaic due to small size	Mosaic of WPC, PFB, and LB	Botha-Brink, et al., 2018
Brasilitherium riograndensis	UFRGS-PV-1308-T	ulna				Mosaic due to small size	Mosaic of WPC, PFB, and LB	Botha-Brink, et al., 2018
Brasilodon quadrangularis	PV-765-T	ulna				Synonomized with *Brasilitherium*	Mosaic of WPC, PFB, and LB	Botha-Brink, et al., 2018
Chiniquodon (syn. Belesodon)	41.1.1.T	radius				only immature tissue	WB in WPC	de Ricqlès , 1969
Cynognathus	SAM-PK-K6235	femur			68.4	past rapid phase of growth	WB in WPC - LB	Both and Chinsamy, 2000
Cynognathus	NMQR 3019	femur			72.38	past rapid phase of growth	WB in WPC - LB	Both and Chinsamy, 2000
Cynognathus	NMQR 3019	femur			100	past rapid phase of growth	WB in WPC - LB	Both and Chinsamy, 2000
Cynognathus crateronotus	NMT RB459	femur				past rapid phase of growth	WB in WPC - LB	Wynd et al., 2018
Diademodon	UCMZ T495	femur			57.95	cyclical growth, past rapid phase of growth	WB in WPC - PFB + cyclical GMs + EFS	Both and Chinsamy, 2000
Diademodon	UCMZ T503	femur			63.77	cyclical growth, past rapid phase of growth	WB in WPC - PFB + cyclical GMs + EFS	Both and Chinsamy, 2000
Diademodon	UCMZ T493	femur			73.39	cyclical growth, past rapid phase of growth	WB in WPC - PFB + cyclical GMs + EFS	Both and Chinsamy, 2000

Diademodon	UCMZ T448	fibula		cyclical growth, past rapid phase of growth	WB in WPC - PFB + cyclical GMs + EFS	Both and Chinsamy, 2000
Diademodon	SAM-PK-K9871	humerus	32.06	cyclical growth, past rapid phase of growth	WB in WPC - PFB + cyclical GMs + EFS	Both and Chinsamy, 2000
Diademodon	UCMZ T492	humerus	39.35	cyclical growth, past rapid phase of growth	WB in WPC - PFB + cyclical GMs + EFS	Both and Chinsamy, 2000
Diademodon	BP/I/3772	humerus	42.23	cyclical growth, past rapid phase of growth	WB in WPC - PFB + cyclical GMs + EFS	Both and Chinsamy, 2000
Diademodon	SAM-PK-K1332	humerus	43.48	cyclical growth, past rapid phase of growth	WB in WPC - PFB + cyclical GMs + EFS	Both and Chinsamy, 2000
Diademodon	UCMZ T447	tibia	77.21	cyclical growth, past rapid phase of growth	WB in WPC - PFB + cyclical GMs + EFS	Both and Chinsamy, 2000
Exaeretodon frenguellii	PVL 2162	fibula		only immature tissue	WB in WPC	Chinsamy and Abdala, 2008
Exaeretodon riograndensis	MCNPV 10001	tibia		only immature tissue	WB in WPC	Chinsamy and Abdala, 2008
Exaeretodon riograndensis	UFRGS-PV-1265-T	humerus		past rapid phase of growth	WB in WPC - LB	Veiga et al., 2018
Exaeretodon riograndensis	UFRGS-PV-1260-T	fibula		past rapid phase of growth	WB in WPC - LB	Veiga et al., 2018
Exaeretodon riograndensis	UFRGS-PV-1166a-T	femur		past rapid phase of growth	WB in WPC - LB	Veiga et al., 2018
Exaeretodon riograndensis	UFRGS-PV-1166b-T	ulna		past rapid phase of growth	WB in WPC - LB	Veiga et al., 2018
Exaeretodon riograndensis	UFRGS-PV-1259-T	ulna		past rapid phase of growth	WB in WPC - LB	Veiga et al., 2018
Galesaurus planiceps	NMQR 3716	femur	63	prolonged moderate growth	PFB - LB	Butler et al., 2019
Galesaurus planiceps	NMQR 3542	femur	89	prolonged moderate growth	PFB - LB	Butler et al., 2019
Galesaurus planiceps	RC 845	fibula	61	prolonged moderate growth	PFB - LB	Butler et al., 2019
Galesaurus planiceps	NMQR 3542	humerus	89	prolonged moderate growth	PFB - LB	Butler et al., 2019
Galesaurus planiceps	NMQR 135	humerus	65	prolonged moderate growth	PFB - LB	Butler et al., 2019
Galesaurus planiceps	NMQR 3542	radius	89	prolonged moderate growth	PFB - LB	Butler et al., 2019
Galesaurus planiceps	RC 845	tibia	61	prolonged moderate growth	PFB - LB	Butler et al., 2019
Galesaurus planiceps	NMQR 3542	tibia	89	prolonged moderate growth	PFB - LB	Butler et al., 2019
Galesaurus planiceps	NMQR 3542	ulna	89	prolonged moderate growth	PFB - LB	Butler et al., 2019
Gomphodontosuchidae indet.	61.4.3.T	radius		past rapid phase of growth	WB in WPC - LB + EFS	de Ricqlès , 1969; Botha-Brink et al., 2012
Gomphodontosuchus brasiliensis	151.1.1.T	indet. long bone		past rapid phase of growth	WB in WPC - LB	de Ricqlès , 1969; Botha-Brink et al., 2012
Gomphodontosuchus brasiliensis	151.1.3.T	indet. long bone		past rapid phase of growth	WB in WPC - LB	de Ricqlès , 1969; Botha-Brink et al., 2012
Gomphodontosuchus brasiliensis	151.2.1.T	rib?		past rapid phase of growth	WB in WPC - LB	de Ricqlès , 1969; Botha-Brink et al., 2012
Irajatherium hernandezi	UFRGS-PV-1072-T	humerus		Mosaic due to small size	Mosaic of WPC, PFB, and LB	Botha-Brink, et al., 2018
Langbergia	NMQR 3282	femurur		cyclical growth	WB in WPC + cyclical GM	Botha-Brink et al., 2012
Langbergia	NMQR 3282	tibia		cyclical growth	WB in WPC + cyclical GM	Botha-Brink et al., 2012

Massetognathus pascuali	PVL 4613	femur	55		66	past rapid phase of growth	WB in WPC - PFB	Chinsamy and Abdala, 2008
Massetognathus pascuali	PULR-V 115	femur	77			past rapid phase of growth	WB in WPC - PFB	Garcia Marsà et al., 2022
Morganucodon watsoni	UCL.ABD no number	femur				past rapid phase of growth	WB in WPC - PFB	Chinsamy and Hurum, 2006
Morganucodon watsoni	UCL.ABD no number	ulna				past rapid phase of growth	WB in WPC - PFB	Chinsamy and Hurum, 2006
Oligokyphus sp.	29.1.3.T	indet. bone				only immature tissue	WB in WPC	de Ricqlès , 1969
Oligokyphus sp.	29.1.1.L	indet. bone				only immature tissue	WB in WPC	de Ricqlès , 1969
Oligokyphus sp.	29.1.2.T	indet. bone				only immature tissue	WB in WPC	de Ricqlès , 1969
Probainognathus jenseni	PVL 4677	humerus				slow, zonal growth	Zonal PFB & LB	Garcia Marsà et al., 2022
Procynosuchus	SAM-PK-8511	clavicle		3.29		prolonged slow growth	WB in WPC - LB	Ray et al., 2004
Procynosuchus	B/P/1/3747	radius		8.24		prolonged slow growth	WB in WPC - LB	Ray et al., 2004
Procynosuchus	TSK 34	rib		3.02		prolonged slow growth	WB in WPC - LB	Ray et al., 2004
Protuberum cabralense	UFRG-PV-1009-T	rib				past rapid phase of growth	WB in WPC - LB	Veiga et al., 2018
Protuberum cabralense	UFRG-PV-1003-T	humerus				past rapid phase of growth	WB in WPC - LB	Veiga et al., 2018
Protuberum cabralense	UFRG-PV-1004-T	humerus				past rapid phase of growth	WB in WPC - LB	Veiga et al., 2018
Protuberum cabralense	UFRG-PV-1008-T	ulna				past rapid phase of growth	WB in WPC - LB	Veiga et al., 2018
Protuberum cabralense	UFRG-PV-1011-T	rib				past rapid phase of growth	WB in WPC - LB	Veiga et al., 2018
Prozostrodon brasiliensis	PV-248-T	femur				zonal growth	Zonal WB & PFB	Botha-Brink, et al., 2018
Prozostrodon brasiliensis	PV-248-T	humerus				zonal growth	Zonal WB & PFB	Botha-Brink, et al., 2018
Scalenodontoides	NMQR 3053	indet. long bone				only immature tissue	WB in WPC	Botha-Brink et al., 2012
Thrinaxodon	SAM-PK-K8004a	femur	18.74		41.98	past rapid phase of growth	WB in WPC - PFB	Botha and Chinsamy 2005
Thrinaxodon	SAM-PK-K8004b	femur	18.74		41.98	past rapid phase of growth	WB in WPC - PFB	Botha and Chinsamy 2005
Thrinaxodon	SAM-PK-K1395	femur	34.53		77.35	past rapid phase of growth	WB in WPC - PFB	Botha and Chinsamy 2005
Thrinaxodon	BP/1/2820	humerus	30.37		75.85	past rapid phase of growth	WB in WPC - PFB	Botha and Chinsamy 2005
Thrinaxodon	SAM-PK-K1121	humerus	32.57		81.34	past rapid phase of growth	WB in WPC - PFB	Botha and Chinsamy 2005
Thrinaxodon	BP/1/5208	humerus	33.46		83.57	past rapid phase of growth	WB in WPC - PFB	Botha and Chinsamy 2005
Thrinaxodon	BP/1/4282a	radius	32.23		96.65	past rapid phase of growth	WB in WPC - PFB	Botha and Chinsamy 2005
Thrinaxodon	BP/1/1730	radius	33.34		100	past rapid phase of growth	WB in WPC - PFB	Botha and Chinsamy 2005
Thrinaxodon	BP/1/5018	ulna	31.87		93.12	past rapid phase of growth	WB in WPC - PFB	Botha and Chinsamy 2005
Thrinaxodon	BP/1/4282b	ulna	33.09		96.65	past rapid phase of growth	WB in WPC - PFB	Botha and Chinsamy 2005
Thrinaxodon	411.1.2.T	ulna				past rapid phase of growth	WB in WPC - PFB	de Ricqlès , 1969
Traversodon ?major	39.4.5.L	humerus				only immature tissue	WB in WPC	de Ricqlès , 1969
Traversodon (Theropsodon)	61.3.3.T	humerus				only immature tissue	WB in WPC	de Ricqlès , 1969
Traversodon (Theropsodon)	61.3.1.T	humerus				only immature tissue	WB in WPC	de Ricqlès , 1969
Traversodon (Theropsodon)	61.3.2.T	femur				only immature tissue	WB in WPC	de Ricqlès , 1969
Traversodon stahleckeri	39.4.3.0	femur			68	only immature tissue	WB in WPC	de Ricqlès , 1969

Trirachodon	SAM–PK–5881a	femur	35.2		100	cyclical growth, past rapid phase of growth	WB in WPC - PFB + cyclical GM	Botha and Chinsamy 2004
Trirachodon	CGP1/79a	radius	40.9			cyclical growth, past rapid phase of growth	WB in WPC - PFB + cyclical GM	Botha and Chinsamy 2004
Trirachodon	SAM–PK–5881d	rib		3.2	100	cyclical growth, past rapid phase of growth	WB in WPC - PFB + cyclical GM	Botha and Chinsamy 2004
Trirachodon	SAM–PK–5881e	rib		2.8	100	cyclical growth, past rapid phase of growth	WB in WPC - PFB + cyclical GM	Botha and Chinsamy 2004
Trirachodon	SAM–PK–5881f	scapula		3.3	100	cyclical growth, past rapid phase of growth	WB in WPC - PFB + cyclical GM	Botha and Chinsamy 2004
Trirachodon	SAM–PK–5881g	scapula		7	100	cyclical growth, past rapid phase of growth	WB in WPC - PFB + cyclical GM	Botha and Chinsamy 2004
Trirachodon	SAM–PK–5881b	tibia	45.1		72	cyclical growth, past rapid phase of growth	WB in WPC - PFB + cyclical GM	Botha and Chinsamy 2004
Trirachodon	SAM–PK–5881c	tibia	62.5		100	cyclical growth, past rapid phase of growth	WB in WPC - PFB + cyclical GM	Botha and Chinsamy 2004
Trirachodon	CGP1/79b	ulna	40			cyclical growth, past rapid phase of growth	WB in WPC - PFB + cyclical GM	Botha and Chinsamy 2004
Tritylodon	B/P/1/5160	humerus				past rapid phase of growth	WB in WPC - PFB	Ray et al., 2004
Tritylodon	B/P/1/5089	humerus				past rapid phase of growth	WB in WPC - PFB	Ray et al., 2004
Tritylodon	B/P/1/4785	humerus				past rapid phase of growth	WB in WPC - PFB	Ray et al., 2004
Tritylodon	B/P/1/4785	radius				past rapid phase of growth	WB in WPC - PFB	Ray et al., 2004
Tritylodon	B/P/1/4785	rib				past rapid phase of growth	WB in WPC - PFB	Ray et al., 2004
Tritylodon	B/P/1/4785	ulna				past rapid phase of growth	WB in WPC - PFB	Ray et al., 2004
Tritylodon sp.	B/P/1/5671	humerus				past rapid phase of growth	WB in WPC - PFB	Chinsamy and Hurum, 2006
Tritylodon sp.	B/P/1/5167	radius				past rapid phase of growth	WB in WPC - PFB	Chinsamy and Hurum, 2006
Trucidocynodon	PV 1053T	radius				only immature tissue	WB in WPC	Botha-Brink et al., 2012

Supplemental Table 4.3. Cortical thickness measurements for sectioned femora of *Scalenodon* and *Luangwa* studied here. Cross-sectional area of transverse thin-sections and medullary cavities were measured in ImageJ and used to calculate cortical thickness (*K*), reported as cortical area (*Ka*) and cortical diameter (*Kd*). All measurements are in μm and μm^2, respectively.

Taxon	Specimen Number	Size Class	Element	Cross-sectional Area	Major Axis	Minor Axis	Medullary Cavity Area	Med Major Axis	Med Minor Axis	Ka	Kd
Scalenodon	NMT RB860	II	femur	348280.21	785.52	564.52	91662.11	458.17	254.73	0.2632	0.5833
Scalenodon	NMT RB1075	III	femur	63151827.77	10876.11	7393.03	5551429.23	3344.92	2113.14	0.0879	0.3075
Scalenodon	NMT RB866	III	femur	143841195	14693.64	12464.19	19284208.43	5730.66	4284.57	0.1341	0.39
Scalenodon	NMT RB864	III	femur	73564696.3	10413.48	8994.63	14756917.42	4682.47	4012.65	0.2006	0.4497
Scalenodon	NMT RB862	III	femur	49381183.12	8499.85	7397.08	13953329.37	4666.85	3806.83	0.2826	0.5491
Scalenodon	NMT RB581	III	femur	72901878.78	9992.29	9289.32	20346294.37	5165.69	5014.95	0.2791	0.517
Scalenodon	NMT RB731	III	femur	127073650.4	13108.87	12342.42	27961667.66	6613.72	5383.04	0.22	0.5045
Luangwa	NMT RB894	I	femur	20262602.45	5708.54	4519.39	4372678.02	2765.55	2013.15	0.2158	0.4845
Luangwa	NMT RB1080	I	femur	26692544.38	5903.17	5757.25	2098359.76	1781.25	1499.91	0.0786	0.3017
Luangwa	NMT RB1078	I	femur	15618223.76	4528.08	4391.65	5184544.41	2784.57	2370.63	0.332	0.615
Luangwa	NMT RB565	II	femur	28566001.85	6549.2	5553.56	4907071.4	2771.79	2254.09	0.1718	0.4232
Luangwa	NMT RB1071	II	femur	46544596.35	8089.79	7325.58	2472719.55	2125.78	1481.04	0.0531	0.2628
Luangwa	NMT RB1072	II	femur	49915949.29	8353.07	7608.58	6448876.43	3398.88	2415.79	0.1292	0.4069
Luangwa	NMT RB882	III	femur	114130561.6	13056.28	11129.94	25883139.22	6285.06	5243.46	0.2268	0.4814

Chapter 5. **CONCLUSIONS**

This dissertation examines bone histology and body size estimates to investigate size/age correlations and life history patterns of non-mammalian synapsids from two key intervals. In Chapter 2, life history patterns are investigated in northern Pangean *Lystrosaurus* species to shed light on the non-uniform effects of the taxon's survival in the immediate aftermath of the extinction interval during the earliest Triassic. In Chapter 3, body size estimates from the near-global distribution of *Lystrosaurus* fossils across Pangea provide new insights on ecosystem health and stability but also indicate that sampling and collecting biases contribute to body size spectra for *Lystrosaurus* assemblages outside of the well-studied Karoo Basin.

By Middle Triassic times, ecosystems across Pangea were recovering and assembling to the modern fauna we see today. In Chapter 4, life history patterns revealed from a systematically controlled ontogenetic series of Anisian traversodontid species critically inform patterns of life history evolution in the mammalian stock lineage and its side branches. Below, I summarize the conclusions from each chapter.

Chapter 2: I and co-authors tested the hypothesis that *Lystrosaurus* from northern parts of Pangea (modern China) had different life history patterns than their southern hemisphere congeners. We found that Chinese *Lystrosaurus* similarly grew rapidly as has been shown in South Africa and Indian *Lystrosaurus* species from the Triassic but Chinese specimens had increased growth marks. This is in contrast to the Triassic *Lystrosaurus* specimens from South Africa, which rarely show slowdowns in growth. In sub-adult sized Chinese specimens, highly vascularized fibrolamellar bone tissue, indicatively of rapid bone growth, is interrupted by up to three growth marks. Interestingly, the largest and presumably most mature specimen in our

sample shows uninterrupted growth. This suggests that *Lystrosaurus* from China had a high intrinsic rate of growth that was developmentally plastic and could arrest periodically, perhaps during times of environmental disturbance.

Chapter 3: I and co-author tested the hypothesis that *Lystrosaurus* body size varies predictably with paleolatitude across the near global distribution of Early Triassic fossil assemblages. In combination with histological results from Chapter 2, our results suggest that mid-latitude Chinese *Lystrosaurus* grew to larger body sizes and may have had longer lifespans than their high-southern latitude relatives. These results demonstrate that the turbulent post-extinction environment of the earliest Triassic typical of southern Pangean ecosystems was not reflected in northern parts of the supercontinent and that tetrapod species living in more temperate conditions enjoyed slightly longer lifespans and reached larger body sizes more readily.

Chapter 4: I compared life history strategies from two coeval cynodont species from the Anisian Manda Beds of Tanzania to provide a comprehensive analysis of intraspecific and interspecific growth patterns. Unlike other life history reconstructions that leverage isolated cynodont specimens from Triassic biozones, this study is the first to sample the entire size series of femora recovered from a temporally and spatially constrained deposit. This allowed for control of local environmental conditions, phylogenetic relatedness, and temporal resolution not available from previous studies. My results indicate that growth strategies differ in closely related cynodont species in ways that cannot be explained by inferred diet, body size, or environment, and instead suggest that inherent differences in bone tissue composition reflect the combined effects of differential rates of growth and adaptations for fossoriality.

VITA

Zoe T. Kulik was born in Bethesda, Maryland. In 2016, she earned a Bachelor of Arts in Geology from Macalester College where she was introduced to the field of paleohistology by Dr. Kristi Curry Rogers. Zoe worked closely with Drs. Curry Rogers and Raymond Rogers throughout her undergraduate career and was hired as the paleohistology lab manager before starting her PhD in Biology at the University of Washington in 2017 where she was advised by Dr. Christian Sidor.